Plasmonic Assay for Molecular-Lipid Membrane Binding, Permeation and Dynamics of Permeation.

A thesis submitted to Dublin City University for the award of PhD

By

Agata Steplewska B.Sc. (Hons)

School of Chemical Sciences,
Dublin City University,
Glasnevin,
Dublin 9.
October 2019

Supervisors:
Professor Tia E. Keyes

Declaration

I hereby certify that this material, which I now submit for assessment on the programme of study leading to the award of PhD is entirely my own work, that I have exercised reasonable care to ensure that the work is original, and does not to the best of my knowledge breach any law of copyright, and has not been taken from the work of others save and to the extent that such work has been cited and acknowledged within the text of my work.

Signed: ______________________________

ID No.: __11318101______

Date: _________________

Acknowledgments

First and foremost, I would like to thank Prof. Tia Keyes, for giving me this great opportunity. I am grateful for all the help and guidance over the last few years. I would also like to thank the technical staff of the DCU chemistry department, who made sure everything ran smoothly and were more than willing to help when needed and provided colouring competitions to keep the stress levels down.

I would like to thank all the extended members of the research group, who were always there to help. In particular Kho, Aurélien, Chris and Aisling, who answered countless questions and helped fix the Raman, god knowns how many times. Also, to Karmel and Guil for their spontaneous wisdom and rants. It was always useful to know others were in the same boat.

A big thank you to my other DCU friends who helped along the way, in particular, Ruth, Asmita, Charlie, and Piers. Thank you for all the support, walks and random gym sessions.

To the Brady's bunch, I owe a lot of gratitude. You guys put up with me since school and I would not have been able to do this without you guys. You guys provided distractions and motivation as needed, keeping me sane. Also thank you for knowing when to stop asking nightmare-invoking questions like "so, when are you finished" *shudders*. So, a big thanks to Rhys, Becca, Eoin, Paul, Cian, Áine, Seánie, Creedo, Rob, Sarah, Anni and Sinéad. You guys are the best!

Lauren, thank you for putting up with all the random and going along with my crazy ideas. You have become one of my closest friends and I think we are both better (if not poorer) for it. Thank you for your advice, support and all the good times. Chris and David, you boys also deserve a big thank you. Both of you helped keep me grounded and high-spirited. Thank you.

Finally, the biggest thanks to my parents for supporting me through this. You were there the entire time (even when you wished you weren't) and your encouragement was more helpful then you would have known. So, thank you.

"Every so often, you have to unlearn what you thought you already knew, and replace it by something more subtle"

-Terry Pratchett

Table of Contents

Glossary of Abbreviations:

Abbreviation	Expanded
AC	Alternating current
AFM	Atomic force microscopy
bpy	2,2'-bipyridine
C6	6-mercaptoal-1-hexanol
CACO-2	Human epithelial colorectal adenocarcinoma cells
CH	Cholesterol
DIBs	Droplet interface bilayers
DNA-AgNCs	DNA-silver nanoclusters
DOPC	1,2-dioleoyl-sn-glycero-3-phosphocholine
DOPE	1,2-dioleoyl-sn-glycero-3-phosphoethanolamine
DOPS	1,2-dioleoyl-sn-glycero-3-phospho-L-serine
DPPG	Dipalmitoyl-L-a-phosphotidylglycerol
EIS	Electrochemical Impedance Spectroscopy
EM	Electromagnetic
FCS	Fluorescence correlation spectroscopy
FRET	Förster resonance energy transfer
FLCS	Fluorescence lifetime correlation spectroscopy
GUV's	Giant unilamellar vesicles
IAMs	Immobilised artificial membrane chromatography
ILC	Immobilised liposome chromatography
LB	Langmuir-Blodgett
LEKC	Liposome electrokinetic chromatography
LOD	Limit of detection
MDCK	Madin-Darby canine kidney
MDE	Relative molecular detection
MEF	Metal enhanced fluorescence
PAMPA	Parallel artificial membrane permeability assay

Papp	Permeability coefficient
PBS	Phosphate buffer solution
PC	Phosphatidylcholine
PDMS	Polydimethylsiloxane
PE	Phosphoethanolamine
PI	Phosphatidylsitol
PMMA	Poly-methyl methacrylate
PMMA	Poly-methyl methacrylate
PS	Phosphatidylserine
Ps	Polystyrene
RT	Room temperature
RRS	Resonance scattering
Ru-DPPZ-Ester	$[Ru(DPPZ)(bpy)(bpyArCOOH)]^{2+}$
Ru-DPPZ-R8	$[(Ru(DPPZ)(bpy)(bpyArCONH\text{-}RRRRRRRR\text{-}CONH_2)]^{10+}$
Ru-Tap-Ester	$[Ru(tap)_2(bpyArCOOH)]^{2+}$
Ru-Tap-R8	$[(Ru(tap)_2(bpyArCONH\text{-}RRRRRRRR\text{-}CONH_2)]^{10+}$
SAM	Self-assembled monolayer
SEF	Surface enhanced fluorescence
SEM	Scanning electron microscope
SERRS	Surface enhanced resonance scattering
SERS	Surface enhanced Raman spectroscopy
SM	Sphingomyelin
SP	Surface plasmons
THF	Tetrahydrofuran
Tjs	Tight junctions
Z	Total impedance

List of Publications & Presentations:

Publications:

Patent no. P12435GB00. “A method and device for assaying the interaction and dynamics of permeation of a molecule and a lipid bilayer”.

“Plasmonic assay for molecular-lipid membrane binding, permeation and dynamics of permeation”, manuscript in preparation

“Investigation of ruthenium (II) polypyridyl peptide conjugates permeation through “nature’s own” bilayers using metal enhanced fluorescence”, manuscript in preparation.

Poster & Presentations:

Plasmonic Assay for molecular-lipid membrane binding, permeation and dynamics of permeation, N.I.C.E. 2018, October, Nice, France. (Poster)

Plasmonic Assay for molecular-lipid membrane binding, permeation and dynamics of permeation, Chemistry Research day 2018, May, Dublin, Ireland. (Flash talk).

Plasmonic Assay for molecular-lipid membrane binding, permeation and dynamics of permeation, Chemistry Research day 2019, May, Dublin, Ireland. (Poster).

Plasmonic Assay for molecular-lipid membrane binding, permeation and dynamics of permeation, Annual Congress of the institute of Chemistry of Ireland 2019, May, Dublin, Ireland. (Poster).

Plasmonic Assay for molecular-lipid membrane binding, permeation and dynamics of permeation, Irish Universities Chemistry Research Colloquium 2019, June, Dublin, Ireland. (Poster).

Plasmonic Assay for molecular-lipid membrane binding, permeation and dynamics of permeation, EBSA ICBP-IUPAP Biophysics congress 2019, July, Madrid, Spain. (Poster).

Abstract:

Plasmonic Assay for Molecular-Lipid Membrane Binding, Permeation and Dynamics of Permeation. - Agata Steplewska

Understanding how a given compound interacts with lipid bilayers at the skin, gut or blood-brain barrier and whether it diffuses through cell membranes is critical information for pharmaceutical and biotechnology industries. Prior to moving to more expensive cell-based testing, potential drugs are usually evaluated for drug-likeness to eliminate targets unlikely to make it through more expensive evaluation in the drug pipeline. This thesis focuses on demonstration of a novel approach of a qualitative membrane permeability assay based on plasmonic enhancement of analyte signal. The assay provides insights into the dynamics of drug-membrane interaction and permeation into the cavity.

Chapter 1 reviews the literature relevant to the key aspects of this work, including the cell membrane, current biophysical models of cell membranes, the microcavity array substrates and their applications in Raman and fluorescence spectroscopy. Chapter 2 outlines the optimisation of sphere assembly, development of gold microcavity arrays, formation of lipid bilayers and their examination of stability and integrity. Chapter 3 investigates the permeation and dynamics using SERS, of two anti-cancer drugs, doxorubicin and daunorubicin at different concentrations. Key Raman peaks for DOPC, sphingomyelin, cholesterol and the two drugs were identified. Through changes in the spectra, we could identify drug-membrane interactions and diffusing into the cavity.

Chapter 4, using an analogous approach to chapter 3, examined the application of the substrates for detection of analyte arrival through fluorescence. MEF allowed for the identification of drug permeation and residence time of the bilayer. Interestingly, different dynamics were observed, dependant on membrane compositions and due to aggregation at higher concentrations. Finally, chapter 5 presents the advancement of the assay to a more microfluidic platform that facilitates for lower volumes while allowing for drug delivery and monitoring. This was applied to more biomimetic bilayer compositions, where it became evident that the presence of a charged lipid has an effect on the permeability of the drugs. Subsequently, the permeation of ruthenium (II) metal complexes was evaluated to determine if their cellular uptake is through passive diffusion. All four ruthenium complexes were found to be impermeable, which is consistent with cell-based experiments, that indicate that they are taken up in cells through active transport mechanisms.

Chapter 1: Literature Review

1.1 Introduction

Anticipating how potential new therapeutic agents interact with human cells is a critical consideration for the pharmaceutical and biotechnology industries. Specifically, understanding how a given compound interacts with lipid bilayers at the skin, gut or blood-brain barrier but particularly anticipating whether it likely to passively diffuses through the cell membrane is very important, particularly for materials with intracellular targets[1–3].

In anticipating drugs with favourable absorption, distribution, metabolism and excretion properties, the Lipinski's rule of five[4,5], which defines chemical properties correlated with drug-likeness, is traditionally used. These are; 1) molecular weight less than 500 amu, 2) number of hydrogen bond donors of 5 or less, 3) number of hydrogen bond acceptors of 10 or less, and 4) an octanol-water partition coefficient (LogP) less than 5. These are broad physiochemical properties that statistically correlate with membrane permeability but there are numerous exceptions and they do not address the complexity of membrane molecular interactions[4].

Increasingly, molecular simulations are being applied to model the permeation dynamics of a membrane[6–8]. However, the time range most typically used for molecular dynamic simulations is too short to observe the full permeation process[9]. There are two models that are mainly used to describe the permeation mechanism; solubility-diffusion and transient pore formation. The first model is also known as the Meyer-Overton theory, originally derived for anaesthetics, correlates membrane permeability to the oil/water partition coefficient[4,9]. The latter model focuses on spontaneous pore formation and a molecules diffusion through these pores. The likelihood of pore formation is small, but studies have shown that they can occur due to antimicrobial peptides, external stress and electroporation to name a few[9].

Drug lipophilicity is a governing factor in a drugs permeability and is widely used to predict membrane permeability. Currently, the first step in determining the lipophilicity of a drug is to experimentally determine the LogP, i.e. the log10 partitioning of a neutral drug species between n-octanol and water. Unfortunately, this method is rather crude as it does not consider factors such as ionisation, pH etc. and in particular does not encompass how the membrane structure is more complicated than an oil layer. The distribution coefficient (logD) takes ionisation into account and is therefore is also widely used to determine a drugs lipophilicity[10].

Parallel Artificial Membrane Permeability Assay (PAMPA) and Cell-based assays are two of the main methods of permeability testing once LogP etc. is determined, although there are numerous other methods available[4,9]. However, both methods have a large number of disadvantages. Cell-based assays can be considered the most bio-representative and uptake in such models can reflect both passive and/or active transport; however, distinguishing between which is occurring can be challenging. Furthermore, cell-culture is expensive and requires considerable user expertise. Also, as most cell lines are from immortalised cells, they may not act as a true model. Cell lines can also be very heterogeneous with the expressed proteins and lipids varying, even within the same cell-lines, culture to culture-based media, passage number and other factors[11,12], and therefore, can be difficult to elucidate specific insights into the cell-drug interactions. PAMPA is a much faster method, amenable to high throughput but can only indicate if passive transport is likely. As the platform does not contain a true bilayer, it cannot be considered very biomimetic and correlation between PAMPA predicted uptake and uptake in live cells can be quite poor[12,13].

In reality, unlike PAMPA, cell membranes are a highly transversally organised structures, formed due to the amphipathic nature of their main constituents; phospholipid. Lipid membranes constitute a significant component of our bodies and are the key barrier a drug encounters as it progresses to its target, so the development of improved, accurate lipid membrane models that accurately reproduce the laterally organised phospholipid bilayer is of key interest to understand drug toxin, or virus permeability and the behaviour of membrane proteins imbedded at these interfaces. Numerous lipid membrane models have been thoroughly studied over the past 30 years[14–16]. Some such as liposomes and single lipid bilayers (SLBs) have been prepared with diverse lipid compositions with lipid ratios designed to mimic specific membrane types, be it healthy or diseased. Proteins and carbohydrates have also been successfully inserted to try mimic a more accurate model, but this has been met with limited success[14].

To accurately evaluate drug-membrane interactions at an artificial bilayer, a sensitive means of interrogation of the bilayer and its molecular interactions is required. The method must also be amenable to the model. Fluorescence and electrochemical impedance spectroscopy (EIS) have been used with great reported success to monitor and evaluate drug-membrane interactions at artificial bilayers[17–20]. EIS allows for information on the resistance and capacitance of the membrane to be obtained, meaning its stability and thickness can be monitored[18,21,22].

Fluorescence is a well-established analytical method for bio-detection fields. Surface enhanced Raman spectroscopy (SERS) has increasingly become of interest due to its sensitivity and ability to provide structural insights[23]. Through the use of surface enhanced substrates, these methods may detect concentrations down to nanomolar concentrations with Raman[23] and fluorescence[24].

Other advantages of these methods are the minimal sample preparation required and their non-destructive qualities. Raman spectroscopy (RS) provides structural information, but shows only weak emission from water[23]. Therefore, it can be used with aqueous media, including buffers that are viable for lipid bilayer models such as phosphate buffer (PBS), meaning they should not interfere with any of the obtained results.

A metal substrate is required for plasmonically enhancing Raman or fluorescence signals. Numerous studies have been completed[23] on different metals, but gold and silver are most widely studied due to their ability to provide the best enhancement while also being chemically stable and inert. A wide variety of nanostructuring[23,25,26], e.g. nano-rods, nanoparticles and nanocavities, have been exploited for surface enhancement. Microcavities are particularly attractive for our purposes as they provide a reproducible platform that allows for the successful formation of lipid bilayers[27].

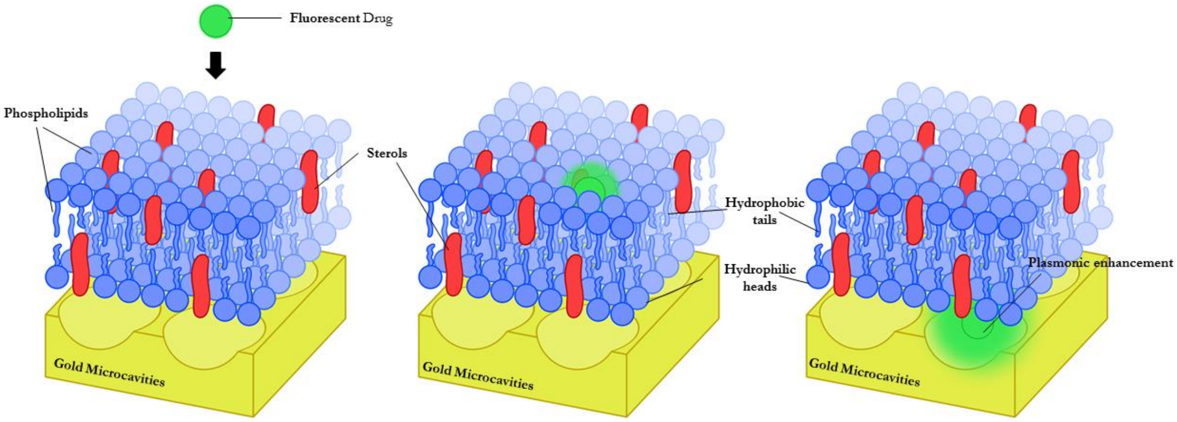

Figure 1: Schematic diagram of the proposed membrane permeability assay. This consists of lipid bilayers consisting of phospholipids and occasionally sterols spanned over 1 µm sized gold microcavities. Drug/dye is then introduced, and emission is monitored using Raman or fluorescence spectroscopy.

The proposed concept behind this study, as shown in Figure 1, exploits SERS and metal enhanced fluorescence (MEF) enhancement to monitor for the arrival of a drug at a location which has high local plasmonic field enhancement, which is behind a lipid bilayer, i.e.. the drug only experiences significant plasmonic field enhancement once it has passed through the bilayer.

The substrates used here were created on gold chips which contain hexagonally close-packed gold microcavities. The fabrication method of the substrates is explained in detail below in section 1.4. A lipid bilayer can be spanned over these cavities using a combination of the LB method and vesicle fusion to create the lipid barrier. The composition and symmetry of the bilayer can be varied using this method which is ideal for mimicking different membranes depending on interest. Raman and Fluorescence spectroscopy was then be used to monitor the platform as a drug is introduced.

Ideally, this work will lead to the development of a membrane permeability model that can successfully detect not only if and how drugs interact with the membrane, but also the dynamics of this interaction and the speed of permeation through into the cavity. This model should allow for the creation of specific membranes of pharmaceutical and medical interest, be it a healthy skin model or a diseased Alzheimer's model, which allows for greater specificity and more accurate knowledge than current permeability models.

1.2 Cell Membranes and their Components

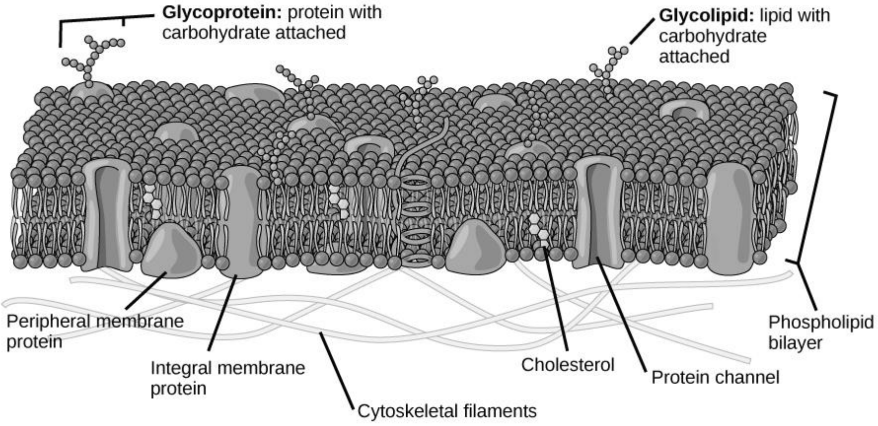

Figure 2: Schematic diagram[28] depicting the plasma membrane found surrounding cells. The membrane is composed of a phospholipid bilayer, cholesterol, glycolipids, glycoproteins, and proteins such as membrane proteins and channels.

Lipid membranes, as shown in Figure 2, are an ordered but highly fluidic structure that surrounds every cell and also the organelles of the cell. Lipid membranes help regulate the flow of nutrients and mediate signalling between cells and they also protect sub-cellular structures. There are three main components to a cell membrane, lipids, proteins, and carbohydrates. Lipids may be sub-divided into phospholipids, sphingolipids and sterols. A carbohydrate can also be attached to a lipid, and is then known as a glycolipid[14]. Phospholipids, as shown in Figure 3, are amphipathic molecules with a lipophilic tail, usually comprising of two long chain saturated or unsaturated fatty acids and a hydrophilic head group, typically of glycerol linked to a phosphate group. Phospholipids self-assemble in aqueous media into a bilayer in which the polar head groups are on the outside and the tails align along the core[14]. Phospholipid bilayers provide an essential support for maintaining structure and function of membrane proteins[15]. Sterols such as Cholesterol (CH), (which typically composes 20-50 % of the bilayer[6]) play a role in structuring the bilayer and signalling. They are composed of polycyclic structures resulting in a hydrophobic moiety.

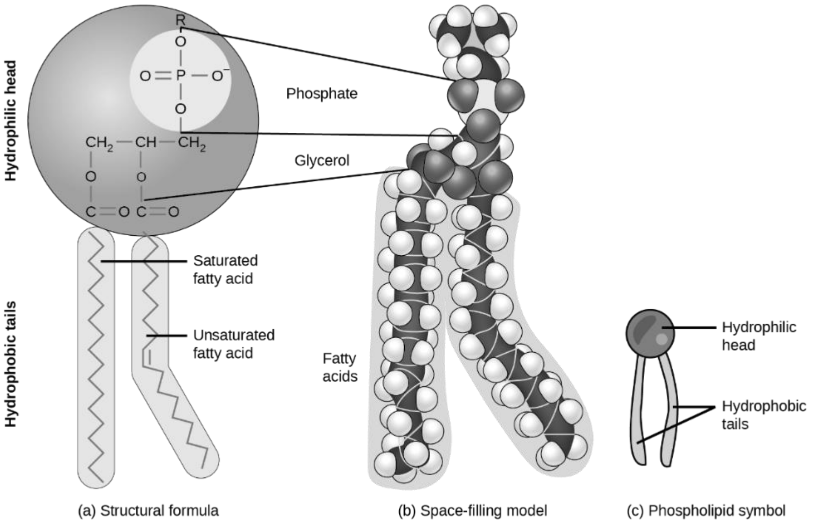

Figure 3: Schematic diagram[28] depicting the structure of a phospholipid. Phospholipids consist of a hydrophilic head made of a phosphate and a glycerol, and a hydrophobic tail, which can be made of a saturated or unsaturated fatty acid.

Typically, in lipid membranes, specific lipids can be observed exclusively in the outer or the inner leaflet. For example, animophospholipids are typically found in the cytoplasmic (inner) leaflet, whereas cholinephospholipids prefer the exoplasmic (outer) leaflet[29]. DOPC (structure shown in Figure 4) is a glycerophospholipid which is naturally occurring within eukaryotic cells. It is most commonly found in the outer leaflet of cell membranes where it functions as part of the permeability barrier[30]. Phosphatidylethanolamine (PE) is the second most common component within mammalian membranes. Its molecular structure consists of a cone-shape, and its function is to promote bilayer-to-hexagonal phase transitions that may facilitate membrane fusion[31]. PE is mainly found in the inner leaflet[32].

Sphingomyelin (structure shown in Figure 5) is a very important component of animal cell membranes. SM's molecular structure is similar to certain glycerophospholipids such as PC, but unlike the latter, it is capable of forming intermolecular and intramolecular hydrogen bonds. The large majority of sphingomyelin is located within the outer leaflet[32]. Cholesterols (structure shown in Figure 5) concentration varies with membrane origin and type. It condenses the bilayer structure and is believed to serve two main functions are to increase the stability of the membrane and to decrease the permeabilty[31].

The inner leaflet of eukaryotic plasma membrane typically contains all of the phosphatidylserine (PS) and phosphatidylsitol (PI) lipids and most of the phosphoethanolamine and cholesterol, and very little PC[32]. Both PS and PI are negatively charged at physiological pH's. The lipids localisation in cytosolic leaflets must be taken into consideration in future development of artificial bilayers as they may influence permeability.

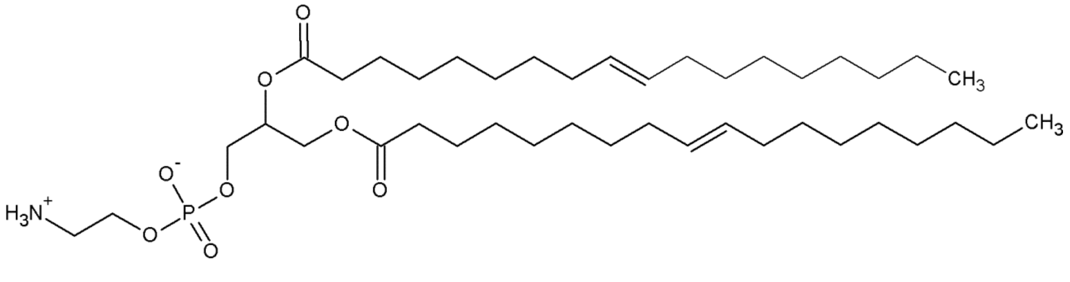

Figure 4: Chemical structure of 1,2-dioleoyl-*sn*-glycero-3-phosphocholine (DOPC)

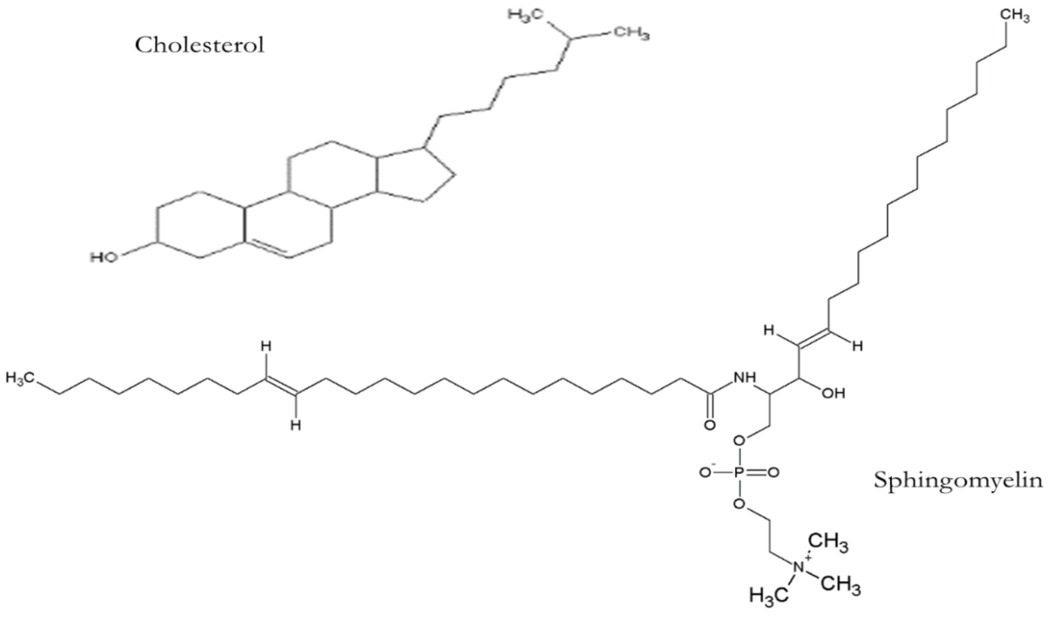

Figure 5: Chemical structure of Cholesterol (CH) and Sphingomyelin (SM).

There are three classifications of membrane associated proteins; integral, peripheral, and lipid-bound proteins[33.] The former are embedded within the bilayer, peripheral are attached to the exterior, and the latter is only within the bilayer boundaries. Cell membranes typically comprises 50 % by weight protein, of which 20 % are transmembrane[14]. Ideally, a bilayer model should be created which incorporates these proteins to mimic a real membrane. Complex protein bilayers are of interest, as they are often important drug targets. G-protein-coupled receptors have been reported to make up the highest percentage of drug targets in humans, followed by enzymes and then transporter proteins. The actual percentages of which are vary from study to study. Interestingly G-protein-coupled receptors only make up roughly 4 % of human proteins[34]. Thus, understanding protein interactions and dynamics within a cell is invaluable information.

Bilayer models also allow for the study of these proteins without the intrusion of other complexities in the cell, allowing for the focus to be solely on the components of interest. The demand for in-vitro cell membrane models has led to the development of numerous types of membrane models including; black lipid membranes, supported lipid bilayer membrane, air-stable lipid bilayer membranes, hybrid lipid bilayer membranes and many more. Each membrane model has its own advantages and disadvantages and depending on the interest of the study, some may be better suited than others. The main models are discussed below.

1.2.1 Liposomes

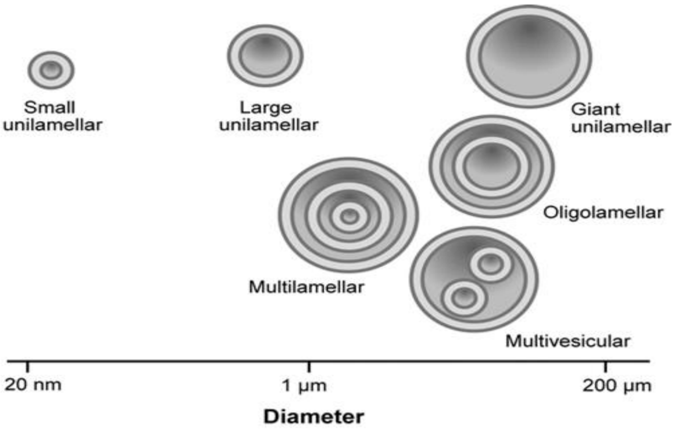

Figure 6: Schematic diagram showing different classifications of liposomes and their typical size[35].

Liposomes, also known as lipid vesicles, were first reported by Dr Alec Bangham in 1964 and are considered one of the earliest membrane models[36]. Liposomes are free-standing structures of quasi-spherical shape[37]. Vesicles are prepared in a straightforward manner, consisting of the rehydration of dried lipids in a polar solvent (typically water), resulting in the spontaneous formation of vesicles. This results in a diversity in the size of the vesicles, as shown in Figure 6, and they can often contain layers within each other, which is known as multilamellar vesicles. To obtain uniform vesicles sizes, extrusion through a polycarbonate membrane or sonication can be used; resulting in 50 to 100 nm sized, small unilamellar vesicles[38]. These are commonly used for drug delivery and drug-membrane interactions[39–42] and for studying the influence of specific lipids such as cholesterol in the bilayer[31,43,44].

Giant unilamellar vesicles (GUVs) are liposomes of 10-100 μm in size, created through the rehydration of the lipids in the presence of an alternating current (AC) electric frield[37,45]. These vesicles are commonly used in optical imaging for examining dynamics[46], lipid rafts[19,45,47], proteins[48] etc. Gaul et al. used GUV's to create physiologically relevant model to explore integrin $\alpha_{IIb}\beta_3$ reconstitution into lipid vesicles through fluorescence lifetime correlation spectroscopy (FLCS). They found that the integrin freely diffused into the bilayer and were able to identify that it preferred liquid disordered phases within the lipids[37]. In this study, small unilameller vesicles were used to create single lipid bilayers.

1.2.2 Single Lipid Bilayers (SLB)

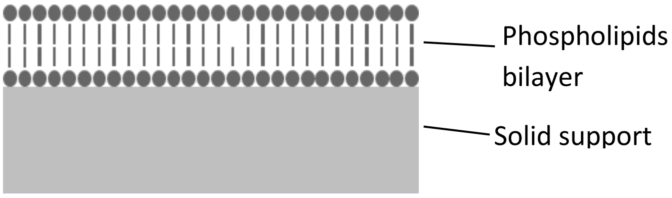

Figure 7: Diagram of a single lipid bilayer spanned on a planar solid support.

Single lipid bilayers (SLB) are continuous lipid bilayers that are assembled or deposited onto a planar solid support. They have proven to be more robust and stable than other prevalent bilayers such as black lipid membranes (BLM), and due to their interfacial nature, allow for surface specific analytical techniques. Lipids in such structures are quite fluidic due to the 10-20 Ǻ water layer which separates the membrane from the solid surface[14]. The water layer depends on surface properties of the substrate and so, there are restrictions on the surfaces that are suitable for this method; as they are required to be hydrophilic, smooth and clean[14]. Materials such as fused silica, mica and borosilicate glass have proven to work best, although others have been used successfully[14]. It has been observed that the hydrophilicity of the support is an important factor for bilayer formation and fluidity, although surface roughness also plays a role and surfaces with significant nanoscale features do not support a continuous bilayer[16].

There are three main methods to create SLBs. Of these, the first consists of the transfer of amphiphilic molecules from an air-water interface to a solid substrate, which is commonly done using a Langmuir-Blodgett (LB) trough. The lower leaflet is created using the LB method while the upper leaflet is created using the Langmuir-Schaefer method. The LB & Langmuir-Schaefer method allows for the creation of asymmetric bilayers. The disadvantage of this method is the difficulty in incorporating transmembrane proteins as they are exposed to the air and can become denatured[14].

The Langmuir-Blodgett method was developed by Irving Langmuir & Katherine Blodgett. This method utilises the ability of amphiphilic surfactants to self-assemble at an air/water interface. This method has become very commonly used due to four main reasons; 1) allows for precise control of the thickness of the monolayer, 2) allows for a homogenous deposition over a range of areas, even very large ones, 3) allows for the creation of multi-layered structures with a varied composition, and 4) works with most solid substrates.

Surface tension is very important for this method to work. Surface tension is created naturally due to the molecule's cohesion; the attraction to each other, which should be equal in all directions. This results in molecules at the air/water surface to have an imbalance in this attraction as they have a larger attraction towards the liquid phase than the gaseous phase. This gives rise to interfacial free energy, as the molecules try to minimise the surface area.

Amphiphilic molecules are widely applied to LB methods due to their ability to orientate themselves, so their hydrophilic end is in the liquid, and the hydrophobic end is in the air. If pressure is applied to compress these, they will form a close-packed homogenous monolayer, known as a Langmuir film. The length of the chain on the amphiphilic molecule effects the formation of this layer, long chains will crystallise on the surface, and too short a chain may form a micelle.

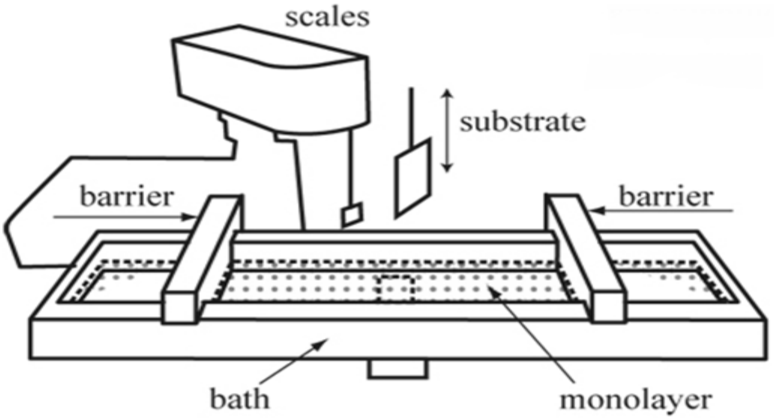

Figure 8: Schematic diagram[49] of a Langmuir Blodgett trough, where the barriers are compressing the monolayer to orientate themselves, while the scales measure pressure ensuring the collapse of the monolayer does not occur.

The LB trough itself is typically made from Teflon, as this material is hydrophobic, minimising lipid adhesion and leakages. The barriers, as shown in Figure 8, are typically made of Delrin, which is hydrophilic and heavy, preventing the monolayer from going under the barriers, or they may also be made from Teflon. The Wilhelmy-plate method is commonly used to measure surface pressure (Π). This is comprised of a plate being partially suspended within the subphase (scales section in Figure 8), the acting force due to the surface tension can then be determined. Thin plates are commonly used due to higher sensitivity. Plates can be made of glass, silicon, filter paper etc. The surface pressure is equal to the surface tension of the liquid alone (γ) minus the surface tension with the monolayer (γ_0).

For the amphiphilic monolayer to be transferred/deposited from the trough to the solid substance, the surface pressure is kept constant as the sample is dipped vertically and then removed. The speed of dipping and removal may affect the absorption of the monolayer onto the substrate (Figure 9). The pressure is critically important to ensuring film packing, usually pressure below 10 mN/cm is ineffective and above 40 mN/cm, film rigidity can pose difficulty and can lead to film buckling. The transfer ratio is the quantity and quality of the deposited monolayer on the substrate. This is the decrease in the monolayer area during a deposition stroke and the area of the substrate. Ideally, this will equal 1 but is often not the case. It is also possible to orient the solid substrate horizontally with respect to the monolayer during dipping; this is known as Langmuir- Schaeffer.

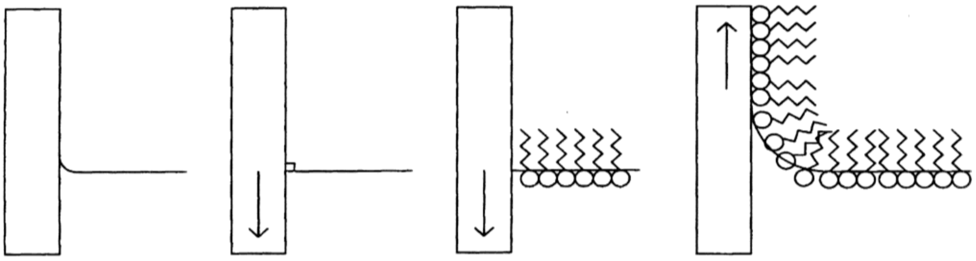

Figure 9: Schematic diagram showing the process of monolayer deposition using Langmuir Blodgett technique.

The second method is the easiest and most versatile method. It is the adsorption and fusion of small unilaminar vesicles from an aqueous suspension to the substrate surface. These vesicles fuse to each other and will then rupture to form a planar supported bilayer. There are various methods to do this. One of which involves the extrusion of multilaminer vesicles through a porous polycarbonate membrane under high pressure. Another method consists of sonification and ultracentrifugation of the aqueous lipid suspension. The quality of the resulting bilayers by all these methods are subject to factors such as the vesicle size, surface charge, roughness, cleanliness, the solution pH, ionic strength and the osmotic pressure. The incorporation of transmembrane proteins is achieved through a gentle process such as detergent removal via dialysis[50].

The third method is a combination of the previous two methods, where the monolayer is created using the LB and the upper layer using vesicular fusion. This combination of methods allows for the formation of asymmetric bilayers with incorporated transmembrane proteins. Other development methods include spin coating, microcontact printing, solvent-exchange deposition and evaporation induced assembly [50].

Single lipid bilayers have been extensively studied and exploited over the years. This ranges from monitoring the lipids[51] themselves, to incorporating proteins[52], to growing crystals[53,54] on them. The LB technique has been commonly used for the development of SLB's. For example, Leverette et al. created phosphatidylcholine (PC) bilayers on planar gold substrates for Raman and infrared reflection-absorption spectroscopy interrogation. Through this, they were able to obtain structural information on their bilayer system[55].

Asymmetric supported lipid bilayers have also been created by using LB/Langmuir Schaeffer technique. Yuan et al. monitored the movement and rearrangement of 1,2-dioleoyl-sn-glycero-3-phosphocholine (DOPC), 1,2-dioleoyl-sn-glycero-3-phospho-L-serine (DOPS) and 2-dipalmitoyl-sn-glycero-3-phosphocholine lipids on mica-on-glass substrates, through AFM and total internal reflection fluorescence microscopy. They tracked lipid molecules for 48 hours and found that the fluorescent dye movement was independent of lipid movement[56].

Vesicle fusion methods are attractive as they also can allow for asymmetric lipid bilayer compositions and for the incorporation of proteins[16]. They also allow for bilayer formation within a controlled patterned formation, which could be exploited for biosensing. Lenz et al. formed bilayers onto grid-patterned Polydimethylsiloxane (PDMS) using this method. Using fluorescence microscopy studies, they observed that the bilayers only formed on the 2 x 2 mm squares of interest[57]. In another study, Kam et al. used vesicles in the development of a microfluidic device. They reported using laminar flow to apply, remove and reconstruct lipid bilayers on a glass surface, shown in Figure 10. Mixed lipid compositions were formed onto the glass substrate. By applying an electric charge through electrophoresis, the charged lipids were caused to migrate unilaterally, as shown by the red lipid movement in Figure 10. The charged lipids were then stripped, and new lipids were applied on the bare surface[58]. This method could be highly useful for biomolecule targeting.

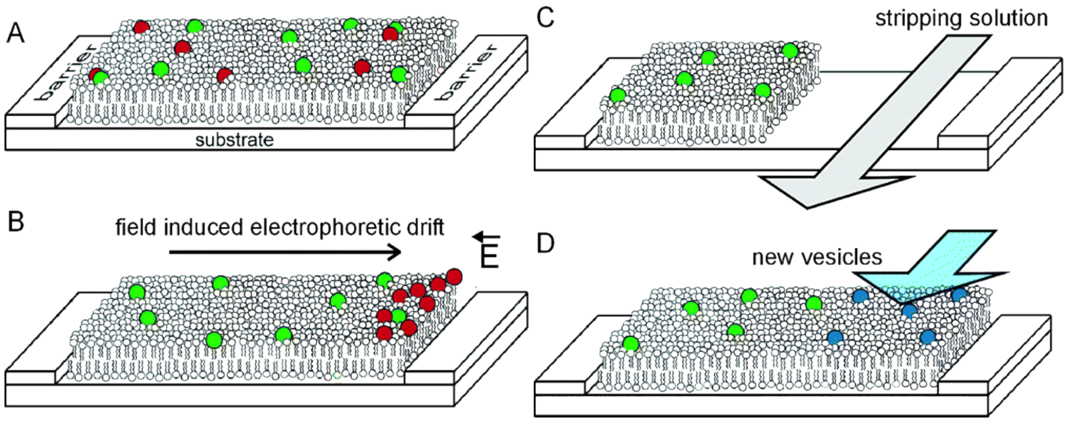

Figure 10: Schematic diagram of the method used by Kam et al. for micropatterning and stripping of lipid bilayers. A) Lipid bilayer was created by vesicle fusion and is confined within microfabricated barriers. Red marked lipids correlate to charged lipids and green to neutral lipids. B) electric field is applied, resulting in the migration of the charged lipids. C) a stream of stripping solution was applied, removing the charged lipids. D) a new species was then applied[58].

1.2.3 Tethered and Cushioned Lipid Bilayers

Tethered lipid bilayers are very similar to SLBs but include a connector between the bilayer and the substrate[29]. They have proven to have long-term stability of up to months and allow for two dimensional fluidity due to the exposure of the bilayer to aqueous reservoirs on both sides[59]. There are two main "tethering units" used; alkanethiol and polymer tethers. Both tethering methods are shown in Figure 11. Alkane thiols were originally used due to their self-assembly capabilities and strong affinity to metals[60]. In fact, thiols spontaneous assemble on gold has been studied in great detail over the years and have been proven to be stable for long periods, even years at room temperature[60]. Long chained thiols have proven to be more thermally stable on gold than their shorter chained counterparts. A looser packing is also observed in shorter chain lengths ($n<8$)[60], this is because of the importance of lateral Van Der Waals bonding along the monolayer chain which contributes to the overall bonding energy of the self-assembled monolayer (SAM).

Polymer tethering, shown in Figure 11, is where the lipid vesicles fuse upon a layer of polymer macromolecules, forming a bilayer. These are supported rather than tethered to the substrate and is known as cushioned lipid bilayers[61]. This support also provides a sufficient enough distance to host transmembrane proteins and to allow ion transport[59]. Thiolipid-based tethered bilayers are suitable for electrochemical applications and are therefore very appealing to many, as the solid substrate has the ability to act as an electrode.

The use of peptides as a tether has also been demonstrated as an attractive method for membrane protein investigation. As shown in Figure 11, this consists of incorporating a protein into the lipid bilayer. Chadli et al.[62] demonstrated protein tethering by using α-laminin thiopeptide as their tethering peptide, where an N-terminal allowed for its binding to gold and its C-terminal was modified with four histidine residues. They showed successful spanning of varying lipid composition in various ratios that contained the lipids such as, PC, phosphatidylserine (PS), phosphoethanolamine (PE), sphingomyelin (SM) and CH. They then inserted a membrane protein and through AFM and fluorescence recovery after photobleaching found that the membrane remained fluid and continuous.

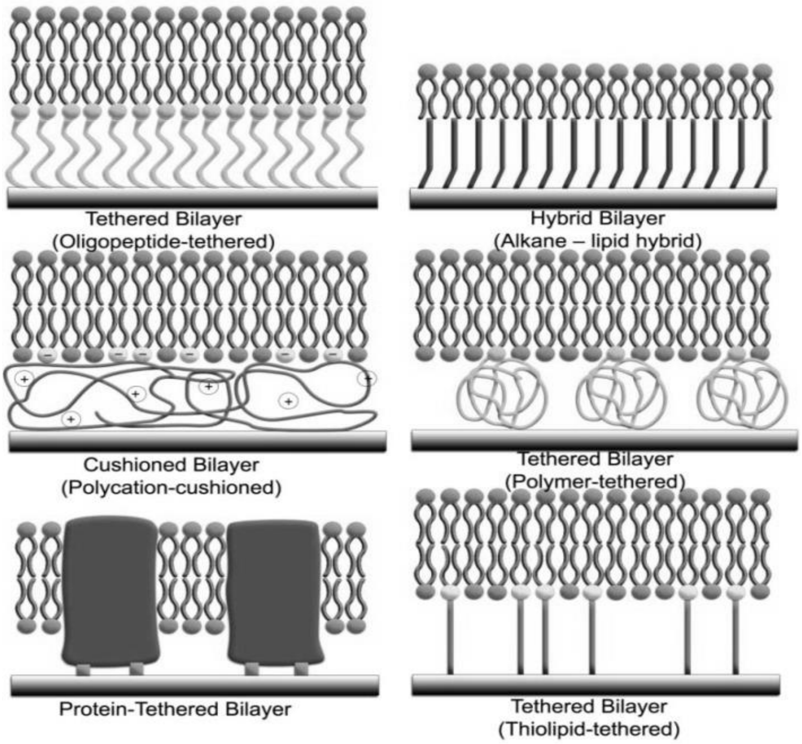

Figure 11: Schematic diagram of different variation of tethered lipid bilayers on solid supports[59].

Steinem et al. reported the successful formation of thiol tethered lipid bilayers on gold substrates by impedance investigation[22]. This lead to Keyes et al. work, which has shown success through the use of thiol tethered lipid bilayers on gold microcavities, where the bilayer is formed through the LB technique and vesicle fusion[17,21,27]. They reported DOPC bilayer stability on gold microcavities for up to 6 hours through electrochemical interrogation[18]. These bilayers allowed for electrochemical study of drug-membrane interaction of nonsteroidal anti-inflammatories, antibiotics and bisphosphonates, allowing for the detection of adsorption and weak penetration of the drugs[17]. The cavities have the added advantage of allowed for study through microscopy due to the pore size of the cavities being substantially large enough.

Im et al. showed similar work with lipid membranes spanning 200 nm diameter sized pores. As shown in Figure 12, lipid bilayers created by vesicle rupture are spanned over gold nanopore arrays, which allowed them to use surface plasmon resonance sensing. They report observing a red-shift in resonance attributed to the incorporation of transmembrane proteins to the bilayer[63].

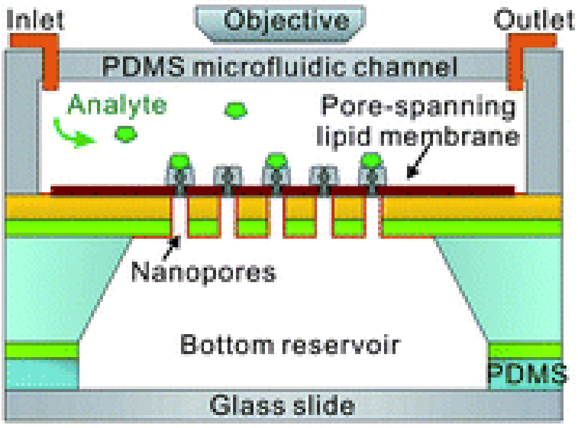

Figure 12: Schematic diagram showing a single channel PDMS flow cell used by Oh et al. for lipid membrane measurements[63].

1.2.4 Droplet Interface Bilayers

Droplet interface bilayers (DIBs) are a recent technique, which allows for the formation of multiple bilayers in parallel. A shown in Figure 13, there are two methods for the formation of these bilayers; I) deposition of an aqueous droplet on a lipid–solvent mixture, resulting in a “lipid-out” assembly. Or II) deposition of lipid vesicles on organic solvent, “lipid in”. These droplets spontaneously form a lipid monolayer which may then collide and form a bilayer[29]. This has proven to be a robust technique which produces DIB’s that can last from days to weeks[64] and is commonly used for investigations on the ionic flux through membrane pores in bilayers. For example, Leptihn et al. used DIBs to study ion channels through electrical activity[65]. Whereas, Castell et al. used the Ca^{2+} flux in a DIBs array, to quantify the membrane protein α-hemolysin’s inhibition through fluorescence measuremtns[66].

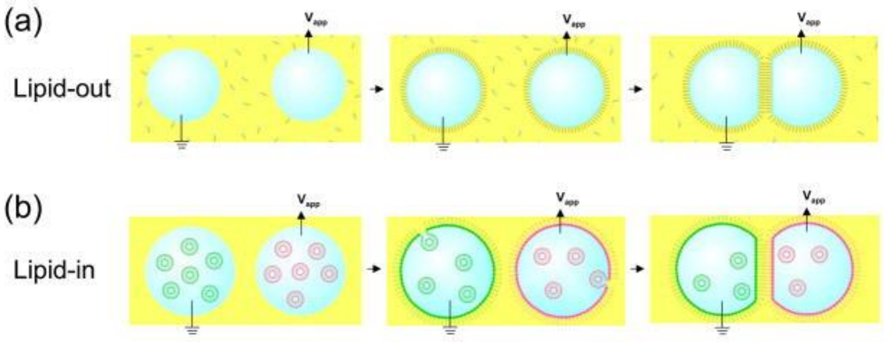

Figure 13: Schematic diagram of the formation of A) lipid-out and B) lipid-in droplet interface bilayers. Where A) Lipids form a monolayer on aqueous droplets when submerged in an oil-lipid solution. Droplets then come together to form a bilayer. And B) consists of vesicle filled aqueous droplets in an oil reservoir. The lipids fuse to the oil-water interface and form a monolayer. Droplets may then bind to form an asymmetric bilayer[64].

Due to their method of formation asymmetric bilayers are possible, as shown in Figure 13[64,67]. One study, incorporated proteins into their asymmetric DIBs and reported that they observed differences on outer membrane protein G's behaviour, depending on which side of the droplet it was inserted into[67]. Maglia et al. used asymmetric DIBs for the screening of membrane proteins by developing protein pore incorporated DIBs. This pore contained diode like properties, which allowed for them to develop a droplet network that could process electrical inputs[68].

1.2.5 Domains, Rafts and Proteins in Lipid Membranes.

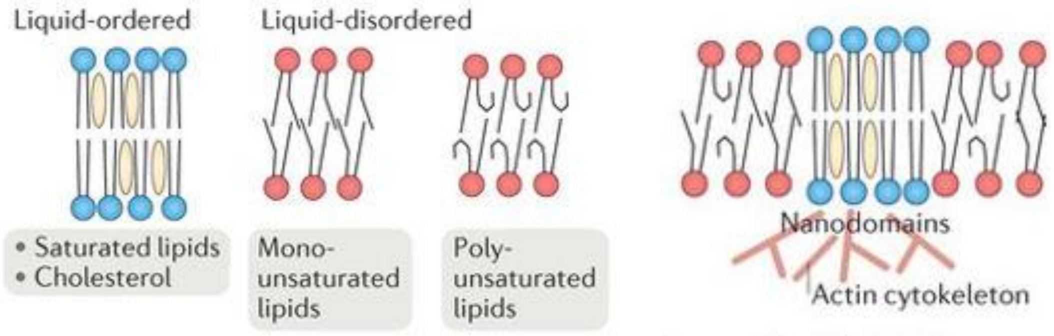

Figure 14: Diagram depicting liquid ordered phases formed in the presence of cholesterol and saturated lipids, and liquid disordered phases which can occur due to mono-unsaturated or poly-unsaturated lipids. And an image of the resulting nanodomains when both liquid ordered and liquid disordered phases occur in the bilayer[69].

The lateral and transversal distribution of lipids within lipid membranes is heterogenous and diverse and can result in domain formation[70]. Due to the variation in melting temperatures, depending on lipid chain length and degree of saturation and the presence of sterols, different classes of lipids are in different physical states, at different temperatures. Lipids may be more "fluidic", when there is low in-plane viscosity and a high number of chain defects or they form a "gel" phase, where there are few defects in the hydrocarbon chain and the domain has a higher viscosity[71].

As shown in Figure 14, the heterogeneous distribution of the lipids can result in liquid ordered and liquid disordered regions. Liquid ordered regions consist of tight packing of the acyl chains of the lipids, while also obtaining high lateral mobility of the lipids. A schematic example of cell formation of microdomains is shown in Figure 14. The cell can form domains such as caveolae, which are small cholesterol-rich domains of 60 nm diameter associated with membrane protein caveolin[70].

Ternary lipid compositions, typically rich in sphingolipids and CH, have been observed to form lipid "rafts"[72], where a CH rich domain is formed with order-preferring lipids[70]. Rafts have been observed to occasionally not contain sphingolipids, however must contain cholesterol[71]. Originally the formation of these rafts was considered to be driven by membrane proteins; however, a study completed by Sevcisk et al.[73], on immobilised raft proteins and saw that it had no substantial effect on the membrane environment, suggesting lipid domain formation is driven by the lipids themselves[71]. Identifying rafts and microdomains within living cells proved difficult for numerous years[70], however more recent studies are utilising fluorescent probes to observe liquid ordered phases in cells[20,74,75].

Due to the tighter packing observed in liquid ordered phases, studies have found that the diffusion rates are approximately 3-5 fold slower than in disordered regions[76]. The incorporation of sterols into fluidic membranes results in membrane thickening. Differences in membrane thickness are proposed to aid in membrane proteins cellular locatisation[77,78]. These are elements that would ideally be included for the development of an advanced biomimetic membrane, specifically if proteins are to be incorporated in the future.

To incorporate proteins within a plasma membrane methods such as nanodisks[79], lipsomes[80], SLBs[81], to name a few, have been used. Polymer tethered planar lipid bilayers removed the issues seen with bilayers directly on a support such as SLBs, which did not allow for membrane proteins to diffuse in the plane of the membrane[82]. A study by Kung et al. incorporated proteins through a pattern mixing of the lipid and the protein for the bilayer. As shown in Figure 15, one method they used comprised of printing proteins onto glass and used vesicle fusion to fill gaps between the proteins to form a SLB. They also reported removing patterned regions from an already created lipid bilayer and exposing the bilayer to proteins, which then fill the newly formed gaps[52]. This could be of great interest for cell-based assays and membrane studies.

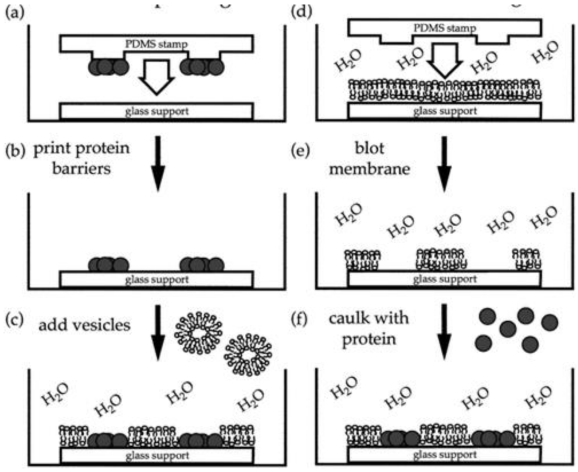

Figure 15: Schematic diagram of the methods used by Kung et al. to created protein incorporated bilayers. A, B and C show the proteins being deposited onto the glass substrate and vesicles disrupting in the patterned gaps between the proteins. D, E and F show a bilayer formed on the glass substrate where sections are removed. Proteins are then introduced to fill the newly formed gaps in the bilayer.

1.3 Current Membrane Permeability Models

The capacity to anticipate how a compound may interact with a cell membrane is of great importance in pharmaceutical and cosmeceutical research. Current models are limited for the reasons explained below. Currently, the most commonly used models are PAMPA and In Vitro cell monolayer models. The permeation of anti-cancer drugs through the cellular membrane is vital in chemotherapeutic design, as most drugs are only cytotoxic once it reaches the cell/tumour interior. Anthracyclines, the focus of this proof of concept study, are known to passively diffuse across the membrane[83,84].

There are a number of mechanisms by which a drug may enter or pass through a cell, such as intracellular, paracellular, passive diffusion and active transport. Intracellular transport such as endocytosis, which occurs within the cell itself, involves the uptake of nutrients and is a regulator of signalling. Endocytosis consists of the formation of an intracellular vesicle by invagination of a plasma membrane[85]. Molecular motor proteins will then carry these along microtubules[86]. Currently, this mechanism is exploited with nanoparticles for drug delivery, though there are difficulties in optimisation, as the uptake is cell-type dependent and can vary depending on size and charge of the nanoparticles[85].

Another major difficulty posed in drug delivery is avoiding lysosomal degradation. Lysosomes have three main functions; post-translational maturation of proteins, degradation of macromolecules and cellular release of enzymes. Impeding the lysosomal activity results in a build-up of undegraded molecules which then induces apoptosis[87]. This provides difficulty in drug delivery. Active transport requires energy for movement, typically it is mediated through the membrane protein which is activated by ATP.

Paracellular transport is the transfer of substance between cells (transcellular transport is the transfer through a cell). It is the main transport route for hydrophilic drugs and is governed by tight junctions (TJs), e.g. transmembrane proteins and cytoplasmic plaque proteins. TJs are multiple unit structures composed of multiprotein complexes. These multiprotein are affiliated with an underlying apical actomyosin ring. Their main function is to regulate the trafficking of nutrients and medium sized compounds. When paracellular transport is exploited for drug delivery, an absorption enhancer is typically added to the drug. It has been found that transient opening of the TJs is optimal over the disruption of the cell membrane (intracellular), as it is less damaging and so is considered in drug delivery design for targets such as the gastrointestinal tract[88].

Passive transport is the non-activated movement of a substance through diffusion, typically due to a concentration gradient. It is understood that the more lipophilic a molecule is, the more readily it will pass through the membrane, this is known as Overton's rule[89]. It is thought that the membrane permeability is proportional to the membrane diffusivity and the oil/water partition coefficient of the permeating species. This is commonly exploited to estimate membrane permeability towards specific drugs. Artificial membrane models such as PAMPA are then required to test these estimates. Passive transport is the primary route most orally delivered drugs use to enter our circulation. Due to this, it is vital to accurately determine the permeation of the drug and why our model, that should mimic passive transport, is of great interest.

Ideally, our model can be altered to mimic healthy and diseased membranes. Information about the blood-brain barrier and how a drug interacts with it is vital. Development of a model that can accurately depict these interactions would allow for crucial information to be obtained which is key to Alzheimer's research etc.

1.3.1 Lipophilicity Models

Drug discovery requires numerous investigative steps from preclinical to clinical testing before it is even considered for human testing. As these steps are progressively costly, it is important to be able to identify parameters such as target identification, target selection and target validation, at very early stages[1]. The estimation of a drugs solubility and permeability are vital to this and are approached both computationally and experimentally. Computational methods include modelling of molecular dynamics etc[90]. Typically, the initial steps of experimental analysis are completed by obtaining a drug's logD, LogP, pKa, etc., to determine the lipophilicity and solubility of a drug.

Lipophilicity indicates the drugs ability to dissolve into non-aqueous solutions, which is of interest as it indicates the permeation ability of the drug. Drugs require lipophilicity within a certain window, as if they are too lipophilic they may remain trapped within the membrane[91]. Whereas if they are too lipophobic, they may not permeate the membrane. Lipophilicity is typically measured through partition coefficient (LogP) which indicates the distribution between an aqueous and organic phase. The distribution coefficient (LogD) can also be calculated, which considers the ionised and unionised forms of the drug and is completed at various pH's. The acid-base dissociation constant (pK_a) is vital as it can influence the lipophilicity, solubility, protein binding and permeability for the drug[92]. Unfortunately, computational work & LogP can only give an estimation and may not be accurate for the drug or for the complexity of the bilayer. Currently, PAMPA and cell-based assays are widely used to experimentally determine drugs permeability. Ideally, these results should agree with the calculated LogP etc.

1.3.2 Parallel Artificial Membrane Permeability Assay

PAMPA is a membrane-based assay commonly used in industry and consists of two microwell plates, as shown in Figure 16. One of these plates contains a porous filter disk at the bottom of each well. The other plate sits under the first plate so that they are in contact and is known as the reserve plate. The filter is coated in an inert organic solvent containing lipid material, to prepare an artificial membrane. One plate is filled with the donor solution, i.e. the drug of interest and the other, the acceptor solution, i.e. buffer. The plates are then stacked and incubated. The drug concentration in the wells is then detected by UV or LC-MS, permeability is then calculated.

PAMPA is limited as it can only determine passive diffusion, though this is still of great interest for most drugs. It has proven successful at acidic pH such as pH 4[12], this is of interest as low pH's are a limitation in cell-based assays. PAMPA does not exploit a true lipid bilayer but a solution of lipid that contains a solvent. Therefore, the organisation of the lipid at the porous filter is unlikely to be a true bilayer and can be considered a poor mimic of a lipid membrane. PAMPA also does not fully correlate with data obtained through cell-based assays on permeability, this is discussed further below.

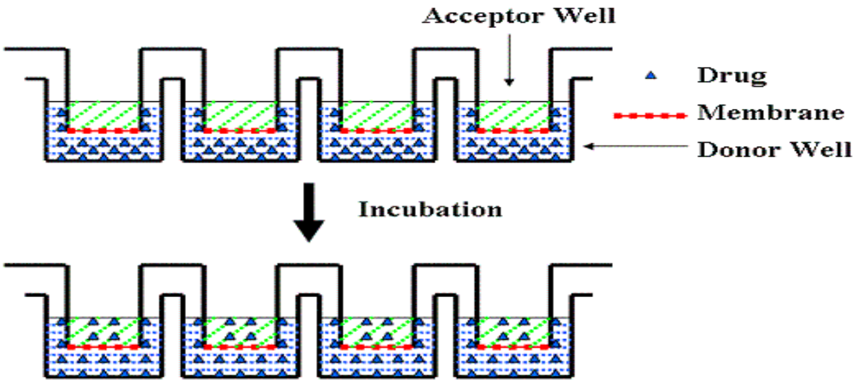

Figure 16: Schematic showing the basic setup of PAMPA[93]. The drug is placed within the donor well and separated from the acceptor well by a membrane containing lipid material. Post incubation the amount of drug within the acceptor well may be quantified.

1.3.3 Cell-Based Assays

Cell-based assays such as Caco-2 are permeability assays which are typically used to predict in vivo drug permeability in the intestine. Caco-2 cells are human adenocarcinoma colon cells grown on porous polyethylene terephthalate membranes in 12 well plates. They simulate intestinal enterocytes. Even though they have been commonly used as a permeation model, they contain an overexpression of P-glycoprotein due to it being a cancerous cell line, which has been demonstrated to effect permeation studies[94]. Caco-2 can also only be used to examine passive drug transport as it contains a low expression of carriers and small pore size, meaning it is not a good model to demonstrate carrier-mediated and paracellular transport. Caco-2 assays are typically done in "Hanks balanced salt solution" like buffers[11], this can cause difficulties as most lipophilic drugs have poor solubility in these buffers. Various approaches have been attempted to try to increase solubility with minimal other effects, one method is the addition of proteins such as bovine serum albumin[11].

In recent times, Madin-Darby canine kidney (MDCK) cells have become increasingly popular as a replacement for Caco-2 cells due to their faster growth rate. When these cells are grown on semi-permeable membranes, they have been known to differentiate into columnar epithelium and form tight junctions[95]. MDCK are obtained from dog kidney cells meaning they are not true human cells but have many common shared epithelial cell characteristics as Caco-2. Similar results are also observed between the two cell lines for passive diffusion, which has led to MDCKs increasing popularity as a cell-based assay[95].

There are a number of disadvantages to cell-based assays, these include; the heterogeneity of cells, their membranes and proteins from cell to cell, even within the same culture. The high cost and slow assay time. Cell-based models also exhibit great discrepancies in results which may prove highly costly in a drugs development. A study was reported, comparing the literature values of CACO-2 at pH 7.4 with PAMPA values obtained at pH 7.4 and pH 5.5. The apparent permeability coefficient (Papp), obtained by Equation 1, of the two showed great variations for numerous drugs including doxorubicin and ibuprofen, where the former showed 0.16 cm^{s-1} for Caco-2 and 0.5 cm^{s-1} for PAMPA at pH 7.4, while the latter had 52.5 cm^{s-1} for Caco-2 and 6.8 cm^{s-1} for PAMPA pH 7.4 and 10.8 for pH 5.5[96]. This study reflects the great discrepancies between the two methods, which indicates the limitations of PAMPA in reflecting cellular uptake. Although it does give an indication of which drugs are permeable. They also observed false negatives, where a drug shows poor results in the models whereas in vivo prove to be extremely permeable and vice versa. As these models are timely and costly, reducing the number of unsuitable drugs reaching this stage in development is of great interest and why our proposed model may prove to lead to a significant increase in successful drugs reaching later stages in drug discovery.

$$\boldsymbol{P_{app}} = (\frac{\boldsymbol{dQ/dt}}{\boldsymbol{C_0 xA}})$$

Equation 1: Permeability coefficient (Papp) for a Caco-2 assay. Where dQ/dt = rate of permeation of drug across the cell. C_0 is the donor compartment at time zero, a = area of cell monolayer[97].

1.3.4 Other Permeability Models

Other methods used to determine permeability are Immobilised Artificial Membrane Chromatography (IAMs), Immobilised Liposome Chromatography (ILC), Liposome Electrokinetic Chromatography (LEKC) and Permeapad. IAMs consists of a stationary phase where monolayers of phospholipids are covalently immobilised onto a silica surface. This is a mimic of a fluid cell membrane on a solid matrix. This stationary phase has a typical lifespan of 3 months before it begins to deteriorate.

ILC is where the stationary phase is gel beads with noncovalently immobilised phospholipid-based liposomes. The method allows for different chemical compositions to be easily and reversibly immobilised on the gel supports. LEKC consists of liposome incorporated buffer that acts as a pseudostationary phase, and is used for drug-membrane interaction detection, where the retention factor correlates to the lipophilicity of the drug. This method allows for the use of a variety of lipids, meaning the system can be as biomimetic or as simple as the study requires, where even proteins have been previously incorporated[91].

Permeapad is similar to most permeability assays, where it measures the transition kinetics of the drug from a donor compartment through a barrier into an acceptor compartment[98]. It consists of phospholipids deposited between two support sheets[99], two chambers and a detection method (typically UV-Vis). It is an easy to use, cost efficient method that has proven to have a higher resistance to pH changes than other current methods[98]. All these methods have their own advantages, but none can be considered fully biomimetic, as except for LEKC, none incorporate true bilayers into the analysis.

1.4 Gold Microcavity Arrays & SERS

Raman and fluorescence spectroscopy are among the key spectroscopes that have shown enhancement by plasmonic interaction with metal substrates[100,101]. Gold and silver are two metals that are most commonly employed as substrates for plasmonic enhancement. For plasmonic enhancement, the metal must have a localised surface plasmon, meaning, the substrate must be nanostructured. This has led to the manipulation of metals to form nanoparticles, nanocavities, nanorods and much more[23]. Raman spectroscopy, fluorescence and fabrication methods shall be discussed below.

1.4.1 Microcavity Arrays

For the creation of a supported lipid bilayer, a suitable substrate was required. Typically, glass has been used; however, gold has also proven to be suitable[27,102] As we needed a substrate that was both plasmonically active, for metal enhanced Raman and fluorescence spectroscopy, that could support a fluidic bilayer and had a volume for capture of reagent following diffusion across a bilayer, we used gold microcavities arrays. When microcavities were prefilled with buffer, they were found to provide an aqueous layer that allowed for the successful spanning for the bilayer while also allowing for SERS enhancement[27]. As shown in Figure 17, the cavities were created using a "nanospheres lithography" method prepared by creating a mask using submicroscopic colloidal polystyrene particles[103]. Gold was then electrochemically deposited around this mask. Once the mask was removed, hexagonally packed cavities remain.

Metal microcavities have been previously reported to show significant plasmonic enhancement in both fluorescence and Raman[104,105]. In one study by Jose et al. it was observed that there was significant enhancement localised in the bottom of the cavity once a solution of $[Ru(bbpy)_2(Qbpy)]^{2+}$ was sonicated in[104]. This study determined that these cavities were slow to fill, and sonication was the only method to successfully remove the air pocket that accumulates at the bottom of the cavity. They also observed that surface quenching was not as large an issue as it was on planar gold[104].

The hemi-spherical cavity architecture is a key advantage as it results in the confinement of the plasmonic field within the cavity[104]. The distribution of the plasmons and the plasmon energy are controlled by the size, aperture and thickness of the cavity. Microcavities have also proven to provide a reproducible surface enhanced Raman[27,106]. The cavities are also reusable, with long-term stability making them very appealing as a SERS substrate.

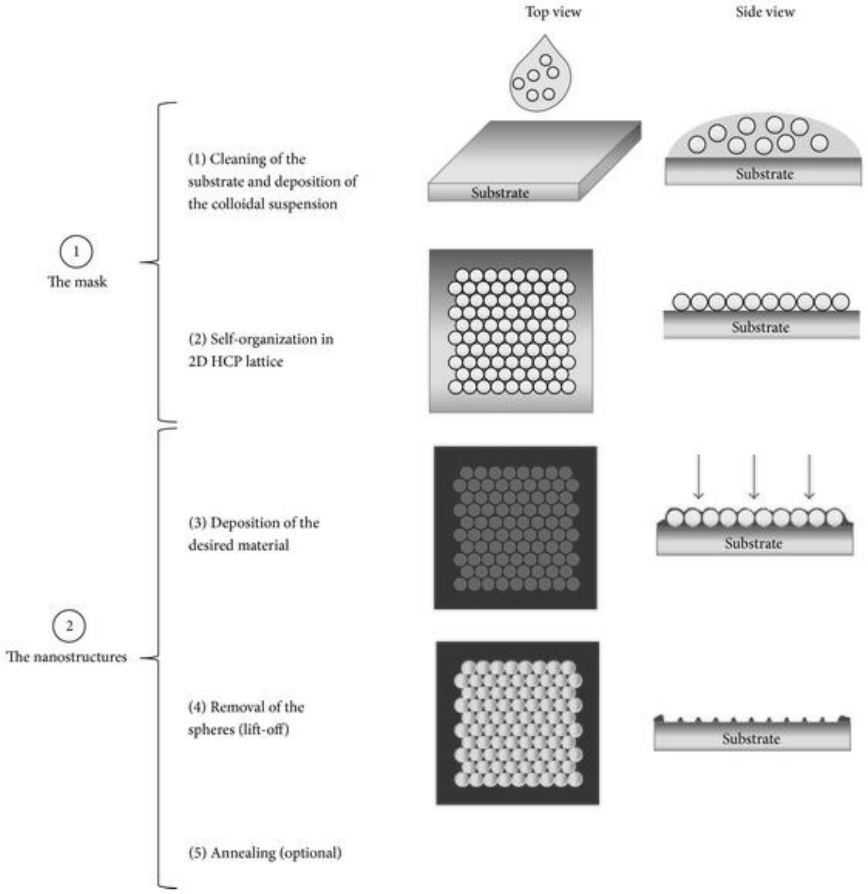

Figure 17: Schematic of the nanospheres lithography process where in step 1: spheres are deposited creating a mask and step 2: gold is deposited around the spheres and then removed.[107]

1.4.1.1 Templated Sphere Assembly and Lithography

Templating sphere lithography is a key technique used to reproducibly create micro-arrays. The Nanolithography method was first described in 1981 by Fischer & Zingsheim[107]. It was observed that once all the solution containing the colloidal particles had evaporated from a glass plate, a monolayer of hexagonally packed spheres had occurred. Over the past number of years, this has been studied in detail[107–109], and it is now understood that this formation occurs in two main steps. When the particles are placed on a surface, they will self-assemble.

Depending on the conditions such as temperature, substrate etc., they may arrange randomly or form hexagonally and close-packed, which is desired in arrays. In the first step of this self-assembly, a nucleus is formed. This is caused when the solvent layer approaches the dimensions of the diameter of the particle. The tops of the particles are deformed as they protrude from the liquid surface; this is due to surface tension effects that pull the spheres together. In the latter step, the solvent evaporates from between the spheres resulting in particle transport towards the nucleus, resulting in a SAM. The surface can then be exposed to an ion beam or vacuum deposition of the chosen metal. The colloidal particles may then be removed. In ion beam methods, isolated posts of the substrate material will be seen, while through vacuum deposition, a thin holey layer of film or triangular elevated structures in a honeycomb pattern, may be observed[103].

In the past, there were two main methods used for the fabrication of these colloidal particle monolayers. The most popular method used by industry was one developed by Dimitrov & Nagayama[110,111]. The method consisted of dipping a glass plate vertically into a solution containing the colloidal particles of interest and then slowly removing the plate. Temperature and humidity have a large influence on the method, and so tight environmental control were required. This method typically achieved reproducible results and has led to its exploitation for numerous uses. For example, Dugay et al. used the "dip-coating" method for the deposition of CoFe carbide magnetic nanoparticles on substrates. This was completed by utilising a coupled glovebox sputtering system under an inert atmosphere to prevent oxidisation, which was a major issue with these particles. Through altering withdrawal speed, surfactants concentration and the substrate's surface, they achieved self-assembly in both thin films and stripe formations[112]. The use of LB deposition for "dip-coating" has been applied numerous times with great success for the formation of close-packed nanoparticles[113–116]. This has ranged from the use of iron oxide[114,115], silver[116], gold[117] and polystyrene spheres[118].

A variation of this method is the "evaporation" or the "air/water interface" method, where the evaporation of the solution results in the colloidal spheres self-assembly onto the substrate. This has been used from simple application of droplets[102,119] onto a surface, to within microfluidic systems[120]. For example, Lone et al. used PMDS to create microfluidic channels and introduced the sphere solution. The method is illustrated in Figure 18. As the sphere solution began to evaporate, it resulted in the higher particle concentration, which aided in the formation of continuous packing[120].

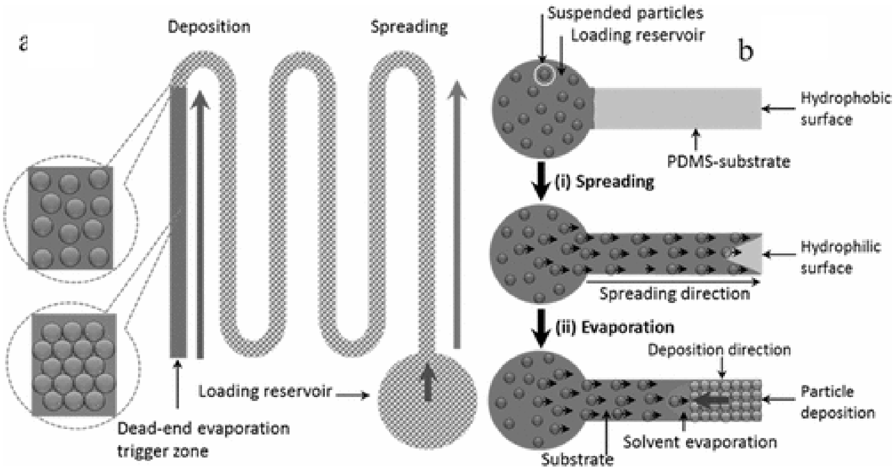

Figure 18: Schematic diagram of deposition process within microfluidic systems used by Lone et al[120]. Sphere solution was loaded into the reservoir and flowed through the designed channels. As it began to evaporate, the spheres self-assembled into a closed-packed monolayer.

However, methods using "evaporation" often experience issues with sphere packing. Such as the development of the "coffee-ring effect", concentric rings or an amorphous stain, an example of each is shown in Figure 19. This is typically due to the packing of the spheres at the outer drying line. The process has been well studied over the years, and it is now an accepted phenomenon for the particles to move radially outwards towards the outer drying line as it evaporates when on a hydrophilic surface[121–123]. Studies have also found that spheres of nanometric size tend to move outwards, whereas larger particles of micrometric size will locate towards the centre of the droplet[122,123]. A study by Morales et al. investigated how non-ionic surfactants effected the evaporation and the resulting pattern assembly. They found that the surface tension dropped as surfactant concentration was increased, where concentric rings occurred at high surfactant concentration, amorphous at low surfactant concentration and coffee-ring in between[124]. Meaning, depending on the application, the packing formation of the spheres may be varied.

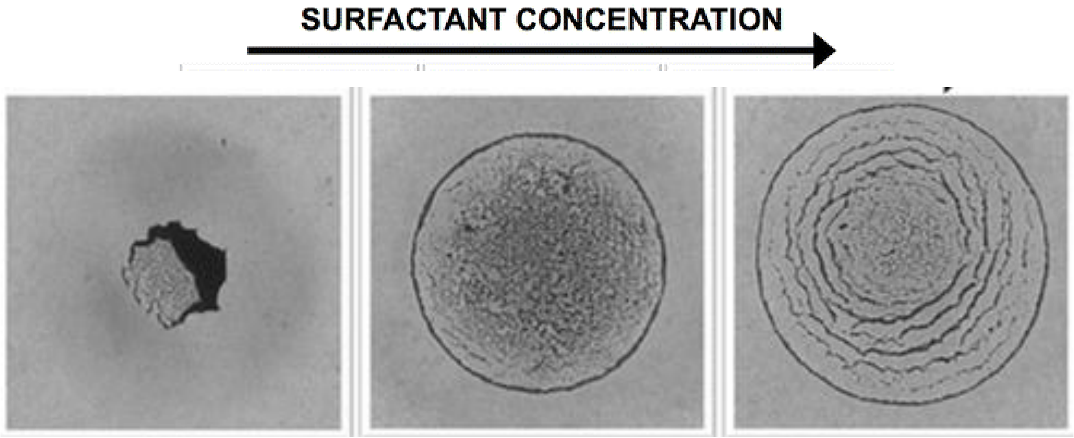

Figure 19: Representative image of the deposition patterns observed through droplet deposition. From left to right: amorphous stain, coffee ring stain and concentric rings. These patterns were observed to occur as the surfactant concentration increased[124].

Another method reported by Halteen & Duyne and was known as the "spin-coating" procedure. A double or single layer of polystyrene (Ps) spheres were added by varying particle concentration and spin speed resulting in close packing. For example, Hulteen et al. used spin coating at 3600 rpm to create monolayers and double layers of Ps spheres. They attempted this at a range of sizes; however, they found 264 nm to give the best results, where 90 % of the time, resulted in near-total coverage. They reported that increasing the sphere concentration in their deposition solution resulted in double layers[108]. Cheung et al. demonstrated a method of using spin-coated Ps masks to create nanopillar arrays. Schematic diagram of their method is shown in Figure 20. 500 nm sized spheres were spun onto silicon wafers at three speed settings. They then used reactive ion etching to modify the spheres. Using "bosh" process, the exposed areas between the spheres was etched, resulting in nanopillars[125].

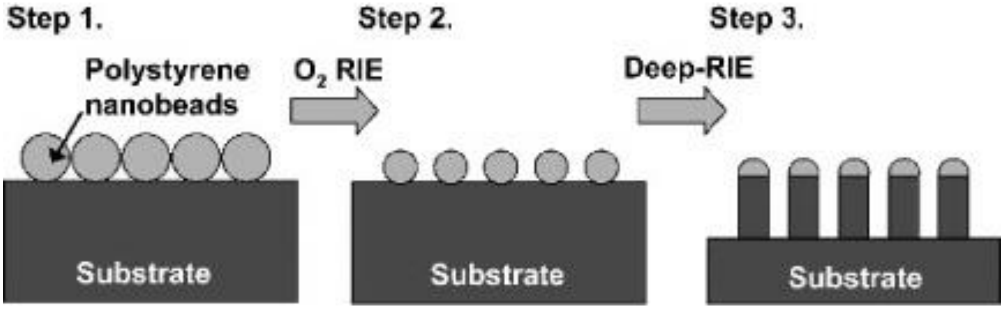

Figure 20: Schematic diagram showing the etching process used to create nanopillars from a spin-coated Ps mask. Oxygen plasma etching was used to change the size of the spheres followed by deep reactive ion etching to create the pillars[125].

Both techniques, dip-coating and spin-coating, have the disadvantages of requiring a very smooth and hydrophilic substrate, and there is no control over the crystallisation process, meaning the results were not uniform.

1.4.1.2 Cavity Formation

Currently, one of the most commonly used methods for the creation of microcavities is the polystyrene sphere templating through electrochemical or vapour methods, which deposits a layer of the substrate of interest, such as gold or silver. The substrate fills in the space between the spheres, leaving a micro-cavity array when spheres are removed[126], as seen in Figure 17. Electrochemical deposition is the method that was used to complete the studies reported here. Using spheres in these methods are useful as they restrict where the deposition process may occur and prevents any chemical modification from occurring beneath the spheres where it would be unfavourable. The size of the spheres determines the size of cavity, while the amount of charge used during electrochemical deposition will determine the depth of the layer and thus the aperture of the pore[104]. The substrate may be modified prior to sphere deposition with cysteamine to improve packing. This increases the substrate-particle reaction as the surface has a positive charge and the spheres are negatively charged. It also increases the wettability of the surface, further improving sphere packing [127]. A study completed by Zhang et al. showed that increasing the cavity depth would also change the cavities hydrophobicity, where an increase in depth increased its hydrophobic state[128].

Electrochemical deposition was used here. Key advantages of this approach include tight control over the thickness of the layers, and the ability to produce thin supported layers, (which can lead to the fabrication of photonic mirrors, leading to more possible applications). No further processing steps are required beyond deposition and high temperatures are not needed with this methodology. Also, there was no shrinkage on the material[105]. One disadvantage of electrochemical deposition is that the lip of the cavities were rounded and not sharp, this may affect the measurement of the pore mouth, which was needed for determining film thickness[105]. However, this was not a disadvantage in our application, as sharp edges have been previously reported to result in membrane rupture[61].

Other lithography methods that are widely reported, though not applied here, include dip-pen lithography, nanografting and conduction tip ARF writing. These have been used to create high-resolution nanopattern over small areas. In contrast, methods such as photolithography and laser lithography can create nanopatterns over large areas but lack the nanoscale resolution of the previous methods. Microcontact printing and nanoimprinting have the advantage of both, having a high resolution over a large area, but specialised stamps are required for these methods[109].

The use of cavity arrays as a substrate for the spanning of a lipid membrane has been successfully and reproducibly demonstrated[27]. Many of the reports have demonstrated that bilayer over aperture are based on nano rather than micron dimensioned pores and for such substrates, electron beam lithography has been used, successfully spanned a bilayer over inverted pyramid cavities, which also allowed for the detection of a single protein[129]. Nano-gratings have also been shown to result in successful bilayer spanning from vesicle disruption[130], indicating a variety of gold structured substrates may be exploited as a platform. Extensive previous work has already proven that our proposed gold micro-cavities can successfully span a lipid bilayer[18,102].

1.4.2 Raman Spectroscopy

Spectroscopy is commonly used to study the interaction of electromagnetic radiation with matter, this can be through emission, fluorescence, adsorption or in the case of Raman, scattering[131]. In Raman spectroscopy (RS), a single frequency of electromagnetic radiation is used to irradiate the sample[100]. The resulting scattered radiation is then measured as a function of its wavelength[132]. Figure 21 schematically represents the Raman process, where both Rayleigh and Stokes scattering can occur. Inelastic scattering occurs when the radiation of a single frequency causes the electrons surrounding the nuclei to become polarised into a short-lived "virtual state", which then relaxes, resulting in the release of a scattered photon. In this process, the inelastic scattering exchanges energy to be passed on to the molecule, meaning the scattered photon will differ by a vibrational quanta as can be seen in Figure 21. When a molecule in the ground electronic state in the lowest vibrational level is then excited under laser irradiation to a virtual state, returns to the ground state. Conversely, if it reverts to a higher vibrational level than prior to excitation, this is referred to as Stokes Raman scattering. When the molecule is excited from a higher vibrational level within the ground state to the virtual state but returns to a lower vibrational level, anti-Stokes Raman scattering has occurred. The most prevalent scenario though, is where there is no change in vibrational state and the molecule reverts to the same vibrational level it originates from. This is elastic, or Rayleigh scattering and has the highest probability and greatest intensity.

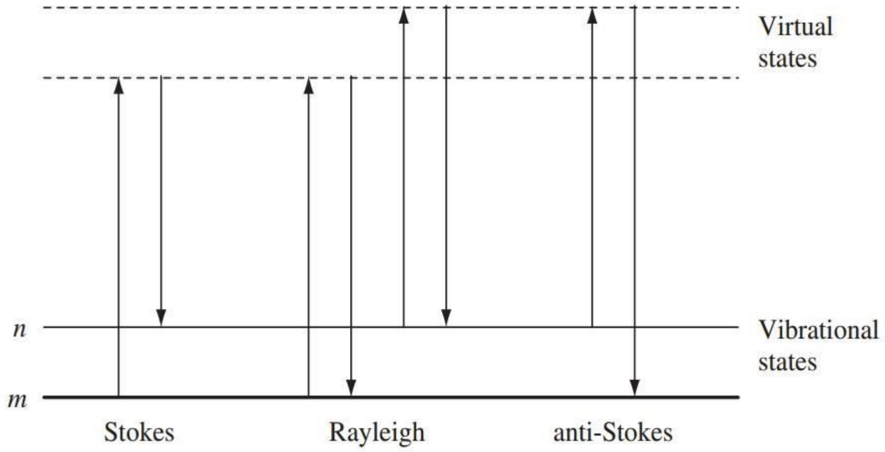

Figure 21: Diagram of the scattering process. m indicates ground vibrational state and n is the first vibrational state[100].

An advantage of Raman spectroscopy, is that the incident radiation does not need to match the excitation energy required of the molecule, as would be the case in IR, and therefore a variety of excitation wavelengths can be used. Raman spectroscopy provides detailed molecular level information and a fingerprint spectrum that can be used for both molecular identity and for concentration. It is a non-destructive method meaning it is very useful in cases where only small volumes of sample are available or if the sample needs to be retained[133]. As Raman bands are narrow and have a smaller likelihood of overlap than in other spectroscopic methods, it is feasible to use this method for multiplexing[134–136]. Another key advantage of Raman spectroscopy is the ease with which it can be applied through microscopy.

Although there are many advantages to Raman as an analytical method, it suffers from a number of drawbacks. Raman scatter is considered a weak process, as only 10^{-6} – 10^{-8} photons will Raman scatter[133]. Additionally, the intensity of Raman scattering is influenced by the wavelength (λ) of the laser, where the intensity is proportional to λ^{-4}.[132] Raman can suffer from fluorescence interference, even from weakly fluorescent materials, which can lead to masking of Raman peaks by a fluorescent background[137]. NIR excitation causes less fluorescence than the visible region or UV, and better penetrability into biological samples.

Due to these drawbacks, research into methods to improve Raman signal intensity were explored[100]. This resulted in other Raman techniques, where the most prevalent are resonance Raman or surface enhanced Raman. In resonance Raman, the exciting laser is coincident with an electronic absorption band from the sample[100]. RRS alone is useful, as it provides up to seven orders of magnitude enchantment of Raman signal from the absorbing chromophore and so is very selective. Any interfering molecule would require to have both the same Raman band and similar excitation energy absorption as the analyte to cause interference[133]. However, the likelihood of resonance excitation is lower, and so can result in weaker signals. Higher power density and wavelengths can be used to overcome these weaker signals; however, this can cause burning or sample degradation.

Surface-enhanced Raman spectroscopy (SERS) can dramatically improve sensitivity, up to 20 orders of magnitude enhancement has been reported, and in some limited cases, even single molecule Raman was observed[138]. However, 5 to 8 orders of magnitude enhancement is more typically found for nanocavity array enhancement such as those used in this study[139]. SERS has the added advantage that it can reduce fluorescence interference, due to fluorescence quenching by the rough metal surface. SERS has resulted in the development of nanorods, nanoshells[140] and other structured substrates from both gold[27,104,141] and silver[142,143] to enhance the signal.

Surface enhanced resonance Raman scattering (SERRS), was also developed to improve sensitivity, it combines contributions from both of SERS and RRS, and can lead to summative improvement in enhancement factor[13]. SERRS differs from SERS, as it requires a chromophore. It measures the chromophores scattering, meaning the analyte may need to be labelled. This can gives rise to difficulty in finding a chromophore that excites at the required wavelength that corresponds with the plasmonic resonance[144]. Although this difficulty, SERRS is proving itself to be a valuable technique.

1.4.2.1 Surface Enhanced Raman Spectroscopy (SERS)

As described, a key limitation in the analytical application of Raman spectroscopy is the low probability of Raman scatter, leading to "weak signal". A typical Raman scattering cross-section is approximately 10^{-29} cm^2 per molecule. When compared to other methods, such as absorption, where this value is around 10^{-18} cm^2 (Ultraviolet) and 10^{-21} cm^2 (Infrared) per molecule[133], it can be considered very low. Surface enhanced Raman scattering (SERS) was first observed in 1973 from pyridine adsorbed on a silver electrode, but the implication of the enhanced signal was not fully understood until four years later[23]. It has been previously stated that SERS has the "potential to combine the sensitivity of fluorescence with the structural information content of Raman spectroscopy"[139], meaning, SERS combines the molecular specificity of Raman spectroscopy with plasmonic enhancement pushing sensitivity to approach that of which is seen in fluorescence.

SERS requires the analyte to be adsorbed or orientated close to a metallic nano-structured interface. Such interfaces give rise to localised plasmonic modes, that when excited by a Raman excitation source, can lead to dramatic Raman scatter enhancement[23]. These metal nanostructures act as "resonators", enhancing the electromagnetic (EM) field of the incident light. Plasmons arise at the metal surface from the mobile electron density, characteristic of metallic bonding, propagating across their surface. Surface plasmons are the coherent oscillation of these conduction band electrons; they can be excited at resonance frequency, i.e. when the incident light wavelength matches the plasmon frequency, then they can absorb and scatter (and emit) light.

Gold and silver have plasmon resonance frequencies in the visible spectral region and so have been widely used for SERS. Silver was found to be plasmonically more active than gold, but gold is more inert, which is an important consideration, particularly for biological applications. These differences are minimised in the red- to near-infrared region and the enhancements become similar[23]. Figure 22 shows the two important types of surface plasmons (SP), propagating surface plasmons and localised surface plasmons. Localised surface plasmon resonance occurs when an electromagnetic wave of a specific frequency interacts with the free electrons of the metal surface, this results in a negatively charged cloud which oscillates at a resonant kinetic energy creating a plasmon, i.e. a near field effect of an electric field occurs due to a coherent movement of all free electrons. This is restricted to a region between 10-50 nm from the surface[145]. Propagating surface plasmons are evanescent EM waves that are bound between the interfaces of the smooth metal surface and the dielectric layer[146]. They arise from the oscillations of the conduction electrons in the metal [147]. High dielectric interfaces i.e. poor conductors of electric current/ high polarizability, are required for propagating SP due to mismatch in momentum.

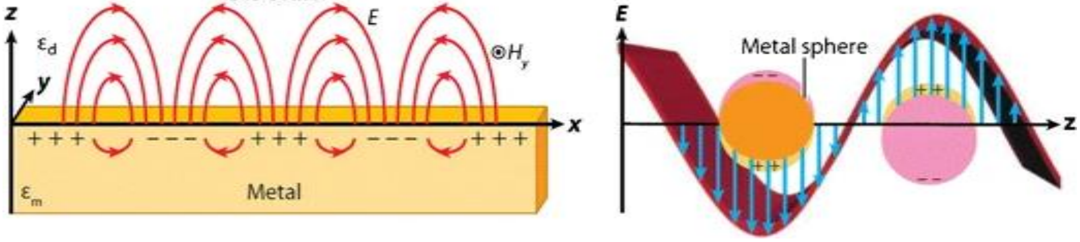

Figure 22: Schematic illustrating propagating and localised surface plasmon resonance[148].

Augmentation of the electric field of the incident light by localised SP's at nanostructured metal surfaces leads to SERS enhancement of molecules oriented within the resulting electric field "hotspots", which is referred to as the electromagnetic enhancement mode of SERS. In addition to electromagnetic enhancement, a second route of SERS enhancement is also believed to occur, referred to as the chemical mechanism. This process is considered the weaker contributing component of the two mechanisms. Chemical enhancement is believed to occur through a process analogous to resonance Raman spectroscopy, where at metals, a charge transfer transitions between the highest occupied molecular orbital of the analyte molecule and the fermi level of the metal. This method of enhancement is expected to be confined to species chemically adsorbed at the metal-interface.

Many nanostructured surfaces have been shown to generate localised plasmonic regions that effectively focus the incident and excited plasmonic electric fields; these are known as hot spots. Hotspots are particularly found in the gaps between two particles or at sharp edges and tips of metal nanostructures[23]. In the case of cavity nanostructures, localised plasmons were found to be trapped within the spherical cavities, where they are largely uninfluenced by the electric fields from the surrounding cavities[149].

Many detailed studies were completed on single-molecule detection through SERS and fluorescence by Kniepp[138] and Moerner [24,150]. In one SERS study, gold bowtie nanoantennas[25] were used to create specific hotspots to allow for an enhancement of 10^{10}. It was also determined that the size of the gaps between the nanofeatures influences the intensity of the hot spots electric field. Marques-Gonzalez et al. report a study based on electromagnetic theory, which predicted that the distance between the nanostructures would determine the localisation of the hot spot field enhancement (Figure 23). Through precisely controlling the gap size between two metallic structures, it was determined that when the gap was decreased, the 1,4-benzendithiol signal was increased. Figure 23 shows the spectra obtained for three sample distances, and as can be seen, a dramatic increase in signal intensity occurs as the gap size is decreased. They then tested the theory using 4-aminothiophenol and similar results were obtained, indicating that there was a corresponding relationship between gap size and hot spots enhancement factors[23].

Another study completed by Chen et. al. demonstrated that not only does nanofeature gap size influence SERS enhancement, but the molecular location within the gap has an effect too. With the use of electron beam lithography, carbonaceous particles were placed at the bottom, on the side and at the top of a nanoslit on a gold substrate with a 15 nm slit gap and

5 nm edge curvature. When Raman spectroscopy was applied, it was determined that the slit with particles at the very bottom gave the largest enhancement factor[151]. As the particle decreased in depth in the slit, the enhancement also decreased, indicating that location within a hotspot will directly affect the enhancement factor.

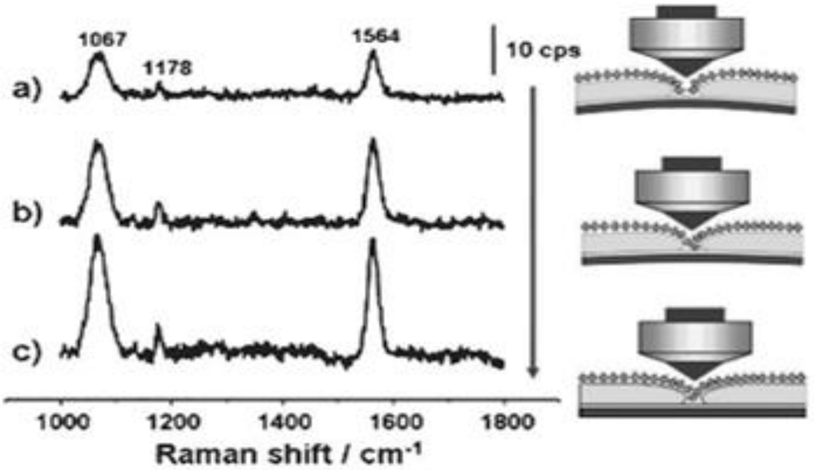

Figure 23: SERS spectra of 1,4-Benzendithiol at different metallic gap junctions a) 0.8 nm, b) 0.6 nm and c) 0.4 nm[152], showing SERS intensity is highly influenced by the gap side, due to "hotspots".

Where analytes with a low Raman cross sections do not possess surface active groups, they can be difficult to detect using SERS. An approach to overcome this is to use an "Affinity coating", to selectively capture the analyte of interest close to the surface, where it cannot itself adsorb[23]. Two common methods to add such capture layers include atomic layer deposition and molecular self-assembly. The former method is appealing, as a thin layer will result in less distance between the analyte and metal surface, hence not inhibiting the enhancement layer as much as a thicker layer would. Molecules commonly used for this thin layer include thiol based ones (self-assembly) which can lead to defects as photooxidation and thermal desorption occur, and aluminium oxide (atomic layer deposition) which is stable even under high temperature while still retaining its ability to interact with polar analytes[23]. Though this is an effective method to overcome difficulties with certain analytes, it removes some of the ability to control hot spot location[23,107].

Many factors need to be taken into consideration when choosing a plasmonic substrate for SERS, such as the stability and reproducibility both across a substrate and between substrates. If the substrate can undergo chemical reactions such as oxidation or changes due to high temperatures and/or pressures, then it is not suitable. Ideally, the substrate must be inert and minimal interactions will occur between it and the analyte, while still being able to selectively capture said analyte. Nonetheless, because of the need for nano-structuring, nanofeature reproducibility, interferences from matrix molecules, and improvement required in sensitivity and specificity detection, SERS based assays and platforms are not commonly used for sensing or analysis. However, the aforementioned combination of sensitivity and detailed structural insights make SERS a particularly attractive prospect for analytical science but improvements in the above issues are required[153].

In the present work, in chapter 2, the improvement of the reproducibly of the substrates was addressed by optimising existing sphere templating methods to reduce instances of poor of discontinuous packing. The size and shape of the cavities are known to influence the enhancement, and therefore electric field simulations were completed to ensure optimal conditions are used. The sphere templating method used here was proven to provide reproducible uniform hexagonal close-packing of the spheres[154]. Meaning, identical cavity arrays should be obtained, however nanoscopic variations such as the internal roughness of the gold within the pore will still occur. As the study will focus on one cavity pore during measurements and not multiple pores, variation across the pores should not be encompasses within the interrogation area. However, some variation will still occur form substrate to substrate and absolute emission enhancement will be influenced.

1.4.3 Metal-Enhanced Fluorescence Spectroscopy (MEF)

Luminescence is the emission of light as a substance in an electronically excited state relaxes radiatively to its ground state. Luminescence is a broad term for emission and can originate through a range of mechanisms, the two more important fluorescence and phosphorescence. The origin of fluorescence can be explained using the Jablonksi diagram, shown in Figure 24. Typically, at room temperature, molecules will occupy the lowest vibrational level of the ground electronic state, known as S_0. When light is absorbed, the molecules is promoted to an excited state (usually a single state S_1 or S_2, where the electron will continue to have an opposite spin state)[155]. Then the excited molecule will lose its excess energy by internal vibration or through collision with solvent oscillators causing it to undergo vibrational cascade and relax to a lower vibrational level in the excited state.

Internal conversion can then occur, which is an isoenergetic crossover, where the original and final states have the same multiplicity, the excited molecule can pass from a low vibrational state of an excited state to a high vibrational level of the ground excitation state if they are of the same energy, this process is then followed by rapid vibrational relaxation. When the molecule then returns to the ground state, it emits the energy in the form of light and is known as fluorescence. In fluorescence when the electron is excited into a higher energy orbital, the direction of the spin is preserved, meaning in even numbers of electrons, the pairs of electrons are arranged in pairs of opposite spins, and this excitation causes no disturbance. Fluorescence is short-lived, typically between 1 and 10ns, where its emission rates are 10^{-9} -10^{-6} s^{-1}.

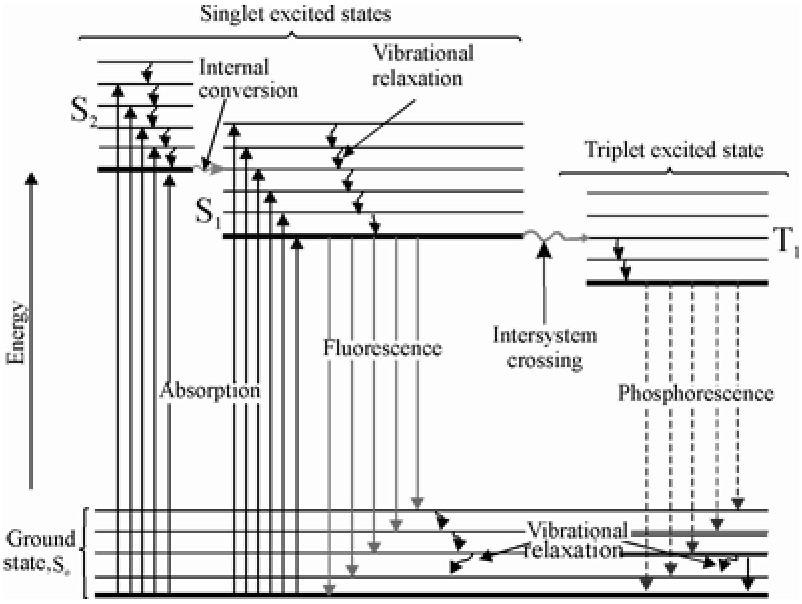

Figure 24: Jablonksi diagram depicting the path of the electron during fluorescence[156].

Phosphorescence is an analogous process but is accompanied by a change in spin multiplicity and is thus a spin forbidden process. In phosphorescence, the spin is reversed and therefore the electron is no longer paired. The molecule is said to be in a triplet state. This indirect crossing from the singlet state to a triplet state is known as intersystem crossing. Phosphorescence is a slower process than fluorescence, where the lifetime can range from milliseconds to seconds[157,158].

In fluorescence, molecules typically emit radiation at a longer wavelength than the radiation they have absorbed, (Kasha's rules). The difference between the absorption and emission maxima is referred to as the Stokes shift[12]. Fluorescence spectroscopy is a highly sensitive method and is capable of detecting single photons[159]. Fluorescence has demonstrated a range of applications and has been exploited in methods such as FCS, confocal microscopy, and stimulated emission depletion microscopy, to name a few.

For organic molecules, phosphorescence is rarely seen in fluid solutions at room temperature due to non-radiative decay and quenching which can deactivate the phosphorescence. However, it is the prevalent emission mechanism observed for metallic phosphors such as Ru (II) complexes due to the heavy atom effect[160,161]. Quenching occurs where ions or molecules decrease the intensity of the emission through; reaction with the luminophore (static quenching), through electron-energy transfer or dynamic quenching. Examples of quenchers include iodide, oxygen and acrylamide. Fluorescence lifetime is not affected in static quenching; however, it is in dynamic quenching, and this is how the mechanisms can be distinguished. Thermal quenching can also occur, where an increase in temperature can decrease the intensity, lifetime and quantum yield of the fluorophore[157,162]. The fluorescence quantum yield is a parameter used to describe the efficiency of a given fluorophore. It is defined as the ratio of the number of emitted photons divided by the number of absorbed photons[162].

Förster resonance energy transfer (FRET) is an important photophysical effect that is commonly used for biological applications. It is a distance dependant, (10 to 60-100 Å[153]) transfer of radiation less energy from an excited donor fluorophore to an acceptor fluorophore. It has been applied as a molecular ruler permitting measurement of the distance between donor and acceptor over nanoscale lengths in vitro and in vivo. FRET transfer occurs through dipole-dipole interactions, where an oscillating dipole exchanges energy with a dipole of similar resonance frequency[101,162,163].

As with Raman spectroscopy, metal surfaces can also influence emission. Emission signal can be enhanced through a mechanism similar to SERS known as Surface enhanced fluorescence (SEF) or metal enhanced fluorescence (MEF). The Purcell effect occurs where the surrounding nano-features influence the emission rate of the fluorescent molecule. This can affect both the spontaneous emission rate of a fluorophore bound at or near a plasmonically active surface and its angular emission pattern[101].

It is known that the presence of an interface modifies the angular emission of the fluorophore[164]. If this interface is reflective, it has been found to give an improved excitation by up to a factor of 4, when compared to a glass slide. Reflective metallic surfaces enhance emission of a fluorophore through a combination of both reflective and plasmonic mechanisms. Plasmonic MEF enhancement occurs through two main processes. One is due to the non-radiative coupling between the excited state of the fluorophore and the surface plasmons from the metal particles, i.e. the plasmonic enhancement, shown in Figure 25. As previously described, plasmonic enhancement is due to electron oscillations near a metal surface which are perpendicular to the surface which causes an evanescent EM field[101]. This non-radiative energy transfer between the fluorophore and metal is influenced by both the strength of the EM field and the degree of spectral overlap between the metal surface and the fluorophore[165] and is known to effect the decay rate of the fluorophore. The second process is due to enhanced absorption of light by the fluorophore from the increased electric fields around the metal nanostructures. As fluorophores located between nanoparticles (hotspots) experience a larger electric field than those in the vicinity of single particles[101], it is of interest to create structures that promote this effect. MEF will result in the change of the fluorophores emission quantum yield and fluorescence lifetime[166]. Lakowicz has stated that for the best MEF enhancement, quantum yields should be relatively low[157].

MEF is a distance dependant process as the oscillation strength if the plasmons decreases with distance. This is reflected in lifetime measurements as the radiation field and the field reflected at metallic interfaces are weakened with increasing distance. As shown in Figure 25, at short distances (below 5 nm[167]), emission is quenched due to nonradiative energy transfer from the fluorophore to the metal. At larger distance (10-30 nm), less energy is transferred to the plasmon and it is enhanced by the electric-field[168]. Numerous studies have been reported to determine the optimal distance to achieve maximum MEF, however the values can vary[101,157,165,169]. Precise control of the distance between the fluorophore and the metal is a complication that needs to be addressed if MEF is to be used as an analytical technique[170,171].

Quantitation of MEF enhancement can be made through the gain in the relative molecular detection (MDE) which is the number of detected photons vs the number of absorbed photons. The reflective surface helps maximise the MDE by redirecting the light towards the detector while the plasmonic effects due to the metal surface increase the EM field at the fluorophores position as this will lead to the excitation rate increasing as the light intensity has increased. The various enhancement processes occurring due to MEF can result in an enhancement of 10– to 15- fold when compared to results observed on a glass slide[164]. All these enhancements help increase the sensitivity capabilities of fluorescence, making it an appealing technique as a detection method.

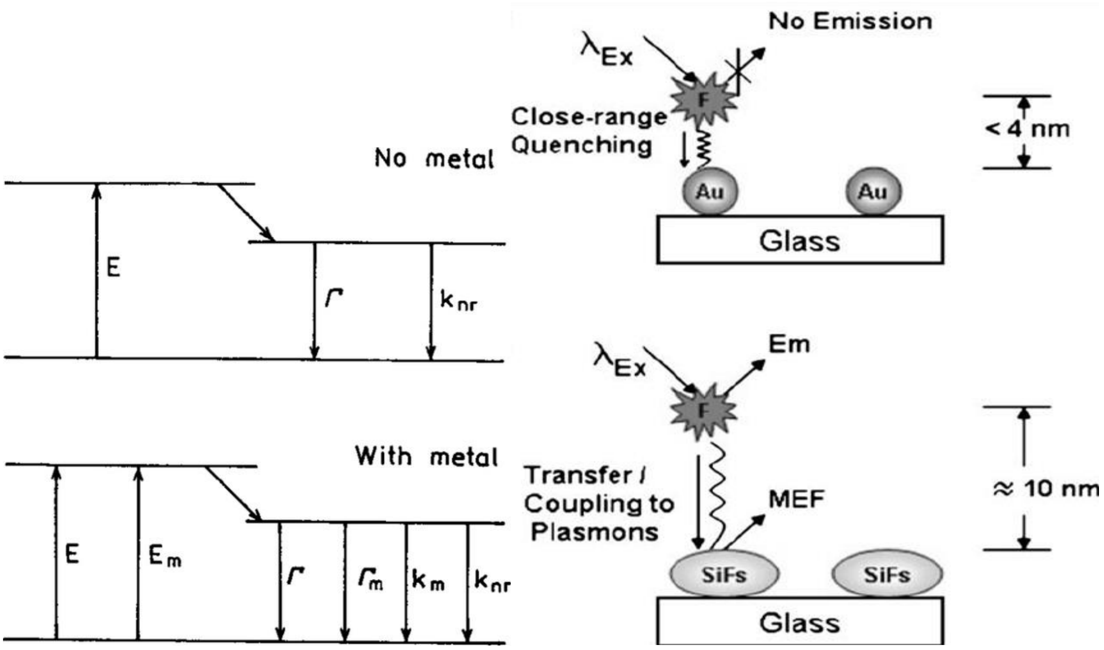

Figure 25: Jabolonski diagram depicting the quenching effect as a metal surface (left) and schematics depicting the quenching (top right), plasmon-coupling effect(bottom right)[169,172]. The Jablonski diagram shows that in the presence of the metal, the radiative decay rate (Γ) and nonradiative decay rate (K_{nr}) or the metal (Γ_m & K_m) also occur. As shown on the right, when the fluorophore is in close contact with the metal surface, energy transfer occurs from the fluorophore to the metal surface and no emission is observe. At an optimal distance between the fluorophore and metal, coupling occurs, resulting in MEF emission.

Ideally, this should all result in a significant fluorescence signal enhancement. Interest in MEF enhancement and its applications, has led to numerous studies involving nanoparticles, nano-rods etc. all of which have shown significant enhancement as the energy flow between the fluorophores and the surface plasmons is considered a major factor of the MEF enhancement. For example, one study utilised MEF through the development of nanoparticles for sensing dye, such as "nanoballs", where a silver core is encapsulated by a fluorophore embedded silica shell[173]. This could then be used to bring imaging dyes to target cells. Another study found that by using gold nanoparticles, they obtained 60-fold enhancement, allowing for detection of volumes down to 270 zeptoliters for low quantum yield fluorophore[174]. One large problem with imaging dyes and other fluorophores is "self-quenching", e.g. fluorescein, studies have seen that in close proximity to silver island films, there was a large decrease in self quenching[167].

The use of MEF for lipid studies has also been examined. Some studies have used methods such as FCS, where the fluorophores signal was enhanced with gold, to examine the diffusion kinetics of lipid bilayers[175] or the phase separation in membranes[176]. Another study, exploited gold nanoantennas to monitor fluorophores diffusion in a lipid membrane[177]. Lohmüller et al. incorporated gold nanoparticles of between 5-7 nm in size into a supported lipid membrane. These particles were selectively modified with proteins, which allowed for their adhesion to live cells, meaning this system may be used for live-cell experimentation[178]. Regmi et al. found through the exploitation of enhancement from nanoantennas that the presence of cholesterol traps sphingomyelin within nanodomains[179]. Overall, the use of MEF is proving to be a valuable technique in examining the dynamics occurring in biological membranes[176,180,181].

Periodic metal cavity array structures are interesting platforms for MEF. The pore structures enables solution encapsulation, while the plasmonic architecture of the metal, along with the hemispherical gold surface, which provides a concave reflective surface, both combine to produce high fluorescence enhancement. The MEF properties of gold cavity arrays were explored by Jose et al.[104,106,182] and it was found that emission enhancement of more than 50-fold were obtained for fullerene and 15-fold for Ruthenium polypyridyl complex. They also showed through confocal microscopy, that emission enhancement was observed at smaller diameter size to the cavity pore, where little significant enhancement was observed from the top surface from the cavities This combined with the evidence that only significant emission enhancement was seen when the probe was sonicated into the cavity (cavities have proven to contain an air pocket unless filled by sonication) indicates that cavity enhancement is highly localised near the bottom of the well[104].

Gimenez et al. reported reproducible emission enhancement on the cavity structures used here. Interestingly, emission was not repeatedly improved upon introduction of nanostructures into the cavity well, as was seen at other cavity diameter sizes[154]. Jose et al. reported emission broadening and red shift of their Ruthenium polypyridyl probe on microcavity arrays, in comparison to the bulk solution, which was attributed to the probe interacting with the metal surface. They also showed that although, surface quenching occurred when the probe was in close proximity to the metal surface, emission was still enhanced 4-fold., which is considerable smaller to the 15-fold emission seen in non-surface bound probe[104].

1.5 Membrane Permeable Drugs

1.5.1 Anthracyclines

In this thesis, two drug models are primarily focused on to test the platform, doxorubicin (Doxo) & daunorubicin (Dauno). Their molecular structures are shown in Figure 26. They are anthracycline antibiotics commonly used in chemotherapy due to their cytotoxicity. They originate as a metabolic side product of a fungus known as Streptomyces[183,184]. There is still no definitive explanation as to how these drugs work, however there are a number of theories. It is believed they work by either, topoisomerase II inhibition, DNA intercalation, or free radical generation[83]. In 2011, a cell based study was completed, that suggested doxorubicin works by process of regulated intramembranous proteolysis[83] i.e. It cleaves a membrane bound protein which allows the liberated soluble messaging molecule to initiate processes, including apoptosis, lipid metabolism etc.

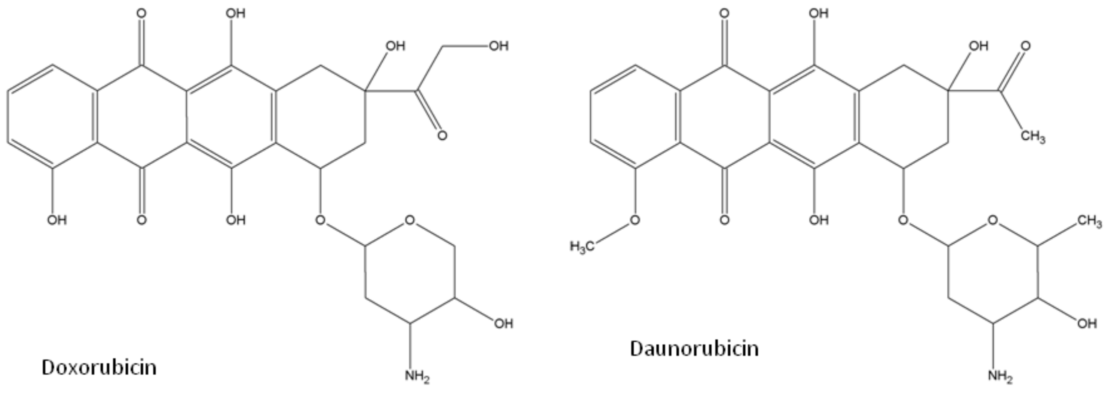

Figure 26: Chemical structure of doxorubicin and daunorubicin.

These drugs were selected as models as they are known to pass through the membrane through passive diffusion. Both drugs are believed to interact similarly with lipid bilayers. They are reported to interact with the membrane electrostatically; between a positively charged amino sugar and the negatively charged phospholipid, and through hydrophobic interactions; where the dihydroxyanthraquinone moiety becomes embedded within the bilayer[41,84]. Doxorubicin has a lower lipophilicity of the two drugs, and therefore is believed to bind more through electrostatic interactions than daunorubicin, which is believed to bind more through hydrophobic interactions[41].

The extent of passive permeation through a membrane is dependent on the composition of the membrane. Gallois et al. suggested that anionic phospholipids decrease the permeability coefficient of anthracyclines[41]. Their study in large unilamellar vesicles indicated that this could be due to the phospholipid polar headgroups tightening as the adriamycin (part of the anthracycline family) was adsorbed on. It has also been reported that the presence of cholesterol does not influence the interactions of these drugs with the membrane, though it does in other anthracyclines such as idarubicin[41].

Another reason for the selection of doxorubicin and daunorubicin in the context of this study, is that both drugs are fluorescent and have been studied within biological samples by both fluorescence or electrochemistry[185,186]. Previously, the limit of detection (LOD) for SERS experiments has been reported to be around 1-2 nM within plasma or serum samples, (though one report found a LOD of 0.1 nM using capillary electrophoresis with laser induced fluorescence, unfortunately, many pre-treatment steps were required for these methods[187]). As the doxorubicin and daunorubicin are typically found in the nM concentration in vivo, the ability to detect at such levels is important. Permeability studies at biomimetic models should ideally be able to match physiological levels. For this SERS and MEF are of interest as they have the capability to detect very low concentrations. Studies such as those completed by Litti et al. have shown that detection of anticancer drugs at low concentrations are feasible [187,188]making this an appealing method to use.

1.5.2 Ru (II) Polypyridyl Luminophores

The second membrane permeable species studied within this thesis were Ruthenium (II) polypyridyl peptide conjugates. The probes were selected as they have demonstrated to be cell membrane permeable. Although in contrast to the anthracyclines, their uptake mechanism appears to be through active transport, as it was found to be temperature dependant[189–191]. As the mechanism is not fully elucidated, we were interested in understanding if the platform could shed light on this mechanism by indicating if passive membrane transport occurs for these species.

Ruthenium (II) polypyridyl complexes are currently under investigation in both anti-microbial and anti-cancer applications. Furthermore, because of Ru (II) polypyridyl complexes' favourable photophysical and redox properties, they have been applied to biological imaging and as phototherapeutic agents[192–195]. Many ruthenium (II) polypyridyl complexes with extended aromatic planar ligands have been shown to interact strongly with

DNA through intercalation, into the major and minor grooves of the DNA structure[189,196–198]. However, application in cells has been inhibited by poor water solubility, thermal instability, and low cellular uptake[192]. Efforts to improve uptake have advanced over recent years. For example, a study completed by Puckett and Barton showed that changing the overall charge, in their case, a +2 to a neutral, did not affect the uptake of the dye by the cells, but changing the lipophilicity did[199]. Work completed by Burke[193,194] & Keyes[200,201], demonstrated that the above disadvantages can be overcome using peptide conjugation to both solubilise the complexes and transport them across the membrane.

Many ruthenium (II) polypyridyl complexes, are luminophores. Analogues of $[Ru(bpy)_3]^{2+}$, the focus of this work are red-emitting probes that have a large Stokes shift with a long-lived emissive state and good photostability[194]. Ruthenium (II) complex emission is typically due to phosphorescence from the triplet metal to ligand charge transfer state[194]. They emit with a modest quantum yield at room temperature, typically up to 10%. Also, due to the large Stokes shift, they emit at high concentrations without evidence of self-quenching, which is useful for small volume work[194].

Two ruthenium (Ru) complexes and their cell permeable peptide conjugates were examined in this study. A Ruthenium dipyrido (3,3-alpha:2', 3'-c) phenazine (DPPZ), and its peptide conjugate, with an attached arginine peptide (R8) and a ruthenium 1,4,5,8 – tetraazaphenanthrene (TAP), also parent and peptide, arginine conjugate. Their structures are shown in chapter 5.

The Ru (II) complexes were synthesized in house by Dr Burke and were previously reported[191,193,202,203]. When DPPZ is coordinated to the Ru (II), the complex shows no or very weak photoluminescence within aqueous solutions at ambient temperature. This is due to the presence of dark and bright excited states located on the 'phenazine' and 'phen' of the DPPZ ligand respectively[193]. The phenazine contains two free nitrogen, which readily bind to hydrogen in water, which causes luminescence to switch off. In the presence of DNA, lipid membranes or organic solvents, intense luminescence has been shown to switch on[198,204]. This indicates that within these studies, no fluorescence should be observed until the complex interacts with the lipid bilayer.

Ru (II)-Tap is a chelating ligand with extended delocalised π-system. It contains six free nitrogen's for interaction, meaning it may undergo six successive protonation in both its ground and excited states[205]. This complex was found to bind with DNA in the nucleus of live cells[202,205]. Due to Ru (II)–Tap high oxidation potential, luminescence can be quenched by the guanine base pair through photoinduced electron transfer. Ru(II)-Tap complexes have been shown to produce more efficient photocleavage of the DNA backbone than other Ru polypyridyl complexes[206]. They have also been shown to form photo adducts with the nucleic acids[206], where a covalent bond is formed between a single ligand of the complex with a guanine base without destruction occurring to the ligand sphere around the metal ion[207]. DNA photodamage induced by Ru (II)-tap-peptide conjugate is oxygen independent. The peptide complex was also found to have slightly longer emission lifetimes, this is suspected to be due to a "protective effect" caused by the peptide, reducing the quenching caused by oxygen[202]. This indicates, that within these studies, the complexes should fluoresce in solution.

Byrne et al. have reported dramatically improved uptake in cells for peptide conjugated Ru (II) polypyridyl's than their parent complexes[191,193,194,202]. An example is shown in Figure 27, where Ru(II) DPPZ peptide conjugate showed clear uptake into the mitochondrial nucleoids in HeLa cells. They also exhibited low cytotoxicity in dark conditions but could stimulate cell death under photoirradiation attributed to DNA photooxidation[193].

Permeability of the Ru (II) polypyridyl complexes was found to be switched off at 4 °C. This suggests an activated mechanism of uptake into cells occurs. However, low temperatures can reduce the fluidity and therefore permeability of the membrane. Chapter 5 thus focuses on the exploration of whether passive permeation can occur for these complexes at model lipid bilayers.

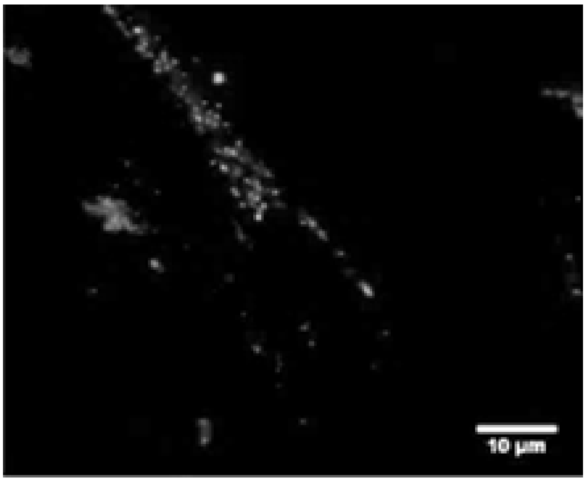

Figure 27: Live confocal imaging of 70 μM Ru-DPPZ-R8 in live HeLa cells in the absence of light at 37 °C. Excitation was at 470 nm, emission 565-700 nm[193].

1.5 Project Scope

As described in the above introduction, periodic gold hemispherical microcavity arrays have been demonstrated to be effective SERS and MEF platforms with enhancement factors of 1 x 10^7 and approximately 50-fold respectively. For MEF, Jose et al. demonstrated that for solution phase fluorophore emission enhancement comes primarily from the bottom of the well, through combination of reflectance effects (shown from enhancement in cobalt cavities not expected to have a plasmon resonant with the excitation or the emission) and the plasmonic fields of the gold cavity[104]. Gimenez et al. has demonstrated that the 1 μm cavity fabrication method used here, results in reproducible microarrays, which showed minimal signal enhancement variation due to nano-structural differences when compared to other sized cavites[154].

Secondly, the gold microcavity arrays have been shown, with appropriate surface modification, to form stable and fluidic lipid bilayers of versatile composition[21,27,102], where stability has been demonstrated to be a minimum of 8 hours for a DOPC spanned bilyer[102]. This thesis focuses on the hypothesis that these two advantages can be combined to provide a useful qualitative assay into whether a molecular species is capable of passively permeating a lipid membrane. As shown in Figure 1, by building a lipid membrane across the array, to enter the cavity, any molecular species must first permeate the membrane to access the cavity interior, where if sufficient enhancement of the Raman or fluorescence signature is obtained, arrival of the drug to the hot-spot at the bottom of the well can be marked.

This thesis is focussed on a proof of concept of this principle. Fluorescence was the primary focus, as the combination of reflectance and plasmonic enhancement was found to be most localised for this method. The drawback of this method is that the enhanced emission will be observed against the background of fluorescence form the species remaining in the contact solution. However, Jose et al. has shown through confocal imaging that the enhanced emission was easily distinguishable from background emission[104]. After sufficient evidence suggests that this proof of principle study can detect if a drug has passively permeated the membrane, the method was improved upon and applied to a permeable species of unknown uptake mechanism, i.e. Ruthenium polypyridyl peptide complexes, as they are observed to be permeable to live cells[191,199,201].

As discussed, the use of metal substrates has proven to result in significant signal enhancement in both Raman and fluorescence spectroscopy. However, reproducibility in signal enhancement between substrates is a known issue, due to the Polystyrene sphere templating fabrication method. The gold microcavities require specific properties to be considered suitable for our proposed study. This includes uniformity, hexagonally close packing and reproducibility. Chapter 2 will initially focus on the optimisation of sphere packing and the development of the microcavity arrays. With challenges encountered in achieving reproducible signal enhancement in plasmonically enhanced spectroscopic methods, the current study is not intended to establish a quantitative analytical assay. Rather, the object was a proof of principle of a qualitative method where a yes/no answer can be provided on permeability across membranes, where membrane compositions can be changed.

Chapter 2 will also focus on lipid bilayer formation, as lipid bilayers have been shown to successfully span over the plasmonically active cavities using a combination of the Langmuir Blodgett trough and vesicle fusion[27]. The stability of the bilayers was determined through electrochemical impedance spectroscopy studies[18]. This platform shall act as our analogue to a single cell membrane, where we will ideally focus on the occurring kinetics at one pore.

Anthracyclines are known as membrane permeable anti-cancer drugs. They are commonly used for drug targeting and delivery, making them of interest for permeability studies. Chapter 3 investigates the permeation and dynamics of two well-characterised anti-cancer drugs, doxorubicin and daunorubicin at different concentrations, through a simple DOPC membrane and through a ternary composition using surface enhanced Raman spectroscopy. This is attempted to determine if this platform is a viable option to detect if a drug may passively diffuse across a lipid membrane. Chapter 4 examined the application of the substrates for detection of analyte arrival using fluorescence. Using an analogous approach to chapter 3, doxorubicin and daunorubicin were applied to DOPC and ternary domain forming bilayers, with metal enhanced fluorescence as the detection method. A non-membrane permeable dye, DRAQ7 was also examined to identify the clear distinction in response when the molecule cannot permeate the membrane and diffuse into the cavity.

Finally, chapter 5 depicts the advancement of the assay to a more microfluidic platform that allows for drug delivery and monitoring. The permeation of a more biomimetic bilayer composition was examined with the previous drugs doxorubicin and daunorubicin, to determine if the presence of a charged lipid has an effect on the permeability of the drugs. In the second part of chapter 5, the permeation of ruthenium (II) metal complexes and their peptide conjugates was evaluated to determine if their uptake in cells was through passive diffusion. As Ruthenium (II) polypyridyl peptide conjugates are also known to permeate a cell. They are suspected to require mediated transport to enter a cell, meaning this study will provide a valuable insight into the mechanism of uptake for these complexes.

Ultimately, this thesis will focus on answering the question, is it possible to use metal enhanced Raman or fluorescence spectroscopy to qualitatively determine if a drug can passively permeate a lipid bilayer.

Chapter 2: Fabrication and Characterisation of Plasmonic Microcavity Array & Bilayer assembly

2.1 Introduction

As described earlier, pore array supported lipid bilayers offer the advantages of liposomes in terms of membrane fluidity and structure, but also offer the versatility (in terms of compositional control) and some of the stability of single lipid bilayers[21,27,102,208,209]. Gold nanocavities have the advantage of being an inert substrate while also providing access to plasmonically enhanced spectroscopy as well as electrochemistry. Cavities may be altered in size to gain the optimal plasmonic enhancement under the specific experimental conditions and excitation wavelength. They may also be selectively surface modified through thiol self-assembly; which is advantageous in controlling the hydrophilicity of the surface for bilayer assembly.

This chapter describes the optimisation of the fabrication method for preparation of gold microcavity substrates, for the support of spanned lipid bilayers. There are numerous methods reported for the fabrication of microcavities[104,107,210]. However, Maher's work demonstrated that pore shape has an influence on bilayer stability, where stable bilayers would not form over cylindrical pores, however, hemispherical pores proved suitable[102]. Meaning, some fabrication method such as ebeam lithography, used to develop the cavities may lead to unsuitable pore shape. Nanolithography employs sphere templating to generate periodic structures and will result in the desired hemispherical pores. It requires an ordered arrangement of spheres, and numerous methods have been reported in literature to achieve this. The methods include spin-coating, Langmuir Blodgett trough deposition and the capillary effect to name a few[107,108,211,212]. The fabrication of microcavities can be completed on numerous types of surface; however, the wettability of the surface has an impact on the packing of the spheres. It has been observed that increased wettability allows for the formation of a thin water film between the substrate and spheres. This film results in a capillary immersion force which assists the assembly of the spheres in an ordered and close-packed manner[105,127].

LB deposition has been reported as a useful approach for the formation of close-packed nanoparticles of diverse composition[113–116]. This has included iron oxide[114,115], silver[116], gold[117] and polystyrene spheres[118]. Typically, a hydrophobic particle is deposited on the water within the trough; however, this is not always the case. A study by Aleksandrovic et al. successfully achieved assembly of cobalt-platinum nanoparticles on gold substrates. These particles contained the hydrophobic ligands, hexadecylamine and adamantane carboxylic acid. These particles could not successfully form a film on the gold substrate though LB deposition with water as they would aggregate and then sink. However, they were able to successfully form a film when particles were deposited onto ethylene glycol & diethylene glycol, resulting in close packing[113].

Similar to the LB method is the use of the air/water interface, where the evaporation of the solvent causes the formation of close packing. For example, Watanabe et al. introduced glass substrates into a suspension containing their colloidal particles (gold 100 nm, 120-270 nm silica or Ps 200 nm). As the solution evaporated, the particles assemble at the meniscus, resulting in a close packing stripe formation[213]. Li et al. reported similar results with silica nanoparticles[214]. A study by Born et al. investigated how the meniscus shape affects the particles assembly. They looked at the assembly using the air/water interface method, dip-coating and capillary force method, where the meniscus shape differs in each. They found that the assembly was affected by the meniscus shape and the contact angle. If the meniscus contained a small curvature, it resulted in more uniform evaporation over the substrate. However, a flat meniscus resulted in nonuniform multilayer deposition[215]. Their results indicate that the meniscus has a substantial effect on the packing and needs to be considered in the trials of these methods.

Spin coating has also been used to create close-packed monolayers of spheres. Through centrifugal force, it causes the solution to be dispersed across the substrate. As the solvent evaporates, it causes the viscosity to increase, meaning the dispersal ceases and a film of spheres is formed[211]. This method has been applied for the monolayer and multilayer formation of quantum dots[216], Co[217], Ag[217,218], Au[219], FePt nanoparticles[220,221] and polystyrene spheres[212,222] to name a few. Spin coating has also been used for other methods such as to develop polystyrene chains. For example, Brulet et al. used small angle neutron scattering to establish chains of up to 45 Å in length that formed after spin coating[223].

Here, the method used to fabricate close packed arrays was developed by Dr Gimenez[154], which used the convection force of the evaporating solution containing Ps spheres to form close-packed sphere templates. Electrochemical deposition of gold allowed for controlled growth of the cavities. The cavities were then characterised using SEM imaging and confocal fluorescence microscopy. The cavity arrays were then used for bilayer formation. Extensive research has already been completed within the group on fabrication of bilayer at pore arrays[21,27,102,209,224], and their established parameters for stability were used in this study. Cavity spanned lipid bilayers were tested for stability, to determine their lifetime, allowing for the maximum experimentation window to be identified. The stability was determined through electrochemical impedance spectroscopy and confocal microscopy. Fluorescence and Raman spectroscopy were completed of background contributing elements as controls.

Three types of bilayer composition that were examined throughout this study are DOPC, DOPC/SM/CH (40/40/20 %) and "Nature's own" (DOPC/DOPE/CH/SM/DOPS) (32/25/20/15/8 %) symmetric bilayers. Lipid components are not evenly distributed throughout the organelles of the cells[225]. The lipids may adopt a variety of liquid-crystalline states or mesophases[226]. Planar lipid bilayers tend to take the lamellar phase, while non-planar lipid components tend to be non-lamellar phases such as inverted hexagonal and cubic phases[226]. A phase diagram such as shown in Figure 28, can be used to determine the phase-composition ratio. It indicates where the liquid ordered, and liquid disordered phases occur, giving an insight on ratios for composition etc. Temperature can also affect whether lipids are in the ordered or disordered phases. It has been shown that a PC/CH (55:45) composition changes from liquid ordered at 15^{0}C to both ordered and disordered between 25 and 35^0 C[50]. As marked in Figure 28, at our chosen ratios of 40/40/20 %, both liquid ordered, and disordered domains should be present.

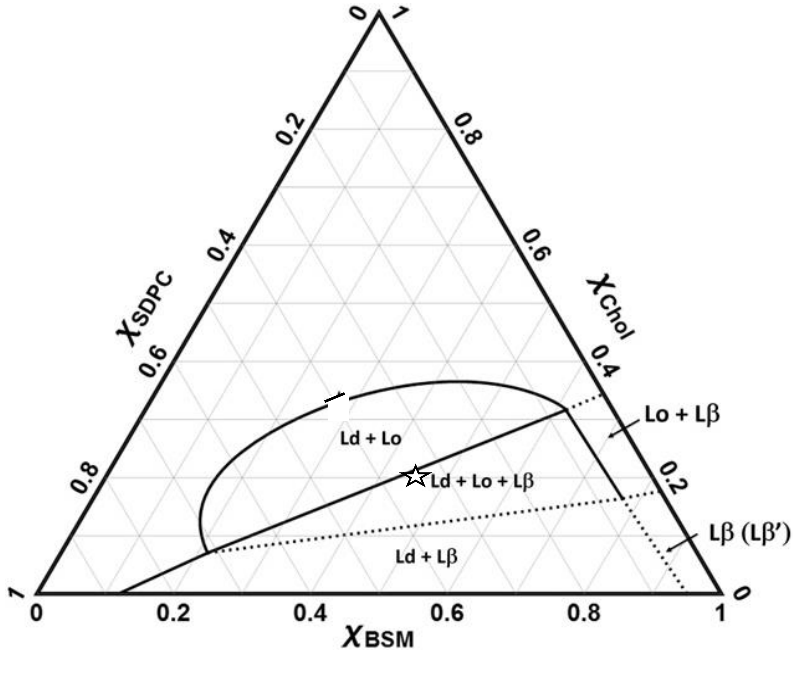

Figure 28: Lipid phase diagram for DOPC/SM/CH at 23^{0}C, where solid lines show measured phase boundaries and dashed lines show boundaries that are putative or extrapolated. [227]

2.2 Materials & Methods

2.2.1 Fabrication of Gold Cavity Arrays

2.2.1.1 Optimal Method of Cavity Formation

Gold wafer discs (AMS Biotechnology limited) consisting of a non-conductive silicon wafer base, a 10 nm titanium layer for adhesion and a 100 nm gold layer were cut into approx. 1.5 x 0.8 cm and then air plasma treated for 5 minutes. The cut gold discs were mounted onto a holder, and 20 µl of 1 µm sized polystyrene spheres solution (Polysciences Inc.) at 1 % (w/v) was deposited onto the gold wafers. A glass slide was then placed over the chip, causing a capillary effect. The mounted chips were placed onto a platform at an angle of 1^0 x 2^0, that encouraged monolayer formation of the spheres. The chips were left to dry overnight at 4 ^{0}C for the liquid to be evaporated fully, resulting in a thin layer of spheres across the chip. The chip was then examined under a light microscope to determine if multilayers occurred. A small area at the edge of the chip is then cleared of spheres using tape to allow for its attachment to instrumentation.

Gold deposition was completed by partial immersion of the sample in a gold salt solution (Technic Inc.) that was previously degassed with nitrogen for 15 minutes. Deposition[105,127] was performed using standard 3 electrode set up. The gold sample acts as the working electrode, while Ag/AgCl electrode is used as the reference and a platinum wire is used as a counter electrode. A potential of -0.6 V was applied by an electrochemical 990 CH workstation. When the optimal charge is reached, the samples were then removed. The optimal charge differs from sample to sample but is reliably identified from the i-t curve, (where it appears at the second rise in current). At this point, gold growth had reached the centre of the sphere, which is most advantageous for our cavities. Typically 100 nm layer of gold had been deposited on the cavities[18]. These were then rinsed with deionised water and left to dry. The spheres were then removed by immersing the cavity in tetrahydrofuran (THF) and sonicating for 30 minutes. The substrates were then characterised by SEM.

2.2.1.2 Langmuir Blodgett Sphere Deposition

The LB trough was cleaned prior to use with ethanol to minimise contaminates. Two tubes of 1 ml of 2.6 % (w/v) 1 µm polystyrene sphere stock solution were centrifuged at 9000 rpm for 5 minutes to precipitate spheres out of the original solution. The liquid was then removed, and spheres were resuspended in 0.5 ml ethanol. The two tubes were then combined, resulting in 1 ml of 5 % (w/v) stock. 300 µl of this stock was deposited dropwise onto the deionised water surface in the Langmuir Blodgett trough (KVS Nima) and left for 5 minutes to allow for ethanol evaporation. The barriers were then compressed and held at a pressure of 20 mN/m. Clean gold wafer chip were then clipped to the dipper of the instrument. The chips were immersed at speed 150 mm/min and then removed slowly at 3 mm/min. When required, cysteamine pre-treatment was completed to alter the surface chemistry. This was accomplished by overnight immersion of clean gold wafer chips (approx. 1 x 2 cm) in 1 mM cysteamine in ethanol.

2.2.1.3 Spin Coating Sphere Deposition

A spinner (metrohm) was used with a platinum SEM stub as a mounting platform for the chip. A clean, planar gold chip of approx. 1.5 cm x 0.5 cm or 1 x 2 cm was attached to the stub. Occasionally, the chip was pre-treated with 10 mM cysteamine in ethanol by overnight immersion. A sphere solution (concentration was varied) was dropcast onto the chip, and the spinner was immediately turned on and then stopped once the chip appeared dry. The following were the parameters varied within the experiment; volume dropcast (10 µl-500 µl), concentration of spheres (0.1-5 %), solvent composition (ethanol: ethylene glycol), spin speed (500 rpm-3000 rpm) and type of spheres used (unfunctionalised & sulfate functionalised spheres). This was completed at room temperature (RT 18-23^{0}C) and repeated a minimum or three times at each parameter variation.

2.2.1.4 Dropcasting Sphere Deposition

Clean gold wafer chips were cut into approx. 1 x 2 cm. Teflon tape was attached to 1/3 of the chip. A 1 % sphere solution in deionised water was prepared from 2.6 % (w/v) stock of 1 µm polystyrene spheres. 50 – 150 µl of the sphere solution was vertically deposited onto the exposed area of the gold wafer chip. These were then covered to protect from contaminants and left to dry overnight. This was completed at room temperature. This was repeated 5-8 times depending on parameters.

2.2.1.5 Air/Water Interface Sphere Deposition

Gold chips of approx. 1.5 x 0.5 cm were placed at an angle within a container. Teflon tape was used to hold the sample in place. 2-7 ml of 1 % (w/v) polystyrene sphere solution was added and left to evaporate in the fumehood. Containers consisted of petri dishes and 10 ml & 50 ml beakers. Each container was repeated 5 time at room temperature.

2.2.2 Scanning Electron Microscopy

Scanning electron microscopy (SEM) is a versatile method that allows for the examination of surface morphology and chemical composition of dry samples. The SEM system consists of an electron gun which accelerates electrons at energy levels of 0.1-30keV. Electromagnetic lenses and apertures focus the beam and define it into a small electron spot on the specimen. This is all performed under high vacuum to allow the electron to travel without any scattering from air. The specimen is mounted on a stage within the vacuum chamber. A scintillator-photomultiplier developed by Everhart and Thornley is commonly used as a detector for secondary electron detection.

All SEM measurements were completed using a Hitachi S-3400n scanning electron microscope. Samples were prepared by mounting upon a carbon backing on a metal stub. The instrument parameters were set to a probe current of 35 kV, aperture size 3 nm and an electron beam at 10 KV. Images were taken across at least 3 different areas per sample to obtain a representative image across the sample.

2.2.3 Surface Modification of Gold Cavities.

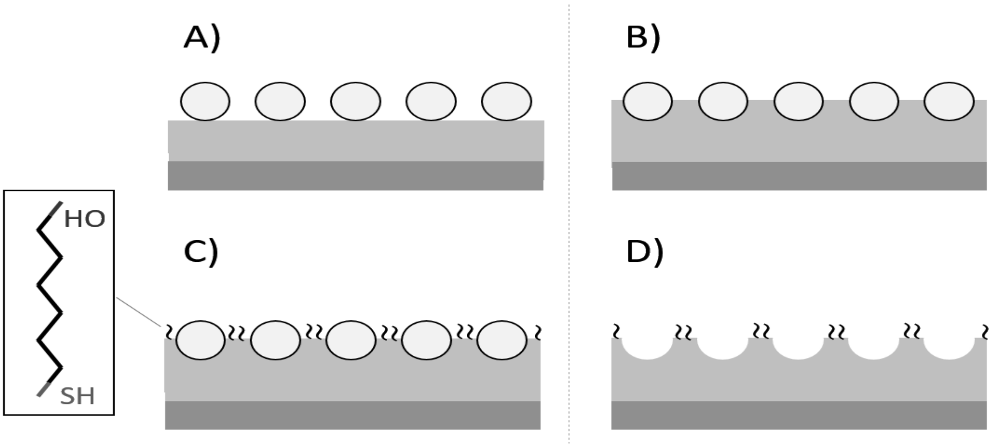

Figure 29: Diagram depicting the modification process of the cavities, where in a) spheres are deposited onto gold wafer chips (chips also contain a silicon and aluminium layer for binding). B) Gold is grown around the spheres. C) 6-mercapto-1-hexanol has self-assembled onto the top surface after overnight immersion. D) spheres are removed through sonication in THF.

The surface of the cavities was selectively modified with a hydrophobic or hydrophilic monolayer depending on need. Most commonly, 6-mercapto-1-hexanol (C6) (Sigma-Aldrich) was used as a blocking agent on the top surface. C6 was chosen due to its ability to partially block the surface while promoting the formation of a lipid bilayer due to its hydrophilic modification of the surface[228]. The modification occurs through self-assembly of the thiol group to the gold, resulting in an ordered self-assembled monolayer. If this is completed before the spheres are removed, then only the top surface is exposed and modified, as seen in Figure 29[126]. The spheres are then removed by sonication in THF for 15 minutes; this time frame is short enough to remove the spheres while not substantially removing the modified layer. The inner walls within the cavities can then be modified with another surface-active species if necessary. The modification was done by a 24-hour immersion of the cavities in a 10 mM solution at room temperature, then samples were dried and stored in a desiccator at 4 ^{0}C.

2.2.4 Formation of Lipid Bilayers

Vesicles were prepared by placing 20 µl of a lipid stock solution (Avanti) of 50 mg/ml in chloroform, into a glass vial and evaporating the chloroform under a stream of nitrogen. This vial was then placed under vacuum for a minimum of 30 minutes to ensure the full drying of the lipids, which were then re-suspended in 1 ml of PBS. The vesicles are then extruded through 100 nm polycarbonate membrane for a minimum of 11 times (complex compositions required a higher number of extrusions), to form monodisperse vesicles.

A Langmuir Blodgett trough (KVS Nima) was used to create the first monolayer of the bilayer. The lipids of interest (1 mg/ml) were deposited onto the surface of deionised water in the trough using a glass syringe and left for 10 minutes to allow for the full evaporation of the chloroform. The barriers were then compressed and held at a pressure of 32 mN/m. Cavity arrays that were previously filled with PBS through sonication, were then clipped to the dipper of the instrument. The cavities were immersed at speed 150 mm/min and then removed at 5 mm/min to ensure monolayer formation only occurs upon chip removal. The chip was then immersed in the vesicle solution at an angle of 25^0 and left for a minimum of 20 minutes. This was completed at room temperature.

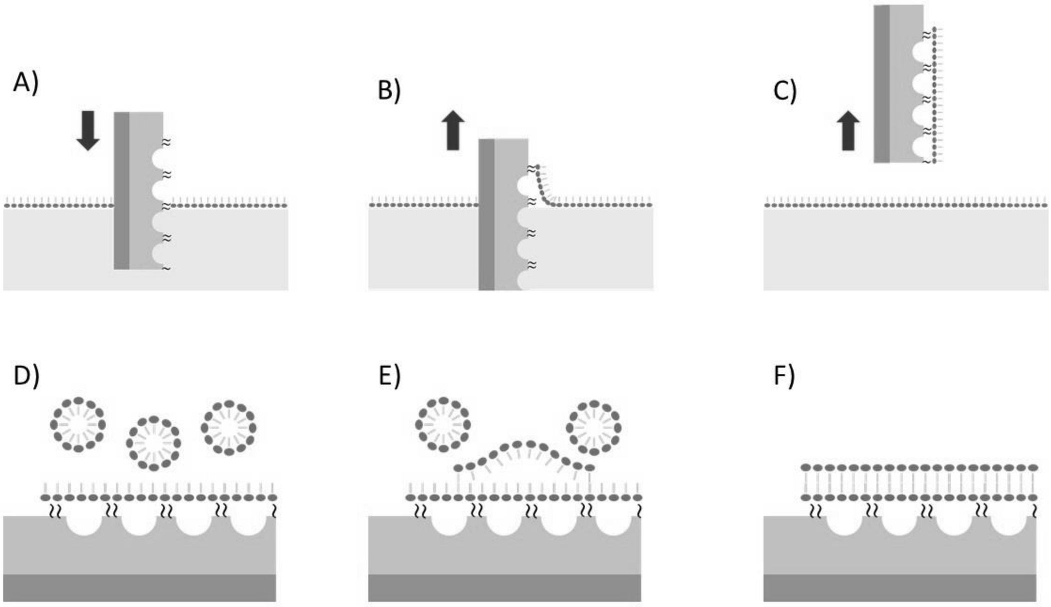

Figure 30: Schematic diagram of the bilayer formation process, where A) introduction of modified cavity chip into solution, B) slow removal of chip allowing lipids to assemble on surface, C) removal of chip with a monolayer formation, D) introduction of vesicles, E) Disruption of vesicles and F) formation of bilayer.

2.2.5 Electrochemical Impedance Spectroscopy

Electrochemical Impedance Spectroscopy (EIS) was completed at room temperature using a standard 3 electrode cell, with a platinum wire as the auxiliary electrode, a silver chloride electrode as a reference and the gold cavity as the working electrode. Impedance was completed on a CH instruments Model 760 electrochemical workstation. PBS acted as the electrolyte solution. The EIS measurements were completed over a frequency range of 100000 Hz to 0.01 Hz with an AC modulation amplitude of 0.01V. Figure 31 is the equivalent circuit model used for all data fitting[18]. Where Rs acted as the solution resistance and Rm was the membrane resistance. Rc was the cavity resistance which remained constant. CPEm and Cpec=dl were the membrane capacitance and alpha value, respectively. Data analysis was completed using Zview (Scribner Associates, v3.4e) software.

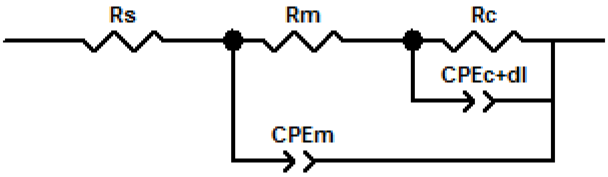

Figure 31: Equivalent circuit[18] model previously developed for Bilayer spanned cavities. Where Rs = solution resistance, Rm= membrane resistance, Rc= cavity resistance, CPEm = capacitance for membrane, Cpec+dl= alpha value.

2.2.6 Absorption & Emission Spectroscopy

Absorbance measurements were completed using a Jasco V-670 spectrometer. Fluorescence emission and excitation were measured using a Varian Cary Eclipse Fluorescence Spectrometer. Slit width of 5 nm and an optical path length of 1 cm were used. PBS was used as the blank solution for baseline correction.

2.2.7 Confocal Fluorescence Microscopy

Confocal fluorescence microscopy is an optical technique commonly used in biomedical science. In fluorescence microscopy, the sample is illuminated at a single selected wavelength, and an image is formed from the resulting fluorescence. Confocal differs from standard fluorescence microscopy due to its ability to create sharp images by excluding any light from the sample that is not from the microscopes focal plane through the use of pinholes. As can be seen in Figure 32, the object not in the focal plane does not reach the detector.

A confocal microscope contains two pinholes, one in front of the light source and one in front of the detector (photomultiplier), resulting in any out-of-focus light to be scattered. As this method only allows for information to be gathered at a single point, to be able to build an image, the image must be scanned, typically in the X-Y plane, where the image is developed on a per-pixel basis. Although this allows for higher resolution imaging, there are disadvantages, as there is a reduction in collected emitted photons, meaning the sample must be illuminated for a longer time or with a high intensity source to ensure an accurate measurement is obtained[191,229,230].

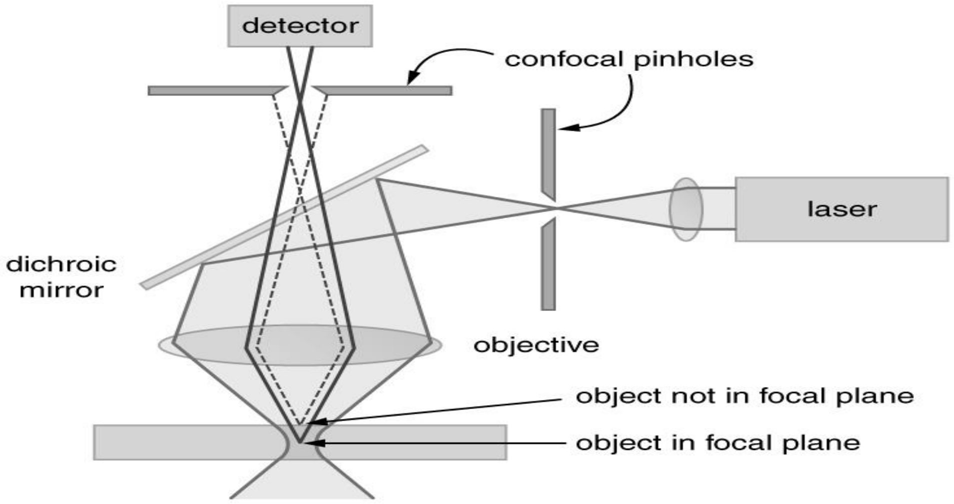

Figure 32: Schematic diagram of confocal fluorescence microscope[231]. Where confocal pinholes only allows light from within the focal plane to reach the detector.

Herein, a Leica TCS SP8 STED super resolution microscope was used for confocal measurements with excitation at 473 nm and emission collected between 512 and 593 nm. Time gating was set at 0.8 ns. A Leica HC PL APO 100 x/1.40 oil immersion lens was used for the measurements. Laser power was set at 1 mW, and a pinhole size of 1.5 nm was used.

2.2.8 Fluorescence and Raman Microscopy

Raman Spectrometers consist of; an excitation source, sample illumination & scattered light collection system, a sample holder, monochromator or spectrograph and a detection system which typically consists of a detector, amplifier and an output device (Figure 33). The excitation sources are commonly a continuous wave laser (typically within the visible region), though pulsed lasers, diode and excimer lasers have been used. As Raman is inherently weak; laser power, focusing of the laser and the collection of the scattered light is of great importance. Collection optics typically consists of an achromatic lens system containing a collecting lens and a focusing lens. The detectors that are commonly used for Raman are photodiode arrays and charged-coupled devices[232].

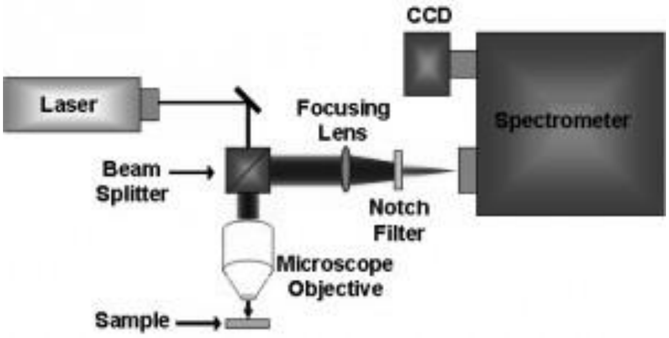

Figure 33: Schematic diagram of Raman spectroscopy setup, showing laser pathway through microscope objective and returning light to the spectrometer and CCD[233].

A Horiba Jobin-Yvon Labram HR 1000 spectrometer attached to an Olympus confocal microscopy was used throughout this thesis for Raman spectroscopy and MEF. A 50x 0.55 Leica PL Fluotar, long distance magnification lens (Leica) was used for all measurements. A Peltier cooled (-70 ^{0}C) charge coupled device detector was used. 473 nm (Argon ion laser) and 785 nm (iXtra single mode diode) were used as excitation wavelength for fluorescence measurements and Raman measurements, respectively, with respective Z (axial) resolutions of 3.12 μm and 5.2 μm[154].

Prior to each set of measurements (and post any changes to objective, grating etc), the instrument was calibrated using the silicon band at 520.7 cm^{-1} from a silicon wafer and the Rayleigh line. Samples were placed either on a clean glass slide or if required to be immersed in liquid, in a small clean glass petri dish, as shown in Figure 34. The laser was focused using the camera and the spectra were taken (note, this would be typically focused on the cavity well bottom. In cases of Raman on bilayer samples, this was then adjusted until maximum lipid spectrum was obtained). Typically, a 50 % neutral density filter and 300 µm slit were used for fluorescence and no filter for Raman.

Drug diffusion was analysed by first obtaining a bilayer Raman spectrum to confirm the bilayers presence and to also confirm the absence of any contamination, while the sample is immersed in PBS. Once obtained, known concentrations of doxorubicin or daunorubicin (Sigma Aldrich) were added to the PBS and spectra were obtained at timed intervals. Exposure time and accumulation number were set as 2 & 10 s respectively. All experiments were completed at room temperature and repeated a minimum of 3 times. The spectra were baseline corrected and analysed using NSG LabSpec 5.0 software.

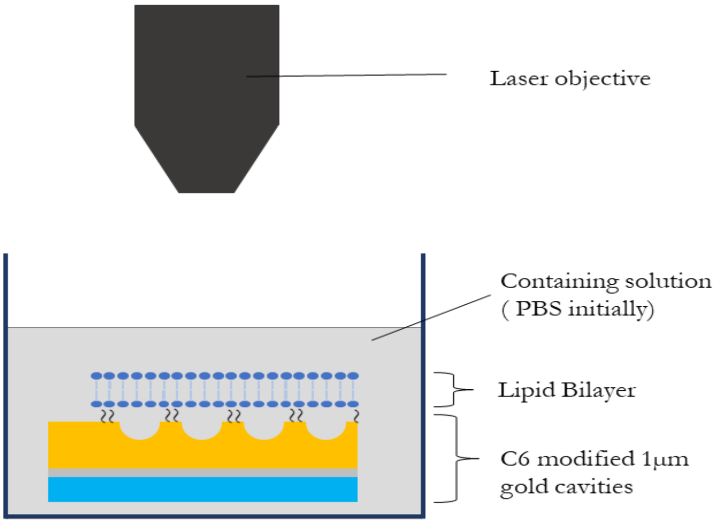

Figure 34: Diagram showing the basic experimental set up used in chapter 3 & 4. Cavity samples are immersed in PBS buffer solution within a glass petri dish, where a 50x 0.55 Leica PL Fluotar, long distance magnification lens allowed for SERS & MEF measurements.

2.3 Results & Discussion

2.3.1 Optimisation of Polystyrene Sphere Packing

For optimal SERS enhancement, and to improve spectral reproducibility across a substrate, ideally cavities should be hexagonally close packed with minimal discontinuity or regions of disorder. Various reported literature methods were attempted to optimise the reproducibly in obtaining a monolayer of close-packed polystyrene spheres to act as a mask for growth of the gold. This including Langmuir Blodgett deposition, spin coating, air/water interface and dropcasting. Functionalised spheres were also used to optimise close packing such as carboxyl and sulfate modified Ps spheres. The gold was also selectively pre-treated with cysteamine to optimise sphere packing due to its efficiency at increasing substrate-particle interaction. This is attributed to the surface becoming positively charged due to the cysteamine, whereas the spheres are typically negatively charged due to sulfate groups present in the suspended solution[127].

Air plasma treatment of the underlying gold wafer was also carried out to improve the hydrophilicity of the surface while also ensuring cleanliness. The hydrophilicity of the substrate has an effect on the packing of the spheres. In evaporation/ meniscus related techniques, on hydrophilic substrates, the assembly occurs due to lateral capillary forces that drive the particles together when the solvent layer thickness is equal to the particle diameter. However, on hydrophobic substrates, the thickness never reaches the particle diameter, resulting in horizontal forces preventing close packing[234]. Details of the steps taken to optimise packing and fabrication can be found below.

2.3.1.1 Langmuir Blodgett Method

The Langmuir Blodgett method was attempted to optimise sphere packing due to its previous recorded success[107,118,222,235]. This method utilises the air/water interface to create a monolayer/ Langmuir film on the substrate. It was found that a high w/v of sphere solution, such as 5 %, was required to obtain a dispersion of the spheres across the deionised water surface within the trough. Precipitation of the spheres out of solution was a regular occurrence with unfunctionalised spheres. Precipitation was most likely due to the spheres hydrophobicity being too low[235]. Sulfate functionalised spheres proved more successful however, repeatable favourable results were not obtained.

Typically, when this method was recorded in literature, the sample was removed at an angle, obtaining a close-packed monolayer[118,222]. However, due to the nature of our LB system, this was not possible. Due to the inability to reproducibly obtain a close-packed monolayer of Ps spheres on the gold surface, the LB method was considered a non-viable option. This method also used a large volume of Ps sphere for dispersal along the trough, which was not ideal or cost-effective, so the LB method was abandoned.

2.3.1.2 Spin Coating Method

The next method attempted to improve Ps sphere packing was "spinning". Variations of spin coating applied to sphere interfacial assembly have been reported[107,222,236]. As a spin coater was not available, we used a "spinner" to create a variation of the method to try develop a close-packed sphere array. As mentioned in section 2.2.1.3, volume dropcast (10 µl-500 µl), concentration of spheres (0.1-5 %), solvent composition (ethanol: ethylene glycol), spin speed (500-3000 rpm) and type of spheres used (unfunctionalised & sulfate functionalised spheres) were the varied parameters. Non–functionalised spheres were tested on both bare gold and cysteamine pre-treated gold. Surprisingly, no differences were observed between the two. Cysteamine pre-treatment should alter the surface chemistry of the gold. Cysteamine has been shown to attach to the gold by the thiol, allowing for the amino group to bind to the PS[237,238]. Due to their short chains, they are known to self-assemble into well-organised monolayers[238]. This monolayer improves the hydrophilicity of the gold. The spheres were suspended in an ethanol/ethylene glycol solution due to ethylene glycols ability to improve sphere spreading by reducing the evaporation rate and alteration of the solvents viscosity[236].

Sphere concentration, speed, functionalisation, volume and concentration was further explored to try obtain a hexagonally packed monolayer. Ultimately, no combination of parameters resulted in a repeatable monolayer of hexagonal close-packing, "spin-coating" was rejected as a viable option. Typically, in literature, higher spin speed were recorded. For example, Colson et al. used a range of 2000-8000 rpm. Through initial MODDE software analysis and principle component analysis, they reported that the sphere ordering was positively correlated with ramp time, whereas rotation speed had a negative correlation. Through spin coating experiments, they then obtained areas of 200 µm^2.[239] As our spinner did not have the abilities to reach such high speeds, it suggests that close packing using spin-coating was beyond our capabilities.

2.3.1.3 Dropcasting Method

The dropcasting approach was a method previously reported within the group and showed adequate packing[18,21,102,119]. However, due to the formation of multilayers, the method was not guaranteed to result in hexagonal packing. Also, variation in the compactness of the packing was observed. Therefore, sphere concentration, gold pre-treatment and solvent composition were varied to improve sphere packing. Gold deposition was also attempted, and parameters were varied for optimal gold growth.

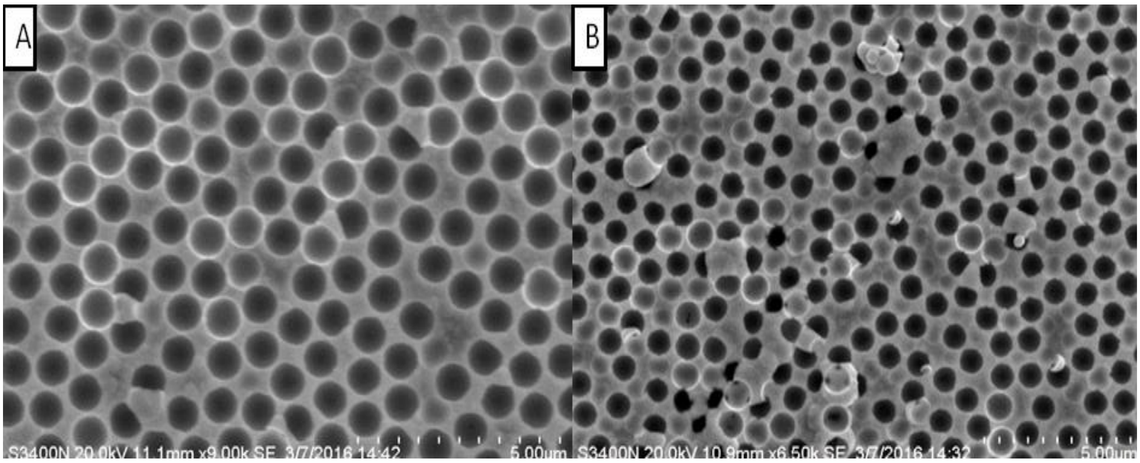

Figure 35: Representative SEM images of 150 µl of A) 2.5 %, B) 0.15 %, (w/v) sphere concentration dropcast onto flat non cysteamine treated gold, then grown at -0.7 V 0.25 C on a CH 660a potentiostat. Both show non-uniformity.

Initially, a range of sphere concentrations from 0.1 % to 5 % (w/v) was examined. 20 µl of unfunctionalised spheres were dropcast onto the gold chips and left to dry. The chips were grown at -0.7 V 0.25 C using a CH 660a potentiostat. As can be seen in Figure 35, similar results occurred regardless of sphere concentration. Multilayer's of spheres were formed which resulted in non-hexagonally packed cavities on the bottommost layer.

Assembly/templating using sulfate modified spheres was then attempted due to their success in the spin coating method. However, the drying of the spheres resulted in the "coffee-ring effect[124]", which is due to the spheres drying in a ring-like stain. Meaning, typically, a monolayer formed in a circle, where the outer regions have a higher concentration of spheres resulting in multilayers. Work by Deegan et al. suggests the formation of these stains is due to the evaporation rate at the edge of the drop being larger than the centre, causing the spheres to be dragged here to compensate for the solvent loss[240]. This is unideal, as monolayer formation is required for close packing, indicating that areas of the array will be unusable. Ideally, the sample would be fully hexagonally close-packed, but as it was not possible to reproducibly obtain this through this method, this approach was rejected.

2.3.1.4 Air/Water Interface Method

The air/water interface method was then examined as it has shown promise in numerous studies [27,104,107,222,241]. This method uses a similar principle to the Langmuir Blodgett method, where a sphere monolayer is assembled at the air/water interface as the solvent evaporates. As mentioned in 2.2.1.5, planar gold was submerged in 2-7 ml of 1 % (w/v) polystyrene sphere solution and the solvent and was left to evaporate in the fumehood. The gold was pre-treated with 10 mM cysteamine to maximise packing. A 1.3 % (w/v) Sulfate functionalized sphere solution were also tested in addition to unfunctionalized spheres. Angle of submersion was varied to optimise sphere packing. Petri dish samples resulted in angles around 30^0, whereas beakers resulted in larger angles between 60^0-85^0. Results are shown in the appendix.

Through these methods, numerous variations of sphere packing were observed. Cysteamine pre-treatment of the gold consistently showed to improve sulphate functionalised sphere retention on the gold chips. The packing of spheres did improve, where LB deposition & spin coating methods gave considerable variation and poor packing. Dropcasting improved to show close packing, however not in a hexagonal pattern. Air/water interface proved to give the best packing from all these methods, however packing was very sensitive to any fluctuations in temperature and humidity. A method optimised in parallel with this work by PhD student Aurelien Gimenez was ultimately used for sphere packing[154]. This method utilised some advantages of the above approaches which resulted in the optimal formation of sphere deposition. This method is explained in section 2.2.1.1.

2.3.2 Characterisation of Gold Cavities.

Gold microcavities were characterised using SEM to ensure uniformity in pore compactness and gold growth. Previous experiments confirmed that optimal formation of cavities was achieved by electrodepositing the gold at -0.6 V, this yielded a cavity depth of approximately 500 nm. The sphere size used, determines the diameter, which in this case was 1 μm. Whereas the sphere solution concentration determines the compactness, in this method a 1 % (w/v) solution had proven to give optimal packing while still resulting in a monolayer. It was observed that if the spheres pack in a multilayer, the bottommost layer of spheres will not be close-packed, resulting in numerous gaps. Figure 36 shows that a close-packed cavity array was achieved. Narrow lines of space occur sporadically, but these are visible under the microscope and can be avoided during focusing, ensuring the measurement is taken over areas of uniform packing. Using ImageJ software, the cavity diameter was found to be reliably 1 ±0.06 μm. Growth was seen to be uniform, in a monodisperse formation and the pore size consistent.

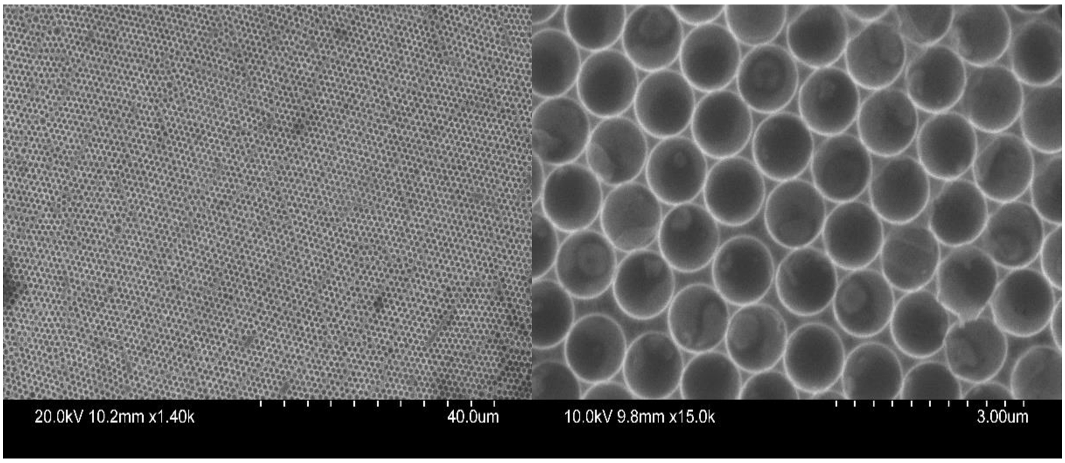

Figure 36: Representative SEM images of 20 μl of 1 % (w/v) unfunctionalised Ps spheres dropcast onto clean gold wafers. This was then covered by a glass slide and left at an angle at 4 ^{0}. Electrodeposition was completed at -0.6 V.

The surface area of the cavities was then determined through image analysis, where a sample region of the SEM images was chosen, and the area of the cavities within was measured. This is then multiplied to represent the whole cavity area. The cavity surface area of 1.5 x 0.8 cm cavity chip was found to be 191. 7197 ±6 mm^2, this can be taken as a representive of an average sample. Interestingly, when 2.88 μm cavities were previously created using the dropcasting method, they reported a similar area of 194 mm^2 [102]. This method has some limitations, as not all regions of the sample shall be uniform in size and compactness. Occasionally a larger or smaller sphere may be observed due to non-uniformity in the sphere solution size. Regions containing non-uniformity are visible under microscopy and excluded when doing Raman analysis.

Uniform cavities in a hexagonal formation are optimal as SERS substrates[104,242]. The roughened gold surface is optimal for greater plasmonic enhancement, whereas the cavity shape itself provides hotspot regions which results in further enhancement. The surface and the interior of the cavities can be modified independently, allowing for specific detection at different locations. The gold is roughened but is still smooth enough to allow for the spanning of bilayers. Which is crucial as though the bilayers are stable; they can be easily disrupted by sharp nanofeatures[14], causing collapse giving misleading data.

2.3.3 Simulations

Numerical simulations were completed by Dr Kho Kiang (DCU) using Lumerical FDTD (finite different time domain) solutions software to model the optical properties of the cavities, i.e. to determine the regions of highest electric field enhancement of these cavities under specific conditions of excitation and angle. FDTD is a numerical technique for solving Maxwell's equation describing optical structures of any arbitrary geometry. It takes into account both the magnetic field and the electric field of the plasmonic substrate. In the simulation, the area of interest is divided into grid-like points where 6 vectors are attributed, 3 for magnetic and 3 for electric fields. The simulation computes the magnitude of both type of vectors at these points until a steady state of the electric field is attained. FDTD is a very versatile method, meaning it can solve a wide range of problems such as those with dispersive mediums i.e. Metals, as well as non-linear media e.g. Kerr effect[243].

The size, shape and depth of the cavities have a significant influence on where the greatest plasmonic enhancement is observed. It has been observed in larger pore sizes (3 μm), that there is plasmonic enhancement occurring near the rim of the cavities. However, from simulations, we have found this is not the case with 1 μm cavities when excited at 473 nm. As the optical constants for gold have been studied in great detail over the years, reported values were used for the simulations[244]. Conformal variant 2[245] (used to calculate the edge) was used as the mesh refinement method, and all simulations were performed with a resolution of 8 nm. For field calculations, the illumination laser bandwidth was set at 0.02 nm and a central wavelength of 473 nm was selected. All simulations were terminated at an auto shutoff threshold of 1×10^{-5} and completed with 0^0 angle on the incident light.

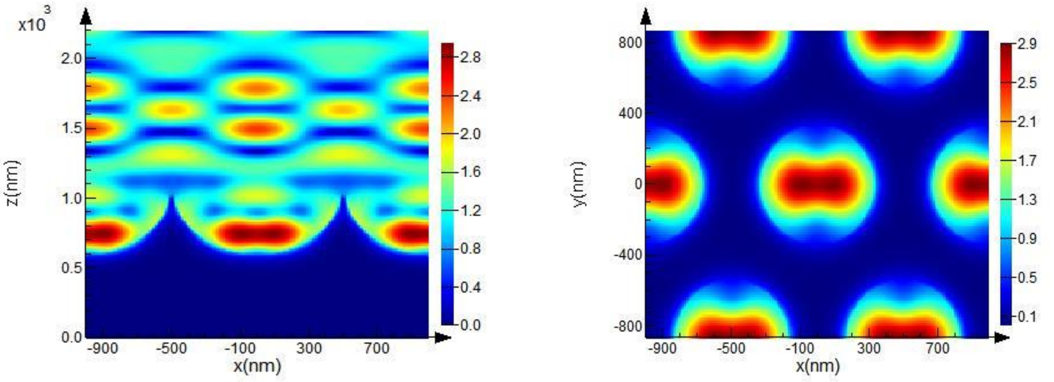

XZ-section **XY-section**

Figure 37: Simulation completed showing local electric field enhancement is localised in the middle and bottom of 1 µm cavity by 473 nm wavelength when under 0° illumination.

Figure 37 shows the FDTD simulation for a 1 µm diameter gold cavity at an excitation wavelength of 473 nm. As can be seen, on 1 µm cavities, a focusing effect of the incident light occurs, which is localised at the bottom of the cavity when the laser is from directly above. It appears that the gold surface & the spherical shape of the cavity causes reflectance that focuses the light into this region. This is advantageous, as the hot spot region is not at the very bottom of the cavity but is localised below the middle of the cavity well, below the bilayer. This is advantageous as it reduces the chance of energy transfer quenching by the gold surface.

The simulations are consistent with theoretical predictions by Bartlett and experimental work presented by Keyes group by Jose et al. [104,105,182]. Where the latter found through confocal fluorescence microscopy studies that emission enhancement was localised near the bottom of 820 nm diameter cavities when excited at 488 nm. The cavity structures also showed SERS enhancement factor of 7 orders of magnitude[104]. Bartlett et al. modelled the plasmons within the cavity. At a range of 100 nm - >10 µm cavities, the localised plasmons within deep cavities were modelled using a Mie scattering approach. This approach examined an isolated single pore and did not consider impact of neighbouring plasmons from adjacent pores. They found that the thickness of the film dictated if Braggs or Mie plasmons dominated, where Mie plasmons became more predominant as film thickness increased[149]. Similar to our studies, the plasmonic enhancement is expected to be within the cavity well, at 0^0 incident angle, i.e. the molecule will only encounter this point after it crosses the model membrane.

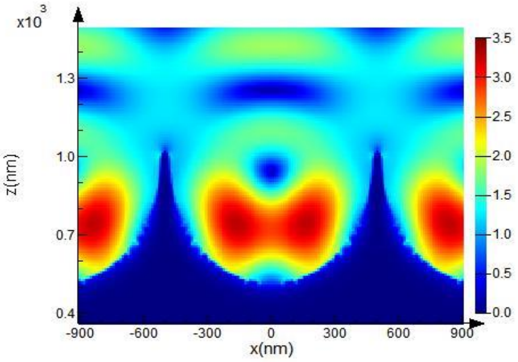

Figure 38: Simulation completed showing local electric field enhancement is localised in the middle and bottom of 965 nm cavity by 633 nm wavelength when under 0° illumination.

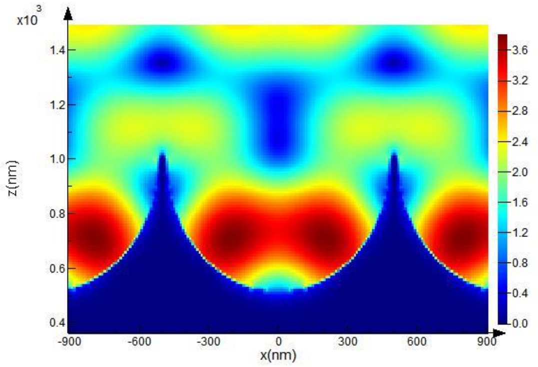

Figure 39 Simulation completed showing local electric field enhancement is localised in the middle and bottom of 965 nm cavity by 785 nm wavelength when under 0° illumination.

Simulations were also completed at excitation of 633 nm and 785 nm wavelength, results are shown in Figure 38 and Figure 39, respectively. Simulations were completed under conformal variant 2, pore size 978 nm, t = 0.5 and pitch 1 μm conditions. As can be seen in the figures, the localisation and intensity of the plasmonic effect differs depending on wavelength. 785 nm shows two strong plasmonic fields localised at the curved outer corners of the cavity, causing a large region of enhancement to be created. There is an overlapping and coupling of these plasmonic fields, which results in a region with weaker fields at the very base of the cavity. Weak enhancement is observed at the top surface area.

Excitation at 633 nm gave weaker plasmonic fields than observed at 785 nm and the peak intensity is located more central to the cavity than the bottom. 633nm excitation also showed no enhancement from the top surface or the region above the cavity. Both excitation wavelengths show clear plasmonic fields, indicating that these substrates are appropriate for SERS measurements under these conditions. Lordon et al. reported through luminescent and SERS studies completed on Ru complexes with 820 nm nanocavities, and observed, as predicated, that the incident angle has an influence on the plasmonic field within cavities. They found that the Raman scatter increased until 20^0, where the intensity then decreased. Whereas, the maximum luminescence was seen here at an angle of $\pm 14^0$ [182]. The simulations and experiments completed in this study were performed at 0^0. However, due to the solid angle of the objective, although excitation is at 0^0, a range of angles are collected.

2.3.4 Determination of Bilayer Formation & Stability

Bilayer assembly was completed using a combination of LB and vesicle fusion, as described in section 2.3.4. This consisted of the immersion and controlled removal of the gold cavity array from the selected lipids self-assembled in LB trough as shown in Figure 30, to form the bottom-most layer of the membrane. The monolayer spanned cavity array was then immersed in a vesicle solution and left for a minimal of two hours to allow for vesicle disruption to form the outermost leaflet, resulting in a bilayer spanned cavity array.

Confocal fluorescence microscopy and EIS were carried out to confirm the formation and stability of the lipid bilayers, respectively. Confocal microscopy can be used to establish the integrity of the bilayer through the use of a fluorescent probe. The probe emission is detectable when located within the plasmonic field of the cavity but not in solution. Meaning, due to the bilayer blocking the cavity, no emission should be observed, indicating successful spanning of the bilayer. EIS data can follow the stability of the bilayer by measuring the resistance variation over time. If the bilayer were to alter in any way, this would be apparent from the decreases to the film resistance. Meaning EIS can be used to establish the time frame the bilayer is stable for and through capacitance, can detect when the bilayer begins to degrade.

2.3.4.1 Determination of Bilayer Formation and Stability through Confocal Fluorescence Microscopy

Confocal fluorescence microscopy was carried out to confirm bilayer formation. Studies were completed under 473 nm excitation, to match excitation conditions for Raman and fluorescent measurements. Bare, C6 and DOPC bilayer modified 1 μm cavities were examined.

2.3.4.1.1 Confocal Microscopy of the Cavities

Figure 40 shows an image of PBS filled unmodified gold cavities under 473 nm excitation. As can be seen, the array is highly ordered over extended areas where large regions of closely packed cavities are occasionally disrupted by a defect. The defects are clearly distinguishable, as they show no emission, resulting in a dark area. Areas of defects are avoided when doing fluorescence measurements as the diameter of the laser spot (approx. 800 nm) is similar to the size of the cavity, allowing for focusing at a single cavity for fluorescent measurements. MEF has been reported to give up to tenfold enhancement[101]. Emission clearly visible from the arrays can be attributed to reflection, scatter and surface gold plasmons. Reflectance on gold nanocavities has been previously noted by Jose et al. through confocal imaging at both 488 nm and 514 nm excitation[104].

The gold substrates emission background may cause an interference in confocal fluorescence measurements. Time gating is a method that allows for the elimination of scatter, reflectance and fluorescence observed from short timescales[246]. The use of time gating was possible for this experiment due to the gold substrates plasmonic emission, reflectance and scatter having a shorter lifetime than the emission obtained from the flurophores[247]. A time gate of 0.8 ns was used, which allowed for the detection of the drugs, as they have reported lifetimes of 1.5 ns[247]. However, the use of time gating will result in the loss of some fluorescence intensity as not all of the emission of the fluorophore is recorded.

To evaluate whether time gating could reduce the background emission, PBS filled cavities were imaged. The cavities were then sonicated in 0.1 mM daunorubicin and the drug filled cavity array was reimaged. Figure 40 (A) shows a representative area of PBS filled 1 μm cavities. Emission due to scatter, reflectance and gold plasmons are clearly evident. Figure 40 (B) shows the impact time gating had on imaging the same area. Scatter and reflectance have been eliminated; however, weak emission due to the golds plasmons is still evident. This is due to the plasmons having a longer lifetime than the time gating. Jose et al. has recorded 19±3 ns lifetimes for 820 nm cavities[104]. A similar lifetime should be obtained at 1 μm, meaning time gating cannot fully eliminate the emission due to the gold. Figure 40 (C) shows the cavity array post sonication in 0.1 mM daunorubicin. Drug filled pores resulted in enhanced emission; however, when compared to PBS filled pores, the background emission makes it challenging to distinguish between the two. Figure 40 (D) shows how effectively time gating removes this background emission, allowing for drug emission to be identified. Brightened pores can be attributed to fluorescence from the drug within the cavity.

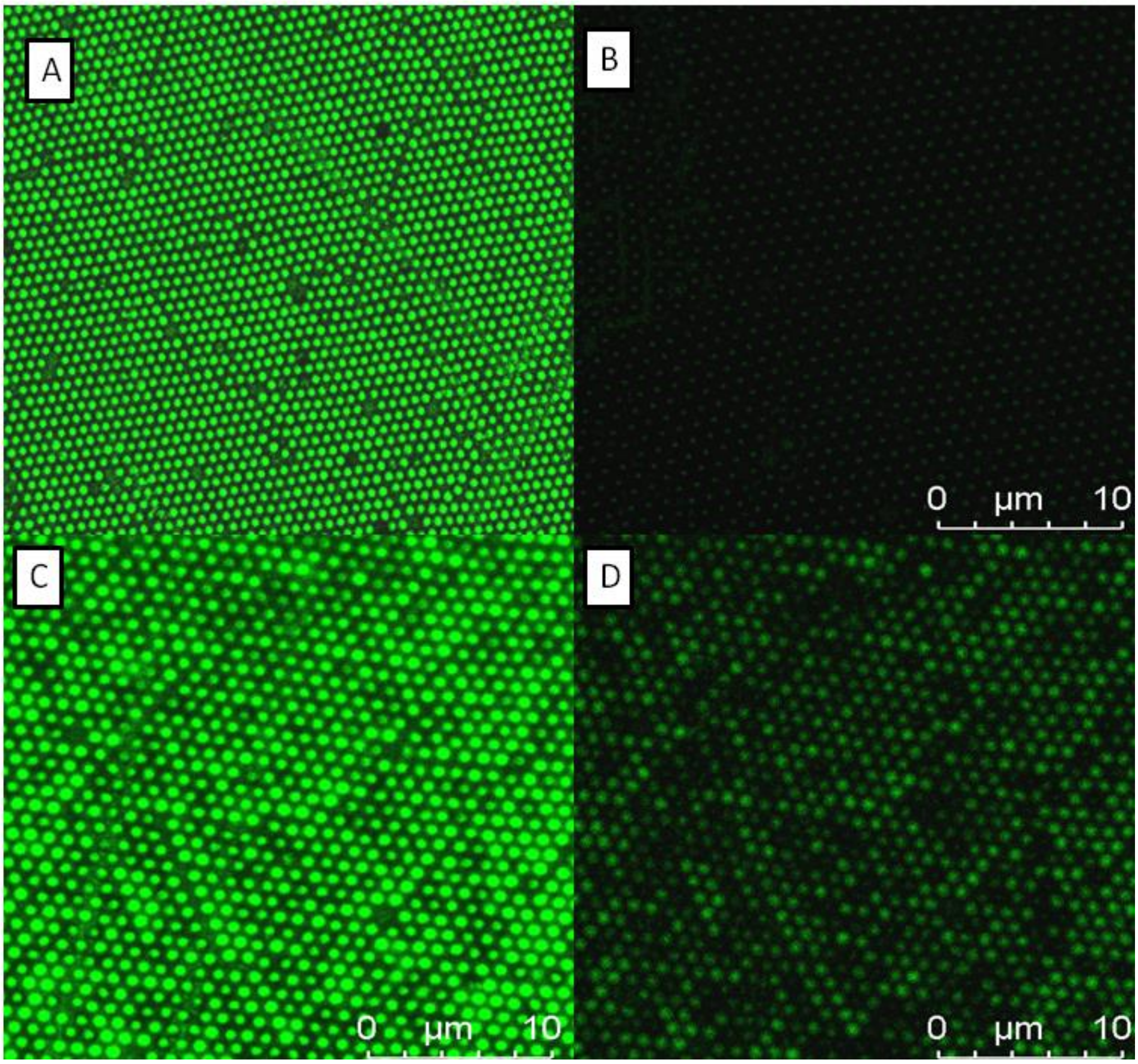

Figure 40: Confocal imaging of a section of gold cavities seen. Bare gold cavities were imaged using time gating (0.8 ns) (B), and no time gating (A). Gold cavities were sonicated in 0.1 mM Daunorubicin and were then imaged with a delay of 0.8 ns (D) and no time gating (C) to minimise the contributions from the gold reflectance and scatter. The samples were excited at Ex 473 nm, and the emission was collected between 512 and 593 nm. The time gating was set to collect emission after 0.8 ns to eliminate scattered light interference from the gold.

2.3.4.1.2 Confocal Microscopy of Bilayer Spanned Cavities

To confirm the presence of a bilayer and determine its integrity, a membrane impermeable probe, Rhodamine 6G was used. The measurements were completed at 473 nm excitation and emission was collected between 530 and 710 nm, using 0.8 ns time gating to minimise any reflectance due to gold, ensuring all fluorescence observed is due to rhodamine 6G.

In principle, if a bilayer has successfully formed, fluorescence from the dye should not be observed. If the bilayer was damaged or is loosely packed, the dye can access the cavity and enhanced fluorescence from the well should be observable. As a control, the cavities were first imaged in the absence of the bilayer. The probe was introduced to C6 modified 1 μm cavities as shown in Figure 41 A. Where, upon probe diffusion into the cavity, emission is clearly observable as an intense spot at each pore. Although the contacting solution also contains the dye, the image with time gating to reduce the reflectance and scatter, clearly indicates that the brightest fluorescence intensity is localised within the cavity. This is important as the axial resolution of this measurement is expected to be similar to that for the bilayer permeation studies completed in this thesis. The results indicate that emission enhancement from the cavity is distinguishable against the background, which the axial dimensions of the focus are expected to encompass.

The Rhodamine 6G probe was then introduced to DOPC bilayer spanned 1 μm cavities (Figure 41 B). With the bilayer in place, no fluorescence from the dye was observed, indicating that the bilayer was fully intact. Low intensity emission is observable, located in the very bottom of the cavity pore; this is similar to what is observed in Figure 40 B, where emission was attributed to gold plasmons emissions. Bilayer spanned cavity were re-examined after 2 hours and no evidence of diffusion of the probe into the cavities was observed, indicating that bilayers remained stable. In a subsequent control, the bilayer was deliberately damaged by increasing laser intensity. At points where the bilayers were damaged, "bright spots" of similar intensity to those seen without bilayer present were observed. Indicating that the bilayer is "leaking", which results in the impermeable dye diffusing into the cavity. Again, this confirms that the bilayer is forming an impermeable barrier to the Rhodamine 6G. Our results are in agreement with an earlier report by Jose et al. on bilayer modified 820 nm diameter gold arrays. Where bilayer modified gold cavities showed homogenous fluorescence from an impermeable probe (5-dedecampylaminofluorescein), indicating successful spanning[27]. Through the use of fluorescence recovery after photobleaching, they demonstrated that the bilayer is fluidic.

A challenge that arose during these measurements on the Leica confocal system was the maintenance of axial-focus throughout the experiment. Because of the small size of the hotspot, the experiment is very prone to a small extent of drift, of which more readily occurred due to the inverted microscope setup. Meaning, the sample had to be refocused periodically to compensate for drift, which can lead to minor differences in the area imaged from the confocal fluorescence measurement. However, as time studies were not completed, this did not affect the measurements significantly. This was not an issue with Raman and Fluorescent measurement on the Olympus upright microscope as the drift was negligible with a long z -length with the x50 Leica objective, ensuring the sample was within the confocal volume.

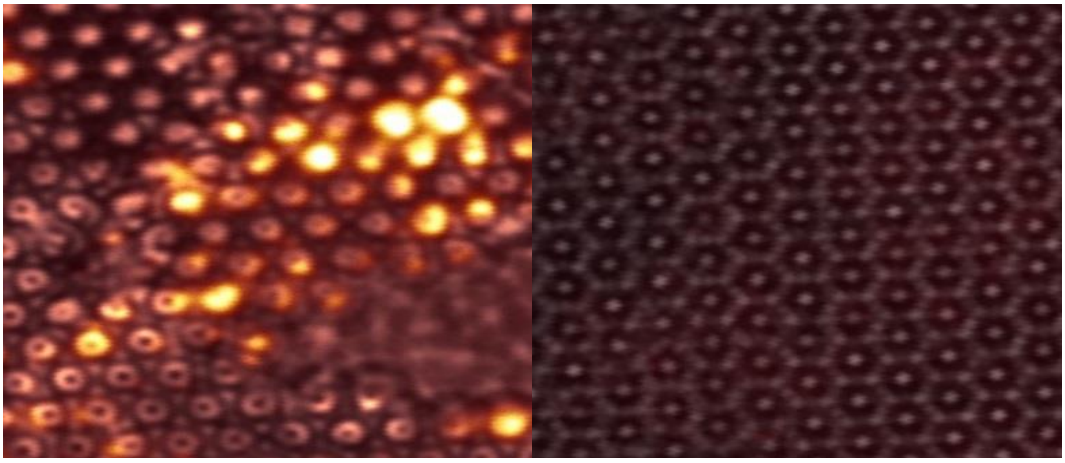

Figure 41: Confocal measurements of 1 µm A) C6 modified and B) DOPC bilayer spanned cavities excited at 520 nm while immersed in 30 µM Rhodamine 6G. Emission was collected between 530–710 nm with 0.8 ns time gating

2.3.4.2 Determination of Bilayer Stability through Electrochemical Impedance Spectroscopy

Electrochemical impedance spectroscopy (EIS) was also employed to confirm bilayer assembly across the pore array and to assess the stability of the bilayers. EIS allowed us to define the experimental temporal window for electrochemical or spectroscopic measurements of the bilayer on gold. Resistance and capacitance data was extracted from the EIS response by fitting the Nyquist & Bode plots to the equivalent circuit model[18] (Figure 31). This model takes into account the resistance from the cavities, solution and membrane. This model uses constant phase elements (CPE) as a capacitor due to the inhomogeneity of the bilayer. Cpec=dl is used to compensate for the double layer capacitance. Typically, the fitting showed good agreement between the raw data (dots) and the model (solid lines) as shown by C6 in Figure 42. The goodness of the fit of the ECM model was accessed from visual inspection of the fits and by the χ^2 values (typically ~0.8×10^{-3}). Nyquist plots provide information on the permeability of the bilayer. Nyquist plots such as the one shown in Figure 42 and Figure 43, show each data point as representative of the impedance at a single frequency[248]. As the frequency decreases, a semi-circle arc is visible. This arc is representative of the capacitance and resistance values of the electrode.

As a control, background EIS of the bare cavities and post C6 modification was obtained prior to bilayer formation. As shown in the Nyquist plot in Figure 42, the presence of the C6 monolayer resulted in a change in resistance in comparison to the bare gold cavities. The addition of a C6 monolayer resulted in increased resistance and a decrease in the capacitance. This decrease has been observed previously in analogous experiments by Maher et al.[18] and can be attributed to the correlation between capacitance and the thickness of the layer on the electrode, which follows the Helmholtz theory, where monolayer thickness is inversely proportional to the capacitance[209,249]. Meaning, when a bilayer is added, a further decrease is expected. Maher et al. reported an approximate 2-fold decrease in capacitance due to the bilayer in comparison to bare gold cavities[18].

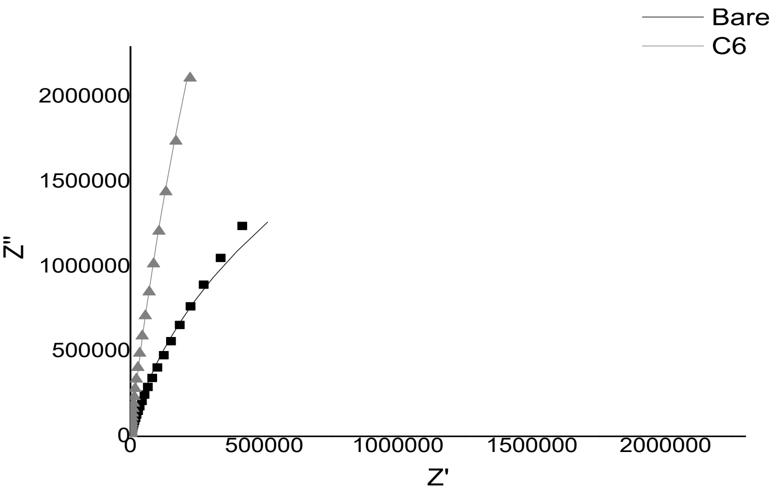

Figure 42: Nyquist plot of bare and C6 modified 1 μm cavities in PBS buffer. Measurements were performed in PBS buffer using a platinum counter electrode, Ag/AgCl reference and gold cavities as the working electrode using AC amplitude of 0.01V at frequency range of 1 MHz to 0.01 Hz. (This plot is one example of the measurement, which was repeated 3 times at RT)

EIS of DOPC & DOPC/SM/CH (40/40/20 %) suspended bilayers were then obtained; these were completed immediately after formation and EIS was periodically measured over 24 hours to determine stability. As shown in Figure 43, the arc of the Nyquist plot is decreasing over time, implying that impedance decreases over time, indicating increasing permeability of the bilayer over time due to looser lipid packing. DOPC bilayers showed minor decreases in resistance, indicating stability until 7 hours, whereas ternary bilayers showed a large decrease at 7 and 8 hours. However, the extracted values such as Delta Rm that are discussed below, implies that the bilayer is still stable at this time frame.

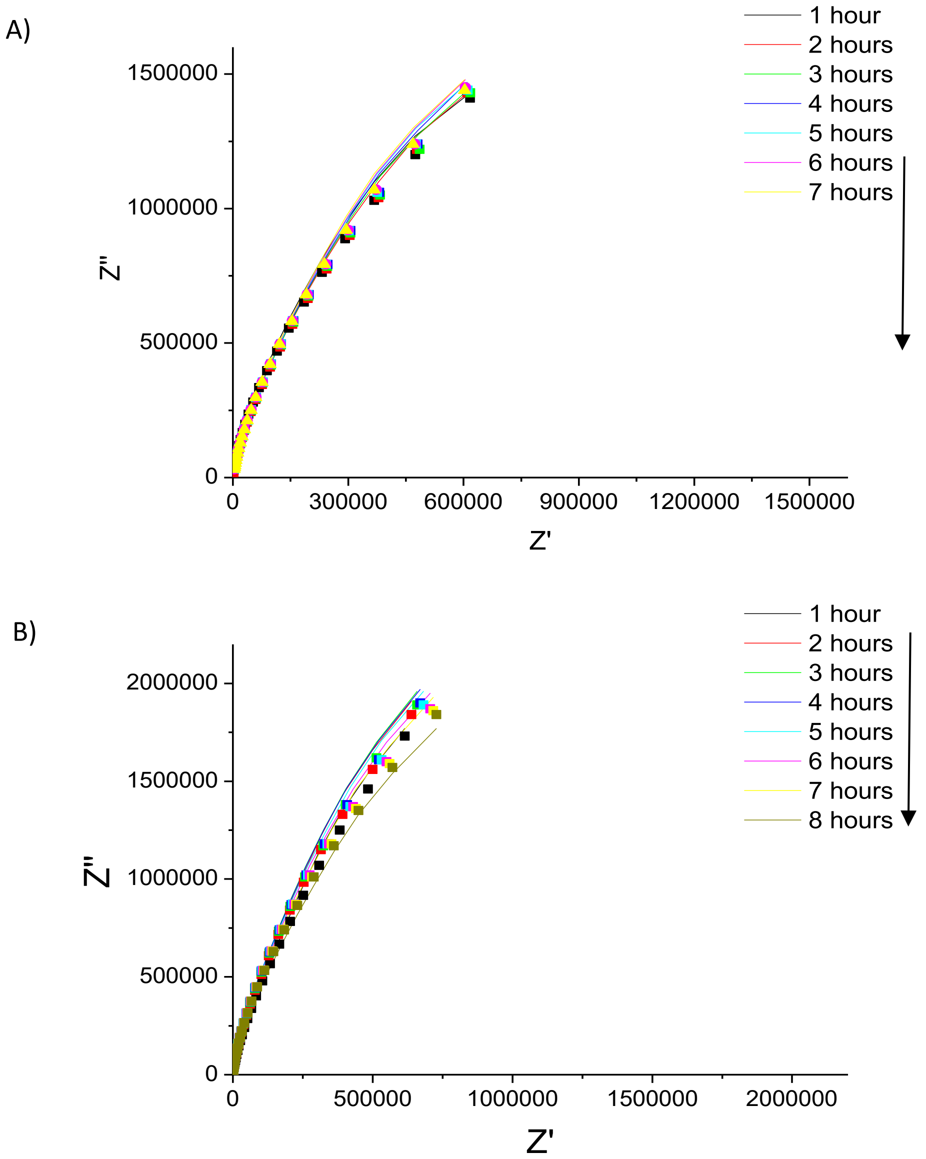

Figure 43: Electrochemical impedance spectroscopy completed on Bilayer spanned cavities. Impedance was measured once every hour for 24 hours to determine stability. Measurements were performed in PBS buffer using a platinum counter electrode, Ag/AgCl reference and gold cavities as the working electrode using AC amplitude of 0.01V at frequency range of 1 MHz to 0.01 Hz. Where a Nyquist plot of DOPC (A) and DOPC/SM/CH (B) show raw and fitted data over a stable period of 7 and 8 hours respectively. (This plot is one example of the measurement, which was repeated 3 times at RT)

As the components of the circuit, including the bilayer, affect both the phase angle and phase shift of the incident AC field. The Bode plot, (Figure 44), provides information on these parameters by plotting the phase of the wave change and phase angle. There are two types of bode plots, impedance (z) vs frequency and the phase shift vs frequency. There are advantages to each. When the data for bilayers was examined on the impedance vs frequency plot, a minor difference between 1 and 2 hours was observed of 150 milli-ohm, which is very small, indicating that the bilayer has not significantly altered and is very stable. This trend continues for 7 hours for DOPC bilayer and 8 hours for ternary bilayers. The latter bode plot provides information on the change in the phase angle, which as shown in Figure 44. Typically, in Bode plots, the low phase shift below 1kHz would be attributed to solution resistance[102]. The final phase shift between -70 and -80, would show the resistance of the system. Figure 44, shows negligible change within this region, indicating the bilayer is stable.

Figure 44 shows the change in resistance over time. Minor differences in the membrane resistance are evident, within experimental error, after the first hour, but the R percentage change remains within acceptable limits (less than 10 %) until 7/8 hours. After 8 hours, the change in resistance becomes drastic due to the bilayer degrading, and the standard deviation between samples also increases from below 0.1 Mohms, to reaching as high as 0.5 Mohms on the DOPC samples.

The ternary bilayer samples proved to be more stable, where the standard deviation remains below 0.2 Mohms. As seen in the phase diagram in Figure 4, a liquid ordered, and liquid disordered domains are expected to co-exist in the lipid composition used here. The raft formation may affect the temporal stability of the bilayer. This is not surprising as the cholesterol containing bilayer is closer packed and will exhibit lower admittance than the bilayer containing only DOPC[84].

An average capacitance value of 6.14 ± 0.17 μF was obtained for DOPC and 5.01 ±0.39 μF for the ternary composition. The lower value for the ternary composition is consistent with previous reports and is attributed to the more rigid packing and greater thickness of this layer compared to the DOPC bilayer due to the expected Lo and Ld phases present in the former[250]. The capacitance shows negligible change for the first 7 and 8 hours for DOPC and Ternary respectively, for example, DOPC showed capacitance of 6.2 μF at two hours and 6.07 μF at 8 hours, implying the bilayer thickness is not changing. A study by Krysinski et al. reported a similar capacitance of 0.66 $\mu F\ cm^{-2}$ for DOPC thiol tethered bilayers. They stated that these values corresponded to previously reported long-chain alkanethiol values and indicated that only the hydrocarbon region of the outer lipid monolayer contributes to the overall capacitance[251]. Interestingly, our capacitance shows a minor decrease over time. The reason for this is not yet fully understood.

This work indicates that for the bilayers spanned microcavities, stability is ensured for a maximum of 7 hours for DOPC bilayers and 8 hours for DOPC/SM/CH bilayers at gold microcavities. Interestingly, Maher et al. reported stability for 6 hours on DOPC membrane; however, this was over a larger pore size of 2.88 μm[18]. As 1 μm cavities resulted in a longer stability time frame, it implies that the bilayer is more stable across smaller pores. Meaning, a balance between optimal plasmonic enhancement and bilayer stability must be considered when choosing pore size for membrane study. In using a close-packed array, where gold deposition is to the radius of the sphere, the planar area between pores is minimised. Previous studies have shown that bilayers spanned over planar regions result in less fluidity, whereas lipid diffusion over a single pore is shown to be more biomimetic, with fluidity and lateral order being analogous with a liposome, and therefore a good analogy to a single cell membrane[21,102].

It is notable, that in analogous arrays made from PDMS, the stability of the bilayers is found to persist for up to 5 days (stability was determined by microscopy and FCS). Even on pores that are up to 3 μm diameter[102]. This is attributed to the oxygen plasma treatment rendering the PDMS superhydrophillic. This level of hydrophilicity is not easily accomplished at gold. It is important to note that EIS is a very sensitive method of analysis, and so, small changes to bilayer packing can result in relatively large changes to measured impedance, even though the bilayer remains intact. Thus the 5 hours stability assessed on the basis of impedance is likely conservative.

Interestingly, an impedance study completed by Steinem et al. found that PC bilayers spanned on gold electrodes were stable for approximately a day according to their capacitance values. They also reported that in the presence of Ca^{2+} ions, the bilayers were only stable for 3 hours in tris buffer[22]. This is of significance as certain proteins may require specific ions to bind to a bilayer, for example, annexin requires calcium to bind[252]. However, for this work, only PBS buffer was used. The experimental window was limited to 5 hours for all experiments and below to ensure bilayer stability. If any evidence was seen that the bilayer was not stable, or showed evidence of degradation, the sample was discarded.

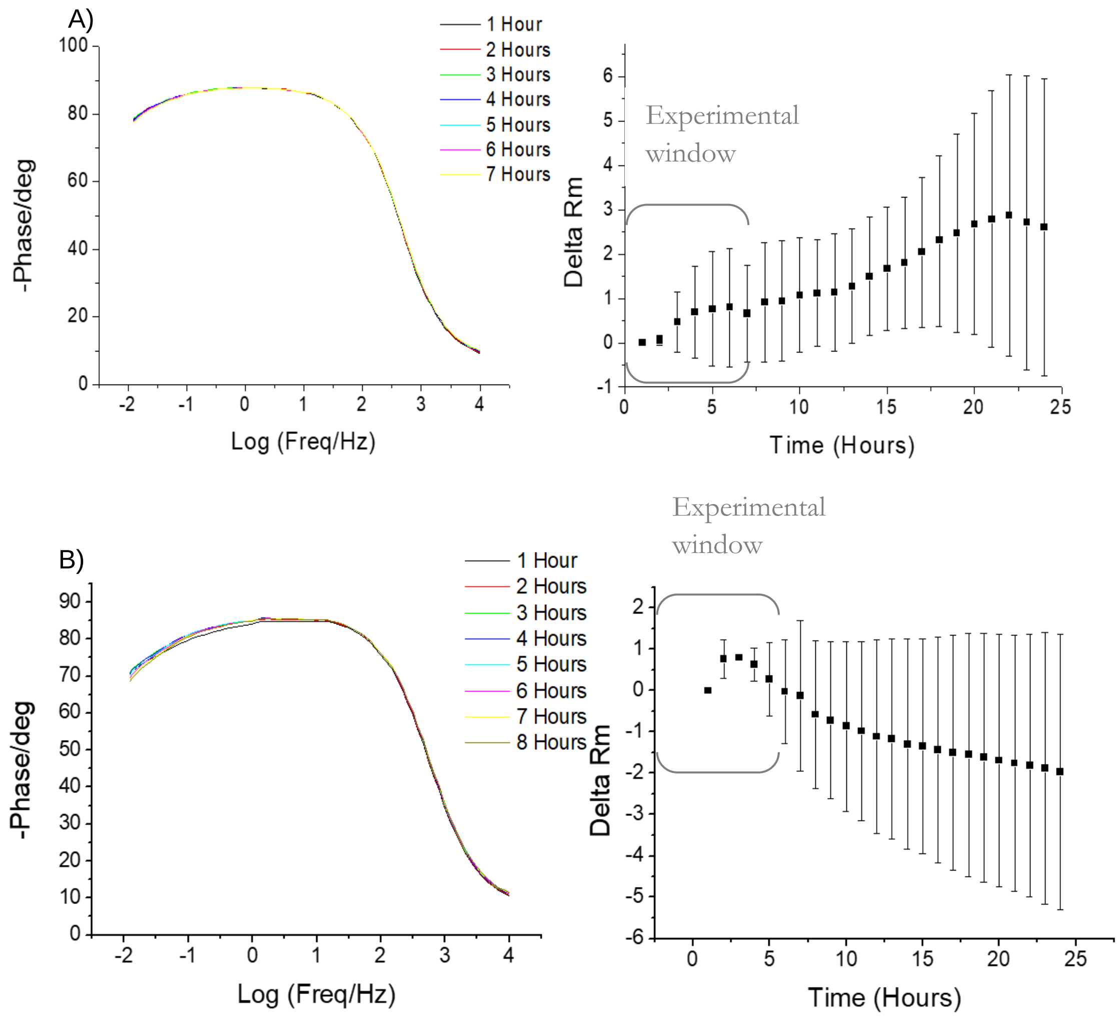

Figure 44: Electrochemical impedance spectroscopy completed on Bilayer spanned cavities. Impedance was measured once every hour for 24 hours to determine stability. Measurements were performed in PBS buffer (pH 7.4) using a platinum counter electrode, Ag/AgCl reference and gold cavities as the working electrode using AC amplitude of 0.01V at frequency range of 1 MHz to 0.01 Hz Where Bode plots of DOPC (A) and DOPC/SM/CH (B) show the bilayer is stable over a period of 7 and 8 hours respectively. Time vs change in membrane resistance for DOPC (A) and DOPC/SM/CH (B) show deviation within our limits (< 10%) within first 5 hours which is within our experimental window and then sample degradation after 7 and 8 hours respectively. (n ≥ 3, at RT)

2.3.5 Bilayer Spectroscopy

A Raman microscope with fluorescence capabilities was used for all MEF measurements as it permitted for the collection of the full emission spectra. The microscope was focused using the white light image, focusing on reflectance at the bottom of the well, prior to measurement to ensure that a single pore was focussed on, in a well-packed region of the array. Therefore, measurements herein reflect what is occurring within a single cavity. Lipid diffusion over a single pore has proven to have fluidity and lateral order closely analogous of a liposome and so is a strong analogy for a single cell[18,21]. Although single pore measurements will result in a lower signal enhancement that those over multipore measurements[253], this approach was taken because; 1) signal from planar regions between cavities will not be included. This is important as lipid bilayers across planar regions have reduced fluidity due to frictional interactions with the underlying substrate. Also, planar areas have no receptacle for drug arrival, and so will likely introduce a second dynamic contribution to signal evolution, complicating interpretation. 2) Furthermore, by monitoring singles rather than extended areas, the measurement will be less subject to variation in pore packing areas of discontinuity, loss of hexagonal packing and variation in surface roughness naturally occurring, which would complicate the kinetic traces obtained for permeation.

Since we are examining single pores, an inevitable concern in microscopy is z-focus drift. To evaluate this, a number of z focus controls were completed (by Dr Kiang Wei Kho), one of which consisted of leaving a DOPC spanned cavity sample in PBS and Raman spectra of the bilayer was measured for over an hour. Data analysis was then completed by monitoring the change in a lipid peak area at 920 cm^{-1}. The results confirmed that any drift occurring is negligible as the variation between the peaks was minor. It appears the confocal volume, which is relatively large with the long-distance 50x objective is relatively insensitive to slight z-drift movement that may occur during measurements. However, the large confocal volume means that we will be obtaining signal from the cavity, the membrane and the contacting solution. As signal contribution from the contacting solution should not change once diffusive mixing is completed, luminescence intensity changes can then be solely attributed to interactions occurring at the membrane and cavity. Our measurements then explore if the changes to emission intensity upon accessing the plasmonic pore, are sufficiently large to be observed against the background.

2.3.6.1 Fluorescent Measurements

Control spectra of potentially contributing background elements were obtained to allow for the distinction between fluorescent contributions due to the background and the drug of interest. Figure 45 shows the spectra for Bare gold cavities, mercapto-hexanol modified cavities and lipid bilayer spanned cavities all in PBS buffer. Weak background fluorescence is observed from the gold cavity arrays, and it remains for the mercapto-hexanol modified cavities and lipid bilayer spanned cavities in PBS buffer. The fluorescence is due to surface plasmon oscillation of the free electrons, which results in golds strong optical absorbance and scattering properties[254]. The plasmonic oscillations of gold have shown a lifetime of 19±3 ns[104], therefore the weak background emission was not unexpected.

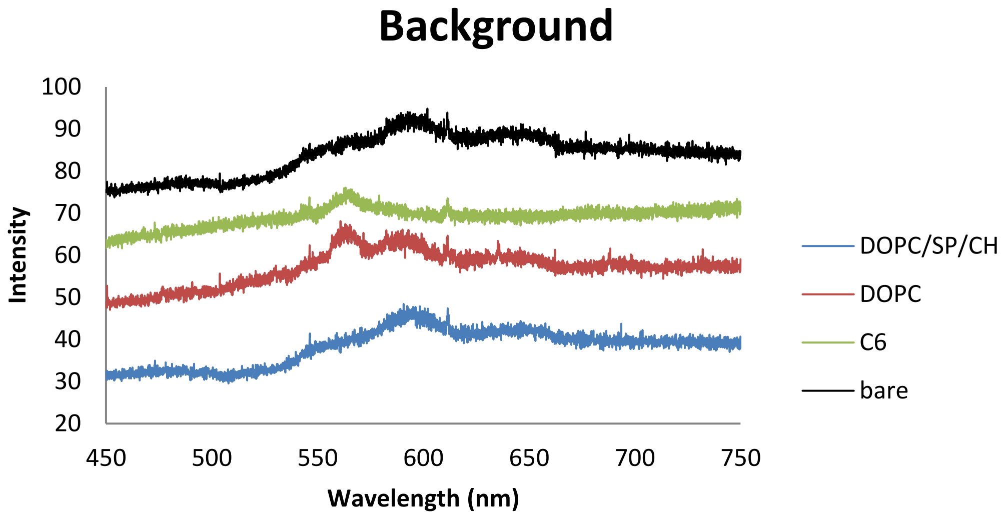

Figure 45: Fluorescence Spectra obtained from Bare gold, C6 modified and bilayer on 1 µm cavities at 473 nm excitation in PBS. Spectra confirms there is only weak background emission from the array, C6 layer and from both bilayer compositions.

2.3.6.2 Raman Measurements

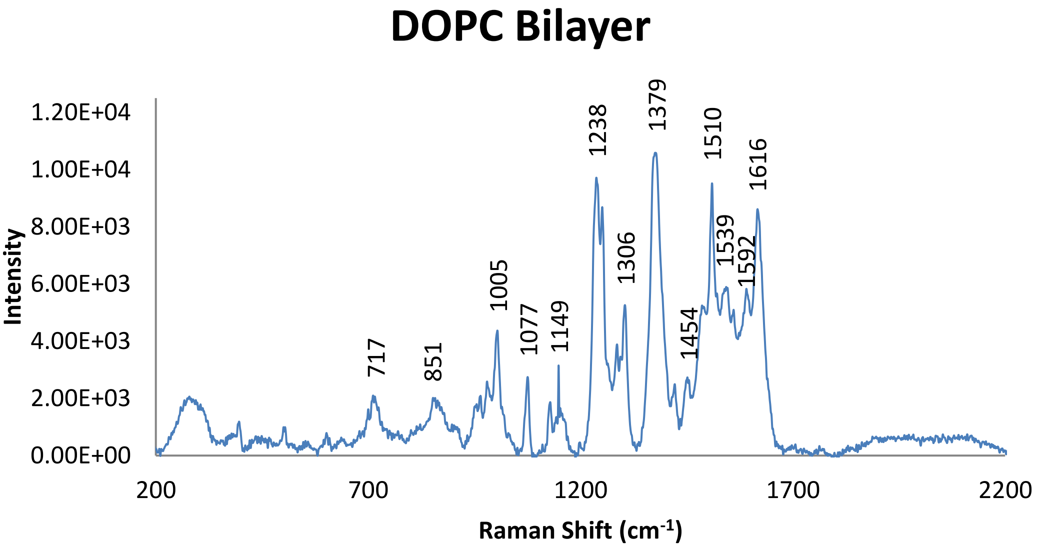

Figure 46: Raman spectrum of DOPC bilayer spanned over 1 µm gold cavities in PBS solution, 785 nm excitation wavelength.

As there is no key difference between the fluorescence spectra of bare cavities and bilayer cavities prior to drug addition, SERS was completed to ensure a bilayer was present and to characterise its Raman spectrum. Figure 46 shows an example of a Raman spectrum of a DOPC bilayer. As seen by the structure in Figure 4, the spectrum contained characteristic DOPC features. A phosphate band appears around 1077 cm^{-1}, which is clearly visible in Figure 46. Other characteristic peaks for DOPC are seen at 720, 1120 and 1620 cm^{-1}, indicating that DOPC is present. The band at 1620 cm^{-1} can be attributed to C=C stretching vibration in the two cis double bonds of the oleoyl chains[255]. While 1120 and 720 cm^{-1} are attributed to stretching of the C-C and stretching of the $(CH_3)_3$ respectively.

Numerous studies have reported the characterisation of lipid peaks, , in particular, DOPC lipids[255,256]. For example, Opilik et al. used tip-enhanced Raman spectroscopy to obtain high resolution images of mixed lipid mixtures on planar gold surfaces. DOPC/DPPC (1:1) monolayers were formed on the gold substrate through LB formation and through Raman spectroscopy they could identify vibrational modes due to the lipids. However, they could not differentiate between the two lipids[255]. Czamara et al. formulated a comprehensive study, tabulating all the modes attributed to 35 lipids through Raman spectroscopy[256].

The Raman modes obtained for the DOPC spanned bilayers (Figure 46) corresponds with the values that have been recorded in the literature[255,256]. Although Raman spectroscopy confirms the lipid is present, it alone does not prove that the bilayer is successfully suspended with no defects, however, combined with Confocal Fluorescence Microscopy and EIS it can be used to determine the integrity of successfully spanned bilayers through methods described in section 2.3.4.

2.3.6.3 Diffusive Mixing/Equilibration Time

Controls were completed to estimate the length of time it would take for the drugs to diffusively mix throughout the containing solution (2 ml). A study was completed to monitor the time it took for maximum fluorescence to be seen in the absence of gold. The drug was added as normal to 2 ml PBS and monitored over time. The fluorescence increased in intensity until approx. 27 minutes, where it then remained constant indicating it had fully mixed, suggesting emission intensity changes after 30 minutes can be attributed to the drug interacting with the bilayer and then entering the cavity. Experiments described in chapter 3 & 4, further confirmed this theory, where on unmodified cavities, no further SERS or fluorescence emission change was detected. However, the residual velocity from drug introduction may result in some variation in the drug diffusion (1-3 min). This is addressed and eliminated in chapter 5.

2.3.6 Spectroscopic Characterisation of Drug Models

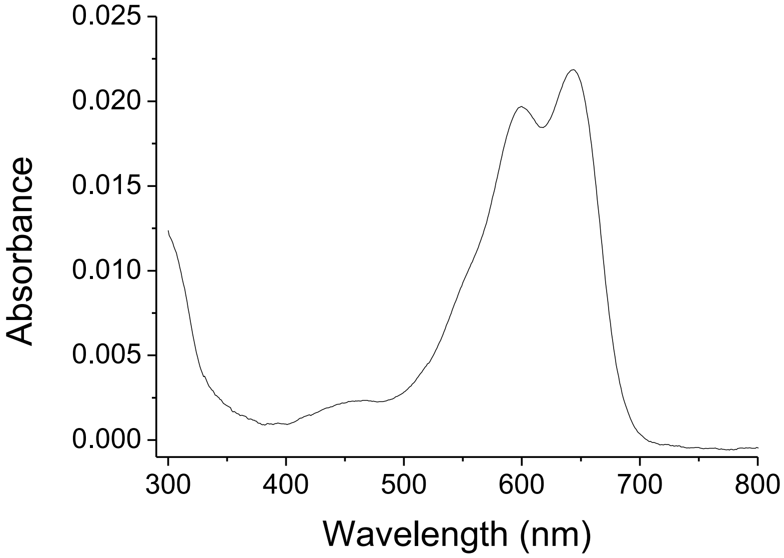

Figure 47: UV-Vis absorbance spectra of 0.75 µM DRAQ7 in PBS solution at room temperature. Dye showed max absorption at 645 nm.

The drugs & dyes examined within this thesis were investigated by UV-Vis and emission spectroscopy. Figure 47 shows the absorbance spectra of DRAQ7. The dye shows maxima at 645 nm and 599 nm. Biostatus states that DRAQ7 has peak absorbances at 600 nm and 646 nm. They also state that the dye may be excited at 488 nm, resulting in fluorescence in the far red-field[257]. Their results agrees with what was observed in this study and with studies in the literature. For example, Akagi et al. used the dye to determine cell death when exposed to cytotoxic agents at 640 nm excitation[257].

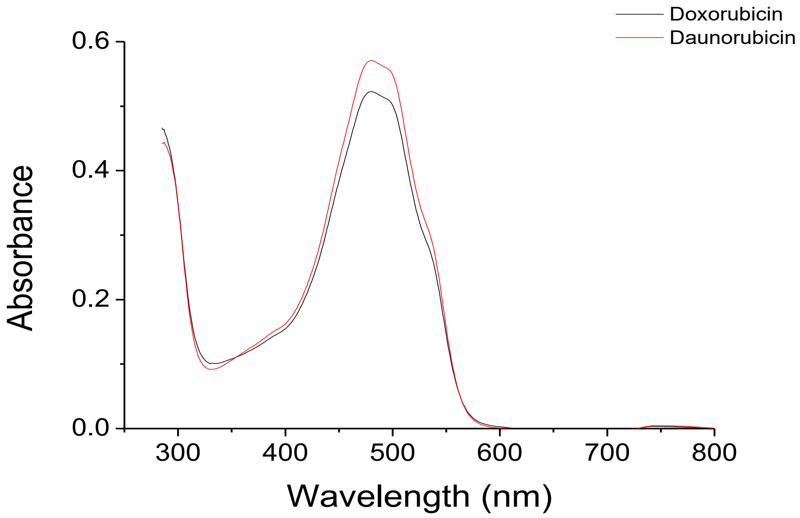

Figure 48: UV-Vis absorbance spectra of 0.05 mM Doxorubicin and Daunorubicin in PBS solution at room temperature. Both drugs showed absorption at 480 nm.

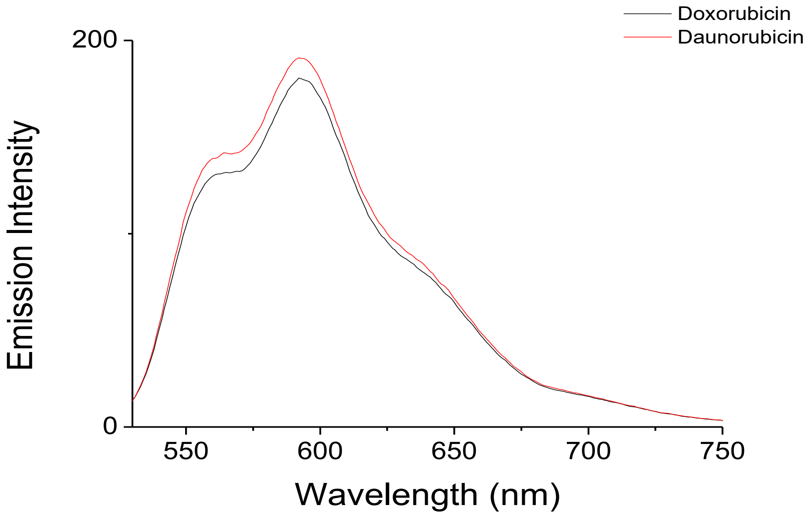

Figure 49: Emission spectra of 0.05 mM Doxorubicin and Daunorubicin in PBS solution at room temperature. Both drugs were excited at 473 nm and emission was collected between 490-900 nm at a slit width of 5nm.

The absorbance spectra of both anthracycline drugs, doxorubicin and daunorubicin in PBS buffer are shown in Figure 48. Peak absorption was seen at 480 nm and 483 nm, respectively. Fluorescence spectroscopy was then completed to ensure our chosen excitation wavelength, 473 nm is appropriate for fluorescent measurements. As shown in Figure 49, when excited at 473 nm, doxorubicin & daunorubicin showed a broad fluorescent peak at 590 nm. Motlagh et al. state absorption at 480 nm and a fluorescence peak at 591.48 for doxorubicin[185]. Htun reported absorption at 490 nm and the maximum fluorescence peak at

590 nm for daunorubicin[247]. This corroborates with the results shown here. Htun also reported a decrease in fluorescence intensity as the solvent polarity was increased[247]. The extinction coefficient of doxorubicin in water (λ = 485 nm) has been reported as 11500 $M^{-1}cm^{-1}$ at 25°C L/mol/cm[258]. Table depicting spectroscopic values for these drugs can be found in the appendix.

The fluorescence spectra of the anthracyclines are dependent on the dielectric constant of the solvent[259]. The fluorescence intensity and emission quantum yield increases as the environment becomes more hydrophobic, i.e. decrease in the dielectric constant causes an increase in intensity. The fluorescence spectra of the drugs were also measured under 785 nm excitation. This was carried out to confirm that when under SERS excitation, no fluorescence interference should be observed.

2.4 Conclusions

Chapter 2 focussed on the development, optimisation and characterisation of the periodic pore array and strategies used for surface modification and deposition of the bilayer.

The development of micro-cavities was a known method within the group[17,21,102,104], however, packing reproducibility was inconsistent. Therefore, other reported methods were evaluated in an effort to improve the reproducibility and packing of the cavities. These methods included LB deposition, spin coating, drop-casting and air/water interface deposition. The methods mentioned showed poor reproducibility or inadequate packing, leading to multilayers or void regions and were therefore dismissed. An optimised method based on work completed by another member within the group, was then used and this approach consistently provided close packing[154]. The optimised method utilised low temperature evaporation which resulted in the spheres close packing. Controlled gold deposition then allowed for uniform cavity growth of optimal depth. This method was then implemented throughout this thesis and all work within the group. The resulting cavities were then characterised using SEM and confocal microscopy, showing that superior hexagonally close-packed cavities were achieved reproducibly when compared to the previous method, where only 1 in 30 samples would be rejected due to defects.

The optimised arrays comprised of cross-section area of 191. 7197 ±6 mm^2 with a uniform cavity diameter of 1 ±0.06 μm. FTDT simulations were completed for cavities of these dimensions and indicated that the most intense electric field enhancement is localised below the middle of the cavity well, well below where the lipid membrane will span. Time gated confocal microscopy from dye filled cavities, as well as from buffer filled cavities, showed emission localised at the bottom of the bare cavity, corroborating the simulations.

Lipid bilayers were successfully assembled across aqueous filled cavities using LB and vesicle fusion. The stability of the bilayers was investigated using Confocal microscopy and EIS. Through EIS a maximum consistent timeframe for both compositions' stability was established as 7 hours for DOPC and 8 for the complex ternary composition DOPC/SM/CH (40/40/20 %), establishing the experimental time frame for all future work. Fluorescence measurements confirmed the bilayers were impermeable to non-permeable dyes, with deliberately damaging the membrane confirming the bilayers are spanning and form an impermeable barrier to the cavity interior.

The absorbance and emission of both Doxorubicin and Daunorubicin were investigated and found to agrees what is reported in the literature[185,247]. Both drugs fluoresced upon 473 nm excitation and showed no fluorescence under excitation of 785 nm, indicating they are valid candidates for the proposed MEF and SERS studies. Background fluorescence spectra of the different components of the platform were taken to ensure no emission was observed that may interfere with the drug spectra, allowing for the platforms use in further chapters. Raman spectra were taken of a DOPC bilayer, allowing for bilayer & drug specific peaks to be identified prior to drug addition. Through diffusive mixing experiment, it was estimated that the drug shall take approximately 27 minutes to diffuse through the 2ml PBS solution and enter the cavity. The components established in this chapter were then used for Raman and fluorescence studies in the subsequent chapters.

Chapter 3: Surface-Enhanced Raman Spectroscopy Detection of Membrane Permeability.

3.1 Introduction

The ability to determine the presence and kinetics of membrane permeability and to gain molecular insights into the interaction of molecules, such as a drug or cosmetic, with human cells is of great importance in the pharmaceutical and cosmetic industry. As previously described, current models have a range of limitations, but most importantly lack of biomimicry. Our proposed approach is to monitor for the arrival time of the molecular species into a plasmonic pores, that is sealed by a phospholipid membrane. The plasmonically enhanced signal in fluorescence or Raman, provides a simple qualitative assessment of molecular permeability. Although fluorescence is more intense, there are a number of key advantages to the use of Raman.; namely, it does not require the compound to be fluorescent and is therefore, more broadly applicable. Unfortunately, as the technique is based on the collection of inelastically scattered light, the signal is often weak[23,100,232]. Therefore, advances such as surface enhanced Raman spectroscopy (SERS) are potentially useful routes to improving senstivitiy[23,131,260]. Even drugs with the weakest Raman cross-section may be detected through SERS, where a large degree of enhancement can be achieved due to the presence of gold plasmonic hotspots[104,151]. Furthermore, in the absence of enhancement, the relatively weak Raman signature from the contacting solutions, even with a poor axial resolution, will not be expected to contribute much interference to the plasmonically enhanced signal seen on drug arrival in the cavity. Furthermore, as Raman is a vibrational spectroscopy, it provides structural information allowing both for identification of the molecule of interest, and for the interrogation of its interaction with the membrane.

The exploitation of the plasmonic effect from the metal surface allows for dramatic enhancement of the signal[105,260–262]. The plasmonic fields that are exploited in SERS arise from the light excitation of oscillations of the electron plasma field along the surface of the metal. The surface plasmon-polariton waves oscillate at the metal dielectric interface, which results in an evanescent EM field that decays exponentially with distance from the metal interface[23,236,263,264]. It has been observed that certain metals give a greater plasmonic effect than others, and with Gold and Silver being most commonly used due to their stability, ease of fabrication and intense plasmonic fields that coincide with visible photon frequencies. Gold microcavities[265] have been previously used with great success as a SERS substrate[104,261]. The conical shape of the cavity provides optimal regions for hotspots to occur, typically found between two metal nanoparticles[100,232], which are known to lead to a larger degree of enhancement[265]. Within these studies, the configuration of the microcavities used as a metal enhancement substrate combined with the roughness of the gold surface, provided optimal regions for hotspot occurrence.

In this chapter, we explore whether the presence of plasmonic hotspot regions within the gold cavity array enables detection of an arriving drug, that has permeated the spanning lipid bilayer can be detected using SERS. In the previous chapter, simulations showed that the proposed cavity size and excitation wavelengths should yield plasmonic enhancement localised in the cavity below the membrane. Water is a weak Raman scatterer[100], which makes Raman an ideal technique for aqueous and particularly biological samples. Meaning a range of buffers, with little background contribution, are available for use with our model. PBS was used as it is a universally applied biological buffer and has been widely used by our group to study bilayers.

Similarly, the lipid bilayer supported at the cavities will give a Raman signature characteristic of the lipid composition[55,84]. Thus Raman/SERS of the cavity supported lipid bilayers will allow for the monitoring of both the bilayer and the drug. As discussed in other reports on cavity array supported bilayers, they are particularly versatile, permitting ready access to different lipid bilayer compositions. As a result of this, through SERS, we may gain an insight into the interactions the drug has with the bilayer while also monitoring the permeability and the dynamics. The cavity array method is versatile as it allows us to alter the lipid bilayer to model different membrane depending on interest and investigate the resulting variations in drug interaction. Meaning, in future, this method may be utilised to investigate a drugs interaction with a specific lipid and to determine how certain lipids may affect the permeability of the membrane.

Raman is frequently explored for biosensing and SERS to an even greater extent[263]. A key advantage is that it allows for multiplexing, due to narrow bands minimising the risk of label overlap[263]. Numerous studies have investigated lipid bilayers using Raman spectroscopy[141,266]. One such study by Taylor et al. investigated lipid "flexing" within the bilayer[267] through the vibrational shifts and intensity fluctuations in the Raman spectrum. Through the use of gold nanoparticles deposited onto silicon chips, the plasmonic enhancement was sufficient enough to obtain molecular identification of the lipids, such as the bending etc. of the molecules as they interact with their environment. Thus, resulting in a high sensitivity method that allows for the tracking of the dynamics occurring within the cell membrane. Kundu et al. looked at how lipids might transfer between membranes[268], by examining how the lipids may exchange or transfer from donor-deuterated DMPC vesicles with DMPC bilayers attached to gold nano-shells. This method could be applied to investigate the "flip-flop" of lipids in membranes.

Anthracyclines are antitumor antibiotic drugs extracted from streptomyces, which consist of a tetracycline ring with a daunosamine group[269]. These drugs are applied intravenously to patients[270]. Doxorubicin and daunorubicin, the drugs selected for study here, are known to give distinct Raman signatures[84]. The excitation wavelength chosen for this study allows for plasmonic enhancement as it is resonant with our emission wavelength, making them of value for testing this method for drug detection. They are considered cell-cycle specific drugs, as they affect cells when they are dividing.

Due to this, their interaction with lipids has been studied in various forms[42,186,271–273]. Methods applied include fluorescence, atomic force microscopy and Raman spectroscopy, to name a few. There have been numerous previous studies completed on these drugs and their interactions in biological systems using Raman spectroscopy. One such study focused on doxorubicin's interactions with cancer cells[271,274]. Morjani et al. used SERS to monitor doxorubicin's interaction with living human cancer cells. Through this work, they were able to identify that the drug targeted the cytoplasm as well as the DNA located in the nucleus. They were able to detect SERS signal from very weak concentrations, up to 10^{-10}M, which is of great interest for biomimetic studies[271,274].

The stability and reproducibility of the lipid spanned microcavity platform was investigated in the previous chapter. This chapter focuses on the proof of concept; of using SERS as a detection method for drug-membrane permeability. The concept of this membrane permeability assay is shown in Figure 1. Lipid bilayer spanned microcavities will act proficiently as the biomimetic membrane and collection well, while also providing plasmonic enhancement of signal. As the drug is introduced into the bilayer, the corresponding Raman signal should be detected at a single cavity (as an analogue of a single cell), and while the drug diffuses into the cavity, the SERS signal should be detected. SERS at appropriate metal surfaces has the capacity to generate a significantly large enhancement[275], and therefore should be clearly identifiable. This approach may prove to be a valuable as a detection method for our lipid membrane permeability models.

3.2 Materials & Methods

Samples were prepared in the same manner as discussed in section 2.2, where all experiments were done at room temperature and repeated a minimum of 3 times, unless stated otherwise. The following deviations were also completed; When forming lipid bilayer for complex compositions, vesicles were extruded at 50 ^{0}C, as Sphingomyelin is in a gel phase at room temperature. All Raman measurements were completed on a single cavity pore. Integrated peak area was obtained using Labspec5 software, which uses Equation 2. Peak limits for the drug peak 1636 cm^{-1} we set at 1629-1659 cm^{-1}.

$$A = \int I(\nu) d\nu$$

Equation 2: Integrated areas equation used by Labspec5 software. where ν is the wave-number.

3.3 Results & Discussion

SERS enhancements vary widely depending on substrates material and structure. Signal enhancement of up to 10 orders of magnitude have been widely reported for gold[23,141,260,276]. For reproducible fabrication of substrates, regular structures are required, rather than fractal structures which are responsible for the highest signal enhancement. Therefore, the trade-off is that the cavity arrays typically offer an average enhancement factor of 6 to 8 orders of magnitude[104]. 785 nm was the chosen wavelength as it coincides well with both the anticipated plasmon excitation for the gold substrates and the excitation of the drugs focused on in this study. Doxorubicin and daunorubicin, as seen in Figure 48, are not excited at 785 nm and therefore no background interference due to fluorescence should be observed.

Control spectra of potential background elements were initially obtained to identify peaks due to scatter from the gold, or Raman modes attributed to 6-mercapto-1-hexanol (C6), residual polystyrene spheres and the lipid bilayer itself. Figure 50 shows representative spectra collected from these elements. As expected, no Raman vibrational modes are observed from the bare gold, and very weak bands may be observed due to C6 at 400-600 cm^{-1} and 1159 cm^{-1}.

Alkanethiols' weak Raman signatures on SERS substrates have been previously noted by Molen et al[277]. Octanethiol shows similar bands to those seen in Figure 50, allowing for confirmation of vibrational modes due to C6 modification or cosmic rays. Cosmic rays are typically only one pixel wide, meaning they are easily identified. They occur at random as a positive spike whose peak intensity can vary[278]. The self-assembly process of thiols has been studied in great detail over the years through Raman spectrscopy[60,279–281]. Therefore, the packing etc. of the thiols was not examined in great detail within this study, nor were their weak Raman signatures an issue, as they were not the focus of this study.

Polystyrene gives an intense and characteristic peak around 1000 cm^{-1}[282], associated with the phenyl ring stretch, which is a useful guide as to whether the spheres have been fully removed. As the samples were examined by white light microscopy or SEM prior to bilayer formation to ensure packing and sphere removal, Raman peaks associated to polystyrene were very rarely observed. Silicon exhibits an intense and characteristic vibrational mode at 520 cm^{-1}, which if observed indicates the sample is defective, as the gold base layer should completely cover the silicon.

Vibrational features attributed to the DOPC bilayer were described in detail previously in Chapter 2, other lipids are noted in section 3.3.1. Characteristic lipid bands were observed at 1620 cm^{-1}, attributed to the C=C stretching vibration in the two cis double bonds of the oleoyl chains[255]. Peaks at 930 cm^{1} and 1236 cm^{-1} are found in the fingerprint region and can be attributed to C-C stretching and CH_2 twist respectively, to name a few. A full table of lipid peaks characterisation is shown in Table 1.

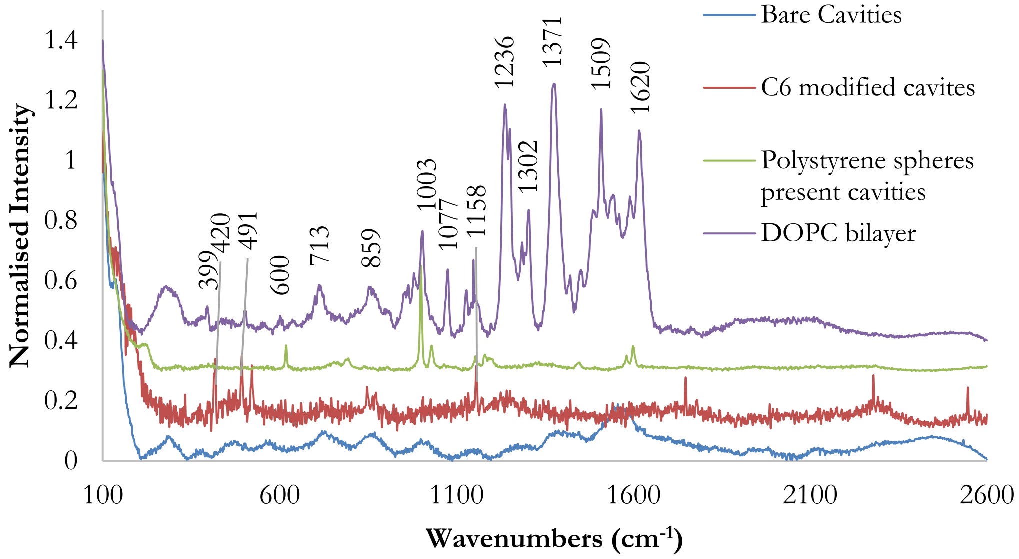

Figure 50: Normalised Raman spectra of Bare 1 µm cavities, C6 modified 1µm cavities, Polystyrene spheres present in 1µm cavities and DOPC bilayer spanned over 1µm cavities, all sample were sonicated in PBS solution and excited at 785 nm. Data is offset for clarity. (n ≥ 3, at RT)

3.3.1 Raman Spectroscopy of the Lipid Bilayer

As previously shown in section 2.3.6 in Figure 46, a spectrum of a DOPC bilayer was successfully obtained, and vibrational bands specific to the lipid were identified. Table 1 shows the assigned bands to corresponding vibrational bands for DOPC, DOPC/SM/CH and literature assigned bands for CH and SM[256].

As ternary compositions were also of interest for these studies, a spectrum was obtained of the DOPC/SM/CH (40/40/20 %) composition, shown in Figure 51. The ternary composition of the bilayer added some complexity in the analysis of the spectrum as there is significant overlap between Raman features associated with DOPC (structure shown in Figure 4), sphingomyelin (structure shown in Figure 5) and cholesterol (structure shown in Figure 5). By using known peaks identified in the literature[255,256,283,284], the peaks were tentatively identified to their sources in Figure 51, where green labels indicate cholesterol, red show sphingomyelin, blue signify DOPC and black is a combination of the bilayer compositions.

Cholesterol, which is the most abundant sterol in animal tissue, has an arrangement of four cycloalkane rings, where one contains a hydroxyl group at the third position and an eight-carbon chain on the far side. It has been shown, in its unbound form, to exhibit well-resolved vibrational bands at 2864 & 2930 cm^{-1} due to CH_2 symmetric stretching and chain-end CH_3 stretching, respectively. Bands are also seen at 1672 (C=C stretching vibrations of the ring), 1442 (CH_2 scissoring modes) and 1087, 1130 & 1178 cm^{-1}(C-C and C-H stretching)[256]. Depending on the type of cholesterol or cholesteryl ester present, these bands may change due to the membrane components interacting with neighbouring lipids.

Sphingomyelin consists of a phosphocholine or phosphoethanolamine polar head group[285] and sphingosine bonded to a fatty acid. It has recorded bands at 1068, 1129, 1295, and 1437 cm^{-1} attributed to acyl chain modes[256]. It also has numerous vibrational bands overlapping with DOPC as can be seen in Table 1. The most common being C=O & C-O-C stretching, deformation of the CH_2 & CH_3 and bending of C-O, C-O-H and C-H groups.

Functional group/ Vibration	Region	DOPC	DOPC/SM /CH	SM[240]	CH[240]
ν(C = O)	1680-1820	1628	1623, 1658, 1751	1670, 1654	1672
ν(C = C)	1500-1900	1510, 1539, 1592, 1616	-	-	-
δ(CH2)/δ(CH3)	1400-1470	1454	1420	1437	1442
δ(CH3)	1380	1379	-	-	-
β(C-O, C-O-H, C-H)	1200-1300	1238, 1306	1290	1295	-
υ(CC) alicyclic,	300-1300	1149	-	-	-
ν (P-O)	1060-1100	1077	-	1096	-
υ(C-O-C) asym	1060-1150	1005	1024, 1174	1129, 1090, 1101	1178, 1130, 1087
υ(C-O-C) / υ(O-O)	800-970	851	879	882,	-
ν asN+ (CH3)3	-	717	627, 748	723	-
υ(Si-O-Si)	450-550	-	587	-	-
δCO3	701	-	-	-	701
δ(C = O)		-	485	-	548,424

Table 1: Characteristic Raman Bands of DOPC, DOPC/SM/CH, CH[256] and SM[256] with assignment. β, bending; δ, deformation; υ, stretching (s, symmetric; as, asymmetric).

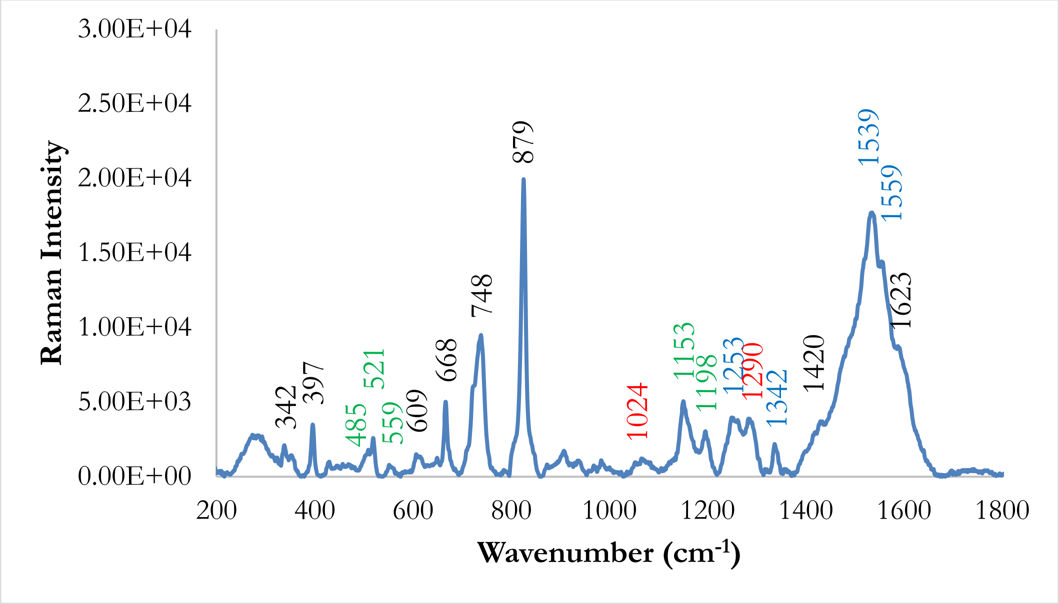

Figure 51: Raman of ternary lipid bilayer comprising of DOPC/SM/CH (40 %/40 %/20 %) spanned over 1 μm gold cavities in PBS solution, at 785 nm excitation wavelength. (n ≥ 3, at RT)

Figure 51 shows a spectrum of the ternary bilayer composition (comprising of DOPC/SM/CH (40 %/40 %/20 %), which on the basis of phase diagrams shown in Figure 28, is expected to be Lo and Ld phase separated at room temperature[286]) spanned over gold microcavities. Surprisingly, this bilayer composition showed weaker Raman spectra than the DOPC alone, with lower signal to noise ratio. Vibrational features between 490-530 cm^{-1} are tentatively attributed to cholesterol[256]. Both DOPC and SM have stretching C-O-C and O-O vibrational modes between 720-890 cm^{-1}, making it difficult to distinguish between the two. All three components show vibrational modes around 1125 cm^{-1} attributed to C-O-C asymmetrical stretching. Modes at 1024 and 1290 cm^{-1} are identifiable as SM C-O and C-O-H bending vibrations, however, from 1400-1700 cm^{-1} there is extensive overlap between the lipids and distinguishing between them becomes difficult. The overlap is due to the lipid's hydrocarbon chains showing bands in the 1400-1500 cm^{-1} region where scissoring and twisting vibrations of the CH_2 and CH_3 groups occur[256]. When comparing the spectra with a simple DOPC spectrum from section 2.3.6, it is evident that there is overlap of DOPC, CH and SM vibrational bands, in particular, those between 1200 and 1700 cm^{-1}. Lipids also exhibit intense bands between 2800-3100 cm^{-1} due to C-H stretching modes[256]. However, as the drug did not show bands in this region, spectra were not recorded past 2600 cm^{-1}.

The coupling and interactions of the lipid components causes changes in the spectra[256] adding complexity to the analysis of ternary lipid compositions. Although the microcavity array allows for well-resolved vibrational bands, interactions between the lipid and the gold & alkanethiol can result in small spectral changes. The changes are usually observed as a small shift in wavelength or change in intensity of the vibrational band.

A key limitation to this method should be noted. SERS is known to have difficulty in reproducibility in signal intensity[276,287]. This is due to the slight variation from substrate to substrate and due to the dependence on the orientation of the analyte to the plasmonic surface[276]. To overcome this issue, the following approaches were made; single cavity measurements were completed as opposed to a wide-field approach with numerous cavities. This was to ensure variation in pore packing, areas of discontinuity and surface roughness, that is common with the Ps templating method used to create the cavities, as well as packing differences of the bilayer over the planar gold in-between cavities, would not cause any further signal variation which might influence the kinetic changes of interest. The spectra were also only taken once focused on the bilayer and the spectra was then normalised to a lipid peak located at 1006 cm^{-1}. This allowed for the intensity to be compared on one sample over time, but not comparable from sample to sample. Another key issues was the temporal resolution of the Raman collection. As the laser intensity had to be kept relatively low as to not damage the bilayer, a high number of accumulation was required to obtain high-quality spectra. Typically, it took 2.3 minutes to take one spectrum, meaning the spectrum is in real time and is subject to change during acquisition.

3.3.2 Raman Investigation of Anthracyclines

3.3.2.1 Raman Signature of the Drugs Alone

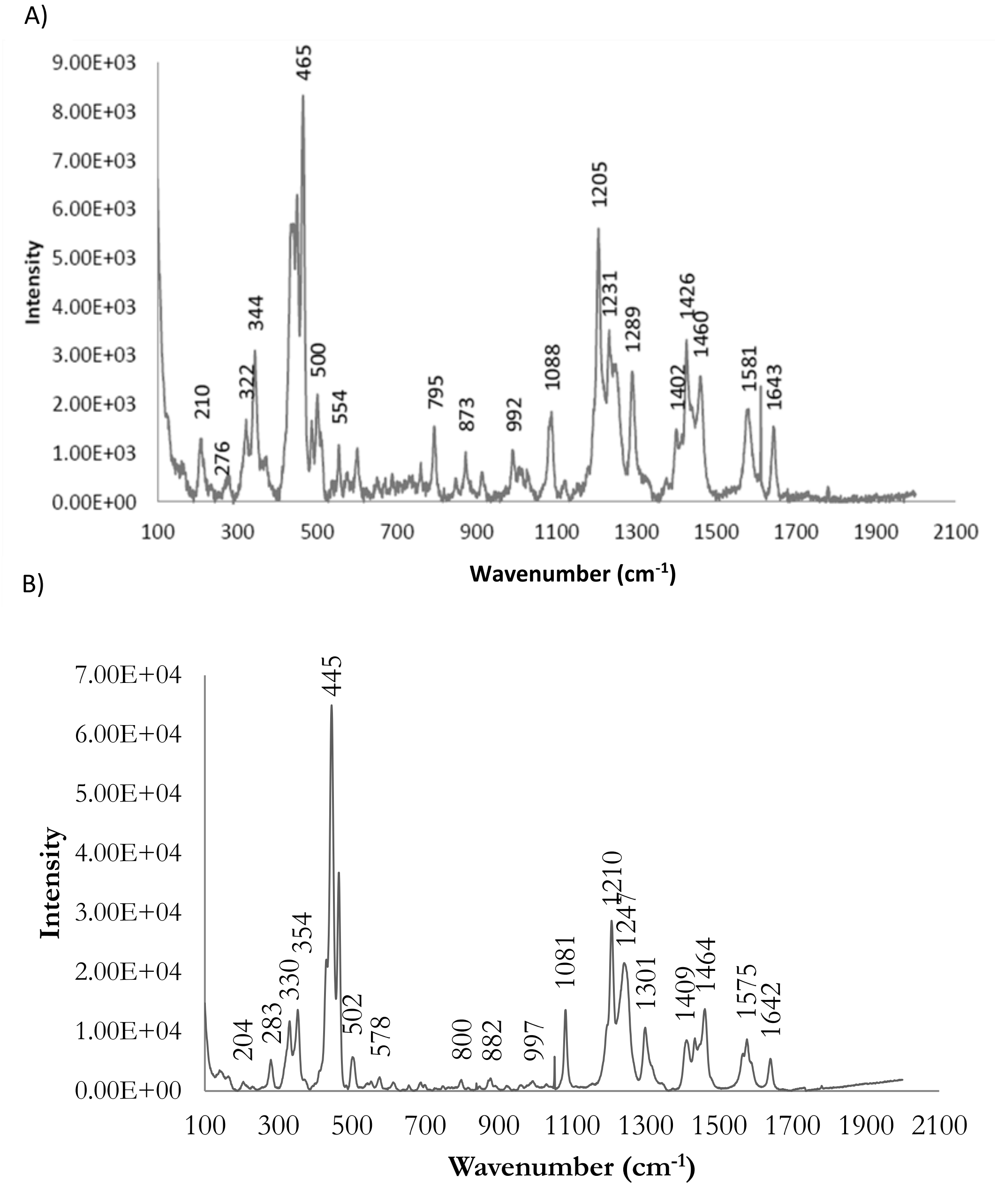

Figure 52: Raman spectra obtained of 0.1 mM A) Doxorubicin B) Daunorubicin, in deionised water on a glass slide, excited at 785 nm. (n ≥ 3, at RT)

Through Raman spectroscopy, both doxorubicin (Figure 52 A) and daunorubicin (Figure 52 B) have been shown to exhibit strong characteristic vibrational bands. Spectra of the drugs as both solid and in solution were obtained for reference, and key marker peaks were tabulated in Table 2. Doxorubicin and daunorubicin are similar in structure (Figure 26) and therefore as expected, show similar Raman spectra. Both drugs showed strong vibrational modes upon 785 nm excitation. As shown in Figure 52, at 444 cm^{-1}, modes due to ring and carbonyl group bending vibrations are visible. The peaks at 344 cm^{-1} are due to a C-C-O and at 465 cm^{-1} are the result of C=O in-plane deformation[288]. The $C-H_3$ wagging vibration of the daunosamine moiety results in a weak band at 792 cm^{-1} and aromatic carbon-hydrogen bending results in a strong band at 1083 cm^{-1}. The region between 1200–1300 cm^{-1} is attributed to in-plane bending motions of C-O, C-O-H and C-H. Vibrational bands at 1205, 1235, 1290 (C-O, C-O-H and C-H bending), 1410-1455 (aromatic ring vibrations), 1428,1455, 1579 (C=C stretch) and 1643 cm^{-1} (hydrogen bonding stretching of C=O) have been documented for these drugs[269]. As seen in Figure 52, these documented peaks are clearly visible, such as the hydrogen bonded C=O stretching mode around 1640 cm^{-1} and skeletal ring vibrations around 1406, 1433 and 1570 cm^{-1}. The identified drug bands, listed in Table 2, were then cross-referenced with the lipid bands, listed in Table 1, to identify what features from the drugs are well isolated from lipid bands.

Functional group/ Vibration	**Region**	**Doxorubicin**	**Daunorubicin**
ν(C = O)	1680-1820	1643	1642
ν(C = C)	1500-1900	1425, 1455, 1579	1464, 1575
δ(CH2)δ(CH3)	1400-1470	1402	1409
β(C-O, C-O-H, C-H)	1200-1300	1205, 1235, 1290	1210, 1247, 1301
ν (P-O)	1060-1100	1083	1081
υ(O-O)/ υ(C-O-C)	800-970	873, 992	882, 997
ν asN+ (CH3)3		792	800
υ(Si-O-Si)	450-550	500, 554	502, 578
δ(C = O)		444, 465	445
δ(CC) aliphatic chains	250-400	210, 276, 322, 344	204, 283, 330, 354

Table 2: Characteristic Raman Bands of Doxorubicin and Daunorubicin with assignment. β, bending; δ, deformation; υ, stretching (s, symmetric; as, asymmetric)[256].

3.3.2.2 Anthracyclines Diffusion across Gold Cavities.

In order to understand if we can follow the diffusion of the drugs through a bilayer into the cavity array through Raman spectroscopy; it was necessary to first monitor the signal obtained when the drugs diffused from solution into an aqueous filled unmodified gold cavity array. This was completed by adding a known concentration of drug, to unmodified 1 μm cavities incubated in 2 ml PBS buffer (typically so that the final concentration was 0.1 mM) and monitoring the Raman signature over the course of an hour. Figure 53 and Figure 54 show spectra of daunorubicin's & doxorubicin's diffusion process. When the cavities are in PBS only, a weak background spectrum is observable. It should be noted that although focus is on the cavities, due to the axial resolution, the confocal volume above the cavities will also be detected. However, once the drug has dispersed through the solution (approx. 27 min according to experiment shown chapter 2), its signal should not alter and is overshadowed once SERS signal is observed when drug enters the cavity.

As shown in Figure 53, no Raman modes are visible prior to or immediately following drug addition. At 10 minutes, weak vibrational bands begin to become apparent, as the drug disperses throughout the PBS. As time increases, the bands evolve in intensity. By 30 minutes well-defined peaks attributed to the drug, such as the ring vibrations at 444 cm^{-1} and the hydrogen bond bending at 1208 cm^{-1}, become apparent. The time-scale of signal evolution corresponds well with the diffusion experiment completed in chapter 2, where it indicated that the drug takes approximately 27 minutes to diffusively mix in the solution and reach the bilayer. The intense well-resolved peaks observed at 30 minutes are attributed to the drug reaching the cavity interior and being plasmonically enhanced.

By 40 minutes the signal has equilibrated and remains unchanged beyond this point as shown Figure 53, as the spectrum at 60 minutes is identical to the one observed at 40 minutes, The spectrum corresponds well to the solution phase spectra shown in Figure 52, with marker bands at 444, 1084 and 1436 cm^{-1} attributed to ring vibrations, aromatic carbon-hydrogen bending and C=C stretching respectively. Notably, the relative intensity of the Raman features on cavity substrates is pointedly enhanced in comparison to the drug in solution. In particular the higher frequency features above 1400 cm-1 are more intense relative to the lower frequency features at the cavities. This is attributed to SERS enhancement. The spectra indicate, that in the absence of a bilayer, it takes approximately 30 minutes for the drug to fully diffuse throughout 2 ml of PBS and reach the cavity surface. And takes up to 40 mins for maximum surface enhancement.

From the simulations in chapter 2, a small degree of enhancement should originate at the top surface, which we tentatively attribute to the weak peaks observed initially. The majority of the plasmonic enhancement should be localised within the cavity, meaning the strong peaks observed at 30 minutes can be attributed to diffusion into the cavity. Indicating that the signal observed can be initially attributed to Raman from the confocal volume, and as the drug diffuses into the pore, the signal is attributed to SERS from the drug within the cavity.

As expected, doxorubicin (Figure 54) showed similar results. As with daunorubicin, weak background spectra were observed when immersed in PBS solution. Upon drug addition (0 min), weak bands become immediately apparent. At 10 minutes, small weak vibrational bands are visible. The intensity of all the Raman bands remains roughly the same from 10 minutes until 30 minutes, at which point the intensity increases, showing strong Raman bands. Between 45 and 55 minutes, the Raman intensity is maximal, suggesting that, as with daunorubicin, it takes approximately 30 minutes for the drug to diffuse throughout the solution and begin to receive plasmonic enhancement from the cavity and between 40-60 minutes, equilibrium is reached, showing full enhancement received from the plasmonic cavities.

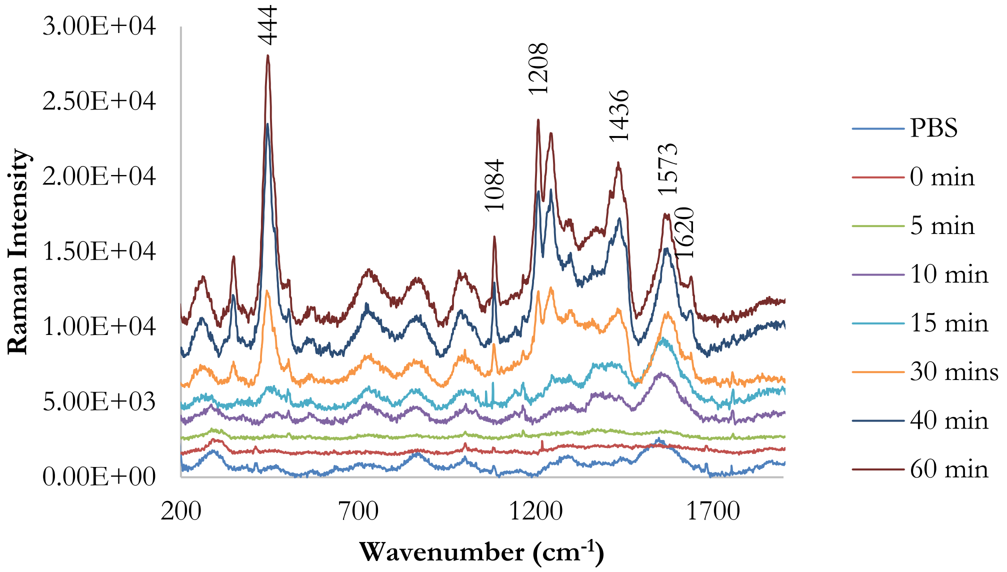

Figure 53: Raman spectra of 0.1 mM daunorubicin introduced to PBS filled bare 1 µm cavities and monitored at a single cavity over 60 minutes. Data was offset for clarity. (n ≥ 3, at RT)

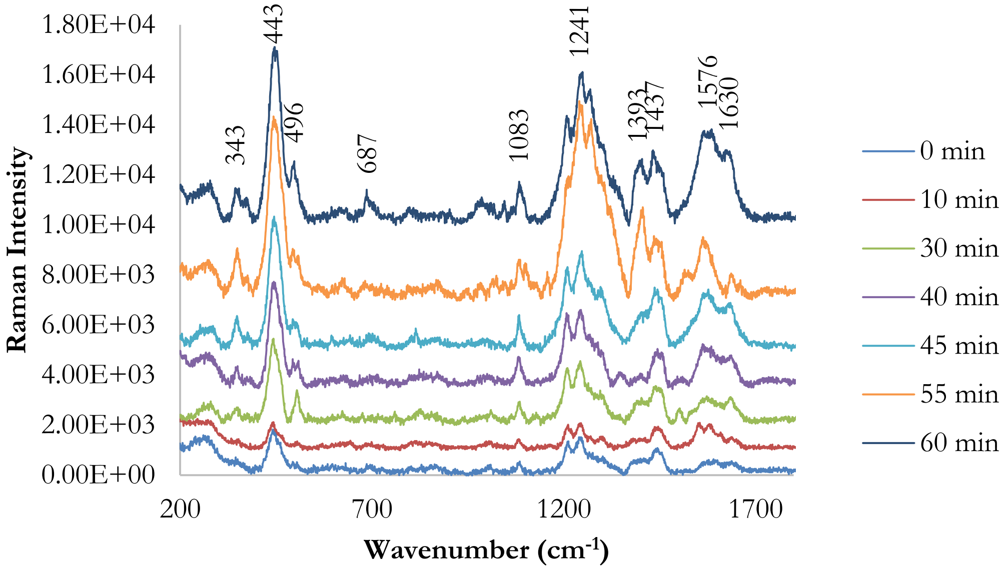

Figure 54: Raman spectra of 0.1 mM doxorubicin introduced to PBS filled bare 1 µm cavities and monitored at a single cavity over 60 minutes. Data was offset for clarity. (n ≥ 3, at RT)

3.3.2.3 Drug-Gold Interaction

All cavity arrays were pre-sonicated with buffer prior to measurement or bilayer assembly. It is established that aqueous filling of the entire cavity is not achieved by simple contact of the array with water[104]. The space in the bottom of the well is not filled unless sonication is applied[104]. Furthermore, once pre-filled, diffusion of dyes into the volume, occurs freely[104]. To confirm complete diffusion of the drug into the cavity volume was achieved and to ensure no drug adsorption had occurred, the drugs were sonicated into the cavities at different concentrations (1 nM – 0.1 mM) for five minutes, and the Raman spectra from 5 locations was measured. The experiment was completed for both bare and C6 top-surface modified cavities.

On bare gold cavities, weak background was solely observed in PBS solution. When 1 nM daunorubicin was sonicated into the cavities, well resolved Raman signal was observed. A similar observation was made at 2 nM and 5 nM. Raman intensity did not reproducibly increase linearly with concentration. Variation in intensity of Raman spectra may be attributed to difficulty focussing the laser on the plasmonic field in the cavities. This reflects a major challenge with the cavity substrate, as small change to focus or microscopic differences in the substrate can cause significant effects to the intensity of the Raman signal. This highlights a common issue with SERS substrates and will need to be addressed should the method be taken further than this initial study.

Cavities were selectively modified as described in Chapter 2. Weak to no vibrational modes were observed for drug sonicated C6 modified cavities, over the concentration range of 100 nM – 0.1 mM. At 1-5 nM, weak vibrational bands were observed, whereas 10 nM showed defined drug peaks. These drugs are known to aggregate[289,290] at the higher concentrations. Meaning, the aggregates could interact with the modified monolayer and hinder its diffusion into the cavity.

After drug incubation with the cavity array, samples were rinsed with deionised water and the Raman signal was measured again to determine if the drug was binding to the gold surface. Across the drug concentrations explored 1 nM – 0.05 mM, there was little evidence, post rinsing, for any resolved Raman signal from the drug. This indicates that minimal to no adsorption had occurred and adsorption can be excluded as the origin of SERS signal post diffusion into the cavities.

3.3.2.4 Effect of C6 on Drugs Diffusion Process

Diffusion studies were completed on 6-mercapto-1-hexanol modified cavities to determine if the modification layer has an influence on the diffusion or enhancement of the drug. This was completed by introducing 0.1 mM doxorubicin/daunorubicin to C6 top surface-modified cavities and C6 fully modified cavities (including the interior of the cavity) and monitoring the Raman signal over the course of an hour. An example of which can be seen in Figure 55. Defined vibrational bands attributed to both drug and C6 are visible for both samples at around 400 (C=O), 1209 (in-plane bending of C-O, C-O-H and C-H), 1400-1460 and 1574 cm^{-1}(skeletal ring vibrations).

For top-surface only modified samples (Figure 55 A), weak Raman bands are evident over time, appearing at a higher intensity around approximately 30 minutes, similar to what was observed with bare samples. Interestingly, the spectrum obtained at 30 minutes shows greater signal intensity than the following spectra. The peak around 1570 cm^{-1} (Skeletal ring vibrations) appears to blue shift, while the peak at 1150 cm^{-1} red shifts. These then return to their original positions at 40 min. The spectral shift is most likely due to the gold plasmons[264]. However, the overall intensity for these top-surface modified cavities is lower than what is observed for bare samples. This indicates one of two occurrences, 1) top surface enhancement is larger than previously thought, but previous simulations indicate this is not the case. 2) The C6 is binding to the drug preventing it from entering the cavity for full enhancement. These drugs are known to aggregate at higher concentrations[289]; this aggregation may increase its likelihood of binding to C6.

C6 modification of both top surface and the interior of the cavities (Figure 55 B) were also examined. At 0 minutes, small vibrational bands attributed to the C6 are visible, such as 400 (C=O) and 850 cm^{-1} (υ(O-O)/ υ(C-O-C)). This is not as evident in the top surface only modified cavities, indicating the plasmonic enhancement is localised within the cavity and thus, corroborating with the simulations completed in Chapter 2. Similar to the previous samples, the signal intensity increased over time as the drug diffused into the cavity. At 20 minutes, intense Raman vibrational bands are visible, and by 40 minutes, no further increase in signal is observed. The Raman signal of the structural information attributed to the region of 600 – 1100 cm^{-1} is more defined on fully modified samples than top surface only modified samples. Upon entry of the drugs into the C6 fully modified cavities, a greater Raman signal is observed over time than for top-surface only modified samples. It is possible that this is due to the entrapment of the drug by the C6 monolayer. The entrapment would immobilise the drug close to the surface and within the plasmonic field resulting in greater signal enhancement.

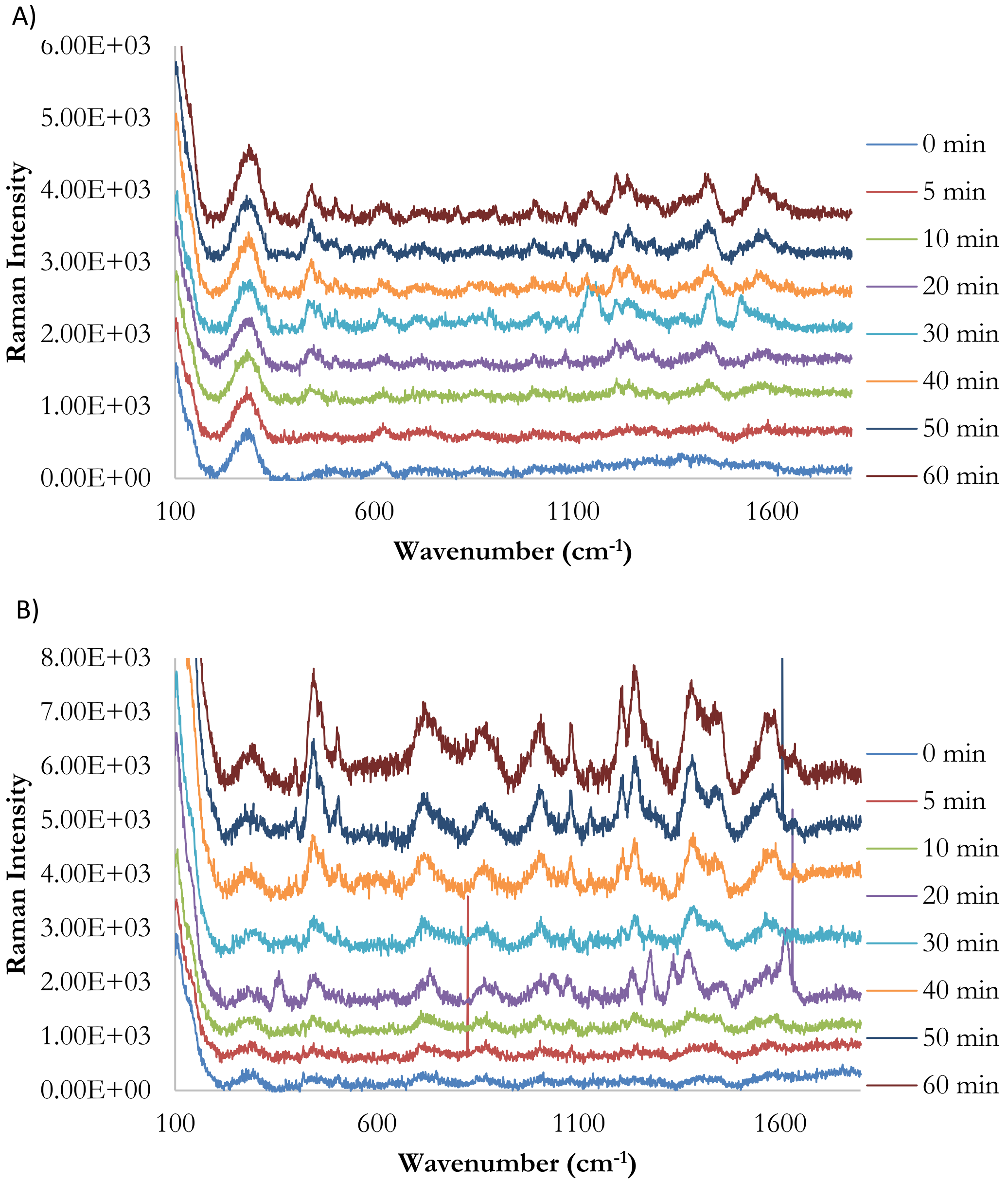

Figure 55: Raman spectra of 0.1 mM daunorubicin introduced to A) C6 top surface only modified and B) C6 modification of both top-surface and interior of 1 µm cavities over time. Samples were prefilled with PBS and excited at 785 nm. Data was focused on a single cavity pore. Data is offset for clarity. (n ≥ 3, at RT)

3.3.3 Raman Investigation of the Interaction of Drugs with DOPC Bilayer

To evaluate if the Raman/SERS response from the drug could be used to interrogate drug-membrane interaction and whether signal evolution could be used to track the drugs arrival across a membrane into the cavity, permeation studies were conducted by introducing doxorubicin/daunorubicin to a DOPC bilayer, or a ternary bilayer spanned across 1 μm cavities in contact with 2 ml PBS solution. Focus was targeted on the lipid bilayer by obtaining its maximum intensity. Due to the axial resolution, signal from the bottom of the cavity pore should also be included, meaning both bilayer and cavity signal should be monitored throughout the study.

As shown in Figure 1, as the drug permeates the bilayer, a SERS signal from the drug is observed. Initial studies were completed with 0.1 mM of doxorubicin and daunorubicin. Spectra were then obtained every 2.5 minutes for an hour. As can be seen in Figure 50 and Figure 52, characteristic and well-resolved Raman peaks can be distinguished at 789 cm^{-1} for daunorubicin, 788 cm^{-1} for doxorubicin and 720 cm^{-1} for DOPC (symmetrical stretching of choline $N^+(CH_3)_3$) and 1639 cm^{-1}(daunorubicin), 1640 cm^{-1} (doxorubicin) and 1620 cm^{-1} (DOPC) (C=C stretching). However, there was significant overlap throughout the spectra of the lipid and drug features and due to this few peaks attributed solely to the bilayer or drugs could be identified. A lipid associated peak at 930 cm^{-1} (C-O-C stretching) and a drug associated peak were identified at 1640 cm^{-1} for doxorubicin, and at 1639 cm^{-1} and 1207 cm^{-1} (δ (C-O-H)) for daunorubicin were also fairly well resolved.

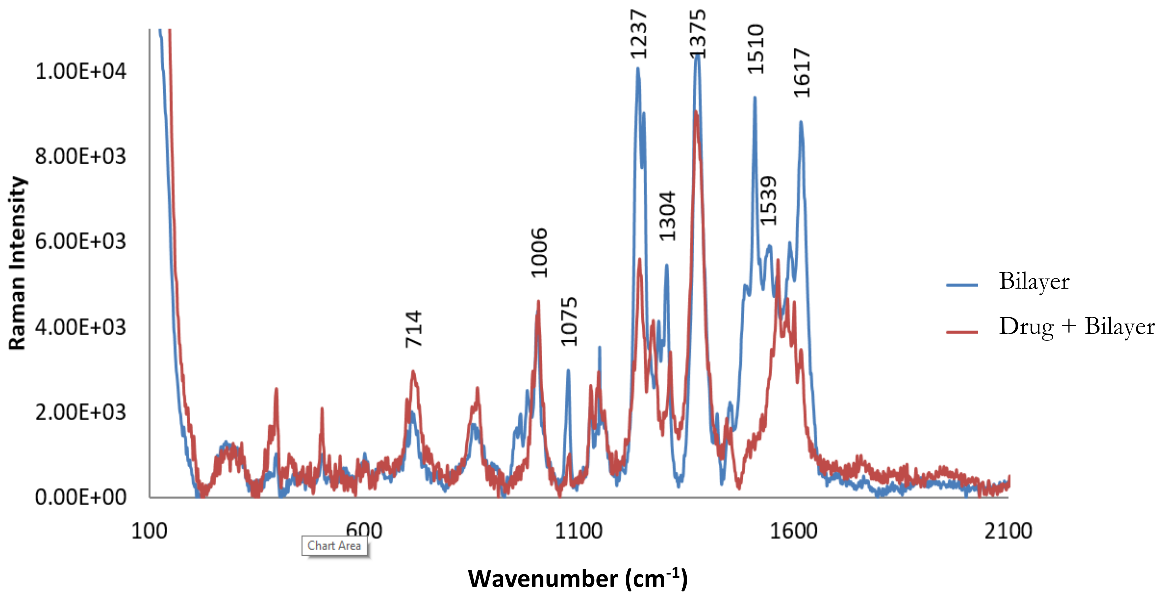

Figure 56: SERS Spectra at 785 nm excitation, of 1 nM of daunorubicin introduced to a DOPC bilayer spanned over 1 µm (PBS prefilled) gold microcavities. Data was focused on a single cavity pore (n ≥ 3, at RT).

Figure 56 shows overlays of spectra obtained from DOPC alone and in the presence of 1 nM daunorubicin. DOPC shows defined vibrational bands at 720, 1120 and 1620 cm^{-1} attributed to C-H$_3$ wagging vibration of the daunosamine moiety, bending of the C-O, C-O-H, C-H groups and C=C stretching vibrations of the ring respectively, are visible in the PBS spectrum, indicating the successful spanning of a bilayer across the cavities.

When the drug is introduced, an immediate change is observed in the obtained spectra. Some bilayer vibrational modes, such as those at 720 and 1120 cm^{-1} remain unchanged, however, others such as modes at 1620 cm^{-1} converge, shifting to a higher frequency and decrease in intensity. These spectral changes indicate molecular interactions are occurring between the drug and bilayer. Another example is observable at 1300 cm^{-1} (β(C-O, C-O-H, C-H)), where the DOPC modes shifts to 1312 cm^{-1} upon daunorubicin addition, suggesting H-bonding interaction is likely occurring at the membrane interface between the drug and phospholipid.

Lipid features across the range between 1500-1620 cm^{-1} shift to a higher frequency, and the peak intensity decreases upon drug addition. Whereas phosphate (P-O) mode also observed at 1075 cm^{-1} does not alter upon the introduction of the drug. The lipid peak at 1006 cm^{-1} (υ(C-O-C) asymmetrical) is unaffected by drug addition and is therefore used as a reference peak for normalisation. Similar behaviour is observed when doxorubicin is introduced to the bilayer. These changes to the vibrational bands provide strong evidence for interaction between the bilayer and the drugs.

To estimate the dynamic response, data was normalised to 1006 cm^{-1} lipid peak and then the area of the drug peaks 1640 (doxorubicin) and 1636 cm^{-1} (daunorubicin) was obtained using the labspec software. Representative data is shown in Figure 57 & Figure 63. As the experiment was focused on the bilayer, the data gathered should, reflect primarily on the interactions occurring within the bilayer. However, as the confocal volume in the z-plane is expected to be elongated, it should encompass the whole cavity, bilayer and solution. Meaning, although the bilayer and cavity are encompassed with in the collection data, the experiment is susceptible to z-drift. The absolute intensity was also found to vary from substrate to substrate, however, the dynamic response proved to be similar across replicates.

On bare cavity samples, as shown in Figure 57, an increase in peak area was observed for approximately 20 minutes for both drug types and then plateaus off. The dynamics can be attributed to the drug diffusing throughout the contacting solution, where after 20 minutes it has fully diffused through solution and cavity. C6 modified cavities followed a similar pattern. Although, (notwithstanding the time-resolution of the measurements) equilibration takes slightly longer, at 25 minutes.

The Raman signal evolution at DOPC bilayer spanned cavities showed different dynamics to bare and C6 modified cavities. Both drugs showed the same initial increase, attributed to diffusional mixing of the drug into the contacting solution. Then, on average, the peak area continues to increase between 30 and 50 min, which then appears to plateau. The signal is not steady and some variation from sample to sample is observed, which may be due to Z-drift or nanoscopic variation in the gold substrate. As shifts to the lipid Raman features are evident during this window, this confirms the drug is in both the bilayer and reaching the cavity, as the confocal volume will encompass both allowing for the observation of their contributions.

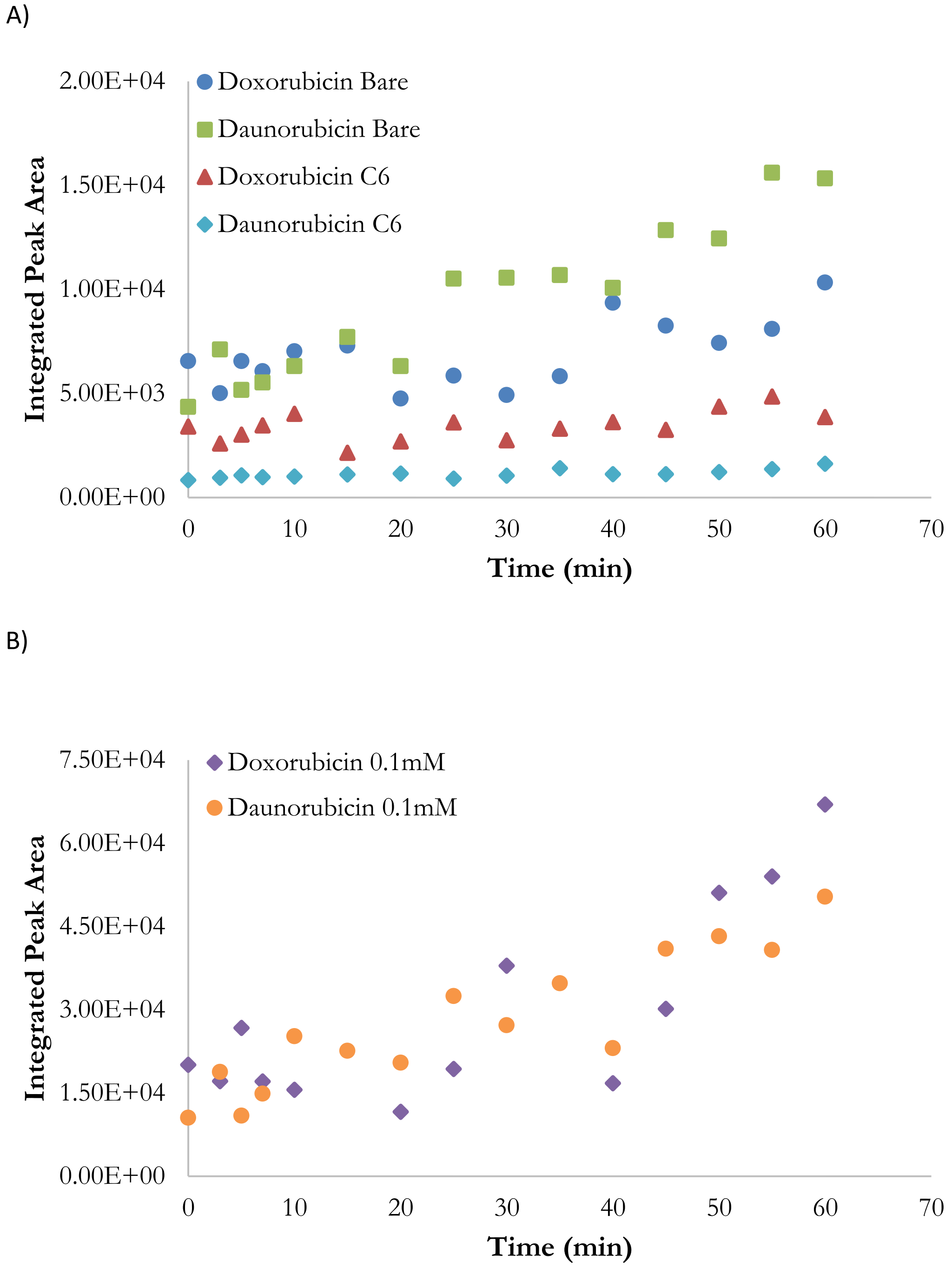

Figure 57: Integrated peak area of the drug peak, 1636 cm^{-1} (peak limits set at 1629-1659 cm^{-1}), obtained at 785 nm excitation of A) bare, C6 modified and B) DOPC bilayer spanned cavity array in 0.1 mM doxorubicin and daunorubicin. (n ≥ 3, at RT)

3.3.3.2 Identification of Lowest Distinguishable Concentration

To be able to accurately ascertain the occurring drug-membrane interactions, the drug Raman peaks must be observable over the lipid peaks. Meaning, identifying the lowest possible concentration of drug that was still decipherable over lipid peaks was required. To evaluate this, varied concentrations of the drug were sonicated into the cavities (in the absence of a bilayer) and the Raman was then measured. Well resolved Raman bands were observed for both drugs down to 1 nM concentration, a representative spectrum is shown in Figure 58. As these drugs are not typically expected to be below 1 nM in physiological conditions, lower concentrations were not examined. The SERS signal to noise was seen to be suitable from the cavities at this concentrations. Therefore, it was then investigated if the signal could be resolved above the lipid membrane background at this concentration.

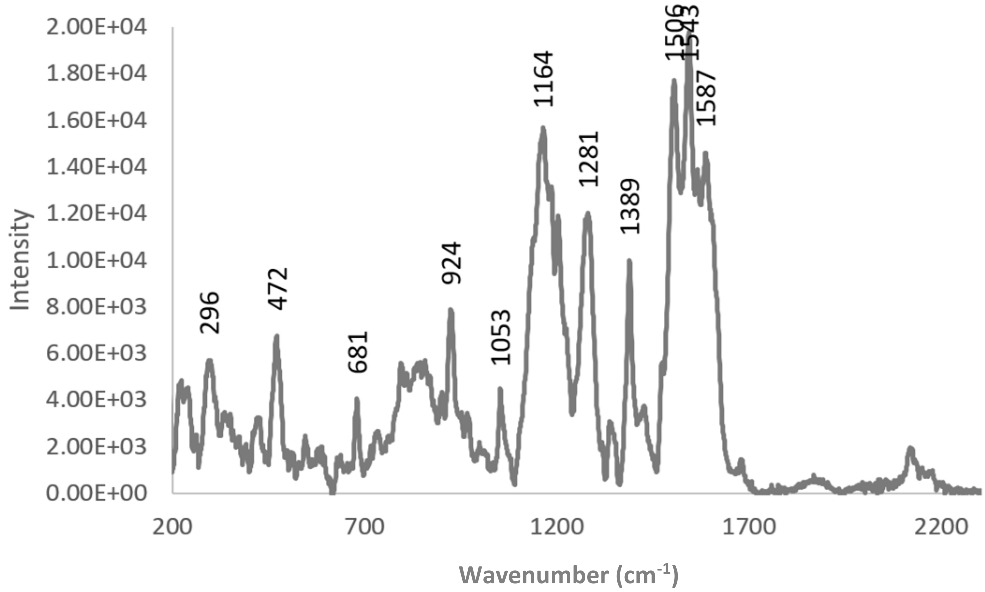

Figure 58: SERS Spectrum (monitoring a single pore) of 2 ml of 1 nM daunorubicin solution sonicated for 15 minutes with 1 µm bare gold cavities excited at 785 nm. (n ≥ 3, at RT)

1 nM of the drug was introduced in the same manner as previous experiments and monitored for an hour (Figure 59). However, when the bilayer is present, distinguishing the drug peaks above the lipid background was challenging. The reference drug peak, 1640 cm^{-1} (ν(C = O)), which is identifiable at higher concentrations were difficult to distinguish at 1 nM (as can be seen in Figure 59). Nonetheless, Raman bands could be distinguished for both drugs down to 1 nM concentration in the presence of the bilayer. A key bilayer peak observed at 1128 cm^{-1} (aliphatic chain vibrations) remains visible regardless of concentration. Peaks such as those found at 720, 496 & 1105 cm^{-1} remain observable are superimposed on drug features.

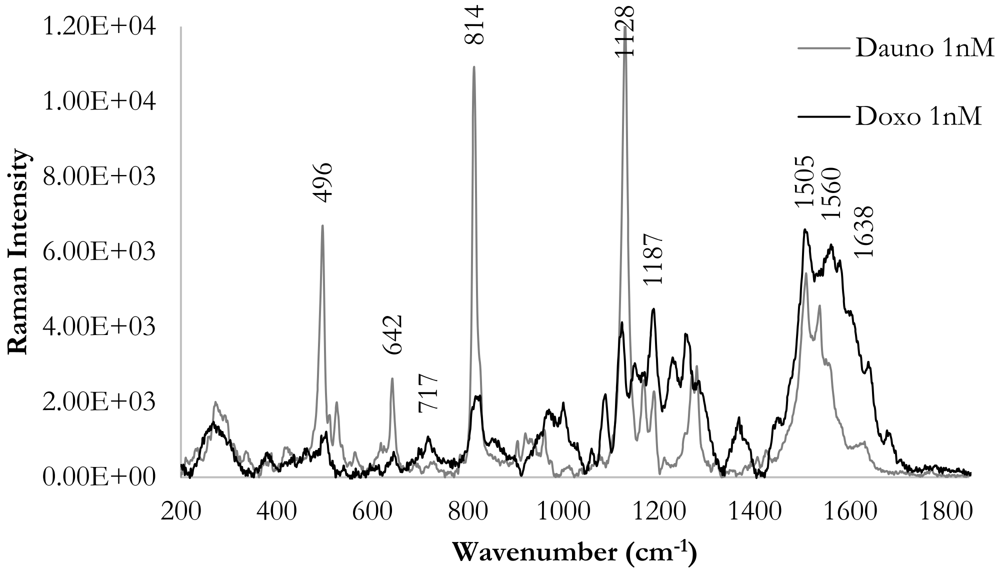

Figure 59: SERS Spectra of 1 nM doxorubicin & daunorubicin introduced to a DOPC bilayer spanned over 1 μm gold cavities in PBS buffer, obtained after initial addition of drug. Excitation wavelength used was 785 nm. Both drugs show defined Raman signatures indicating that this SERS method is sensitive enough for detecting nM concentrations of these drugs. Data was focused on a single cavity pore (n ≥ 3, at RT).

3.3.3.3 Concentration Dependence of Response

DOPC permeation experiments were completed over a range of drug concentration to encompass both administration concentrations and physiological concentrations, from 0.1 mM to 1 nM. Experiments were completed in the same manner as previously described in this chapter, with the concentration of added drug being the sole variation. Both drugs are believed to embed themselves within the polar head group regions[84]. At physiological pH's (of blood & plasma, pH 7-9[291]), doxorubicin should be a neutral species, whereas daunorubicin should have a positive charge[273]. The presence of a charge can cause differentiation in how the drugs interact electrostatically with the bilayer, which contains DOPC, a zwitterionic lipid. One study found through fluorescence spectroscopy and electron spin resonance on immortalised hamster B14 and NIH 3T3 mouse fibroblasts, that if 20 μM doxorubicin is added, the membrane experiences greater rigidity. Whereas, at 0.5 μM doxorubicin, a small increase in fluidity is seen. From their work, they concluded that the drugs intercalate mainly into the hydrophobic core, and the surface of the bilayer is only affected at high concentraions[292].

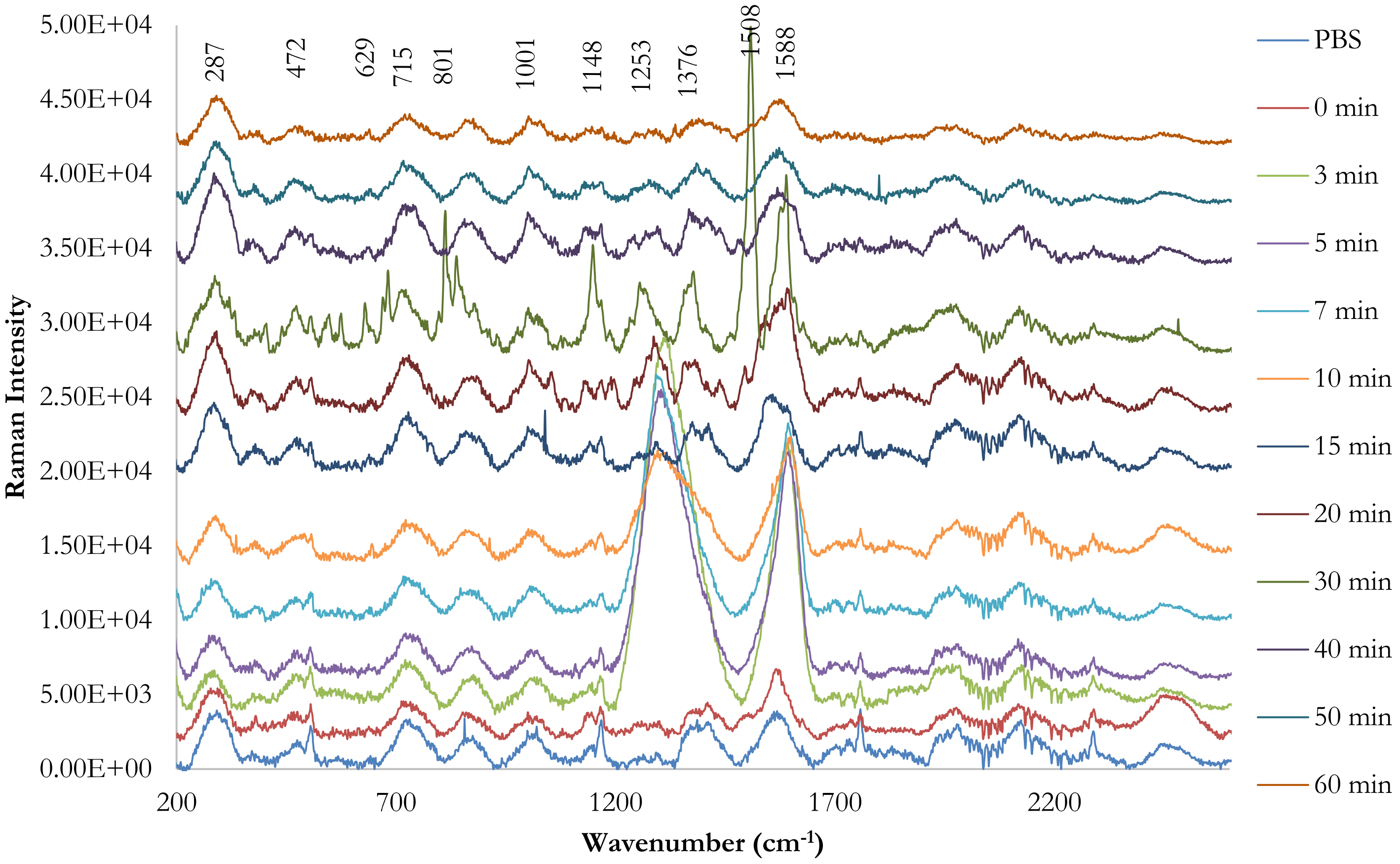

Figure 60: SERS spectra of 2 nM daunorubicin introduced to a DOPC bilayer spanned 1 μm cavities (PBS filled) over time, excited at 785 nm. Data is offset for clarity. "PBS" is bilayer spectrum prior to drug addition, "0 min" indicates immediately after drug addition. Data was focused on a single cavity pore (n ≥ 3, at RT)

Interestingly, at the lowest concentration of the drug explored at DOPC bilayers (1 nM & 2 nM), an optical phenomenon was observed, where a broad feature between 1200 – 1700 cm^{-1} appeared between 3-15 minutes. This features was consistently observed across replicates, however, the exact time-frame was found to vary and the features usually disappeared by 15 minutes. An example of this peak increase can be seen in Figure 60 at 3 min. The features are too broad to be Raman modes and are tentatively attributed to scatter or the refractive index. A possibility as to why this is visible at lower concentrations and not high ones, is likely because the Raman signal is weak at this concentration and so is not masking the effect. It is also notable that at lower concentration a sinusoidal oscillation is observed in the background. This is a weak phenomenon and is only sometimes observed, it is attributed to laser diffraction from the ordered array.

As seen in Figure 60, as the drug is added at 0 min, the spectrum decreases in intensity at peaks such as 1400 (δ(CH2)/δ(CH3)) and 1750 cm^{-1}(ν(C = O)). After 3 minutes, a broadening and intensity increase is observed at 1280 and 1550 cm^{-1} attributed to C-O & C-H bending and C=O stretching, where the former is a drug associated peak, and the latter is DOPC associated, suggesting drug-membrane interactions are occurring. This broadening only appears to occur at concentrations lower than 100 nM, as it was not visible at higher concentrations, where the stronger drug signal would obscure the peak broadening.

At 15 minutes these peaks decrease in intensity, and the spectrum shows both bilayer and drug vibrational bands. At 30 minutes, well-resolved peaks associated to the drug such as 882 cm^{-1} attributed to O-O stretching, are visible, which then decreased by 40 min. At 60 minutes, only bilayer specific peaks are visible, suggesting that the drug has passed through the bilayer and is now residing in the cavity. Meaning, at low concentrations (2nM), depending on if the focus is on the bilayer or within the cavity, different information may be obtained. This is of interest, as even though a large confocal volume is used, allowing for signal from both above and below the bilayer to be collected, depending on where the primary focus is on, information specific to the bilayer can be obtained.

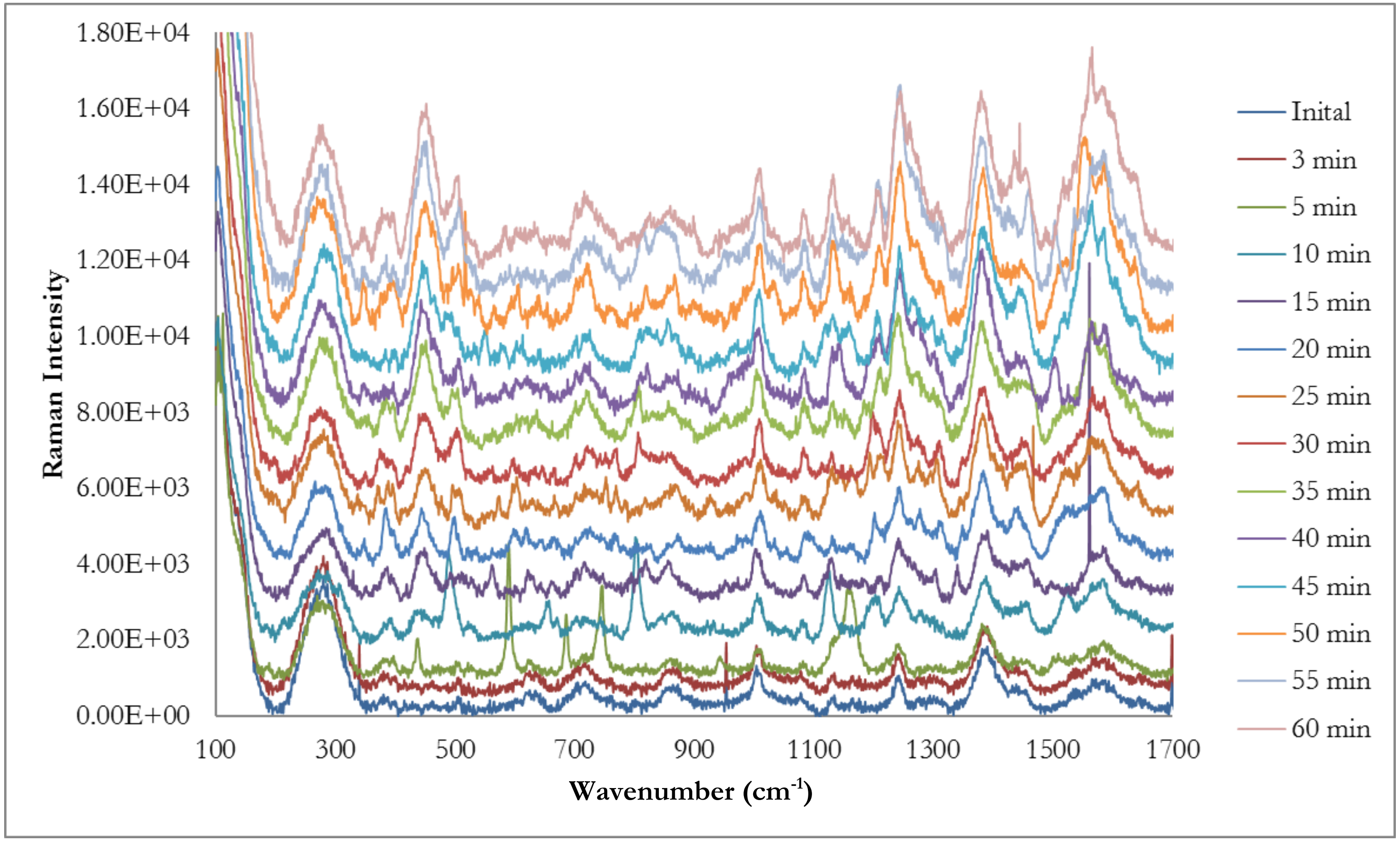

Figure 61: SERS spectra of 0.1 mM daunorubicin introduced to a DOPC bilayer spanned 1 μm cavities (PBS filled) over time, excited at 785 nm. Data is offset with time increasing for clarity. Data was focused on a single cavity pore (n ≥ 3, at RT)

Unsurprisingly, at the higher concentration, 0.1 mM, of daunorubicin (Figure 61), vibrational bands are more intense. In both cases well defined bilayer peaks were observed prior to drug addition such as 793 (ν asN+ (CH3) 3), 904 (υ(O-O)/ υ(C-O-C)), 1061 (ν (P-O)), 1451 (δ(CH2)/δ(CH3)) and 1619 cm^{-1} (ν(C = O)) . Upon drug addition, vibrational bands, 1572 (υ(C=C) and 990 cm^{-1} (υ(O-O)/ υ(C-O-C), attributed to the drug become apparent. In the case of the higher concentration, by 10 minutes, drug vibrational bands are clearly visible over the bilayer bands. The intensity remains similar from 10 to 30 minutes (attributed to drug diffusion in solution), where it then further increases. This pattern agrees with our hypothesis, where the drug immediately begins to interact with the bilayer upon addition but does not reach full bilayer insertion until 30 minutes. Where it receives minor top-surface enhancement from bilayer residence and is fully dispersed amongst the solution, and then begins to diffuse into the cavity, being further enhanced.

At 2 nM, it is evident when the drug is interacting with the bilayer and diffusing through, due to the large increase in Raman signatures. However, at 0.1 mM due to the intensity of the drug vibrational bands, it is difficult to identify and monitor lipid bands as they have a weaker cross-section and are obscured by drug signal. Although this does provide more information on bilayer-membrane permeation dynamics than weaker concentrations. For example, in Figure 62, at 15 and 25 minutes, bilayer-drug bands are mostly visible, whereas, at 40+ minutes, drug vibrational bands dominate bilayer bands. This is taken to indicate, that at the earlier time point where concentration within the cavity is low with minimal signal enhancement, the drug is arriving at the bilayer and at 40 minutes it is diffusing into the cavity. This is possible due to both signal from the bilayer and cavity being obtained due to the large confocal volume. Meaning, we are observing in real time what is happening to a single cavity, which in future, with more complex lipid membranes, can ideally mimic what would occur in a single cell.

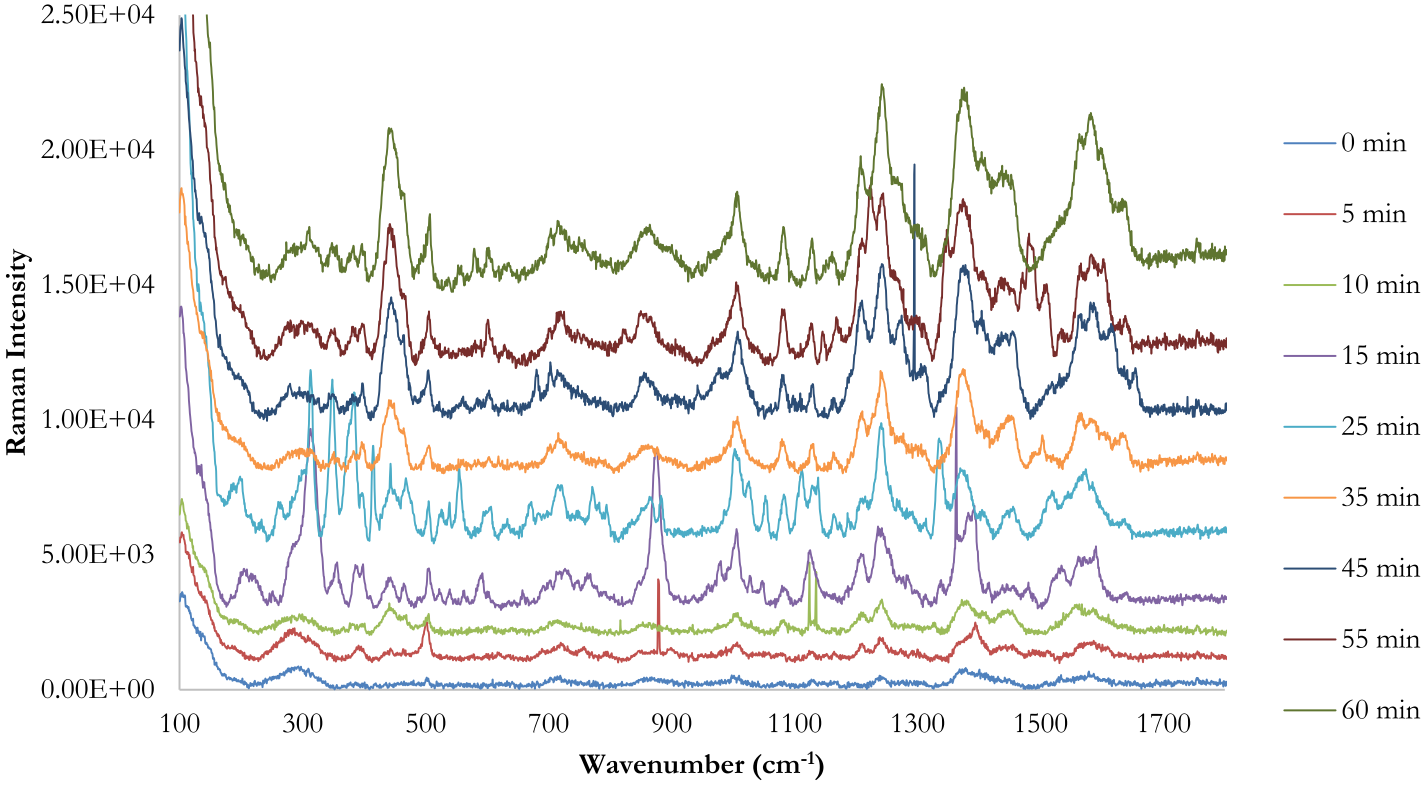

Figure 62: SERS spectra of 0.1 mM doxorubicin introduced to a DOPC bilayer spanned 1 µm cavities (PBS filled) over time, excited at 785 nm. Data is offset with time increasing for clarity. Data was focused on a single cavity pore (n ≥ 3, at RT)

The membrane permeation of the anthracyclines was examined across a range of concentrations from 0.1 mM - 1 nM. Both doxorubicin and daunorubicin were detectable at the lower concentrations; however, as previously described, posed more difficulty to distinguish from the bilayer background. The dynamic evolution of SERS signal was plotted versus time using the integrated peak areas of the marker bands for doxorubicin (1640 cm^{-1}) and daunorubicin (1636 cm^{-1}). An example is shown Figure 63. Interestingly, a different set of kinetics is reproducibly observed at the higher concentrations than the lower nM concentrations. For 0.1 mM-50 nM, an initial increase in peak area is observed for 20-30 minutes. The peak area then rises (with fluctuations) until 50 minutes where it then plateaus. For the concentrations range 10-1 nM, the peak area increases until 20 minutes, where it then decreases until 35-50 minutes, which is followed by a plateau. (2 nM shows a refocusing issue at 35 min). The origin of this difference is unclear, it may be due to the lower concentrations being more prone to artefacts from z-drift or there may be a subtle difference occurred depending on concentration.

Overall, the kinetics suggest an initial rise and increase due to drug diffusion through the solution, followed by drug insertion into the bilayer. A decrease in peak area was widely seen which may be attributed to photodecomposition or the drug diffusing out of the bilayer. Overall, particularly at lower concentrations, using peak area for selected markers as the indicators the data showed variability. This may be due to laser drift. Any minor shift in focus proved to cause an effect on the peak area. This suggests that although this method can provide in-depth information on the occurring drug-membrane interactions, it cannot in the format used here, provide accurate information on the occurring dynamics, but can provide evidence of permeation. Improvement in the fabrication of the gold cavities would be required before this would be possible to try obtain accurate information on the kinetics of the drug permeation.

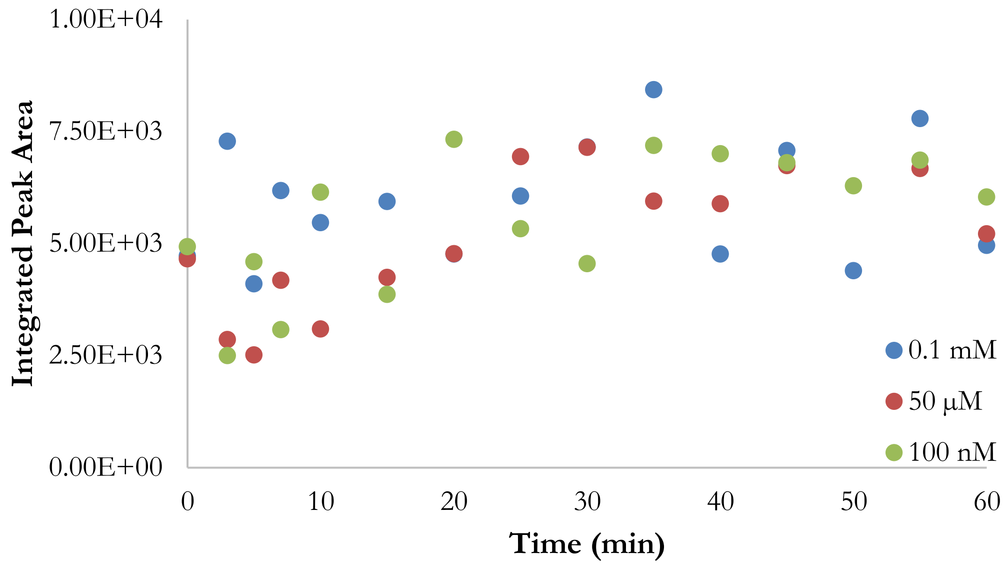

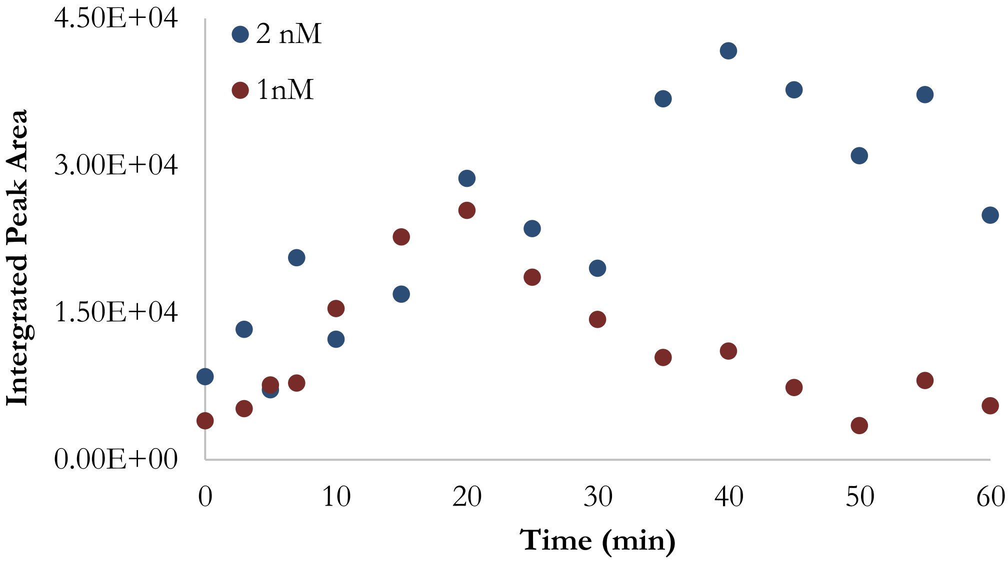

Figure 63: Dynamic changes to the Raman band found at 1639 cm^{-1} obtained at 785 nm excitation of DOPC bilayer spanned 1 µm cavities in 1 nM, 2 nM, 100 nM, 50 µM and 0.1 mM daunorubicin. ($n \geq 3$, at RT)

3.3.4 Raman Investigation of Drug and Ternary Bilayer Interaction.

As the end goal of this project is to develop a biomimetic permeability assay, the bilayer composition was changed to a ternary composition to include SM and CH. The ternary composition comprising of DOPC/SM/CH (40/40/20 %), is not strictly a physiologically ratio. However, it is well known to be phase forming and is expected to form fluidic DOPC enriched Ld and more rigid CH/SM enriched Lo phases which are thought to mimic rafts, believed to form in cell membranes[286]. Ternary bilayer composition preparation and subsequent Raman experiments were completed in the same manner as previous DOPC bilayer experiments. Figure 64 shows a Raman spectra of a ternary composition bilayer in just PBS buffer and the bilayer after 50 minutes incubation in 0.1 mM daunorubicin.

As with the DOPC bilayer, shifts in both lipid and drug related peaks were observed. Peaks such as those at 301 (deformation of CC aliphatic chains), 520 (bending of the CH_2 in ring) and the range between 1700-2200 cm^{-1} (C=O and C=C stretching) increase in intensity after drug incubation. The peaks at 1538 (ν(C = C)), 812 (υ(C-O-C)), 719 (asymmetrical stretching of choline $N+(CH_3)_3$)[256] and 392 cm^{-1}(deformation of CC aliphatic chains) decrease in intensity. Whereas the peaks observed between 1123 – 1385 cm^{-1} appears to red shift. This region is attributed to the in-plane bending of the C-O, C-O-H and C-H. Meaning both peaks associated with the bilayer and the drug can be identified. As with DOPC bilayer spanned cavities, this change in bilayer associated vibrational bands indicate that the drug is intercalating into the bilayer.

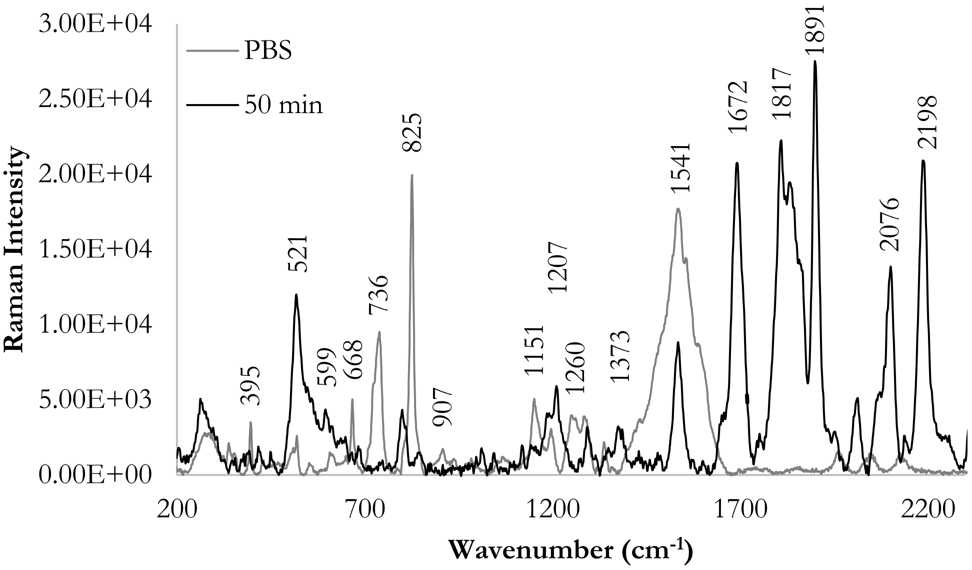

Figure 64: SERS Spectra (785 nm excitation) when 0.1 mM of daunorubicin introduced to a DOPC/SM/CH bilayer spanned over 1 µm (PBS filled) gold microcavities, Where PBS is bilayer spanned cavity alone in PBS solution. Data was normalised to 1006 cm^{-1} band. Measurement was focused on a single cavity pore (n ≥ 3, at RT)

Figure 65 shows spectra of 100 nM doxorubicin's interaction with a ternary bilayer composition. Repeatedly, upon addition of the drug (0 min), bilayer peaks are predominantly observed. At 15 minutes, intense drug peaks become apparent, taken to indicate that the drug has diffusively mixed into solution and has reached the membrane. As time increases, drug peaks then dominate the spectrum, and lipid peaks become difficult to distinguish.

Data was normalised to a phosphate peak as previously described, and Raman peak area was acquired on drug only associated peaks, to minimise any deviation caused by liquid ordered/disordered phases. The different phases, Lo and Ld, are identifiable using Raman spectroscopy by the C-H stretching vibrations within the 2800 – 3100 cm^{-1} region. Where the intensity ratio between 2850/2880 and 2935/2880 peaks may be used to identify the phase. Low ratios indicate higher conformational order of the hydrocarbon chains of the lipid[293]. Meaning, in future, we may identify if the region where the data is obtained is predominantly a liquid ordered or disordered region and observe if there is a difference in drug-lipid interaction due to this.

The introduction of SM and CH into the membrane is expected to decrease its fluidity. One study, by Speelmans et al. which looked into doxorubicin's diffusion across mixed composition liposomes through fluorescence emission, observed that when doxorubicin inserts itself into the headgroup region of the bilayer, it results in tightening of the region and therefore causes a hindrance to any unbound drug trying to permeate the membrane[272]. They found that the addition of SM and CH to the DOPC membrane strongly decreased the transport of doxorubicin. Where SM, showed binding affinities to both DOPC and the doxorubicin drug, whereas CH showed little to no binding with the drug[272]. It was observed that in the presence of CH, doxorubicin would preferentially partition close to the water-lipid interface. They also observed an increase in hydrogen bonds in both lipid and water molecules[186].

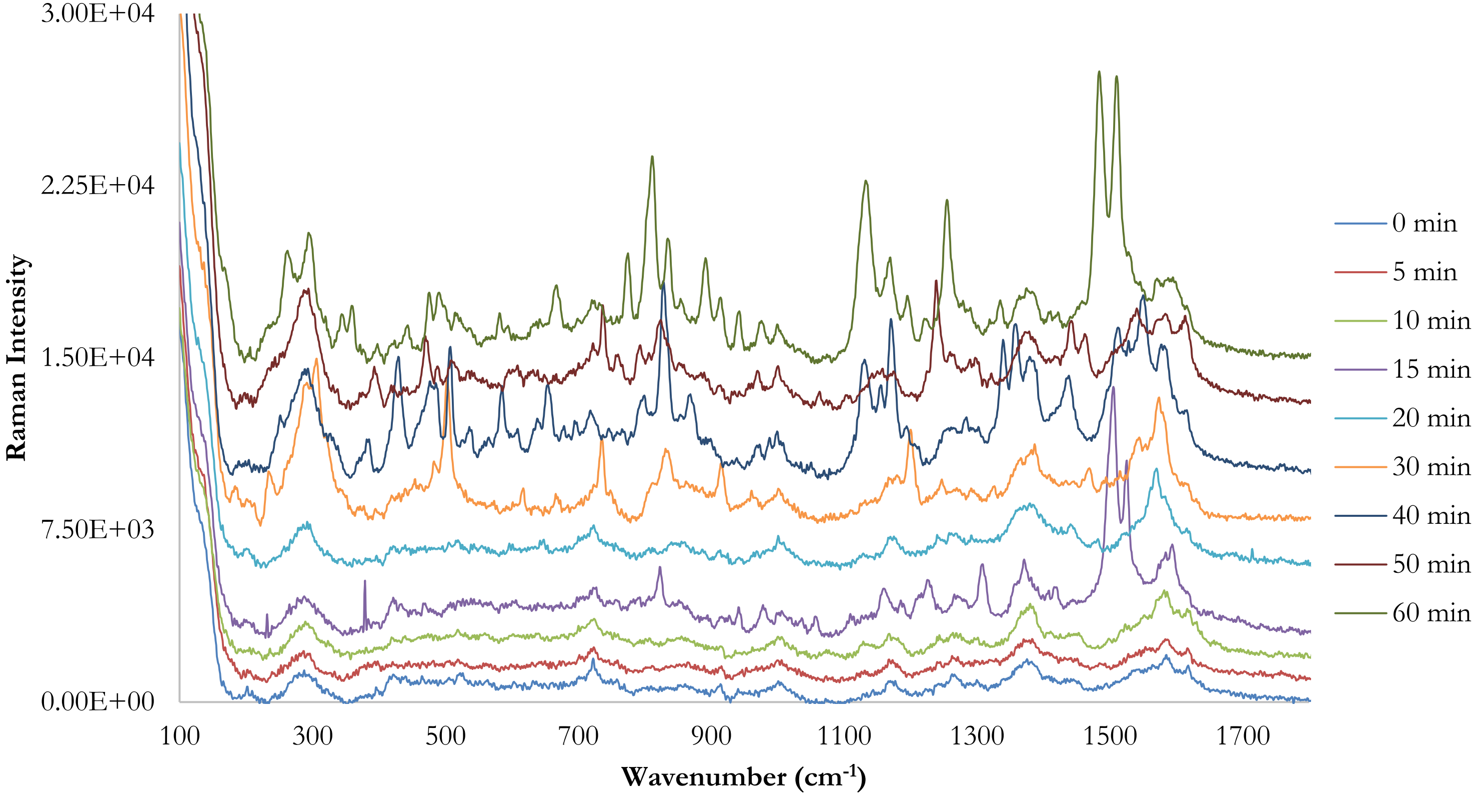

Figure 65: Sample SERS spectra (785 nm excitation) of 100 nM doxorubicin introduced to DOPC/SM/CH bilayer spanned over 1 μm (PBS filled) gold microcavities. Data was offset for clarity. Measurement was focused on a single cavity pore (n ≥ 3, at RT)

3.3.4.2. Effect of Concentration on Ternary Composition.

The evolution of the Raman spectra of the ternary composition were evaluated at three drug concentrations, 0.1 mM, 50 μM and 100 nM, using the Raman bands previously described. Representative peak area data for doxorubicin is shown in Figure 66. Both drugs repeatedly showed similar responses across all concentrations, where initial increase in Raman peak area for the first 25 minutes is due to dispersal of the drug through the contacting solution and initial interaction of the drug with the bilayer. The peak area then decreases slightly and plateaus. There are no significant changes to intensity beyond approximately 30 minutes and this seems to suggest that the bilayer is not being permeated. This may be due to higher rigidity caused of the ternary composition. Meaning the increase in signal observed can be attributed to the drug dispersing throughout the confocal volume, which is expected due to the axial resolution. Notably, the peak area for the 0.1 mM drug was lower than that observed for 0.05 mM or 100 nM. The peak area suggests that at this concentration, the drug is less SERS enhanced, indicating that it is not penetrating the bilayer or reaching the cavity. This may be due to aggregation of the drugs, which has been noted at higher concentrations and is confirmed in the fluorescence studies in chapter 4[289,290]. Interestingly, daunorubicin shows the same dynamics as doxorubicin at all three concentrations.

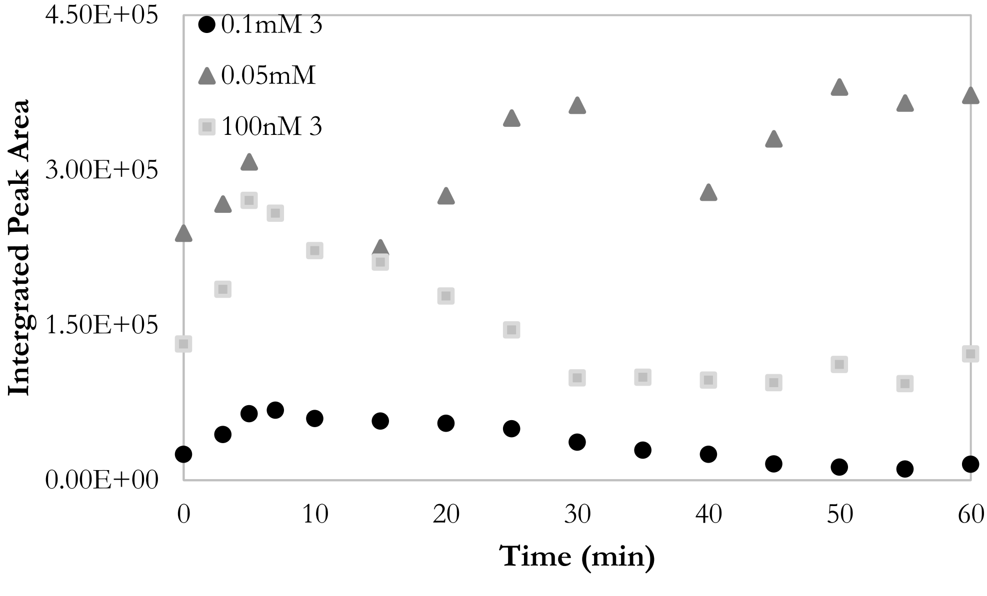

Figure 66: Peak area of the drug peak at 1636 cm^{-1} obtained at 785 nm excitation of DOPC/SM/CH bilayer spanned cavity array in 0.1 mM, 0.05 mM, and 100 nM doxorubicin. (n ≥ 3, at RT)

The peak area of the ternary composition was then compared to the DOPC composition to determine if composition has an influence on the dynamics. As the first 20-30 minutes is attributed to the drug dispersing through the solution, this was expected to remain the same. Following this, the change in peak area at 0.05 mM and 100 nM with both drugs, were very similar at both DOPC and ternary composition.

The peak area indicates that below a certain concentration, the composition of the bilayer does not affect the drug's interaction with the membrane. This may be due to the drug aggregating above a certain concentration[289] and therefore resulting in different kinetics. The data is consistent with a report by Alves et al. who showed through fluorescence quenching studies, that daunorubicin has a higher affinity for membranes composed of just PC over mixed compositions also containing SM and CH[273]. The difference between bilayers could be attributed to DOPC's higher fluidity, allowing for the drug to imbed itself easier into the membrane than in the ridged ternary composition.

3.3.5 Planar Vs Cavity Gold

Permeation studies were then attempted on bilayer spanned planar gold substrates to determine the difference in the enhancement between planar and cavity substrates. From the simulations completed in chapter 2, a small amount of enhancement should be expected from the top-surface of the substrate. However, as SERS is a distance-dependant method[132,260], it is unlikely for the bilayer to receive full enhancement from the cavity well, only enhancement from the top-surface and the edge of the cavity well. Nonetheless, due to the axial resolution of the system, focusing on the bilayer should ensure the bottom of the well in also sampled. Meaning signal from both should be observed.

Planar substrates proved challenging to obtain a lipid vibrational spectrum prior to drug introduction. Multiple repeats and substrates were attempted with both DOPC and DOPC/SM/CH bilayers. Figure 67 shows an example of experiments completed on both bilayers on cavity substrates and planar substrate, where little to no evidence of SERS of the bilayer was evident on planar substrates.

In contrast, cavity substrates showed clear, defined vibration bands. Both DOPC and ternary bilayer planar substrates Raman intensities appeared to be approximately an order of magnitude smaller than cavity samples. Due to the Raman bands on the planar sample being so weak, they appear to be overlayed by broad background vibration, making identification challenging and imprecise.

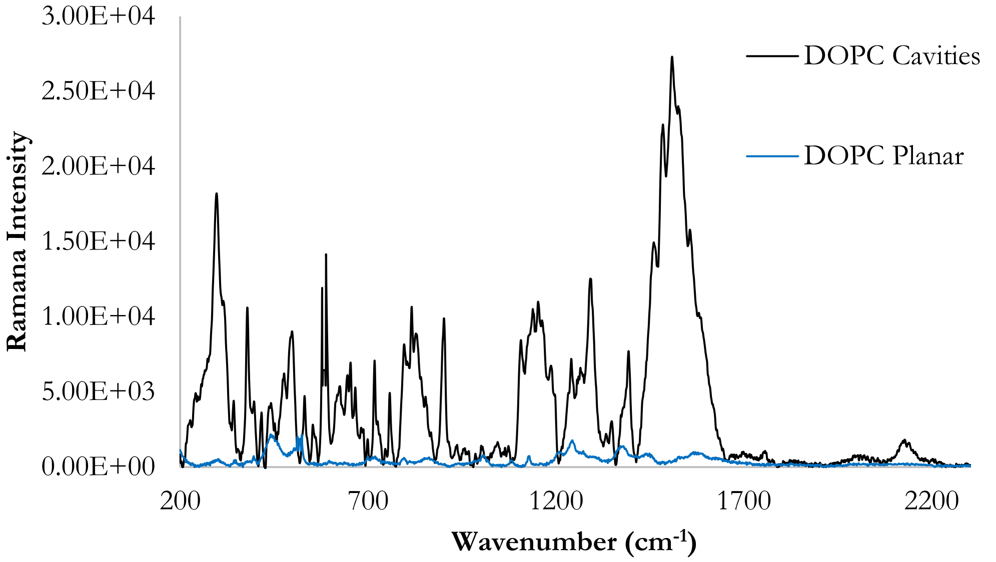

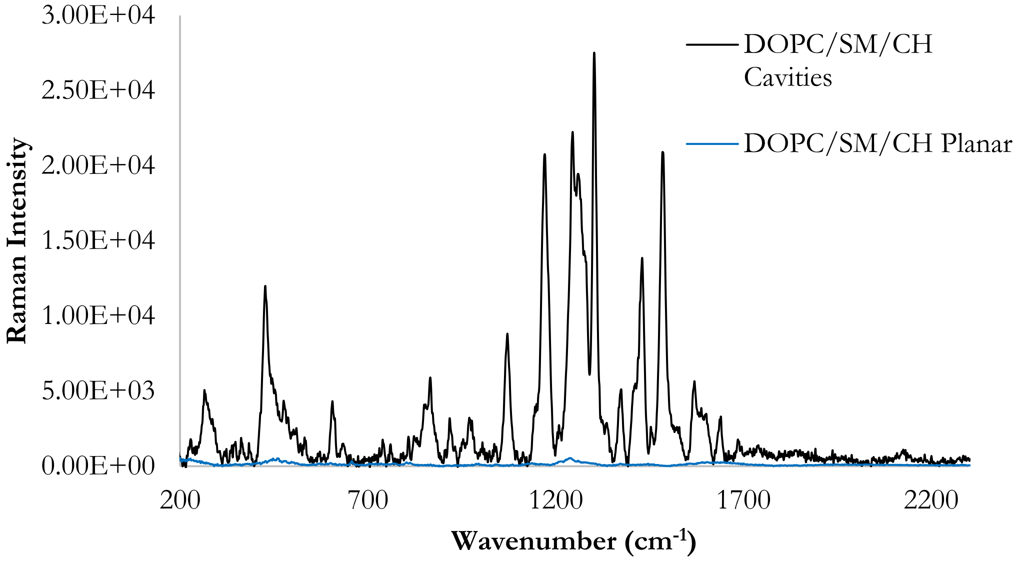

Figure 67: Raman Spectra of Planar gold substrates vs cavities with DOPC and DOPC/SM/CH bilayers in 2 ml of 0.1 mM daunorubicin. Excitation at 785 nm. (n ≥ 3, at RT)

Previous studies have shown enhancement factors of between 6-8 orders of magnitude for these cavity substrates[104]. The data shown is consistent with this and shows that they are highly suited to obtaining Raman spectra of true bilayers. The well resolved Raman signal of the bilayer at these substrates opens the possibility to deeply interrogate the bilayer structure and the molecular interactions. It should also be noted that previous studies through EIS and FLCS have shown that lipid diffusion over a single pore is highly biomimetic and has fluidity and lateral order more similar to cell membranes than what is seen on planar areas[21,102]. Bilayers across planar areas have shown tighter membrane packing resulting in reduced fluidity which can influence drug permeability. This is a further reason for focusing on a single pore in this study, as multi-pore measurements would include the planar regions found between the pores, which would be less analogous of a single cell membrane.

3.4 Conclusions

Determining drug permeability and optimising this process is vital in drug and cosmetic industries. Studies examining how drugs interact and permeate a lipid membrane provides critical information which helps minimise the volume of unsuitable drugs reaching expensive late-stage testing. Current methods are either not very biomimetic such as LogP[10] or PAMPA[9,12], or are time consuming, such as cell-based assays[11]. For these reasons, the development of a membrane permeability assay as a precursor step to cell work is of great interest, and through the use of SERS, a label-free, non-destructive method may be obtained. Within this chapter, the potential for using SERS as a method to detect membrane permeability was examined.

Herein, we demonstrated use of gold micro-cavities as SERS substrates for the support and evaluation of lipid bilayer and studied their interactions with representative membrane permeable drugs. Lipid bilayers were successfully spanned over these cavities and were found to remain stable for the duration of the experiment, corresponding with currently used methods[27]. Through the use of plasmonic enhancement, these bilayers could be detected by their Raman signatures and even the separate components within the membrane were identified and shown in Table 1. Where reported peaks[256] such as 548 (C=O deformation), 701 cm^{-1} (δCO_3) attributed to cholesterol, 723 and 1290 cm^{-1} attributed to sphingomyelin's asymmetrical stretching of $N^+(CH_3)_3$ and bending of C-O and C-O-H groups were seen. DOPC showed vibrational stretching of C=C at 1520, 1539, 1592 and 1616 cm^{-1}. Common bands to all three lipids were seen due to vibrational stretching of C=O and C-O-C (asymmetric).

The Raman signatures of the drugs alone were characterised (Table 2), and similar bands were found for both drugs, such as deformation of C=O at 444 and 445 cm^{-1} and deformation of CH_2 & CH_3 at 1402 and 1409 cm^{-1} for doxorubicin and daunorubicin respectively. The evolution of Raman signature in contact with the solution and unmodified cavity arrays was extracted, confirming that it takes approximately 30 minutes for the drug to completely diffuse throughout a 2 ml solution.

The drug was then introduced to a bilayer spanned cavity. From the obtained data, the results suggested that SERS was capable of identifying drug interaction and diffusion through a bilayer due to the spectral shifts and intensity changes. However, due to the variation of SERS enhancement substrate to substrate, intensity was not comparable from sample to sample. A focus for future work may be to address this limitation by generation of identical substrates to reduce sample-sample variations.

Due to the sensitivity of this method, subtle differences were observed between two similar drugs' interaction with the bilayer, with resolution as low as nanomolar concentrations, demonstrating an advantage over current, less biomimetic methods, such as PAMPA. However PAMPA provides quantitative information that this method still lacks[294]. Furthermore, differences were observed on ternary compositions, indicating that this method may be suitable for complex biomimetic compositions. When compared to planar gold studies, the cavity samples consistently revealed dramatically better defined and higher intensity vibrational bands than planar samples. Taken together, these advantages indicate that cavities developed during this work are effective as SERS substrates and suitable for future practices.

Through use of SERS, insight into doxorubicin and daunorubicin interaction with membranes was obtained. While the Raman intensity varied from sample to sample due to the nature of SERS substrates, reproducible well-defined spectra were obtained and showed both lipid and drug peaks and their changes over time. Despite the great care was taken to minimise variation, and though this method could provide valuable information into drug-membrane permeability, further improvements are recommended before development into an early stage testing method. Chapter 4 examines the use of MEF as a suitable method to detect membrane permeability and chapter 5 describes the development of an enclosed low volume cell to overcome some of the identified issues of this novel technique.

Chapter 4: Fluorescence Detection of Membrane Permeability

4.1 Introduction

Plasmonically active substrates can be exploited for the enhancement of fluorescence signals, as well as for SERS. Metal-enhanced fluorescence has been widely explored from the perspective of bio-diagnostic fields[167], imaging dyes[173], in assays[295], biosensing[296] and for nanoprobe application[297]. Although its application in quantitative sensing is still limited, likely for the same reason SERS has not been widely adopted[164]. Metal enhanced fluorescence on a reflecting substrate, can enhanced emission if it is in phase, or reduced if it is out of phase. This effect is known as super-radiance and sub-radiance, respectively. Angular emission is also enhanced at mirrored surfaces, which on average can result in a four-fold enhancement. The combination of these effects with plasmonic fields can induce a good degree of enhancement, allowing for a greater signal to be obtained[101]. Because of competing quenching processes, at the surface, as described in chapter 1, and also because reflectance/focussing plays a role, there is a trade off in MEF that means the intensity of fluorescence is maximised at a specific distance from the metal surface[275], typically 10 to 20 nm from the surface.

As described in chapter 2 and 3, lipid bilayers can be readily spanned over aqueous filled gold cavity surfaces[14102,208], creating a pore spanned bilayer model. The gold cavity arrays have been shown to provide significant MEF enhancement originating both from the optical effects of the cavity and plasmonic enhancement. Together, these techniques can provide a sensitive and novel means of detecting drug permeation of phospholipid bilayers of truly biomimetic compositions. As MEF is a distance dependant technique for enhancement to occur, traditional SLB's which only provide a small water layer, typically 1-2 nm between the lipid and gold surface would not be suitable. Therefore, the use of cavity substrates has a unique advantage as by the introduction of cavities, this distance is created and allows for metal enhancement. For these studies, gold was used over silver, due to its inert properties, biocompatibility and its higher success in fabrication of microcavity arrays.

In the previous study, lipid bilayer supported cavities were exploited for drug-permeability studies using SERS. In this study, analogous experiments were completed using MEF. Fluorescence has been commonly used for biophysical and biomedical applications due to its high sensitivity. Through quenching, resonance energy transfer and anisotropic decay, it can provide information on the fluorophores exposure to a solvent, donor-acceptors proximity and the internal dynamics and motions of membrane and proteins, respectively[169].

Therefore, fluorescence had been widely used for imaging, drug discovery, immunoassays, and many more.

Here, we investigate if the highly localised MEF, observed in the pore arrays reported to date, can be exploited to mark both if and when permeation of a fluorescent drugs arrival across a spanned lipid membrane. In this chapter, we initially again assemble pore spanning lipid bilayers, assess their stability and integrity, using a membrane-impermeable dye, DRAQ7, using fluorescence and then by comparing temporal changes to fluorescence intensity of this probe with the permeable fluorescent drugs doxorubicin and daunorubicin explored by SERS in chapter 3. The purpose is to understand if the profile of intensity changes observed between impermeable and permeable probes is distinguishable and thus to establish if MEF might form the basis for an assay of permeation.

DRAQ7 is an anthraquinone compound commonly used in cell imaging as it stains nuclei in dead or permeabilised cells[257]. It is known to emit in the far-red field but is also sub-optimally excited by 488 nm laser. It is commonly used to differentiate between live and dead cells due to its non-permeant properties with live cells[298]. The dye readily binds to nuclear DNA, but as it cannot penetrate the plasma membrane of living cells, it can be used as an indicator of membrane degradation. Also, DRAQ7 has no known influence on cell response, growth, etc[298]. Therefore, the detection of fluorescence emission from the cavities in the presence of the bilayer was not expected, meaning this could be used to indicate homogenous spanning of the bilayer.

Our studies examined the fluorescent intensity changes elicited from a permeable and impermeable drugs/drug analogues in contact with lipid bilayer models of two membrane composition: DOPC and DOPC/SM/CH (40/40/20 %) and compared the effects of bilayer supported at SLB and cavity array on signal evolution. There are additional challenges in applying MEF over SERS for detection of permeation/arrival time by plasmonic enhancement, in that because of the axial resolution of the detection volume, if the fluorophore is sufficiently fluorescent in blank buffer, it will contribute a continuous background to the fluorescence signal, which is not an issue in Raman because of the tremendous differences in amplification of SERS over Raman signal. Nonetheless, we demonstrate here, that, because of amplification of fluorescence signal, both when the drug binds to the membrane and when enhanced by MEF, a dynamic signal is measurable above background that enables distinction between permeable and non-permeable species.

4.2 Materials & Methods

Samples were prepared in the same manner as discussed in section 2.2 with the same deviations as discussed in section 3.2. A Horiba Raman/fluorescent microscope with a CCD detector was used for all MEF measurements as discussed in section 2.3.6. All experiments presented were performed at a minimum in triplicate. Any measurements in which it was evident, from EIS or fluorescence that the bilayer had not fully formed or had degraded, were discarded (<5%). Peak area limits were set at 640 - 840 nm for DRAQ7 and 520 - 750 nm for doxorubicin & daunorubicin. All MEF experiments focused on a single cavity pore.

4.2.1 Quenching Experiment

Microcavity array experiments were completed as described in section 2.2.8, on both bare and DOPC modified arrays with 0.1 mM doxorubicin. 0.25 M potassium iodide (Sigma) was introduced to the contacting solution and fluorescence measurements were taken every 5 minutes for 1 hour.

4.3 Results & Discussion

4.3.1 Metal Enhanced Fluorescence Spectroscopic Determination of Bilayer Stability

To confirm the integrity of the lipid bilayer assembled across the microcavity array and to ensure that it acts as a barrier to membrane impermeable species, control experiments were carried out by incubating the microcavity supported DOPC bilayer with DRAQ7. DRAQ7 is a widely used membrane impermeable marker of cell death[257,298], as it is impermeable to intact membranes permeating only after membrane integrity is lost, as mentioned in section 4.1.

0.75 μM DRAQ7 was introduced to the contacting solution (aqueous PBS buffer, pH 7.4) at the distal interface of the lipid bilayer supported cavity array and, in parallel as a control, an analogous experiment was carried out at an aqueous filled cavity array in the absence of a bilayer. Fluorescence spectra under 633 nm excitation were collected focussing on a single pore, were collected immediately upon the administration of the dye and then every 5 minutes over a two-hour period.

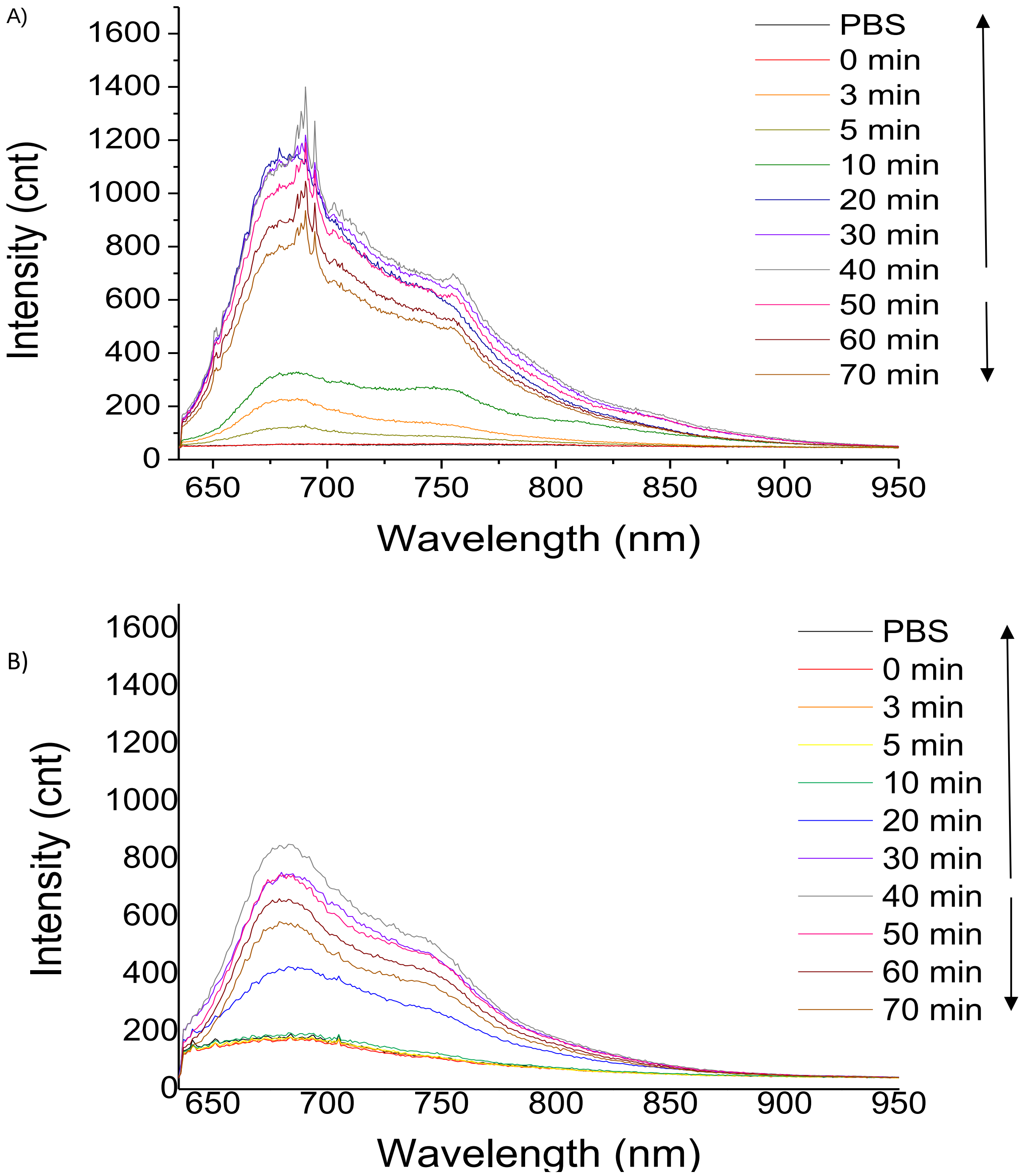

Figure 68: Time evolution of fluorescence spectra obtained during incubation of 0.75 µM of DRAQ7 with A) unmodified bare 1 µm cavities, and B) DOPC spanned lipid bilayer cavities at 633 nm excitation. Where PBS indicates no probe is introduced, and the following are spectra obtained within the first 5 minutes, followed by every 5 minutes for up to 70 minutes. Measurements was focused on a single cavity pore (n ≥ 3, at RT).

Figure 68 (A) shows that in the control, i.e. in the absence of bilayer, the fluorescence from the DRAQ7 evolves in intensity, peaking at 20 min. Notably, when the probe intensity peaks around 20 min, Raman vibrational bands emerge superimposed on the fluorescence spectra between 670 -720 nm. These were attributable to DRAQ7 at 435, 514 (stretching of the Si-O-Si), 1170 (CC stretching), 1240, 12881, 1318 (Bending of C-O, C-O-H, C-H), 1412, (deformation of $(CH_2)/\delta(CH_3)$, 1586 and 1650 cm^{-1} (C = C stretching). A Raman spectrum of DRAQ7 alone in solution was completed, (Figure 69) and was confirmed to have matching peaks to those observed superimposed on the fluorescence of the bare cavity sample. The fluorescence intensity stabilises between 25-30 minutes and intensity then decreases, attributed to some photobleaching of the probe due to extended irradiation.

DRAQ7 was added to 2 ml PBS solution in the sample chamber in the absence of gold to estimate the time for diffusive mixing to equilibrate within the sample chamber. This is shown in Figure 69 B. The fluorescence intensity evolution here followed a similar pattern as in the presence of cavities, with signal peaking and stabilizing from 20-30 min. As observed in the presence of the array, the fluorescence intensity decreased over extended measurement times, confirming this was likely to photobleaching from prolonged exposure of the laser.

From control experiments in presence of the array, but in the absence of a bilayer, it was evident that the gold cavities provided a significant degree of enhancement, as there was an 800 % increase in signal intensity in their presence. This indicated that the gold microcavities provide sufficient enhancement to enable observation of intensity changes associated with membrane permeation over the background from solution contained within the axial focus. As the simulations completed in chapter 2 indicate, a strong fluorescence enhancement was expected to be observable from the mid-bottom of the well when the drugs emission or absorption peaks lie within the red-to-NIR region, which was the case here. It has also been previously shown that it is possible to get up to 50-fold MEF enhancement from these cavities[104].

Based on the evidence of the data in chapter 2, the first 27 minutes of the fluorescence signal can be attributed to the diffusive mixing of the probe within the solution volume. Beyond this, any changes to intensity can be attributed to changes induced by membrane, when it is present and to metal enhanced fluorescence from arrival at the cavity. This conclusion is supported by the evidently enhanced Raman signal, attributed to surface enhanced resonance Raman (SERRS) arising from the same plasmonic enhancement as the fluorescence. As described, because of the 3 μm axial resolution of the microscope for fluorescence measurements, when focussing on the lipid membrane we are interrogating both solution above the cavity, as well as the cavity and bilayer. When focus is on the bilayer or slightly below it, about 50% of the confocal volume will be the contacting solution. However, contribution from this volume, once diffusive mixing is completed, is not expected to change, so any further increase in intensity can be attributed to the cavity enhancement (and changes induced by membrane when it is present).

When DRAQ7 was introduced to the contacting solution at a DOPC bilayer spanned cavity array (Figure 68 B), the evolution of the fluorescence was initially similar to bare cavities but peaked at around 10 min, but at an intensity that was approximately half of the final intensity of the bare cavity array. Crucially, no Raman vibrational bands were evident at any point throughout the temporal window. This result indicates that in the presence of the bilayer, the fluorescence was only weakly metal enhanced (as intensity was greater than solution alone) and that SERRS was not observed, indicating that the probe did not reach the cavity interior. Thus, we can conclude that the DOPC bilayer has formed, is intact and maintain its integrity throughout the experiment, acting as an impermeable barrier to the DRAQ7. After 40 min, as before, DRAQ7 fluorescence intensity was reduced, indicating some photodegradation. As the bilayer is about 5 nm thick, modest MEF enhancement of the drug in solution above the array is likely to arise from the top surface of the array.

To evaluate the integrity of a more complex lipid bilayer composition, the same experiments were then repeated at a ternary, domain forming lipid bilayer composition (DOPC/SM/CH, 40/40/20 %) spanned across the array. Here again, Figure 70 shows the emission increase upon administration of the dye to the 2 ml solution due to its diffusion into the solution volume. The final fluorescence intensity on the ternary spanned cavity arrays was an order of magnitude less than the final fluorescence intensity observed at unmodified cavity arrays. Therefore, the ternary bilayer was also confirmed to be fully formed, showing that this composition also forms an impermeable barrier to DRAQ7 at the cavity array.

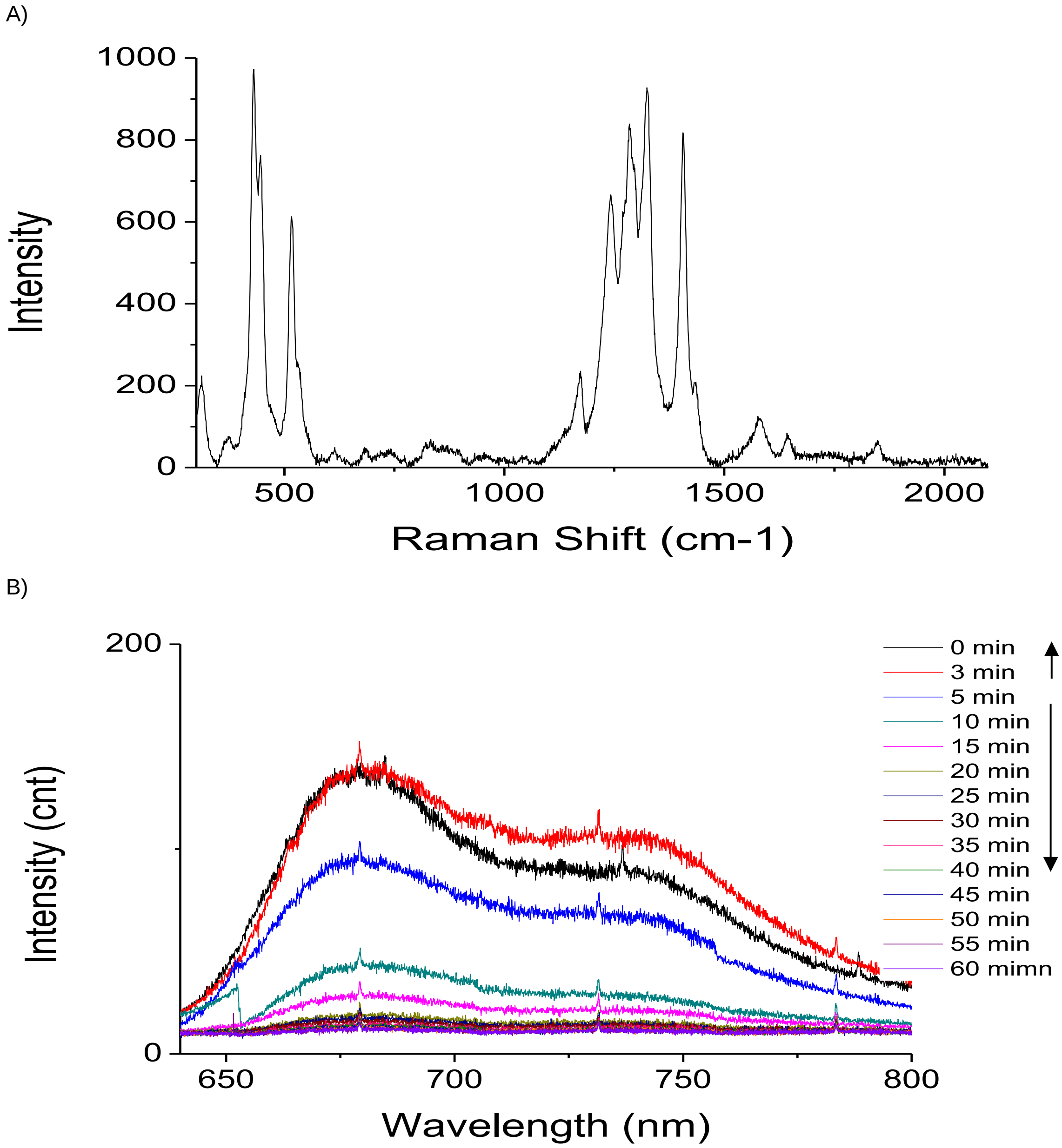

Figure 69: A) Raman spectrum of 10uM DRAQ7 on 1 µM gold cavities at 785 nm excitation. B) Time evolution of fluorescence spectra obtained after addition of 0.75 µM of DRAQ7 to 2 ml PBS buffer at 633 nm excitation. Where PBS indicates no probe is introduced and the following are spectra obtained within the first 5 minutes, followed by every 5 minutes for up to 60 minutes. Peaks seen at 680, 740 and 780 nm are artefacts due to the detector. (n ≥ 3, at RT)

The difference in emission intensity between the probe at DOPC and ternary compositions is interesting. The presence of cholesterol in membrane will be expected to thicken the membrane[299]. The change in thickness reported depends on composition and method of interrogation, but typically ranges from 0.5 to 1 nm. For example, Bleecker et al. reported that the difference in thickness between Lo and cholesterol enriched Lo phases is 1.69 nm via x-ray diffraction studies[300], which is one of the higher thickness differences reported. Nonetheless, we speculate that reduced emission intensity observed at the ternary membrane is due to the increase membrane thickness, which increases the distance between the probe and the top surface, eliminating any MEF seen for thinner DOPC membrane. The DRAQ7 experiments provide excellent evidence for the presence and integrity of the membrane, through the absence of MEF enhancement in the presence of the bilayer. It also shows good evidence that the proposed method provides sufficient enough signal enhancement that the interaction with the membrane and arrival in the cavity can be readily marked above the background contained within the axial focus of the microscope.

To evaluate the dynamic response, the integrated fluorescence peak area was plotted against time (Figure 71). Repeatedly, in all cases: bare, DOPC & DOPC/SM/CH bilayer cavities, an initial fluorescence increase was observed as the dye dispersed through the solution. Some photodegradation was observed in the bare and DOPC bilayer cavities. It was evident that no permeation occurred in the complex DOPC/SM/CH composition. As discussed above, no permeation occurred at the DOPC membrane (confirmed as the SERRS signal observed at bare cavity was not evident), but some MEF from the top surface occurs. It cannot be completely excluded that some of the signal comes from dye leakage at DOPC, given it is an unsaturated lipid, it is not as tightly packed as the ternary composition[69,76]. Nonetheless, the absence of SERRS and also from parallel studies in our group by Raman, suggest DOPC is also impermeable[301].

In summary, control experiments using an impermeable probe DRAQ7, confirmed the presence, integrity and stability over the experimental window over bilayer spanned microcavities of both DOPC and ternary composition membranes.

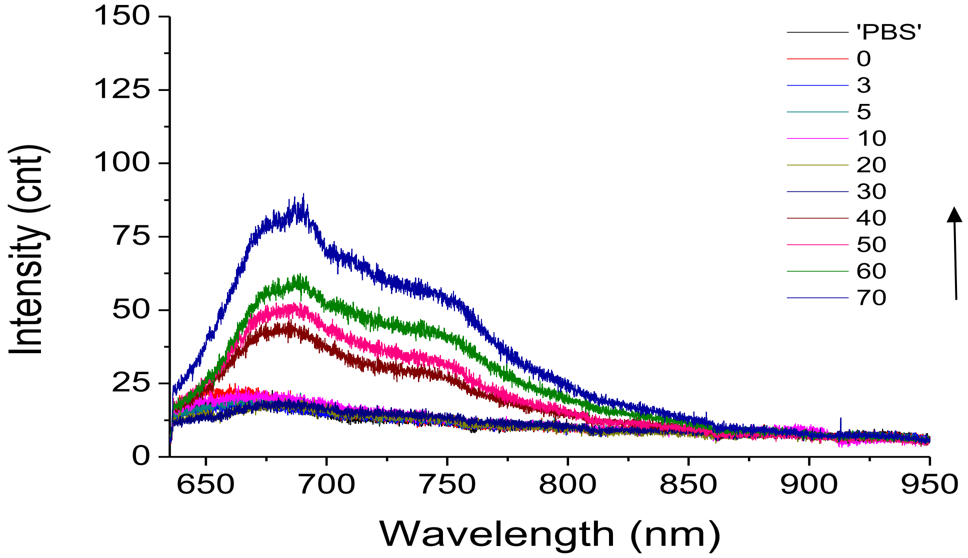

Figure 70: Time evolution of fluorescence spectra obtained during incubation of 0.75 µM of DRAQ7 with DOPC/SM/CH (40 %/40 %/20 %) spanned lipid bilayer cavities at 633 nm excitation. Where PBS indicates no probe is introduced and the following are spectra obtained within the first 5 minutes, followed by every 5 minutes for up to 70 minutes. Measurements was focused on a single cavity pore (n ≥ 3, at RT).

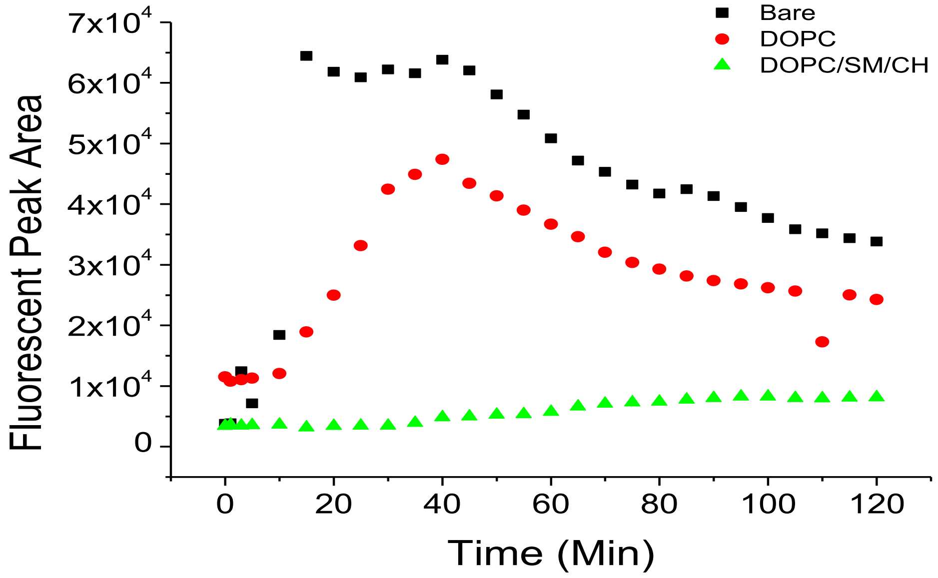

Figure 71: Integrated fluorescent peak area (peak limits 640-850 nm) at 675 nm obtained from 633 nm excitation fluorescence spectra from 1 µm bare cavity, DOPC bilayer and DOPC/SM/CH (40%/40 %/20 %) cavity array with 0.75 µM DRAQ7. (n ≥ 3, at RT,)

4.3.2 Investigation of Anthracycline - Membrane Interaction

4.3.2.1 Fluorescence Emission upon Drug Addition

Having established that the membrane was intact and presented a barrier to cavity entry, experiments were then carried out on membrane-permeable anthracycline drugs, doxorubicin and daunorubicin. These anticancer therapeutics are very similar in structure (Figure 26 in Chapter 1) and only differ where doxorubicin terminates with a primary alcohol and daunorubicin with a methyl group. Both drugs are thought to be passively permeable to the cell membrane and interact electrostatically with the bilayer and will embed itself at the polar head groups[41], where Daunorubicin tends to embed itself deeper than its counterpart Doxorubicin[41,84,259,272,302]. It should be noted that Doxorubicin and daunorubicin are both administered intravenously, however as they are vesicants[270], but can cause extensive tissues damage and blistering outside of the vein. Thus, alternative delivery methods, such as liposome encapsulation[43], have been explored which will change their delivery in vivo.

The fluorescence spectra of doxorubicin and daunorubicin in solution were shown in section 2.3.6. They exhibit fluorescence maxima at 600 nm, and a shoulder on the peak is centred around 640 nm. To evaluate the rate of diffusion, the cavity samples were sonicated in PBS buffer prior to measurement, to ensure cavities were filled and the drug was introduced to the contacting solution (2 ml volume). In all cases, over time, the emission intensity dramatically increased.

Figure 72 and Figure 73 shows the evolving fluorescent emission spectra of 0.1 mM daunorubicin and 0.1 mM doxorubicin respectively, following their introduction into the solution in contact with the array. The experiment was carried out at arrays, both with and without assembled lipid bilayers. Without a bilayer, as shown in Figure 72 A), the drug's fluorescence was observed to increase immediately upon drug addition. This intensity doubled at 5 minutes, then continued to increase until 30 minutes, where the intensity levels off. The initial jump in intensity, followed by a slower increase was attributed to diffusive mixing of the drug into the contact solution and entering the cavities unimpeded and reaching equilibrium.

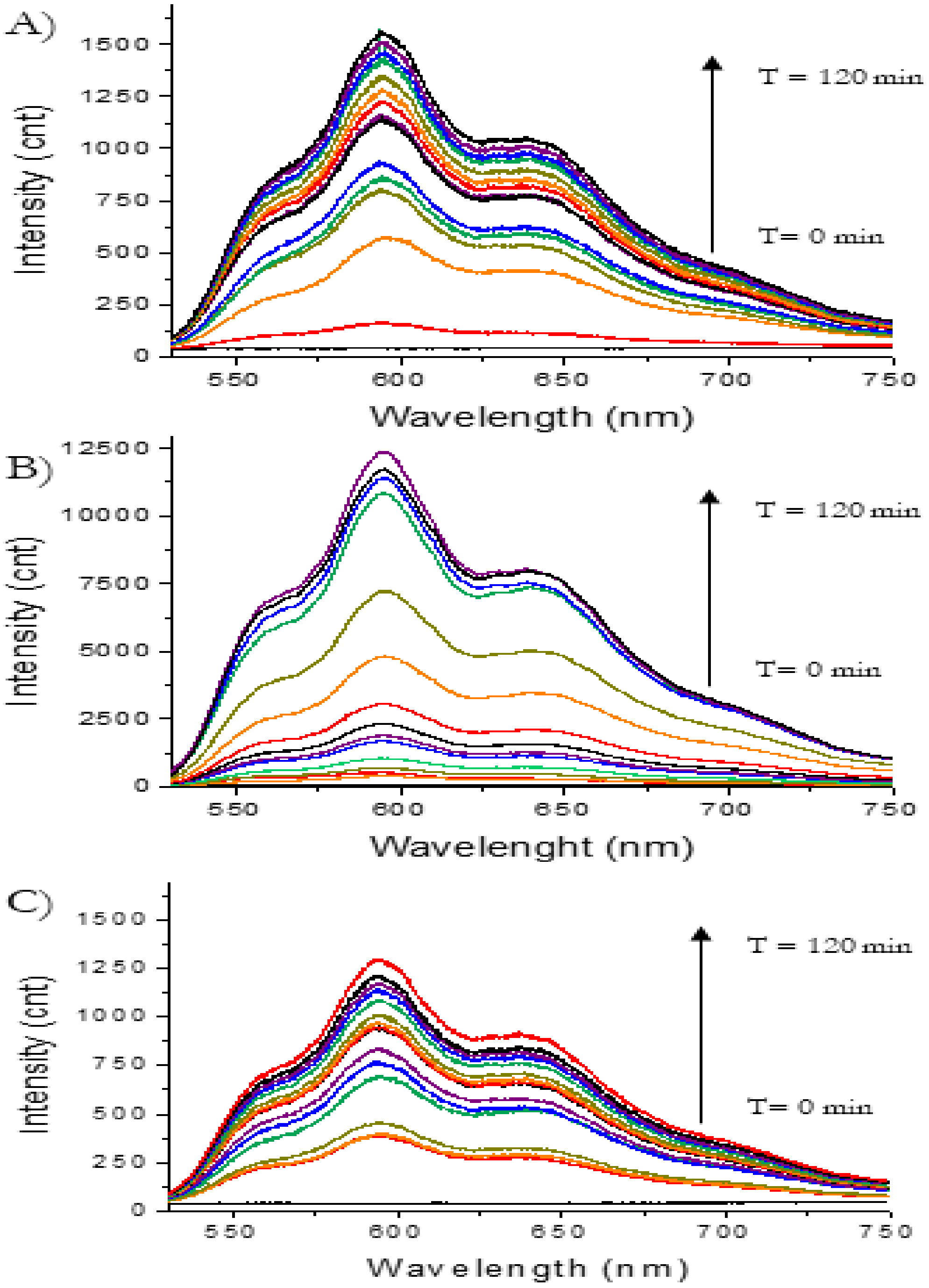

Figure 72: Time evolution of fluorescence spectra obtained when 0.1 mM Daunorubicin is introducted to A) 1 µm bare cavities, B) DOPC and C) DOPC/SM/CH spanned cavities at 473 nm excitation. Where PBS is prior to addition of drug, which is then followed by immediately after drug introduction and the following are spectra obtained every 5 minutes for up to two hours. Measurements was focused on a single cavity pore. (n ≥ 3, at RT)

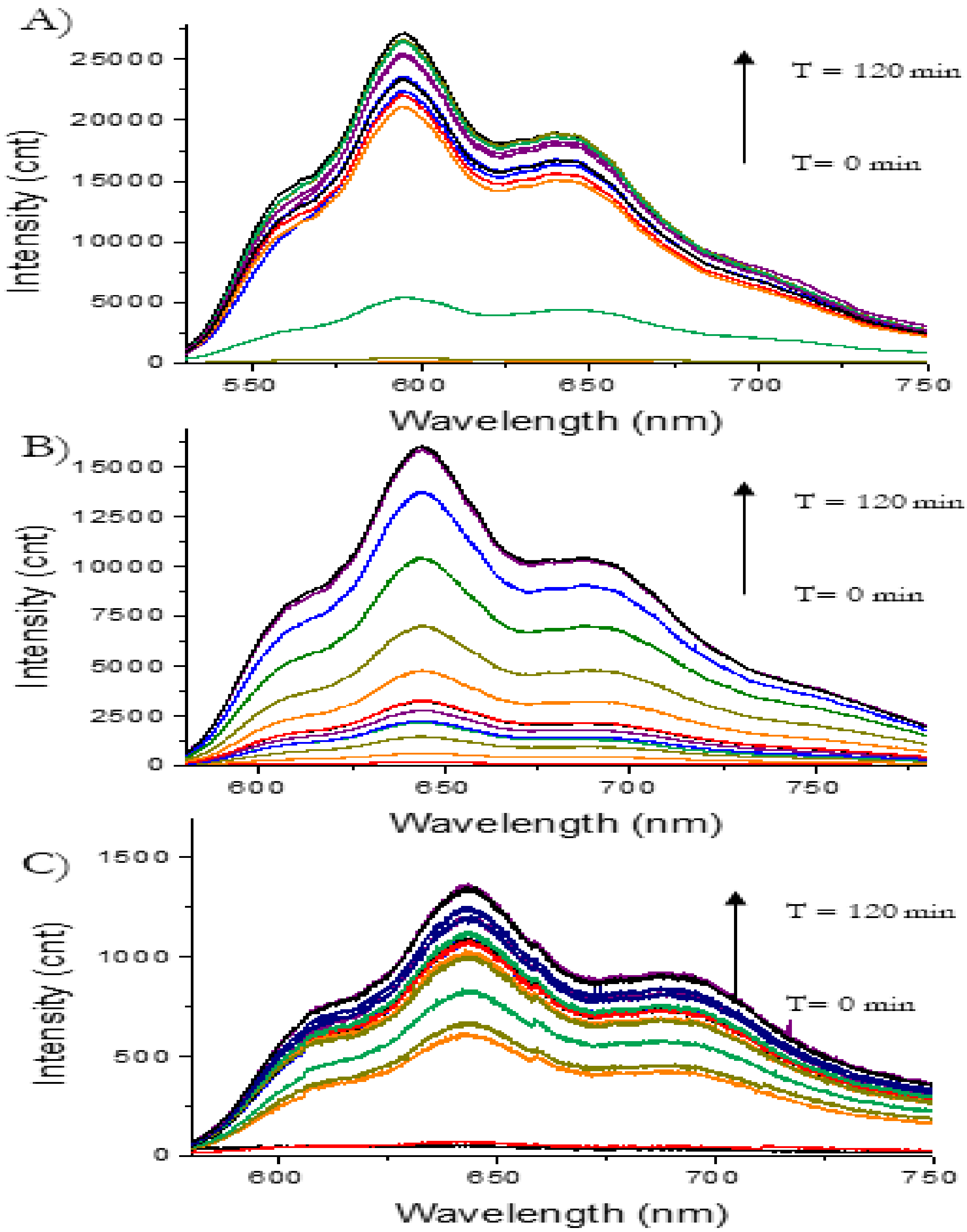

Figure 73: Time evolution of fluorescence spectra obtained when 0.1 mM Doxorubicin is introducted to A) 1 µm bare cavities, B) DOPC and C) DOPC/SM/CH spanned cavities at 473 nm excitation. Where PBS is prior to addition of drug, which is then followed by immediately after drug introduction and the following are spectra obtained every 5 minutes for up to two hours. Measurements was focused on a single cavity pore. (n ≥ 3, at RT)

At the DOPC bilayer modified arrays (Figure 72 & Figure 73 B), the initial increase in fluorescence intensity associated with diffusion through the contacting solution is as expected and is similar to arrays without bilayers, however between 25 to 60 minutes instead of signal plateauing as observed at the bare cavity array, a slow rise in intensity is seen, which is then followed by a dramatic increase in intensity until 95 minutes. Then, at approx. 105 minutes, the intensity stabilises. This behaviour, which is very different to the bare cavity array indicates that the bilayer is impeding the diffusion of the drug into the cavity. After 25 mins, the continued dynamic change to intensity is attributed to gradual increase in metal enhanced fluorescence as the drug lodges in the membrane and slowly crosses it. No evidence for self-quenching of drug is seen, however, due to the expected emission enhancement of the drugs in the bilayer[84], if it had occurred, it would be masked by the membrane emission enhancement.

Figure 72 (C) & Figure 73 (C) shows analogous experiment carried out at a ternary lipid composition, DOPC/SM/CH (4/4/2) for daunorubicin and doxorubicin respectively. The absolute fluorescence intensity for ternary lipid composition samples were very low in comparison to DOPC bilayer samples or even bare cavities. Although variation between substrates may influence the absolute emission intensity, repeatedly, the final fluorescence intensity was found to rarely reach the magnitude observed in DOPC samples. This observation indicates that the drug was much less permeable to ternary bilayer compositions. The tighter packing, greater thickness and lower charge of this SM and Chol containing membrane[31,250,303] likely both reduces drug-membrane association and permeation. Furthermore, the aggregation of the drug[289,290] which is expected to occur in solution at the mM concentration used in this experiment may impede binding diffusion of the drug, preventing it from fully diffusing through the bilayer and entering the cavity.

Our data is consistent with other studies on CH and SM containing bilayers and liposomes[43,303]. One study reported that the inclusion of CH into PC/PE liposomes in Hepes-buffer resulted in the reduction of thermal-induced drug leakage[43]. Another reported that regardless of other lipid ratios, the presence of CH in PC liposomes significantly decreased doxorubicin's release from the liposomes[303]. Daunorubicin has been shown to intercalate into ordered domains, where it decreases membrane fluidity, unless CH was present, where CH prevents this from occurring. It is thought that CH prevents daunorubicin from establishing electrostatic interactions with the phospholipid headgroups[273]. Cholesterol is well known to stabilise the bilayer, in turn decreasing fluidity[43,84,286,303,304], and permeability. It is interesting that such differences are readily discernible using the MEF approach here.

4.3.2.1.1 Spectral Shift

Both daunorubicin and doxorubicin are known to exhibit environmentally sensitive fluorescence. For example the association of doxorubicin with the bilayer causes an increase in fluorescence quantum yield[41] and a shift in λmax[41]. Therefore, it is of interest to examine any peak wavelengths changes during fluorescence evolution. Doxorubicin shows a broad fluorescent peak centred around 600 nm that exhibits shoulder peaks at 560, and 639 nm in water. The peak position at 600 nm remains quite constant over time, however, small shifts in the shoulders and their relative intensity were observed over time. As shown in Figure 74, the shoulder at 639 nm increased in relative intensity around 15 minutes, this then recovers and small increases were observed until 90 minutes, where no further changes were observed. The shoulder at 560 nm appeared to follow a similar pattern. These shifts occurred in both the presence and absence of the bilayer and therefore are not attributed to the lipids or the top surface modifications (polarity effect). Rather they are likely to arise from plasmon resonance effects[264]. Indicating that the drug reaches the cavity through the bilayer.

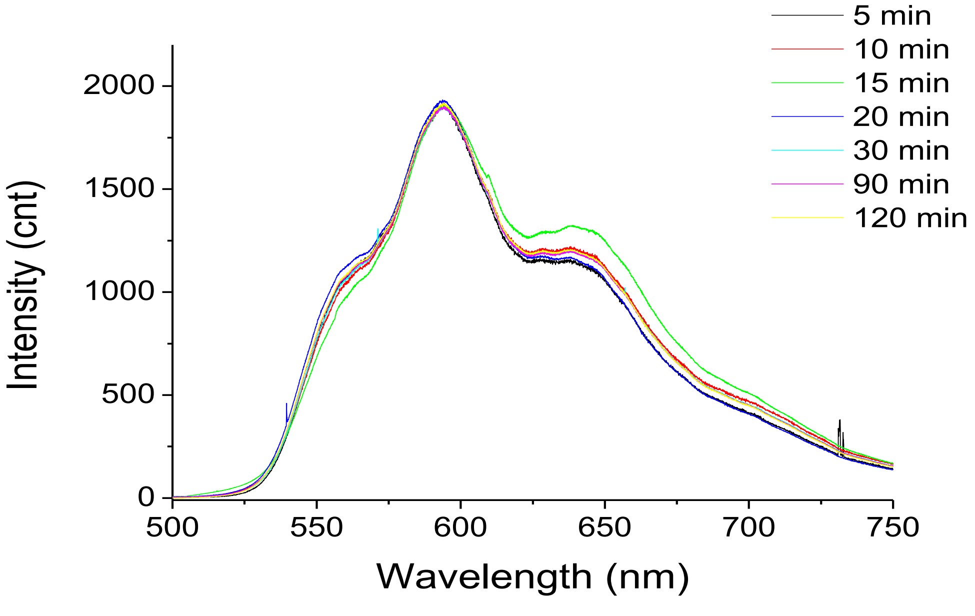

Figure 74: Time evolution of fluorescence spectra obtained for 0.1 mM Daunorubicin is introduced to a DOPC spanned lipid bilayer over 1 μm cavities. Spectra have been normalised and overlayed for clarity. Measurements was focused on a single cavity pore. (n ≥ 3, at RT)

4.3.2.2 Fluorescence Emission Dynamics of Bare and DOPC Microcavities

To evaluate the dynamic response, the integrated fluorescence peak area was plotted against time for drug diffusion at unmodified and bilayer modified cavities. As the earlier data showed, clear distinctions in the dynamics of fluorescence change were evident between the unmodified and bilayer modified cavities. Note, although the absolute intensity may vary from sample to sample, the dynamic response was found to be fairly reproducible between replicate measurements.

Based on the diffusive mixing experiment described in chapter 2 and the DRAQ7 fluorescence experiment, it is expected to take approximately 27 minutes for the drugs to fully diffusively mix through 2mL solution. In all of the measurements in this chapter, using the 2 ml sample chamber, the first 20-30 min can be attributed to the diffusive mixing of the drug and contacting solution. And, any subsequent change can be attributed to interaction with the bilayer or diffusion into the array.

As shown in Figure 75, consistent with the diffusive mixing controls at unmodified cavity arrays, the evolution of the fluorescence from the drug takes 20 minutes to stabilise. The final intensity is at least an order of magnitude higher than for the associated solution in the absence of the cavities and this is attributed to the drug reaching the cavity interior and experiencing MEF. Given that the cavities are 0.5 μm deep, it is not expected that the diffusive mixing that includes the cavities would take noticeable longer than without, as the additional volume the drug has to traverse is so small. Nonetheless the fact that the exterior solution and cavity solution (the cavities are prefilled with blank solution) equilibrate within the mixing window indicates that there is no impediment to their filling under these conditions. This is not surprising given the open nature of apertures and high % area of the array that is open compared to top surface.

In contrast to bare substrates, at DOPC or ternary bilayer composition cavities, the fluorescence intensity continues to evolve after the 30 min diffusive mixing window and equilibrium is delayed. This is clear evidence that the bilayer is in place and presents a barrier to cavity access. Figure 76 and Figure 81 show a clear distinction in the kinetics occurs post drug diffusion through the contacting solution. Figure 77 shows that depending on the concentration of the drug, the dynamic profile changes at DOPC. At higher concentrations of drug ($\geq$0.1 mM) at DOPC bilayers there were three dynamic region observed which are discussed in detail below. Similar results were seen with both drugs.

It is also of interest to note, that although the drug diffusion experiments in Figure 76 were repeated in identical format, including production of the substrate through to bilayer formation etc., some variation can be observed. Sample 3 was completed a week later than 1 & 2 and while the trend in intensity change is followed, after 85 mins, a shallower rate of peak area increase was observed. As per SERS, absolute reproduction of cavity internal nanostructure is difficult to control, and this will have knock-on effects for emission enhancement observed. Both because the electric field may vary but also if a cavity is for example misshapen, reflectance will change. Although these parameters are difficult to control using lithography, as in these measurements we are concerned with kinetic profile and not the relative intensity changes as they are not crucial to identifying if membrane permeation is occurring but does make any potential quantitative measure e.g. concentration unsuitable by this approach.

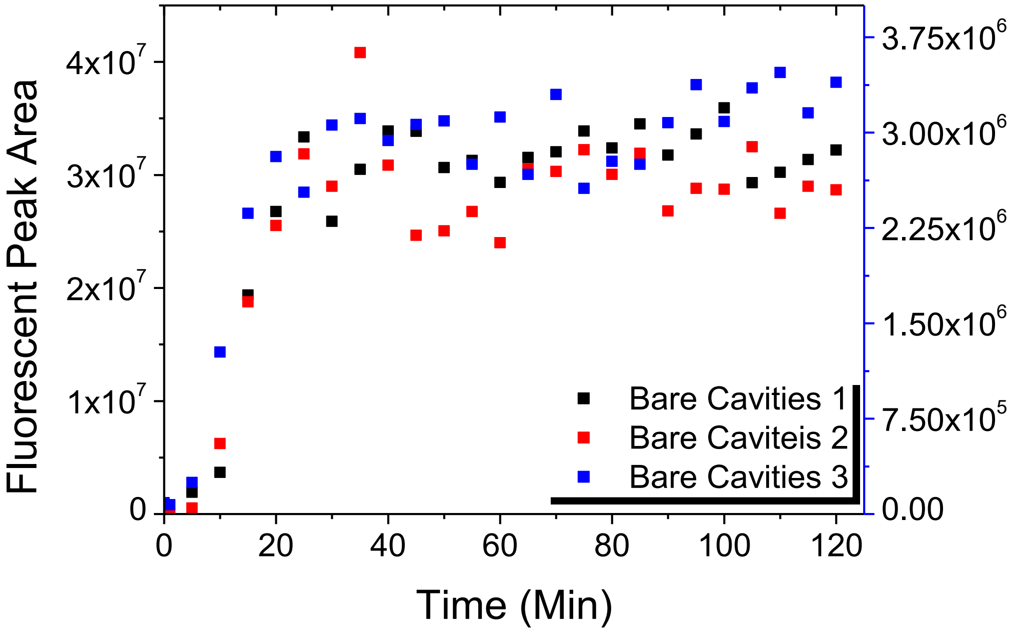

Figure 75: 0.1 mM Doxorubicin: dynamic changes to integrated fluorescent peak area obtained under 473 nm excitation for 1 µm bare unmodified gold cavity array. Sample 3 is set on a secondary axis for clarity due to lower intensity obtained from sample. (peak limits set as 520 - 750 nm)

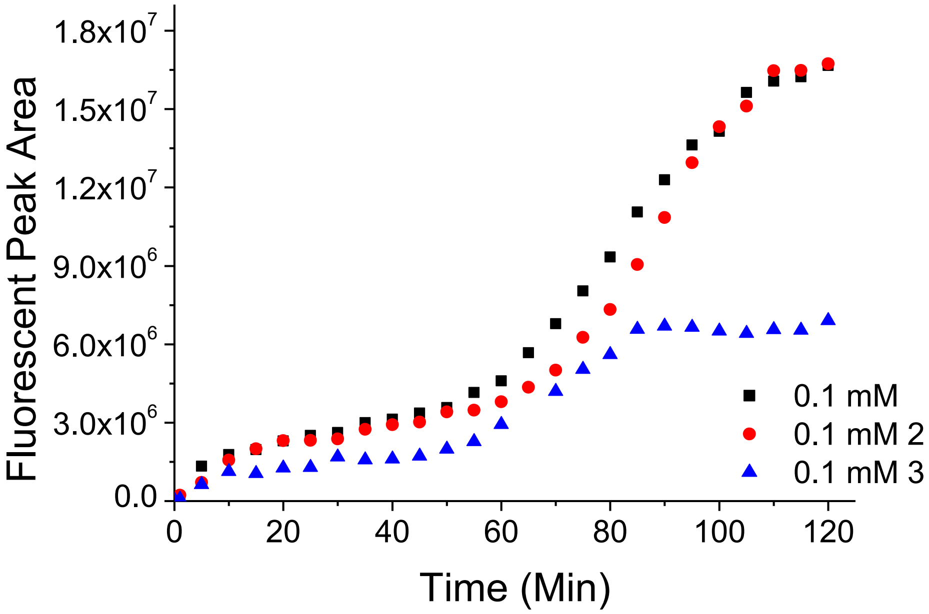

Figure 76: 0.1 mM Doxorubicin: dynamic changes to integrated fluorescent peak area obtained under 473 nm excitation for DOPC lipid bilayer spanned over 1 µm gold cavity array. (peak limits set as 520 - 750 nm)

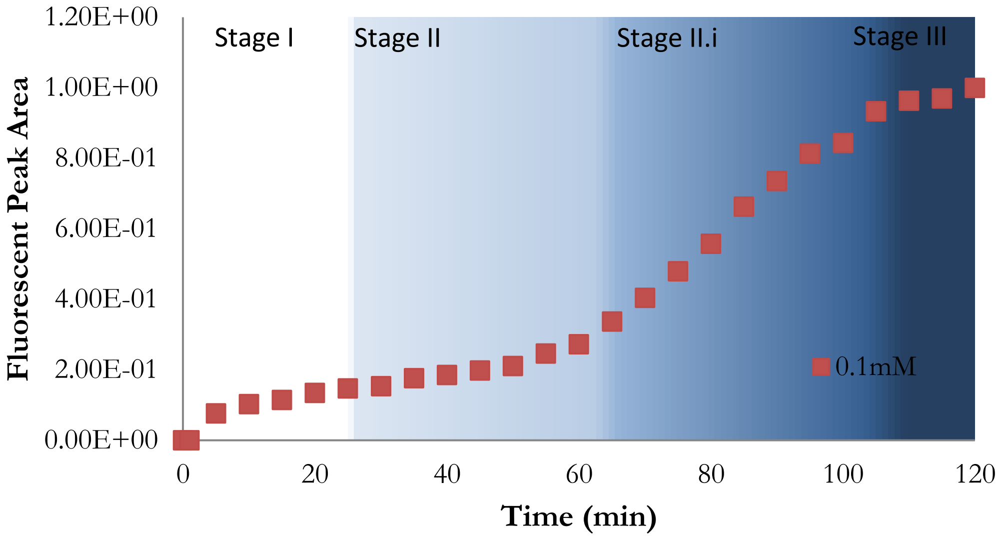

Figure 77: Normalised data from 0.1 mM Doxorubicin diffusion of DOPC spanned 1 µM cavities at 473 nm excitation, with each phase of diffusion noted. Section I: the time taken for the drug to diffuse across the solution. Section II: the time taken for the drug to reach and reside within the bilayer. Section II.i: the drug diffuses into the cavity resulting in an increase in enhancement, and Section III: equilibrium of drug concentration across the solution, membrane and cavity has been reached. Data was normalised for clarity.

For 0.1 mM doxorubicin, evolution of the spectral intensity show distinctive stages compared to cavity array without the membrane. As shown in Figure 77, diffusive mixing (Stage I) is followed by an increase in fluorescence (Stage II), attributed to bilayer residence and cavity residence. At higher concentrations, nominally greater than 0.1 mM, the signal evolution shows a distinction between bilayer and cavity residence, and the latter is assigned as Stage II.i. Equilibrium is then reached, evident by plateau in peak area (Stage III).

Stage II was tentatively attributed to the slow kinetics associated with permeation of the drug through the bilayer, i.e. reflecting the drugs residential time in the bilayer. In the presence of the bilayer, both interaction with the bilayer and plasmonic enhancement are expected to contribute to intensity changes. Self-quenching can also be a possibility. However, it has been shown that these drugs can exhibit up to a 20 fold increase in fluorescence intensity[259] when they are imbedded in the bilayer, suggesting self-quenching should not have a large impact. A study by Gallois et al. looked at 10 different ratios of PC/phasphatidic acid/CH bilayers and found that the hydrophobicity of the molecule effected its ability to penetrate the bilayer, more so than bilayer composition[259]. Furthermore, doxorubicin has been shown to aggregate at higher concentrations and in the presence of certain ions, such as phosphate, citrate and sulphate[290289]. It was also found that in the presence of a phosphate buffer, doxorubicin forms fibrillar aggregates. The aggregation is thought to occur due to the anions in the buffer bridging the drug molecules, which then stack through π-π interactions[290]. In the presence of a bilayer, an increase in fluorescence was observed, suggesting the drug aggregated along the bilayer[84], preventing or impeding permeation.

In Stage II.i, a large fluorescence intensity increase was observed at high concentrations (0.1 mM), which is attributed to cavity enhancement (note drug-membrane associated enhancement is also a large contributor to the overall emission here). As doxorubicin has relative lipophilicity of – 1.67 and daunorubicin of 0[41] , they were both likely to remain substantially within the bilayer, suggesting enhancement is due to both the drug residing in the bilayer and in the cavity.

Final equilibrium is reached (Stage III), evident as plateauing of emission intensity was eventually reached approx. 100 minutes after administration of the drug. At this point, the drug was presumed to be distributed across the contacting solution, bilayer and cavity. The experiments were very reproducible in terms of the kinetics of diffusion; however, the absolute fluorescence enhancement varies with substrate. This was expected as the enhancement depends critically on internal cavity architecture which is difficult to control in templating.

4.3.2.2.1 Examination of Equilibrium Dynamics

To confirm that the plateau at approx. 100 minutes was the final equilibrium, an extended experiment over a 5-hour window was investigated to ensure no further changes occurred. Experimental parameters identical to previous experiments where 0.1 mM daunorubicin, were applied, only time was extended. As shown in Figure 78, it was found that after 120 minutes, regardless of sample type i.e. bare, planar, bilayer, (6-mercapto-1-hexanol (C6) excluded), equilibrium had been reached and no further changes occurred. This was evident as when both samples reached equilibrium, they maintained their peak area, with a Standard deviation of ±0.052 for bare and ±0.056 for bilayer samples.

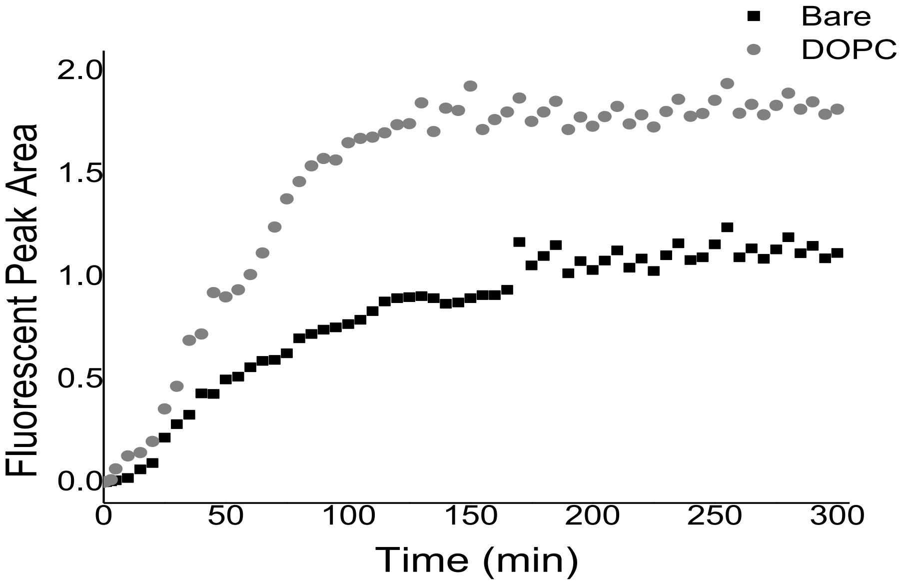

Figure 78: Normalised peak area at 600 nm Fluorescence spectra obtained from Bare and DOPC lipid bilayer spanned over 1 μm gold cavity array with 0.1 mM Daunorubicin in an extended five-hour study. (n ≥ 3, at RT) (peak limits set as 520 - 750 nm)

It is known that MEF is distance dependant but typically is at maximum between 8 - 10 nm from the metal surface[275]. This is due to competition between enhancement from the local field and energy transfer to the metal surface resulting in a loss of excitation. Due to the hemispherical shape of the cavities, once the drug had reached the cavity it should receive metal enhancement that has been concentrated into the centre of the cavity (as seen in the simulations completed in section 2.3.3). This is consistent with our observations as there was a dramatic increase in fluorescence once the drug had diffused through the bilayer into the cavity. Notwithstanding the fact that emission intensity is expected to increase when the drug intercalates into the bilayer, the difference in final intensity between the permeable DOPC and impermeable ternary bilayer indicates that significant enhancement is observed due to MEF at the cavity.

4.3.2.2.2 Investigation of contribution of Top-Surface Enhancement to signal

Interestingly, it was noted that the C6 layer that is used as an interfacial bilayer support at the top surface of the cavity array inhibited plasmonic enhancement when it was applied to the cavity interior. When samples were modified with 6-mercapto-1-hexanol on both the top surface and within the cavity, a much lower fluorescence intensity compared to only top-surface modified cavities was observed (Figure 79). This was true for both bilayer samples and non-bilayer samples. This observation indicates that in measurements under our usual conditions i.e. only top surface modified, only modest enhancement is occurring from the top surface and the bulk of enhancement can be attributed to bilayer binding/preconcentration & cavity enhancement.

When a DOPC bilayer was spanned over cavities, that were modified on both the top surface and within the cavities, an order of magnitude increase in intensity was observed. However, this increase in intensity was approximately 23% lower than DOPC cavities with only the top layer modified. This suggests in measurements under regular conditions i.e. only top surface modified by C6, very little enhancement occurs due to the top surface and the increase in intensity can be attributed to bilayer & cavity enhancement and the preconcentration of the drug within the bilayer. This agrees with simulations previously mentioned.

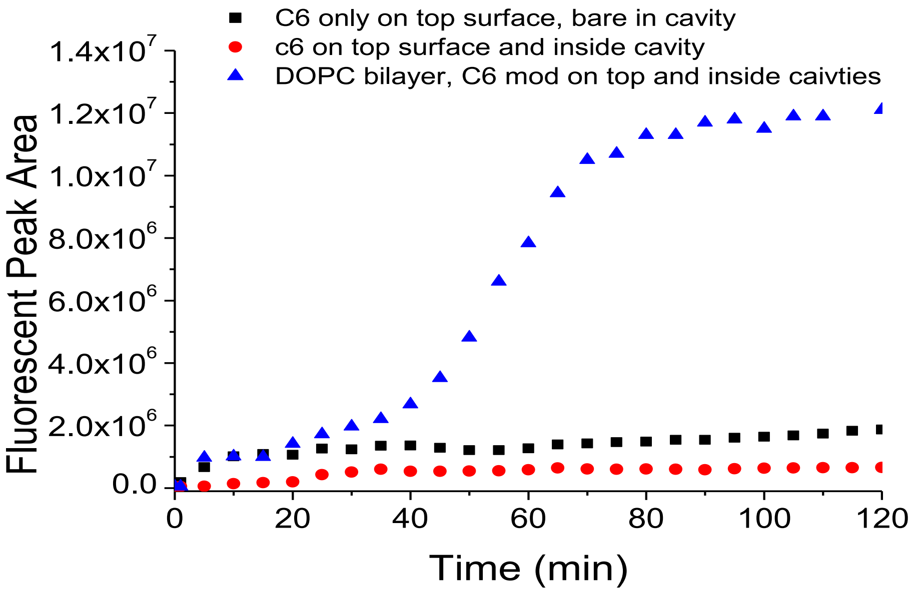

Figure 79: Spectra of integrated fluorescent peak area at 600 nm when excited at 473 nm. 0.1 mM Doxorubicin added to 1 µm cavities and monitored over 120 minutes. All cavities contained C6 modified top surface. Two samples also had the inner surface of the cavity modified with C6. Only one sample contained a bilayer. Faster rate of equilibrium observed across samples with both top surface and inner cavity modified. (n ≥ 3, at RT)

4.3.2.2.3 Investigation on Cavity Enhancement

A control was carried out (under the same conditions as previous experiments), to evaluate the contribution to fluorescence enhancement that arises from drug capture at the bilayer, as within the focal volume, contributions from the contacting solution, bilayer and cavity are combined. This is of interest, as, as described above, bilayer association is known to significantly increase quantum yield for doxorubicin and daunorubicin[84].

To gain some insight into this, potassium iodide was introduced to the bilayer spanned cavity array after the drug emission had equilibrated. KI was used, as it is a quencher that is impermeable to the membrane, i.e. it is not expected to reach the cavity but has shown to penetrate into the hydrophobic region within a bilayer[305]. KI has a complicated quenching mechanism, thought to involve both heavy atom effects and electron & energy transfer mechanisms[306], which will have different distance dependences and combined with its penetration into the bilayer, is expected to quench the probe in the contacting solution and in the bilayer, but it should not quench drug emission from within the cavity. Thus, enabling us to make an estimate of what contribution the drug within the cavity has to the overall emission intensity.

To achieve this, 0.25 M KI was introduced to 0.1 mM doxorubicin incubated bare and DOPC spanned 1 μM cavities after equilibrium had been reached. In cavity arrays without bilayers, the fluorescence intensity decreased on addition of KI by 87.5%. Indicating quenching had occurred for the free solution. In DOPC modified arrays, the fluorescence intensity decreased by 70% upon KI addition. In other words, nearly a 90 % decrease in intensity was observed when the bilayer was absent, but less than 70 % when the bilayer was present.

This result indicates, 1) a successfully spanned bilayer had formed, as not all drug was accessed by the KI. 2) that about 20% of emission intensity is attributed to drug enhanced by MEF (i.e. within the cavity). It indicates, consistent with previous reports on the effects of bilayer on fluorescence intensity of doxorubicin and daunorubicin, that significant portion of the intensity enhancement observed, is attributed to bilayer binding. However, it is important to remember that the cavity is small compared to the interrogation volume (where cavity volume is approximately 0.26 x 10^{-22} m^3), and so, this result indicates substantial MEF is occurring. Furthermore, this effect is specific to doxorubicin and daunorubicin drugs, as their emission is explicitly enhanced by the bilayer. The result indicates that in the present case, monitoring for drug arrival is feasible from MEF and should more effective in molecular species whose emission is not so strongly impacted by the bilayer.

4.3.2.2.4 Concentration Dependence on Dynamics of Uptake

Typically, the therapeutic plasma concentrations of anthracyclines lie in the nanomolar range. To ensure we were working within physiologically meaningful concentrations, the concentration range from 2 nM to 0.1 mM was examined, which spans administered concentration at site of injection to plasma levels. The sensitivity of the assay is expected to depend on the fluorescence quantum yield of the analyte and its enhancement under the conditions used. One of the reasons these drugs were selected is that their quantum yields are relatively modest. The quantum yield of doxorubicin has been reported as 9 %[185]. MEF works best for compounds of relatively low or modest fluorescence intensity[157]. For both doxorubicin and daunorubicin nanomolar concentrations of the probe were readily detectable by fluorescence at the array. To understand if signal showed a systematic metal enhanced response to concentration, a calibration curve was completed, but although systematic changes were evident, the response was not appropriate for quantitative studies due to the fluctuations in absolute intensity, again this can be attributed to challenges in reproducibly controlling nanostructures within the cavities.

Permeation of doxorubicin and daunorubicin as a function of concentration was examined at both DOPC and ternary DOPC/SM/CH (40 %/40 %/20 %) (shown in section 4.3.2.3.1) bilayer compositions across mM, µM and nM concentrations. For both drugs, concentrations below 0.1 mM fluorescence profile and permeation kinetics followed a similar behaviour at all concentrations examined, though permeation rate was slower for the lower concentrations. At 0.1 mM, the fluorescence profile change can be attributed to permeation of the aggregated drug.

The rate of uptake (Figure 80) at 2 nM of both drugs at a DOPC bilayer followed a similar trend to those at 100 nM concentration, where both showed the initial increase, followed by a small steady increase in fluorescence. However, at 2 nM, a distinction was observable, this was due to lower reproducibility at such low drug concentrations, as we are close to the detection limit.

The behaviour at low concentrations is consistent with a study completed by Heywang et al. Their study was completed with pirarubicin, another drug from the anthracycline family that is similar to those used in this study. It was shown, that on silver substrates, at low concentrations (0.4 µM), the anthraquinone was perpendicular or tilted on the substrate i.e. Parallel to the phospholipid chains, meaning at low concentrations it stayed imbedded in the bilayer[84], which corroborates with what had been observed at 2 nM concentration where only fluctuations of the drug being in the bilayer was observed, never actually entering into the cavity. At higher concentrations (2 µM), they found that the pirarubicin would go completely out of the bilayer and orientate along the silver so that it would remain in contact with the polar headgroups of the lipid[84]. In the cavity substrates, at low concentrations such as 100 nM, the initial intensity increase due to the drug entering the bilayer is observed, however the additional increase due to cavity enhancement was not seen. This suggests the drug is not entering the plasmonic well located at the bottom of the cavity. Which would be the case if the drug is localised close to the bilayer.

At higher concentrations, the rate of uptake is reproducible across replicate measurements, 2 nM however, showed fluctuations in the emission. The aggregation of the drug and residence of the drug in the bilayer may have caused the fluctuations observed in fluorescence intensity at 2 nM, or it may be that we are at the limit of our detection window. In either case, 2 nM proved unreliable and higher concentrations were more closely examined. Other detection modalities based on fluorescence or electrochemistry of anthracyclines in plasma or serum samples have yielded 1-2 nM as their LOD for anthracyclines[1]. For the experiments herein, 100 nM was taken as the lowest concentration for accurate detection of the drug-membrane dynamics.

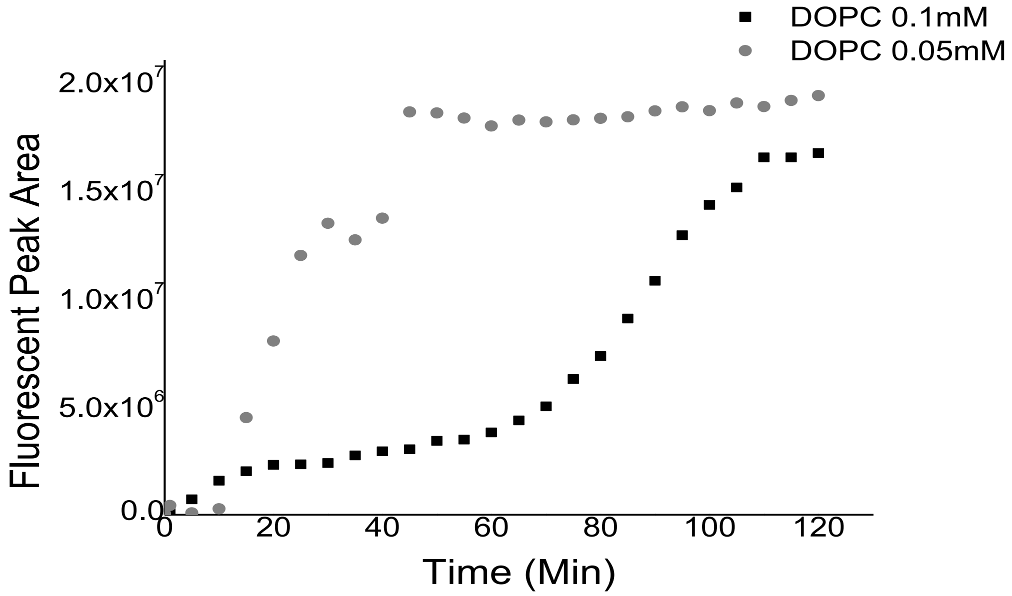

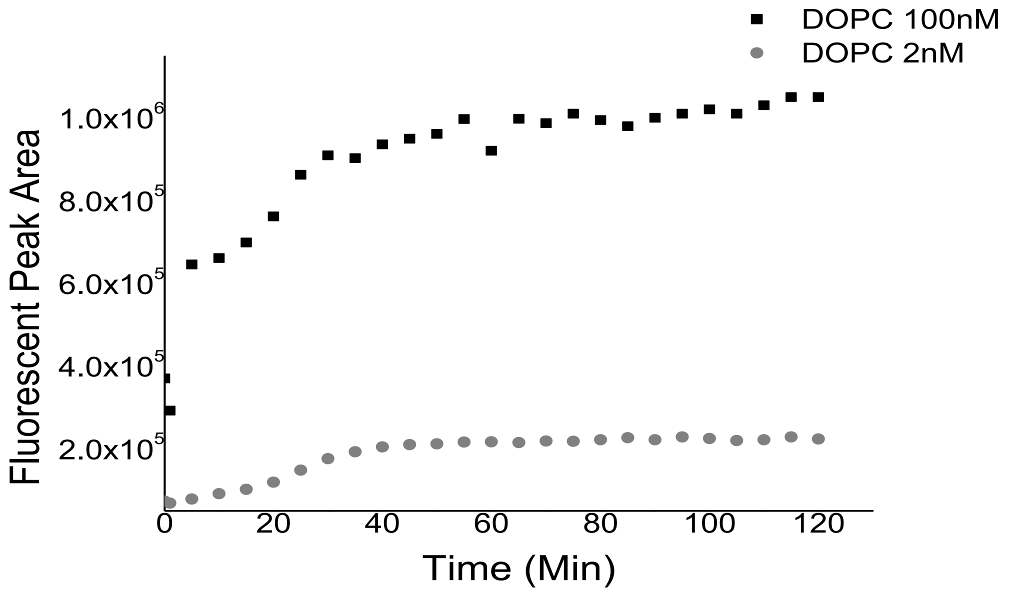

Figure 80: Integrated fluorescent peak area of Daunorubicin excited at 473 nm measured at 0.1 mM, 0.05 mM, 100 nM & 2nM on DOPC Bilayers spanned over 1 μm gold cavities. Where 2 nM is shows a different kinetic profile to higher concentrations and is taken to be the limit of analysis. (peak limits set as 520 - 750 nm)

4.3.2.3 Fluorescence Emission Dynamics of Ternary Bilayer Spanned Microcavities

For doxorubicin at the ternary bilayer composition, shown in Figure 81, the final fluorescence intensity was on average an order of magnitude lower than observed at the DOPC bilayer or at bare cavities. (notwithstanding variation in emission intensity due to variation in the pore as discussed above.)

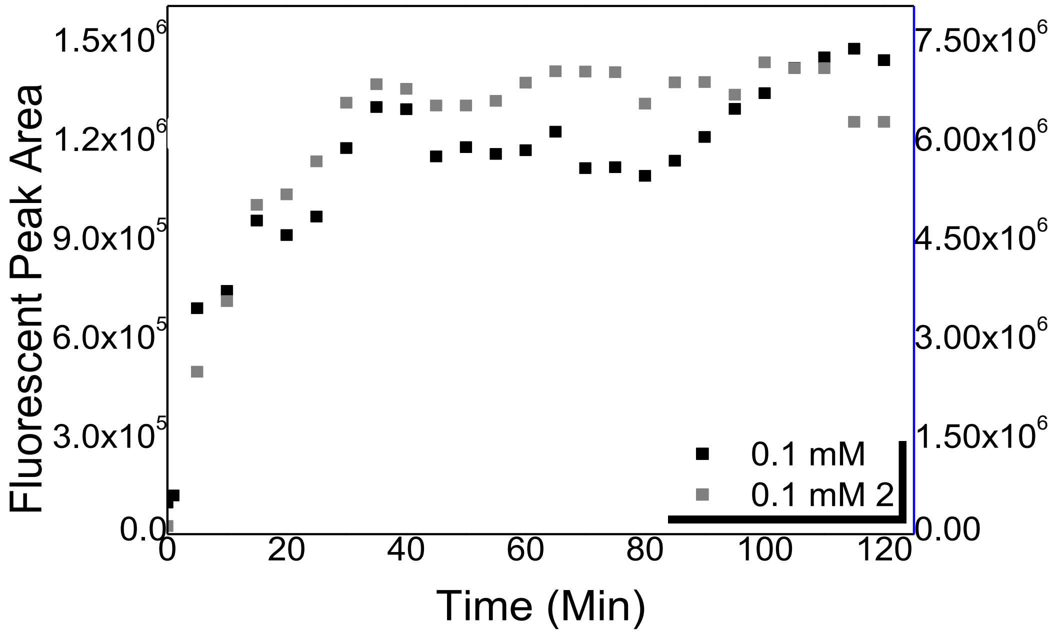

Figure 81: 0.1 mM Doxorubicin: Rate of change to integrated fluorescent peak area obtained under 473 nm excitation for DOPC/SM/CH lipid bilayer spanned over 1 µm gold cavity array. Sample 2 is placed on secondary axis for clarity. (peak limits set as 520 - 750 nm)

The rate of fluorescence evolution showed a progressive intensity increase during the first 25 minutes post drug administration, attributed to diffusive mixing into the contacting solution. This was followed by a reduced rate of fluorescence increase until equilibrium was reached at approximately 40 minutes. The shallow increase is attributed to the drug intercalating or adsorbing at the bilayer[84] but the intensity and final intensity was lower than expected on the basis of the MEF controls, and indicate that little of the drug reached the cavity interior. Similar to the DRAQ7 control experiment, it suggests that the penetration/intercalation of the drug into the bilayer is weaker than for DOPC. The data indicates poor permeation of doxorubicin through the ternary composition, again this is consistent with other reports on the effects of cholesterol on membrane association and permeability[304].

4.3.2.3.1 Concentration Dependence on Dynamics of Uptake

At nanomolar drug concentration, the ternary, domain forming[286,307] lipid composition behaviour was very similar to DOPC alone, although the final intensity was considerably lower. The integrated dynamics of fluorescence peak area also proved similar. Both drugs were considerably less permeable through the ternary composition than DOPC. Which, as described, is attributed to the lower admittance of this bilayer, due to its cholesterol/SM containing Lo phases.

To compare the dynamics of drug membrane interactions across different species, the slopes were obtained for Stage II for all concentration & Stage II.i, at 0.1 mM at both DOPC and DOPC/SM/CH bilayers. This is shown in Table 3. The time periods for each stage remained consistent between bilayer and drug; however, the transition from regions varied in a concentration dependant manner. "Stage II", where it was considered the drug was interacting with the bilayer and slowly diffusing through, showed variation between concentrations and drugs. Both drugs were expected to interact with the bilayer in similar manners due to their very similar structures (Figure 26). However, daunorubicin's greater lipophilicity is thought to lead to its deeper penetration into the bilayer core[84]. Both Duanorubicin and Doxorubicin have been observed to aggregate, and this effect can inhibit cellular uptake[289,290].

As shown in Table 3, 0.1 mM showed a very similar slope for fluorescence intensity change versus time across both bilayer compositions on both drugs. This suggested that at this concentration, the drugs behaved in a very similar way and this is attributed to the drug aggregating at this concentration. Interestingly, daunorubicin average normalised slope tended to be higher than doxorubicin's in both DOPC and ternary bilayer composition, suggesting it diffuses faster across the bilayer to the cavity. Daunorubicin showed an average slope of 2.35 x10^{-5} ± 9.41 x10^{-3} in DOPC and 3.67 x10^{-3} ± 3.69 x10^{-3} in crossing the ternary bilayer, whereas doxorubicin had 5.01 x10^{-4} ± 1.05 x10^{-4} in DOPC and 4.67 x10^{-4} ± 3.5 x10^{-4} in ternary. These differences may be due to daunorubicin's greater retention at the DOPC bilayer compared with doxorubicin, which would be consistent with differences in the lipophilicity of the two species. Data also confirms that the ternary bilayer composition is considerably less permeable to these drugs than DOPC alone.

Stage II	Doxorubicin DOPC	Daunorubicin DOPC	Doxorubicin DOPC/SM/CH	Daunorubicin DOPC/SM/CH
0.1mM	3.57 x10^{-3} ± 1.32 x10^{-3}	3.75 x10^{-3} ± 3.01 x10^{-3}	3.73 x10^{-3} ± 8.14 x10^{-4}	5.40 x10^{-3} ± 1.15 x10^{-2}
50 µM	6.20 x10^{-3} ± 5.75 x10^{-3}	4.2 x10^{-3} ± 6.12 x10^{-3}	8.77 x10^{-3} ± 3.94 x10^{-3}	3.27 x10^{-3} ± 8.54 x10^{-3}
100nM	1.16 x10^{-2} ± 7.4 x10^{-3}	2.33 x10^{-4} ± 2.29 x10^{-2}	1.50 x10^{-3} ± 2.97 x10^{-3}	1.51 x10^{-2} ± 1.47 x10^{-2}

Stage II. i	Doxorubicin DOPC	Daunorubicin DOPC	Doxorubicin DOPC/SM/CH	Daunorubicin DOPC/SM/CH
0.1mM	1.69 x10^{-2} ± 1.86 x10^{-3}	5.8 x10^{-3} ± 5.09 x10^{-3}	7.77 x10^{-3} ± 4.61 x10^{-2}	2.93 x10^{-3} ± 1.99 x10^{-3}

Table 3: Slopes obtained from the integrated area of the fluorescent peak at 600 nm. Stage II ranges between 30-65 minutes, Stage II.i between 60- 105 minutes.

In Stage II.i, at high concentrations, where the drug was in the membrane and diffusing into the cavity, in the DOPC bilayer, the slope for doxorubicin was greater than daunorubicin by a factor of 10, indicating doxorubicin was permeating faster than daunorubicin. In the ternary bilayer, the behaviour was more similar for both drugs. The dynamics indicate that doxorubicin interacted similarly in both DOPC and ternary bilayer and diffused quickly into the cavity, whereas daunorubicin was more influenced by the bilayer's composition. This suggests that these substrates have the capabilities to monitor a drugs interaction with different lipid composition and may give us insight on how this effects their diffusion.

4.3.2.4 Comparison of Planar and Cavity Enhancements

As controls, fluorescence studies of the drugs were completed on bilayers spanned across planar gold substrates to compare the MEF enhancement obtained at planar gold and from structured hotspots. These studies were completed on bare, DOPC bilayer and DOPC/SM/CH bilayer substrates. The substrates were created and treated in the same manner as the cavity samples and examined under the same conditions with 0.1 mM of drug. Examples of the integrated fluorescent peak area at 600 nm for bare (Figure 82) and DOPC bilayer spanned planar gold (Figure 83) are below.

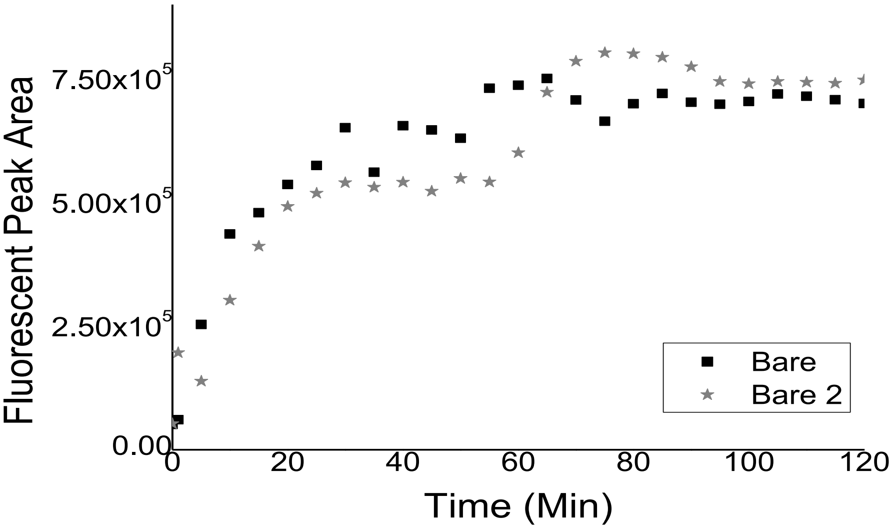

Figure 82: 0.1 mM Doxorubicin: rate of change to integrated fluorescent peak area obtained under 473 nm excitation for planar gold samples. (peak limits set as 520 - 750 nm)

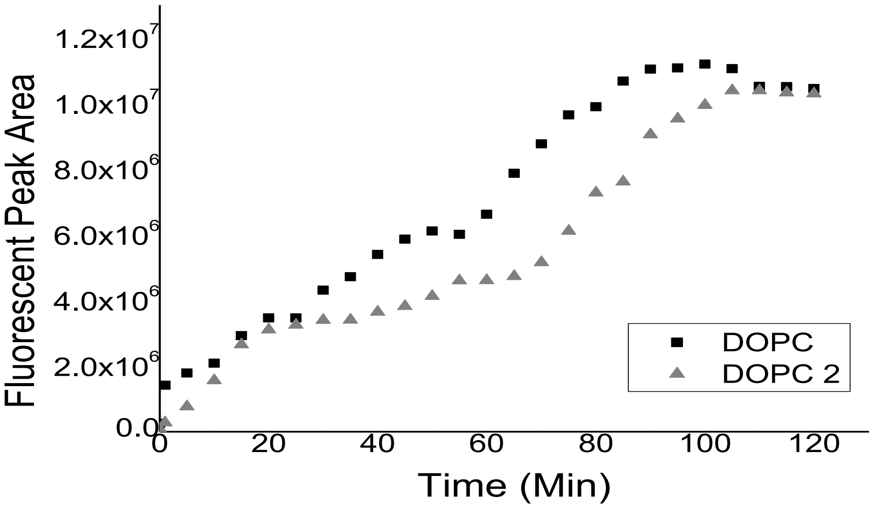

Figure 83: 0.1 mM Doxorubicin: rate of change to integrated fluorescent peak area obtained under 473 nm excitation for DOPC bilayer spanned over planar gold. (peak limits set as 520 - 750 nm)

The bare gold emission signal increases over approximately 20 minutes due to diffusive mixing and then stabilises. When compared to cavity samples, the final intensity for identical concentration in an identical volume was lower by a factor of 10^2 for planar samples. This shows evidence of the extent of fluorescent enhancement from the cavity. Particularly given that solution alone under the same conditions reached only half the emission intensity seen for cavity samples, after diffusive mixing, indicating that the gold is enhancing the emission signal.

As expected, for DOPC bilayers on planar substrates diffusive mixing was complete at 20 minutes. The emission dynamics then showed continued emission increase, with shallow slope similar to DOPC modified cavity samples. This is further evidence that this time period immediately following mixing is attributed to drug assembly at and residence in the bilayer. At equilibrium, a typically maximum intensity was seen at ‘x10^6’ magnitude.

Similar to the cavity arrays, the ternary bilayer on planar substrates yielded lower levels of intensity than the DOPC planar substrates. A fluctuation in intensity was observed in the bilayer residence time, similar to that observed in ternary bilayer cavity samples. Diffusive mixing occurs for 20 min then a slow rise in intensity is observed that reaches equilibrium at 40 minutes at an intensity of 10^3. This is consistent with much weaker association and penetration of the drug in the bilayers as observed at the cavities[84].

The fluorescence emission peak area dynamics at bilayer planar samples showed similar pattern and time frame for each stage, as observed in cavity samples but at a much lower intensity range. Indicating that the cavity platform was providing ample plasmonic enhancement which results in an observable difference in fluorescence intensity.

4.4 Conclusions

A novel approach to understanding drug-membrane permeability using MEF to follow and mark drug arrival time at membrane and underlying was examined using bilayer supported cavity arrays. The presence, integrity and stability of the bilayer spanned cavity array were initially established using a membrane impermeable dye, DRAQ7. Through these studies, it was found that bilayers formed and remained stable and thus impermeable to DRAQ7 for the duration of the experiments agreeing with previously reported studies[18].

The bilayer spanned cavity arrays were then used to study the permeation of chemotherapeutic drugs, doxorubicin and daunorubicin. Fluorescence from the drugs was followed over time as they diffused through the contacting solution and interacted with the bilayer. The spectroscopy of the drugs could also be followed and the shoulder at 650 nm for both drugs and bilayers spectra, showed spectral changes over time, attributed to MEF from golds plasmons[264]. Demonstrating a benefit of using this system, the platform generated reproducible dynamics, irrespective of the emission intensities, as evident by the similar slopes between samples (Table 3).

Through the rate of peak area emission change, post initial diffusion of the drug throughout the contacting solution, the bilayer supported cavities gave sufficient evidence to identify residence/aggregation of the drug within the membrane and diffusion into the plasmonic pore. In agreement to reported studies, drug aggregation was clearly observed at higher concentrations[289,290] and a preference for bilayer residence was observed at lower concentrations[84]. Membrane enhanced fluorescence proved to have a greater contribution to the overall intensity than previously accounted for. It would be of interest to repeat the quenching experiment with membrane permeable drugs whose emission is not influenced by the membrane, as a comparison to those studied here. This would allow for a more accurate estimate of the contribution the cavity has on the overall emission intensity.

The differences observed between the kinetic response of the membrane permeable drugs and the non-membrane permeable DRAQ7, where the latter showed no change in the rate of emission increase after the diffusive mixing stage (27 mins). Whereas, the membrane permeable dyes showed change, this confirms that although the volume above the cavity is contributing to the signal, once diffusive mixing has been completed, it does not contribute to any further changes. Meaning the large axial resolution which is beneficial for obtaining signal from both the bilayer and the cavity, is not negatively impacted by the inclusion of the confocal volume above the bilayer.

The dynamics observed for MEF proved to be highly reproducible in comparison to the results obtained through SERS in chapter 3. While SERS allowed for greater insight into the drug-membrane interactions. MEF allowed for the kinetics of permeation to be identified. Although, both methods allowed for detection of drug permeation, MEF allowed for more reproducible identification of bilayer residence and permeation into the cavity through the diffusion kinetics. In future, this method will be developed into a platform as a membrane permeability model, allowing for a non-destructive technique to accurately determine the diffusion of a compound of interest on biomimetic bilayers.

Overall, the data obtained, suggests that this method has strong prospects for application as a membrane permeability model. Through the use of surface enhanced fluorescence, fluorophore emission intensity may be exploited for the monitoring of diffusion time through a membrane. In future, this method will be used within an enclosed microfluidic platform and EIS will be completed in situ, allowing for enhanced monitoring of the bilayer stability. The enclosed system will allow for greater control over volume etc during measurement. Improvement in the fabrication process would provide near identical samples, further improving reproducibility. Recommendations also include a commercial grade laser source, allowing laser intensity to remain consistent. With the changes presented here, this platform design will be an easy to use, reproducible method for membrane permeability detection.

Chapter 5: Nature's Own Bilayer Composition & Ruthenium Polypyridyl Complexes

5.1 Introduction

Having established in the preceding chapter that MEF at the cavity supported lipid bilayers can be used to qualitatively determine if a species is membrane permeable, we next moved to a molecular species for which a mode of permeation at cells is not established to see if this method could yield insights into whether the material is passively permeable or not. We studied the permeability of Ru (II) metal complexes peptide conjugates, that have been demonstrated to be cell permeable at live cells; but the mechanism of uptake is not established. At live cells, the uptake was observed to be the temperature dependent, where permeability switched off at 4^0C, indicating that uptake is by an activate mechanism, possibly endocytosis.

In this chapter we advanced the platform format by enclosing it into a microfluidic device, to reduce the volume and the mixing/diffusion time. This also reduced the quantity of reagent required, improving cost efficiency and improving the reproducibility of the measurement. The bilayer composition of a true cell membrane is highly complex and varies depending on cell type and also between species. Single lipid models, as described in the previous chapters, are a good starting point as they have the unique structure of the bilayer, hydrophobic core and zwitterionic hydrophilic exterior, but they lack the greater complexity, including domains and lateral organization known to exist in membranes, e.g. the eukaryotic plasma membrane. Thousands of lipids are found in plasma membranes; so, this would be impossible to replicate in a model. However, an approximation can be made. Here, to replicate the lateral heterogeneity of a true membrane, a composition developed originally in collaboration with Prof. Barry Lentz coined "nature's own" was used[31]. Nature's own composition consists of five of the most commonly found components of the plasma membrane. The composition consists of DOPC (32 %), 1,2-dioleoyl-sn-glycero-3-phosphoethanolamine (DOPE) (25 %), CH (20 %), SM (15 %) and DOPS (8 %) and is close to a fusogenic composition[31].

A symmetric composition was investigated initially, although typically, DOPS is only to be found on the inner leaflet[51]. The ratios examined in this composition is of great importance as it has been noted that at specific ratios, membrane fusion and rupture may be affected[31]. In particular, the CH and SM ratio is important as CH is known to decrease the permeability of the membrane while increasing the stability[31,76,308]. In DOPC and DOPE monolayers, CH will induce a negative curvature, and in a more complex composition, will cause membrane rupture without the presence of SM[31]. CH has also shown to decrease the depth of water's penetration into a lipid bilayer[309]. Whereas, SM alone has a smaller degree of membrane rupture or leakage than CH alone, but shows minimal fusion[31]. Preferably, at the optimal SM/CH ratio, membrane rupture will be significantly reduced without causing a large degree of fusion reduction, while also enhancing the leaflet packing.

DOPE has a cone-shaped structure which promotes spontaneous negative curvature in the membrane and is thought to reduce lipid packing, promote stalk formation and membrane merging. It has also been known to increase water permeation and decrease the packing observed in the outer leaflet within liposomes[31]. Also, high levels of DOPE has resulted in membrane rupture[31]. At certain ratios of DOPC/DOPE, a balance can be found between the bilayer fusion and rupture, making these two lipids of great interest for biomimetic studies[31].

DOPS, with its negative charge, can inhibit membrane fusion due to electrostatic repulsion[31]. It has been observed that in mixed lipids, phase separation occurs between the charged disordered lipids and neutral ordered phases[47]. DOPS has also shown that it transitions from disordered phase to an ordered phase by the adsorption of calcium ions. These ions bind to the negatively charged head groups of DOPS, and therefore reducing the surface charge density. This also results in a decrease in the spontaneous curvature of the membrane[47]. As DOPS is the most abundant anionic lipid found within eukaryotic membranes[310], it is important to consider for biomimetic studies.

DOPC/DOPE/CH/SM/DOPS (32/25/20/15/8 %) composition was spanned over gold microcavities using LB and vesicle fusion, as with previous experiments. Nature's own composition should result in domain formation, however, these should be on the nanoscale, whereas the previous ternary composition had larger domains. This composition has been previously attempted within the group and has led to the successful creation of GUV's and for bilayers spanned over PDMS cavities. FCS was completed on nature's own composition spanned on glass and the diffusion coefficient was found to be 2.58 ±0.65 $\mu m^2/s$. Interestingly, as they increased the temperature from 21 °C to 37 °C, the coefficient was found to increase up to 12.43 ± 0.90 $\mu m^2/s$[37].

Metal complexes are increasingly of interest in both imaging and in medicine, in particular for their anticancer/antitumor activity. Currently, platinum (II) based complexes are the most widely used metal based anti-cancer therapeutic. However, due to metal complexes chemotherapeutics lack of cellular selectivity, other cells, such as rapidly proliferating cells, are commonly affected by these off-target effects[311]. These off-target effects lead to unwanted side effects, meaning development of other more selective drugs, are of great interest. Currently, only two types of Ru (III) drugs are in clinical trial; however, numerous have shown positive results in vivo and in vitro studies. The chemistry of ruthenium complexes, in particular, Ru (II) and Ru (III) have been studied in great detail and are well established in materials and medicinal chemistry.

The ruthenium(II) polypyridyl complexes that were examined within this work are ruthenium 1,4,5,8–tetraazaphenanthrene (Tap) and ruthenium dipyrido (3,3-alpha:2', 3'-c) phenazine (DPPZ), as a parent ester complex and with an attached arginine peptide (R8). Their structures are shown in Figure 84. For ease of the reader, $[Ru(tap)_2(bpyArCOOH)]^{2+}$, $[(Ru(tap)_2(bpyArCONH\text{-}RRRRRRRR\text{-}CONH_2)]^{10+}$, $[Ru(DPPZ)(bpy)(bpyArCOOH)]^{2+}$, and $[(Ru(DPPZ)(bpy)(bpyArCONH\text{-}RRRRRRRR\text{-}CONH_2)]^{10+}$, will be referred to as Ru-Tap-Ester, Ru-Tap-R8, Ru-DPPZ-Ester and Ru-DPPZ-R8 respectively.

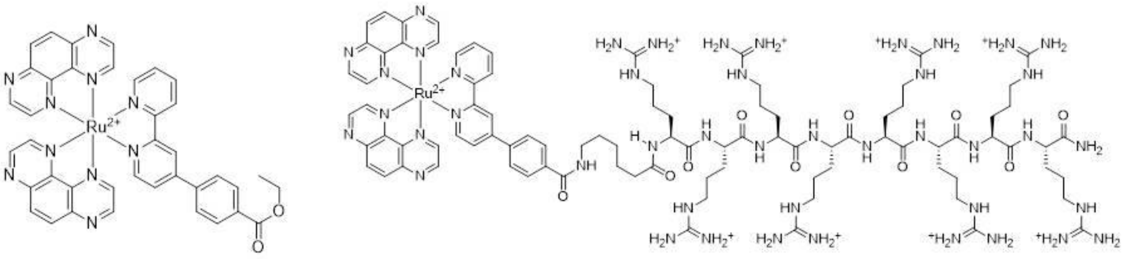

Ru-tap-ester
$[\mathrm{Ru(tap)_2(bpyArCOOEt)}]^{2+}$

Ru-tap-R8
$[\mathrm{Ru(tap)_2(bpyArCONH\text{-}ahx\text{-}RRRRRRRR\text{-}CONH_2)}]^{10+}$

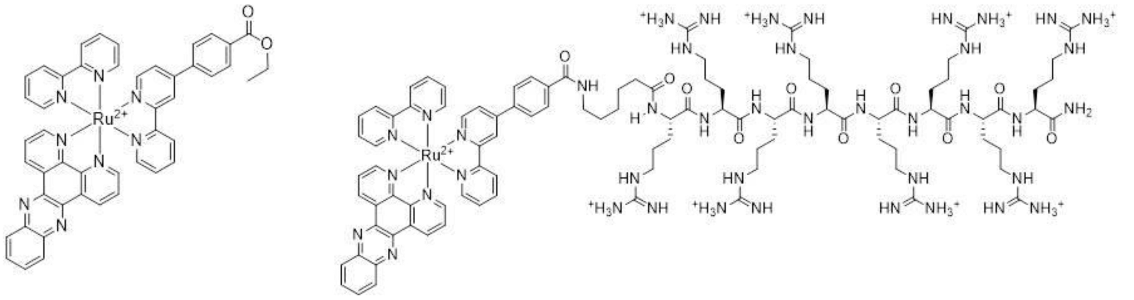

Ru-dppz-ester
$[\mathrm{Ru(dppz)(bpy)(bpyArCOOEt)}]^{2+}$

Ru-dppz-R8
$[\mathrm{Ru(dppz)(bpy)(bpyArCONH\text{-}ahx\text{-}RRRRRRRR\text{-}CONH_2)}]^{10+}$

Figure 84: Schematic structure of Ruthenium dipyrido (3,3-alpha:2', 3'-c) phenazine with and without peptide arginine. And ruthenium 1,4,5,8 – tetraazaphenanthrene with and without peptide arginine.

Both complexes are known to associate with DNA but transduce this binding in different ways. Ru-Tap complexes are known to be very luminescent in aqueous media. In the presence of DNA, a light-induced electron transfer occurs, where the tap ligands oxidise a guanine base. The rate of electron transfer is dependent on where the complex binds in relation to the location of the guanine base. In guanine monophosphate, the process is slow due to it being diffusion controlled. However, in polynucleotides, once the Ru-Tap complex is intercalated, the process takes hundreds of picoseconds[197]. The intercalation can lead to photocleavage of plasmid DNA and has been shown to lead to the formation of photo-adducts of the complex with guanine units of oligonucleotides or tryptophan residues of polypeptides[206,207]. Photoadduct formation was confirmed by gel electrophoresis and Atomic force microscopy for the former and dialysis and UV-vis absorption for the latter[207,312]. Due to photo-adduct formation, this complex has been commonly used for DNA studies as a molecular tool and probe.

Ru-DPPZ complexes behave as a photoswitch, as they are not luminescent in an aqueous solvent, but are when imbedded in DNA[189]. As shown in Figure 84, the Ru-DPPZ ligand contains two free nitrogen on the phenazine ring. These nitrogen readily form hydrogen bonds in water which quenches luminesce and reduces the intensity magnitude by 2-3 orders. However, when the ligand is intercalated in DNA, the nitrogen are shielded from the aqueous solvent, resulting in a luminescent excited state[189].

This "light switch" effect has been known since 1990[198], and since then, many studies have been completed to provide insight into the mechanism. For example, one study by Coates et al. used RRS to identify the excited state intercalative interaction between Ru-DPPZ complex and calf-thymus DNA[313]. Work by Nair et al. through steady-state and time-resolved photoluminescence studies, determined that Ru-DPPZ complexes were affected by the polarity of the solvent[314], whereas Demas et al. observed a large discrepancy between the quenching of emission intensities and the lifetimes of the complex in water and acetonitrile[315]. A study by Chambron showed that the ligand may be protected from water, through the use of organic micelles[316]. The light switch property has led to the utilisation of these complexes as targeting and imaging probes.

Although of value in both sensing/imaging and for phototherapy, Ru (II) polypyridyl complexes are typically not permeable to the cell membrane. Barton's studies reported that simple $[Ru(bpy)_2(dppz)]^{2+}$ complexes have poor lipophilicity and therefore it is unable to permeate into cells[199]. Zhu et al. tried to improve the cellular uptake of Ru-DPPZ by the introduction of biochemical agents that are weak acids containing bulky aromatic hydrophobic moieties such as PCP and tolfenamic acid. Through flow cytometry and confocal microscopy, they found that the presence of these agents showed a large increase in cellular uptake[317]. Shen et al. used a liposome approach to deliver $[Ru(phen)_2dppz](ClO_4)_2$ in MB-231 breast cancer cells. The dye was encapsulated in liposomes, which resulted in emission, allowing for the tracking of its passage through the cell. Once the dye was released from the liposome, it would then only emit when bound to DNA. They found that the presence of the liposome slowed the uptake of the dye; however, after 6 hours, it had a 15 fold higher accumulation in the cell than free floating dye without any liposome[39].

Our group have carried out extensive studies in focussing on the use of peptides to drive functional Ru (II) imaging agents and phototherapeutics across the cell membrane and into specific organelles. The addition of peptides to ruthenium complexes was completed to improve the molecules targeting efficiency[195]. Previous work completed by Barton, Burke et al. etc. have shown that these peptide complexes allow for selective targeting[193,202,318]. Therefore, it is of interest to identify any difference in permeation occurring with and without this peptide. It is expected that the peptide complexes should result in a higher luminescence intensity than the parent "ester" complexes. The higher intensity would be due to the peptide acting as a blocker, preventing the hydrogen bonding from occurring at the phenazine nitrogen's which would result in luminescence switch off. A number of studies have observed that certain Ru complexes will accumulate within mitochondria, endoplasmic reticulum or the lysosome than within the nucleus of the cell[195,199,319]. It has been shown that those Ru complexes will cause mitochondrial dysfunction or activate apoptosis pathways[195,320].

Most recently, work carried out on the ruthenium complexes by Byrne[193,194,202], showed that they worked optimally as a sensing dye at 100 μM for the Ru-Tap complexes and 70 μM for the Ru-DPPZ. At these concentrations, they were clearly able to identify Ru-Tap complexes modified with a NF-κB transcription factor peptide, going into the nucleus of live HeLa and CHO cells due to the extinction of the complexes luminescence as it bound to the DNA. They observed the viability of the cells under imaging & dark conditions and efficient cellular destruction upon irradiation. Through RRS, they were able to confirm that the Ru-Tap complex remained within the nucleus of the cell after loss of emission.

Whereas, Ru-DPPZ complexes modified with a mitochondrial penetrating peptide were found to localise within the endoplasmic reticulum in live HeLa cells. The peptide conjugate showed rapid uptake by the cell, where emission was visible after 1-hour incubation in the dark. A NF-κB transcription factor peptide was also attached to Ru-DPPZ complexes, however, uptake was slower, where it took approximately 2 hours to reach the cytoplasm and 24 hours to penetrate the nucleus and bind with DNA. The parent complex, Ru-DPPZ-Ester, was found to be unable to penetrate the cell. The dyes also proved to be suitable for stimulated emission depletion microscopy, which is of great importance in the imaging community, as this allows for better resolution than traditional confocal microscopy.

Numerous studies have been completed to examine the interaction of Ru (II) lumiphore complexes with lipids. One study by Guo et al. incorporated the ruthenium complex. $[Ru(bpy)_2(dppz)]^{2+}$ into dipalmitoyl-L-a-phosphatidylglycerol (DPPG) & DPPG/CH vesicles and observed how in CH levels below 30 %, emission intensity would increase with temperature as it reached lipid phase transition temperatures. The emission was attributed to the membrane "protecting" the phenazine nitrogens from the aqueous solution. Spectral shifts were also observed due to the binding of the drug to the bilayer and due to the presence of cholesterol[321]. Cosgrave et al. demonstrated how $[Ru(dppz)_2PIC]^{2+}$ and its peptide conjugate showed emission after it bound to dipalmitoylphosphatidylglycero vesicles, where previously, it was non-emissive in PBS buffer. They also noted that after incubation in cells, the parent complex only emitted from the outer membrane, whereas the peptide conjugate showed emission from sub-cellular structures, which was then seen to be the nucleus and cell organelles[200].

As Ru complexes are increasingly being tested for their suitability as imaging and targeting probes, examining these dyes' membrane interaction and passive diffusion can provide valuable information to help advance suitable candidates for clinical trials. As the parent complexes and peptide conjugates studied in this work are impermeable and permeable respectively, examining this through a passive diffusion study could provide valuable information on how they are mediated into the cell. This would allow for an insight into the uptake mechanism of dyes/drugs which would be a useful application of these membrane permeability assays.

5.2 Materials & Methods

Samples were prepared in the same manner as discussed in section 2.2 with the following deviations.

5.2.1 Platform Development for Microfluidic Device

A microfluidic platform was developed to create an enclosed system for the membrane permeability assay. The optimisation steps involved in its development are described in the appendix. A laser cutter (5.2.1.1) was used to cut all Poly-methyl methacrylate (PMMA) sheets required. The final platform used for all experimentation is described in section 5.2.1.3.

5.2.1.1 Laser Cutter

An Epilog Zing laser cutter with CorelDraw software was used for all PMMA cutting required. PMMA sheets of 3mm, 1 mm and 0.3 mm thickness were obtained from Radionics and were cut using a CO_2 laser zing 16 model 10000.

5.2.1.2 PDMS Development

Polydimethylsiloxane (PDMS) substrates were made using Sylgard 184 silicone elastomer kit (Dow Corning), by mixing a 10:1 ratio of the elastomer and curing agent. The elastomer was mixed and put into a desiccator for a minimum of 30 min. The solution was then poured into a PMMA mould and cured at 110 ^{0}C for 2 hours. The PDMS solution was then allowed to cool and was carefully peeled from the mould, resulting in a PDMS block of uniform size with a chamber for the cavity to sit into.

5.2.1.3 Optimal Platform Development

The final developed platform is shown in Appendix Figure 111, sample 7. Two pieces of PMMA were cut into 68.4 by 35.8 mm rectangular pieces, where the second piece only consisted of an outline. A rectangular piece of 50 x 12 mm (including attachments at the end) was also cut, and the pieces were assembled as shown in Figure 85 "PDMS 1", as a curing chamber. PDMS was then left to cure within the chamber and when removed, contained the imprint, which acts as the cavity chip placement well.

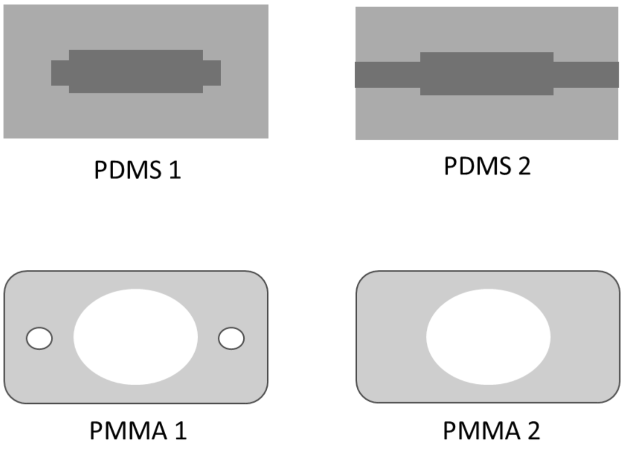

Figure 85: Schematic diagram PDMS and PMMA sections used to create platforms described below. PDMS 1 is a rectangle of PDMS with an indent allowing for cavity sample to sit within. PDMS 2 is the same as PDMS bar an extension of the indent to the edge of the PDMS. PMMA 1 is a 300 nm PMMA sheet cut with three holes. PMMA 2 is the same as PMMA 1 but with only one hole.

A 0.3 mm PMMA sheet was cut into a rounded rectangle of 53.3 x 21.8 mm, with one circle of 161 mm and two circles of 2.1 mm diameter (Figure 85 PMMA 1). A 22 mm circular glass coverslip (from VWR) with 0.13-0.17 mm thickness was glued onto the large circular hole with Araldite rapid action adhesive resin.

Cavity sample were placed within the PDMS 1, and PMMA 1 was glued on top. 1mm wall thickness silicone tubing (VWR) was then attached to the smaller holes, and the system was enclosed into a holder to form a seal. Figure 87 shows an image of the final platform.

5.2.2 Bilayer Formation

Vesicles were prepared by placing 20 μl of a lipid stock solution (Avanti) of DOPC/DOPE/ CH/ SM/DOPS (32/25/20/15/8 %) in chloroform, into a glass vial and evaporating the chloroform under a stream of nitrogen. The vial was placed under vacuum for a minimum of 30 minutes and were re-suspended in 1 ml of PBS. The vesicles were then extruded through 100 nm polycarbonate membrane at 40^0 C for a minimum of 15 times to form monodisperse vesicles.

A Langmuir Blodgett trough (KVS Nima) was used to create the first monolayer of the bilayer. The lipids of interest (1 mg/ml) were deposited onto the surface of deionised water in the trough and left for 10 minutes to allow for the full evaporation of the chloroform. The barriers were compressed and held at a pressure of 32 mN/m. PBS filled cavity arrays were then clipped to the dipper of the instrument and immersed at speed 150 mm/min. The chip was then removed at 5 mm/min for monolayer formation.

After cavity array samples were removed from the LB trough, the chips were placed within the cavity chamber of the PDMS substrate. Top cover pieces were glued into place with Araldite rapid action adhesive resin. VWR silicone tubing was attached and the PDMS substrate was placed within the holder and clipped to form a seal. Vesicle solution was injected in and the sample was then left for a minimum of 1 hour to allow for vesicle disruption into the top layer at an angle of 25^0.

5.2.3 Absorption & Emission Spectroscopy

Measurements were completed as stated in section 2.2.6 with the following deviations. Slit width and scan speed were varied to improve emission spectra.

5.2.4 Fluorescence & Raman Microscopy

As with the previous chapters, a Horiba Labram HR instrument was used with 50x 0.55 Leica PL Fluotar long distance magnification lens. 473 nm & 633 nm excitation wavelengths were used for luminescence measurements. The instrument was calibrated using silicon prior to use. Samples were placed in an enclosed microfluidic platform. The laser was focused using the camera and spectra were taken. Typically, a 99.9 % neutral density filter and 900 μm slit window was used for luminescence. The measurements were completed as discussed in section 2.2.8. Peak limits were set as 640 - 850 nm for DRAQ7 measurements, 520 - 750 nm for doxorubicin & daunorubicin measurements and 560 – 820 nm for Ru complex measurements. All MEF experiments focused on a single cavity pore.

5.3 Results & Discussion

5.3.1 Development of Enclosed Raman Platform

The key goal in this thesis was to create a simple ready to use microfluidic device that permitted the use of low reagent volumes and improved reproducible positioning of light and sample. Therefore, to advance the platform described in previous chapters, an enclosed system for Raman & fluorescence measurements was developed.

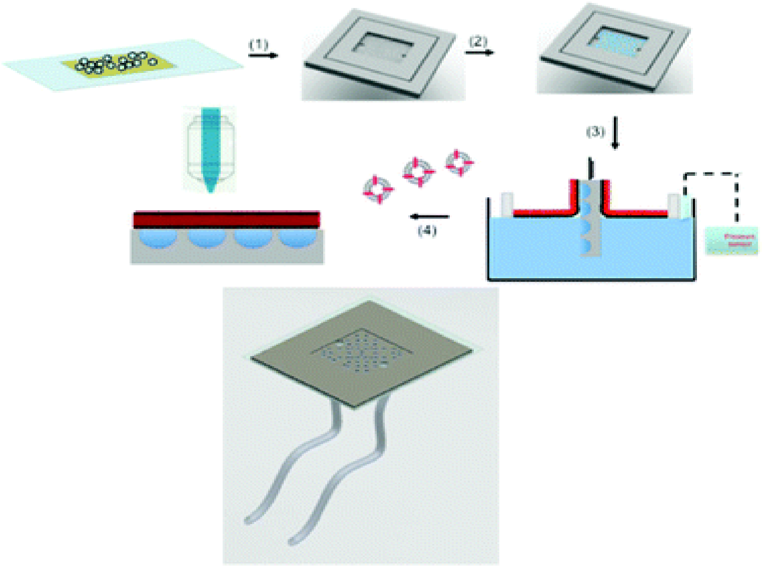

Figure 86: Schematic diagram of PDMS substrates previously developed for fluorescence lifetime correlation spectroscopy[21]. Polystyrene spheres are dropcast onto mica. 1) PDMS is then cured at 150 ⁰C over the sphere template. PDMS is then peeled off and spheres are removed with THF. 2) Cavities are sonicated in buffer. 3) Lipid monolayer is formed using the LB trough. 4) vesicle fusion then creates the upper lipid layer to form a bilayer. Bottom image shows a representation of the filled cavities on PDMS within the flow chamber.

Due to work previously completed on PDMS substrates within the group[102], PDMS was considered for the development of a single-use platform. The original PDMS array was developed for cavity measurements with FCS, and therefore alterations were required. As shown in Figure 86, Ps spheres were allowed to dry on mica glued onto glass, PDMS was then cured onto the sphere template. Spheres were then removed, resulting in PDMS cavities. The cavities were then filled through sonication, followed by LB monolayer deposition. Two holes were then punched at the ends of the PDMS substrate and a cover glass slide was glued on, to create a microfluidic flow chamber. Teflon tubing was attached to the holes to allow for solution introduction. Vesicle disruption was then completed to form the upper leaflet of the bilayer[21].

The previously reported method was adapted to allow for the gold cavity sample to sit within a well in the PDMS. Originally a glass coverslip was added to create an enclosed system. Tubing was added to the bottom of the PDMS as entry points; unfortunately, this led to leaking. Leaking was not an issue with the original PDMS substrates for FCS, because it used and inverted configuration. As we have an upright microscope system, this created an issue. The attempted fabrication methods are described in the Appendix.

The final version of the platform is shown in Figure 87. PDMS 1 and PMMA 3 set up were used. (PMMA 3 is a modified version of PMMA 1 where it was smaller in size (53.3 x 21.8 mm), and therefore, did not fully cover the top surface of the PDMS; this allowed for a better seal). A holder was created that enclosed the system under pressure to minimise leakage. 3 mm PMMA was used to create a holder for the PDMS and tubing. 1.5 mm PMMA was created as a top cover. Clips were then used to enclose the system as shown in Figure 87. This system was tested by injecting a PBS solution into the sealed system and monitoring for leakage or change over the course of 5 hours. The system proved to work reliably with only occasional leakage which occurred where inadequate tubing connection was made. The flow cell, shown in Figure 87, was then used for all work completed in Chapter 5, where the glass clover slip allowed for measurements without interference.

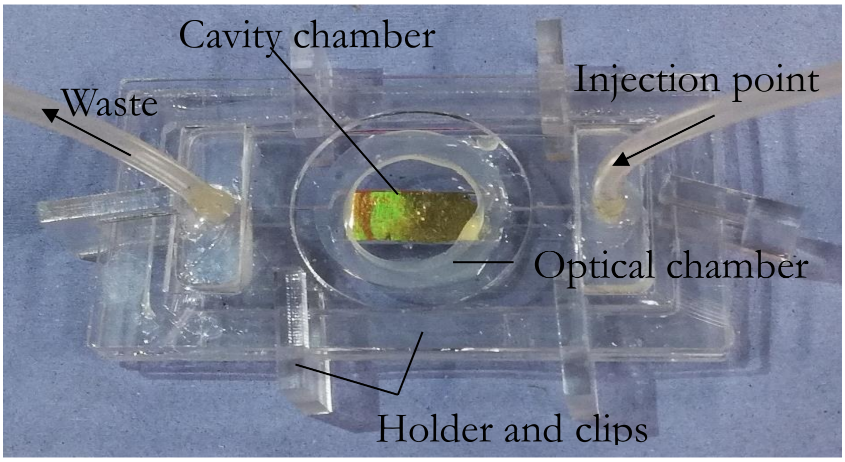

Figure 87: Representative image of the enclosed platform developed for MEF & SERS studies. Cavity samples were placed into a PDMS chamber and sealed with a PMMA cover containing a glass cover slip. Tubing was then added, to allow for the introduction of solutions. This was then placed into a PMMA holder and clips were used to maintain the seal.

5.3.2 Preparation of "Nature's Own" Microcavity Supported Lipid Bilayer and Determination of Bilayer Stability

EIS and fluorescence spectroscopy were used to interrogate the stability of Nature's owns bilayer spanned cavities. The electrochemical and fluorescent experiments were completed in a similar manner to those described in Chapter 2. The electrochemical impedance signal was monitored over time following bilayer preparation, to give immediate indication of changes in the bilayer. Fitting the impedance data to the Nyquist plot allowed for the monitoring of the film's resistance and capacitance over time, providing insight into changes to the membrane's permeability and thickness. This allowed for the identification of a time frame where resistance changes were below 10%, which was then used at the maximum experimental window. In parallel, monitoring the fluorescence of a membrane impermeable dye, provided further confirmation of the presence of a bilayer and its barrier properties, as indicated by minimal enhanced fluorescence in contrast to the probe at a cavity array without the bilayer barrier

5.3.2.1 EIS Study of Bilayer Stability and Definition of Experimental Temporal Window

As described section 2.3.4.2, the EIS experimental set up included a three-electrode electrochemical cell, composed of a working electrode (the gold array), reference (AgCl) and counter (platinum wire) electrode in contact with aqueous PBS buffer. Resistance and capacitance values were extracted by fitting the EIS data to Nyquist plots using the equivalent circuit model shown in Figure 31[18].

As each cavity electrode is slightly different in terms of packing and area, change to resistance is quoted rather than absolute resistance change. An example of the resistance changes to nature's own spanned cavities is shown in Figure 88. Figure 88 shows that although some of the spanned cavity arrays showed minimal change in Delta Rm (>0.4 Mohm), indicating long term stability. However, samples showed a decrease in resistance after 10 hours where the resistance change exceeded 2.5 Mohm, indicating the bilayer was deteriorating. This was therefore treated as the maximum time frame for bilayer viability, i.e. nature's own bilayer composition is stable for 10 hours. However, between 5 and 10 hours, delta Rm would fluctuate above 2 Mohm. Whereas below 5 hours, samples typically did not exceed 2 Mohm. Although, the errors appear large in Figure 88, values were well within our previously established stability limits[21,102]. Due to this, 5 hours was used as the experimental time window used to ensure bilayer stability and reproducibility.

Interestingly, nature's own bilayer composition showed an average capacitance of 5.27 ±4.69 x 10^{-2} μF over the 10-hour stability window. This is very similar to the 5.01 ±0.39 μF that was seen for the ternary composition and is much lower than the 6.14 ± 0.17 μF seen for DOPC. It indicates that the bilayer thickness was similar for both nature's own and the ternary composition, as capacitance is inversely proportional to bilayer thickness. Unsurprisingly, DOPC's bilayer thickness was shown to be thinner than nature's own.

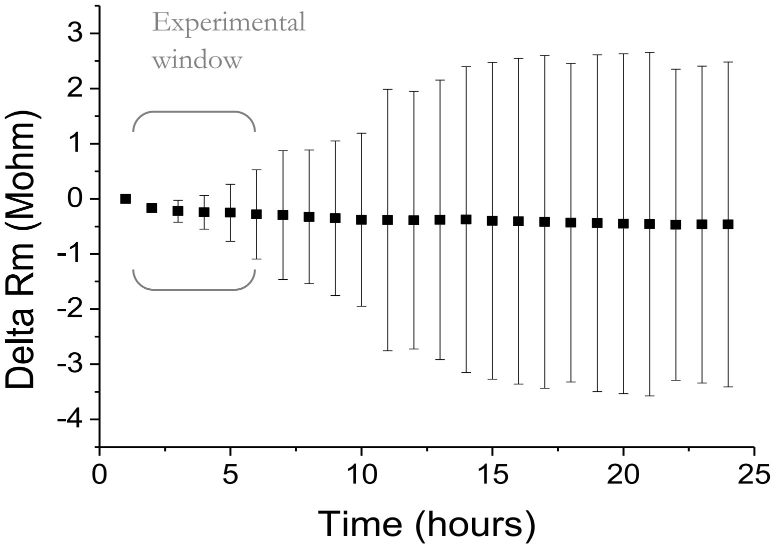

Figure 88: Time vs change in membrane resistance electrochemical impedance spectroscopy completed on Nature's own Bilayer spanned cavities. Impedance was measured once every hour for 24 hours to determine stability. Measurements were performed in PBS buffer using a platinum counter electrode, Ag/AgCl reference and gold cavities as the working electrode using AC amplitude of 0.01V at frequency range of 1 MHz to 0.01 Hz. Error bars indicate standard deviation across 5 samples. (N ≥5, RT).

5.3.2.2 Interrogation of Stability by Fluorescence.

Fluorescence microscopy was used to investigate the stability and integrity of the "nature's own" bilayer composition. This was done by measuring the MEF signal from a membrane impermeable probe in a similar manner to section 4.3.1. The fluorescence measurements in this chapter were completed within the enclosed microfluidic platform described in section 5.2.1.3. This consisted of a sample chamber to hold the cavity substrate while in an enclosed environment that allowed for fluid introduction. All measurements focussed on a single pore within the array.

The enclosed system allows for precise monitoring of the sample, where the exact volume of liquid was more reproducibly controlled. The initial diffusion/mixing step, where the drug/dye was introduced and diffused throughout the solution was also eliminated. The removal of this stage simplified the kinetics and eliminated any variation in emission due to the contribution of the drug dispersing through confocal volume or due to the residual velocity upon drug introduction. In this system, the drug/dye was premixed in PBS buffer and introduced to the sample. Spectra were initially taken of the bilayer cavity samples in contact with blank PBS buffer. The drug/dye was then injected into the platform and measurements were taken every 5 minutes for two hours. Data was then analysed, and the integrated fluorescent peak area is shown in Figure 89.

As described in the preceding chapter, DRAQ7 is a membrane impermeable fluorescent probe was used to investigate the integrity and stability of the bilayer over 2- and 5-hour experimental windows. As seen in Figure 89, upon application of the dye, an increase in fluorescence intensity was observed between the initial 20-40 minutes of the experiment, until a maximum fluorescence intensity was achieved, where the signal then plateaus or decreases. The decrease was attributed to photodecomposition expected from the continuous irradiation. The maximum emission intensity observed at nature's own spanned bilayers proved higher than the intensity observed with bare cavities (Figure 68 A), DOPC (Figure 68 B) or ternary bilayer composition (Figure 70). Although the absolute intensity would vary among substrate to substrate due to nano-variations in the MEF substrate, the maximum intensity was reproducibly higher for nature's own composition than bare cavities, suggesting that the intensity increase is not solely attributed to cavities enhancement. The higher intensity was unexpected but indicates that DRAQ7 is binding to the bilayer. This was suspected to be attributed to electrostatic binding to DOPS, and indeed although DRAQ7's molecular structure is proprietary; Biostatus were able to confirm that the dye is positively charged.

To examine if interactions were occurring between the charged species', the experiment was repeated but with DOPS removed from nature's own composition. This was completed in two different ways, where DOPS was simply removed, and where DOPS was replaced with DOPC. Both bilayers successfully formed and yielded similar results. A sample spectrum is shown in Figure 90. In the absence of the charged lipid, fluorescence intensity only reached a max that was over 50% lower than observed for the ternary bilayer composition (Figure 70). The kinetics showed a similar profile to previous DRAQ7 experiments, confirming bilayer integrity. Furthermore, it demonstrated, 1) nature's own bilayer composition is tightly packed, impermeable for DRAQ7 and likely thicker than even the ternary composition. And 2) the negative charge present on DOPS is interacting with the positive charge on DRAQ7, causing binding and a large increase in fluorescence intensity.

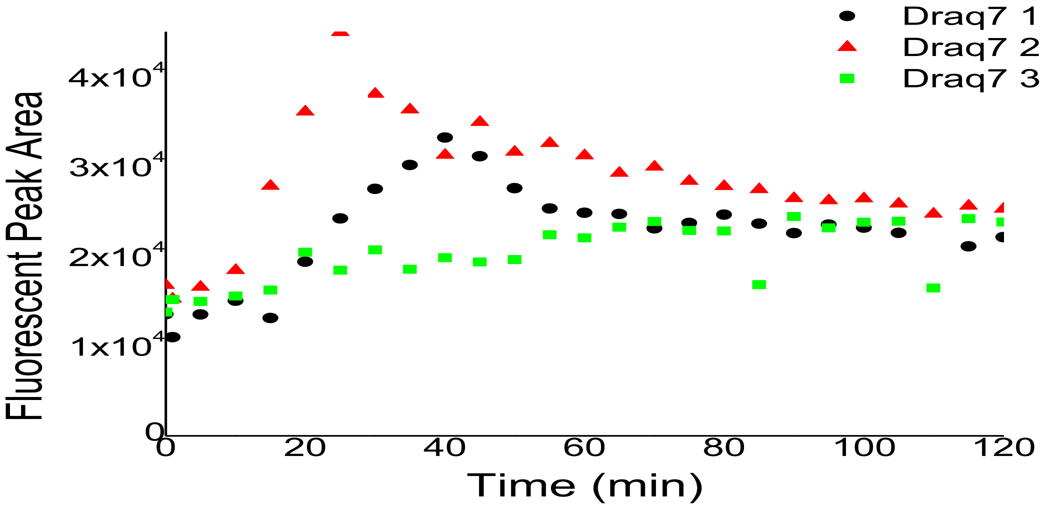

Figure 89: Fluorescent peak area at 690 nm (652-800nm) obtained from 633 nm excitation fluorescence spectra from Natures own spanned 1 µm gold microcavities with 0.75 µM DRAQ7. Measurements was focused on a single cavity pore. (Three measuremtns are shown at RT, exposure 2s)

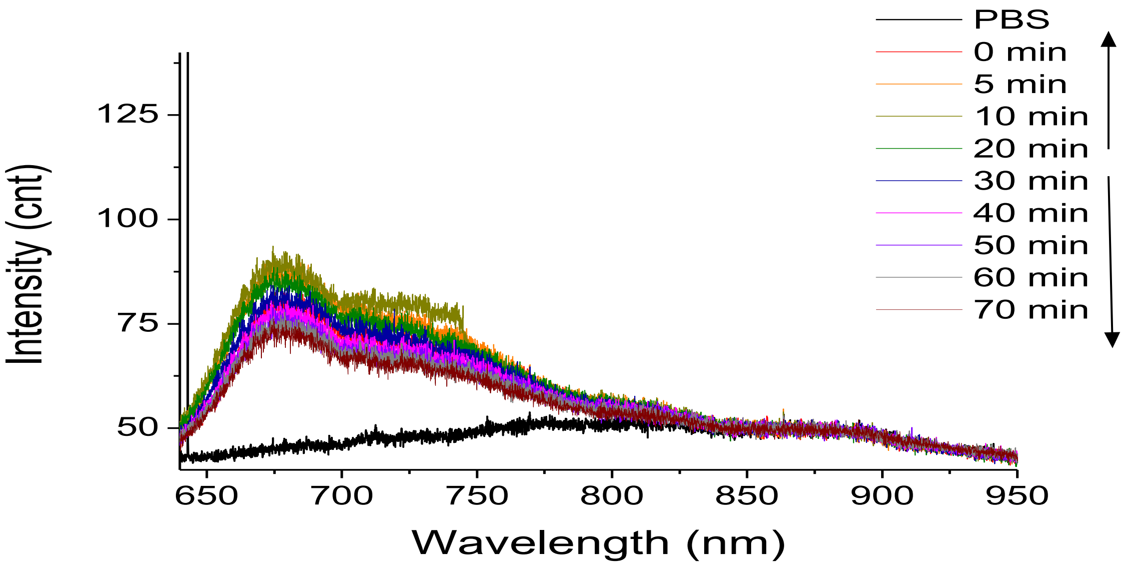

Figure 90: Time evolution of fluorescence spectra on incubation of 0.75 µM of DRAQ7 with DOPC/DOPE/CH/SM (32/25/20/15/8 %) spanned lipid bilayer cavities at 633 nm excitation. Where PBS indicates no probe, 0 min is where drug is introduced, and the following are spectra obtained every 5 minutes for up to 70 minutes. Exposure time and

accumulation were set at 2s and 10 respectively. Measurements was focused on a single cavity pore. (N ≥6, R)

Due to the interaction occurring between the charged molecule and lipid affecting the overall intensity, the rate of fluorescence increase were more closely examined. After the initial fluorescence increase, the fluorescence plateaus and remains stable throughout the experimental window. The emission suggests that the bilayer was successfully formed and remains stable for a minimum of 5 hours. Any defect or deterioration in the bilayer will result in an increase in fluorescence, but as this was not observed, even in the extended 5-hour experiment. The bilayer composition was found to be stable for our experimental time window.

5.3.3 Interaction of Anthracyclines with Nature's Own Composition

Doxorubicin (Figure 92) and Daunorubicin (Figure 91) (0.1 mM) were introduced to nature's own[31] bilayer composition and monitored over a 2-hour period to examine the permeation at more complex bilayer compositions. The experiment was completed in the same manner as described in section 5.3.1, where bilayer-spanned cavity sample were positioned within the microfluidic platform. Measurements were initially taken in blank PBS buffer, then sample drug was introduced, and measurements were taken every five minutes for 2 hours.

Upon the drugs introduction to Nature's own composition, immediately a peak with fluorescence maxima at 600 nm and a shoulder peak at 640 nm was observed. Interestingly, there was a difference in fluorescence temporal profile between both drugs. The fluorescence emission profile for doxorubicin (Figure 92) followed a similar trend as observed at DOPC bilayer samples (Figure 72), where there was an initial increase, followed by a slow steady increase over time until a maximum was reached. Whereas daunorubicin's behaviour (Figure 91) was closer to that observed at the ternary composition (Figure 73). Where, an initial increase occurs and fluorescence maxima was then quickly reached, and intensity then decreases slightly and appears to have reached an equilibrium. This suggests the two drugs experienced different kinetics during their diffusion.

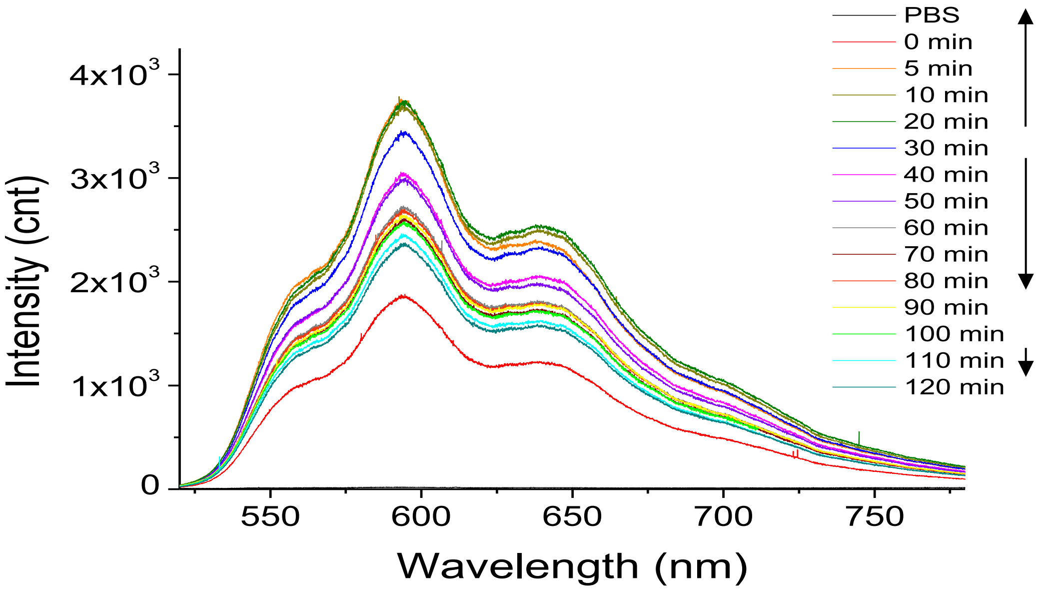

Figure 91: Time evolution of fluorescence spectra obtained when 0.1 mM Daunorubicin is introduced to Nature's own spanned 1 µm cavities at 473 nm excitation. Where "PBS" is bilayer spectrum prior to addition of the drug, 0 min is immediately after drug introduction, and the following are spectra obtained every 5 minutes for up to two hours. Measurements was focused on a single cavity pore. (N ≥3, RT)

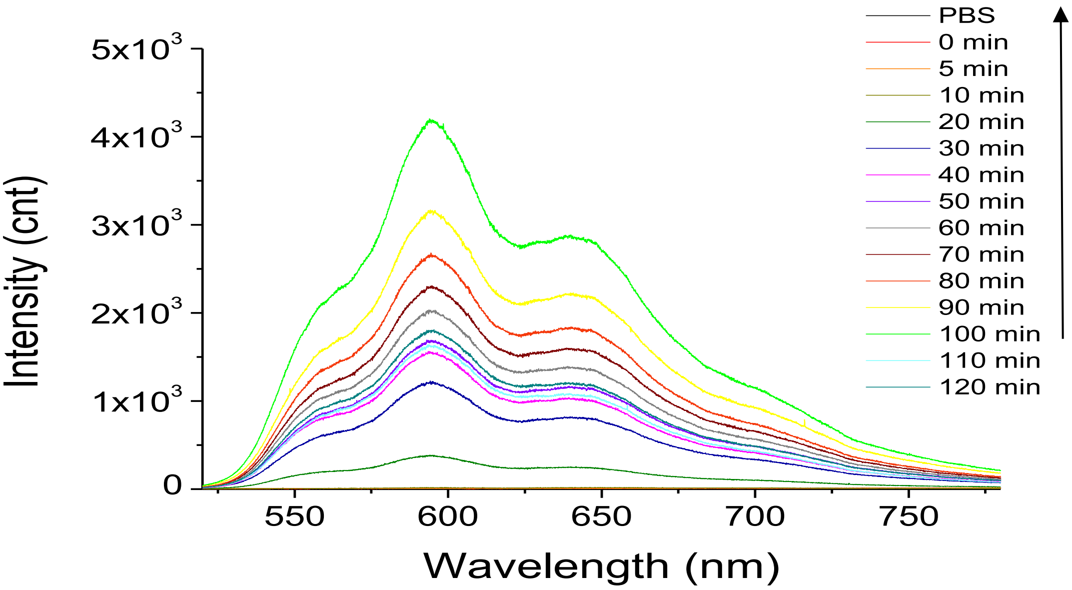

Figure 92: Time evolution of fluorescence spectra obtained when 0.1 mM Doxorubicin is introduced to Nature's own spanned 1 µm cavities at 473 nm excitation. Where "PBS" is bilayer spectrum prior to addition of the drug, 0 min is immediately after drug introduction, and the following are spectra obtained every 5 minutes for up to two hours. Measurements was focused on a single cavity pore. (N ≥3, RT)

Data analysis was completed to determine the occurring kinetics in the same manner as the work completed in chapter 4. The integrated fluorescent peak area is shown in Figure 93. Daunorubicin (Figure 93 A) showed an initial sharp increase in peak area due to the drug entering solution and then remained at equilibrium over the course of the experiment. In the extended 5-hour experiments, no further change was observed, apart from minor fluctuations which may be attributed to some photodegradation. As there is no initial diffusion step, the kinetics observed should be due to the drug intercalating into the bilayer. The kinetics suggest that daunorubicin had not permeated the bilayer but binds at the membrane, as there was no secondary increase in peak area attributed to the drug diffusing into the plasmonic field of the cavity.

Conversely, doxorubicin (Figure 93 B) showed a steady increase in fluorescence throughout the two-hour window and the extended 5-hour experiments. Interestingly, in the first 10-20 minutes, only a small increase in peak area was observed, the area then increases linearly with an average slope of $3.37 \times 10^3 \pm 6.11 \times 10^2$. There are two possible reasons for this increase in peak area; 1) The drug is permeating the bilayer and being plasmonically enhanced, although an equilibrium should be reached if this is the case. Or 2) the drug is interacting with a component of the bilayer, and this is resulting in the increased fluorescence.

The evident differences in interaction of doxorubicin and daunorubicin with Nature's own composition compared with DOPC and DOPC/SM/CH compositions was surprising. The two drugs differ only by their terminal groups which is a primary alcohol and a methyl group respectively[302]. However, an important distinction is their charge, daunorubicin is known to have a positive charge at physiological pH's[42], whereas doxorubicin is neutral. As these experiments were completed in PBS buffer (pH 7.4), it should have a positive charge. As nature's own composition contains DOPS, a negatively charged phospholipid, this may be causing the discrepancies between the two drugs interactions.

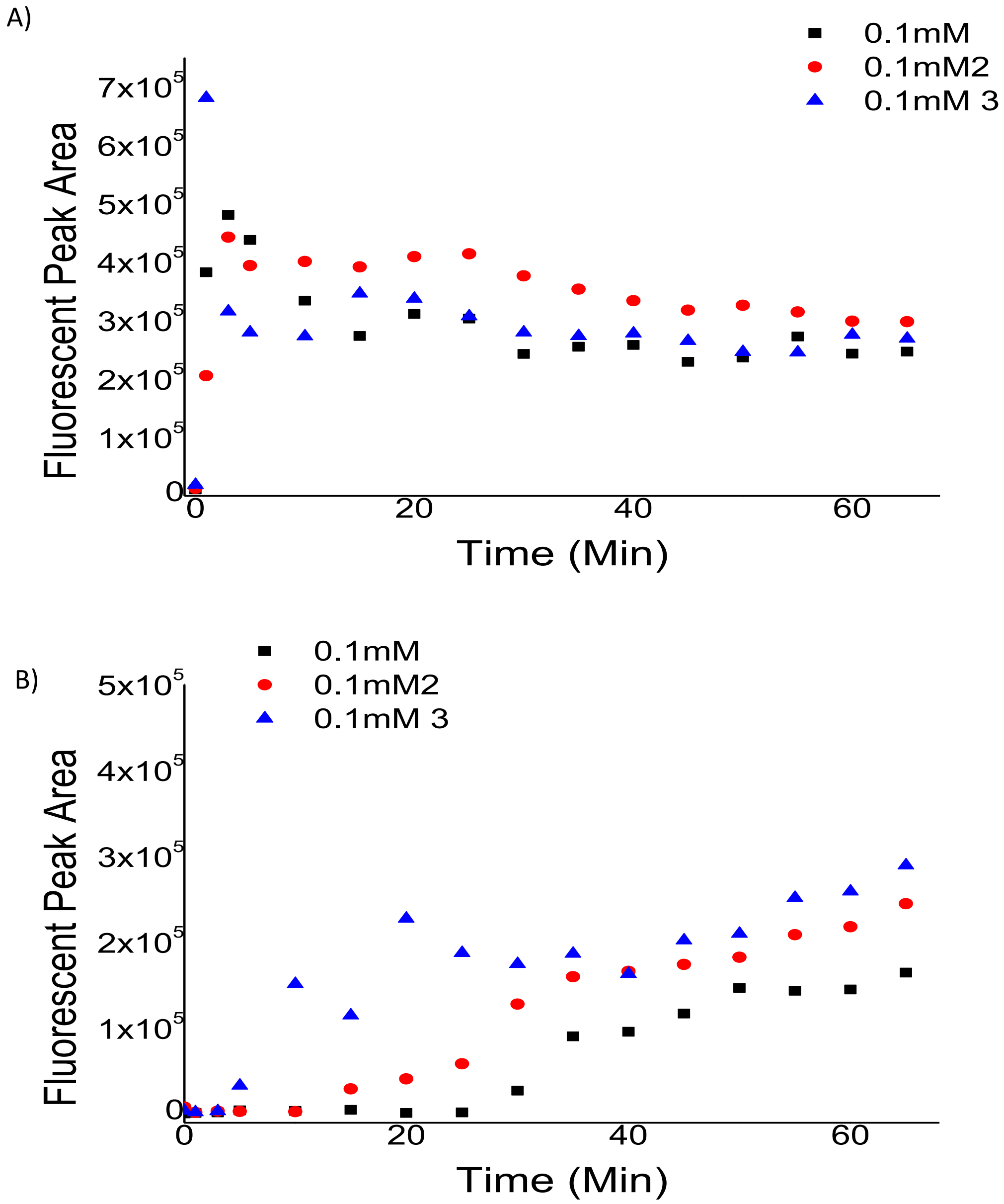

Figure 93: Fluorescent peak area of three replicate measurements at 600 nm obtained from 473 nm excitation fluorescence spectra from Natures own spanned 1 µm gold microcavities with 0.1 mM A) daunorubicin B) doxorubicin.

The daunorubicin data, as shown in Figure 93 A), showed good reproducibility in the evolution of the peak area, where an average peak area of 2.94 x 10^5 ± 1.19 x 10^4 was seen. Absolute intensity showed variation from sample to sample as expected with MEF substrates due to microscopic differences in the fabrication process. Daunorubicin is known to have electrostatic interactions with the bilayer headgroup, resulting in its backbone to be bound in the membrane[273]. Due to the presence of a positively charged phospholipid, the drug would be expected to interact electrostatically with the bilayer. DOPS has shown to increase daunorubicin's affinity and stoichiometry of binding in the membrane. However, in the presence of cholesterol, this affinty has been shown to be reversed[273]. The peak area data suggests that the drug binds to the bilayer, to an extent that prevents or reduced its diffusion into the cavity. This suggests the initial increase in fluorescence intensity was due to the drug in solution and bilayer enhancement[84]. The permeation dynamics are similar to those observed with the ternary composition, which also indicated impermeability. The data suggests that in the presence of a charged lipid or liquid ordered domains; daunorubicin cannot diffuse through the membrane.

Figure 93 B) shows the rate of change of doxorubicin's emission peak area. Unlike in daunorubicin, an increase in peak area was observed over time. The data suggest that the drug is embedding itself in the bilayer for approximately 30 minutes. After this time period, the drug begins to diffuse through the bilayer into the cavity, receiving plasmonic enhancement or it is interacting with the charged lipids within the bilayer. This could be due to the microdomains of lipid ordered phases occurring due to the lipid composition[48]. Or due to doxorubicin's tendency to aggregate[289,290], hindering in its diffusion. As the dynamics show a continuous rise across the 5 hours, this indicates that the drug did not reach equilibrium within the time window for these experiments.

When the rate of diffusion through the membrane is compared to DOPC and DOPC/SM/CH bilayers, differences are evident. As the transmission filter was changed to a higher density (from allowing 1 % through, to allowing 0.1 %) for these experiments due to increased laser power, the absolute values obtained for fluorescence intensity and peak area cannot be compared between nature's own and the previous DOPC and DOPC/SM/CH experiments. Therefore, only the dynamics were compared. Even after eliminating the diffusion step in the first 30 minutes of the sample, the kinetics of the DOPC & ternary bilayer are very different from what is observed in nature's own, as the former showed four distinctive stages in the rate of diffusion, whereas the latter showed impermeability. CH and SM decrease the fluidity of the bilayer[272] and have previously proven to be impermeable for the drugs in the ternary composition. However, in the case of doxorubicin, the drug could still permeate the nature's own bilayer, indicating that either DOPS or DOPE caused the bilayer to remain permeable and allow for diffusion. Doxorubicin has shown to have a strong affinity to negatively charged lipids[259]. SM has also shown an affinity to bind with doxorubicin; However, CH does not[272]. Meaning the presence of DOPS and SM in the bilayer should increase the likelihood of the drug remaining in the bilayer.

From this work, information on the rate of permeation was investigated. Through the use of a microfluidic device, immediate qualitative information on drug-membrane permeability was obtained, where even subtle difference between similar compounds were identified.

5.3.4 Investigation of Ruthenium Complexes and their Permeation of the Lipid Bilayer

Ruthenium(II) polypyridyl complexes have been widely studied for their DNA binding and potential as probes in diagnostic/imaging and therapeutic applications[195,196,196,197,205,322]. Here, ruthenium complexes conjugated to peptides, which have been previously extensively studied in cells such as HeLa, were examined within an enclosed microfluidic platform described in 5.2.1.3. Ru (II) polypyridyl complexes are suitable for MEF studies as although luminescent, their quantum yields are relatively low (where Ru polypyridyl have reported 2-5% quantum yields in aerated solutions at RT, Ru-DPPZ-Ester and Ru-Tap-Ester showed 0.29 & 0.28 ϕ_{1um}^{d} in water[203]). It is believed, based on temperature dependent[323] studies in cells, that these probes are taken up by an activated process, i.e. protein mediated endocytosis etc, where uptake was switched off at 4 ^{0}C. The bilayer spanned cavity platform allows for the exploration of the passive permeation. Meaning, if any uptake is observed, it was likely that permeation of these complexes is at least in part passive within cells.

5.3.4.1 Emission & Absorption Spectroscopy of Ruthenium Dyes

Spectroscopy was completed to obtain the absorption (Figure 94) and emission (Figure 95) properties of the chosen dyes. This was to ensure the luminescence could be excited at 473 nm. The spectroscopy of the ruthenium complexes in PBS buffer were examined. Table depicting spectroscopic values can be found in the appendix. All four dyes absorbed at 216 and 280 nm. The Ru-DPPZ complex showed peaks at 360 and 456.2 nm, which can be attributed to ligand-centred transition and broad metal to ligand charge transfer bands, respectively[203]. As shown in Figure 94, all four complexes show metal to ligand charge transfer around 450 nm, where the Ru-Tap complexes peaks were at 414 and 467 nm. When excited by 473 nm, all dyes showed a broad emission, with a λmax around 640 nm except for Ru-DPPZ-Ester, which was at 695 nm as shown in Figure 95. Ru-DPPZ is exceedingly weakly emissive from water[314,322], therefore, its lower emission than Ru-Tap was expected.

The conjugates were also examined in acetonitrile. The spectroscopy of the Ru-Tap complexes showed no difference from PBS, whereas the Ru-DPPZ complexes were blue-shifted to 600 nm. This shift is due to the polarity of the solvent affecting the stability of the charge transfer of the ligand. Thus, in PBS buffer (polarity index of water is 10.2[158,324]), the λmax is red-shifted, while in acetonitrile (polarity index of 5.8[158,324]) it is blue shifted. It was not unexpected for the parent and peptide Ru-Tap complexes to show similar absorbance and emission spectra, as this was demonstrated previously by Burke et al. They also recorded absorption at 415 and 460 nm and phosphorescence at 640 nm, in water and PBS buffer[202].

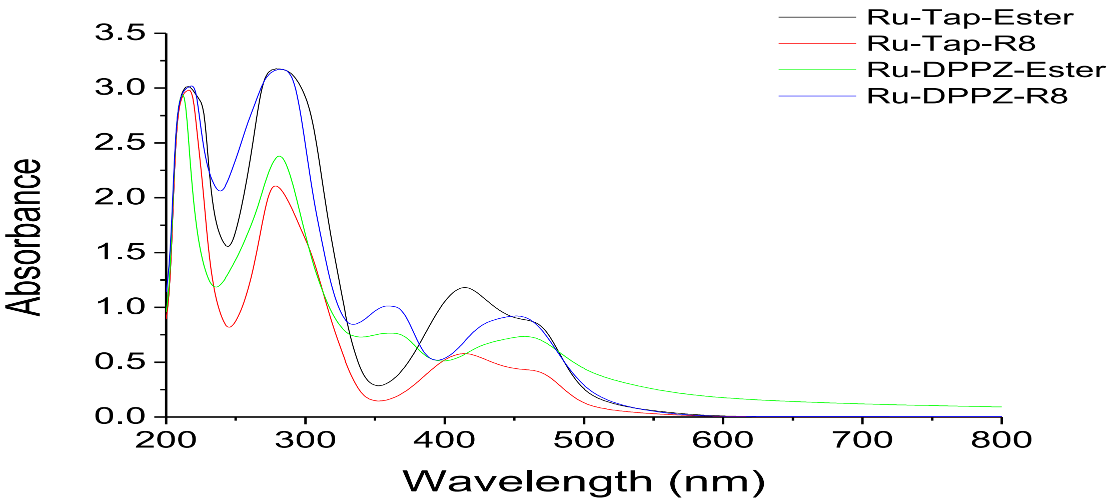

Figure 94: UV-Vis absorbance spectra of Ru-Tap-Ester, Ru-Tap-R8, Ru-Dppz-Ester, Ru-Dppz-R8 in PBS solution (pH 7.4). (13.48 mM Ru-Tap-Ester, 3.32 mM Ru-Tap-R8, 16.02 mM Ru-DPPZ-Ester & 5.03 mM Ru-DPPZ-R8)

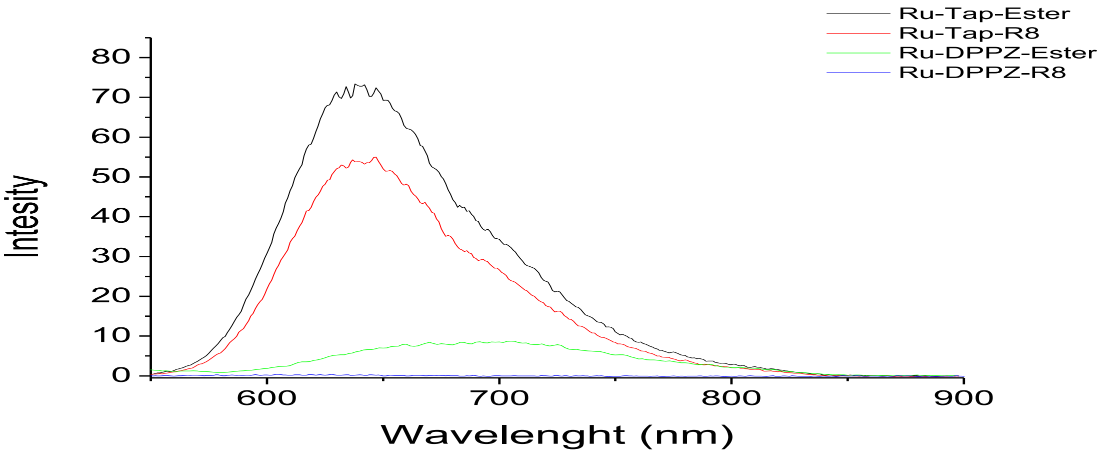

Figure 95: Emission spectra of 13.48 mM Ru-Tap-Ester, 3.32 mM Ru-Tap-R8, 16.02 mM Ru-DPPZ-Ester & 5.03 mM Ru-DPPZ-R8 in PBS solution (pH 7.4). All dyes were excited at 473 nm, and emission was collected between 500-900 nm at a slit width of 5 nm, except for Ru-DPPZ-Ester which had a slit with of 10.

5.3.4.2 Emission Measurements of Ruthenium Complexes

To evaluate the maximum enhancement achievable when the complexes reach the gold surface, initial controls were completed in the absence of the bilayer. This also allowed for the detection of any background and baseline emission that occurred from the enclosed platform and the dyes themselves. Due to the axial resolution of the microscope, the contact volume above the cavity is included within the interrogation area, however as the emission contribution from this volume should not alter after full dispersal of the dyes, it should not influence the emission kinetics observed when the dyes are interacting with the bilayer or cavity. It should be noted, that although this method allowed for reproducible measurement of the rate of luminescence increase i.e. to identify if a drug is permeating the bilayer, the luminescence intensity showed variation from sample to sample due to the nature of the cavities. Any luminescence intensity discussed in this chapter was averaged for comparison purposes and exact emission values are not used.

The ruthenium complexes (0.1 mM) were injected into the enclosed platform (in the absence of gold) and monitored over a two-hour window to observe if the platform causes any spectral interference, and to obtain the baseline emission from the complexes alone. The emission spectra for both Ru-Tap and Ru-DPPZ complexes show a similar λmax to those observed when completed in a quartz cuvette using a fluorimeter, indicating the enclosed platform causes no interference or spectral shift. Interestingly, the peptide complexes show a lower luminescence intensity than their parent complexes for both Ru-Tap and Ru-DPPZ at the platform.

The emission of the ruthenium complexes was then examined at planar gold samples within the enclosed platform and monitored for a two-hour window to verify enhancement due to the presence of gold. An intensity increase in the presence of gold was expected, as the gold itself even without the presence of nanostructures, should provide enhancement[254,325], as shown in the previous work in Chapter 4. The emission profiles were comparable to those observed for the solution alone at the platform. The samples emission intensity showed an approximate 2-fold decrease for Ru-Tap-Ester, no change for Ru-Tap-R8, 28-fold increase for Ru-DPPZ-Ester and 4.4-fold increase for Ru-DPPZ-R8.

Once again, the intensity observed for the Ru-DPPZ peptide complex was lower than that observed for the parent complex; however, the intensity for the Ru-Tap-R8 complex remained the same. Interestingly, the intensity observed for Ru-Tap-Ester on planar gold was lower than what was observed in free solution. It is known that close proximity to the metal surface, approximately 0-5 nm, can both increase and decrease the radiative decay rates of fluorophores[101], while also causing resonance energy transfer to the metal surface[326].

The differences in intensity show a subtle distinction between the parent and peptide complexes, where the latter may photo decompose more readily than the parent. If the peptide orientated itself onto the gold, then the fluorophore may be protected somewhat from the surface quenching, explaining why they might photodegrade at a quicker rate than their parent complexes. Another possibility for the decrease in luminescence intensity is that the peptide complexes may aggregate or precipitate out of solution to an extent, however, there was no visible evidence of this.

5.3.4.2.1 Influence of Cavities on Ruthenium Emission Intensity

The dyes were introduced to cavity samples to observe the enhancement properties and to identify if any spectral shift occurred due to plasmonic effects[264]. From simulations and the results described in chapter 4, it is expected that the cavities will yield signal enhancement once the dyes diffuse into the well. 0.1 mM of the ruthenium complexes were initially examined on bare cavity substrates within the enclosed platform over a 5-hour time window to ensure full dynamic window was recorded. Platforms and cavities were prefilled with PBS buffer. Spectra were taken focusing on a single cavity prior to dye addition, immediately after dye additions and then every 5 minutes.

Ru-Tap complexes emit in aqueous solutions but switch off when bound to DNA. The quenching is due to electron transfer from the guanine molecule. It has also been noted that Ru-TAP are slightly less emissive in organic solvents compared to aqueous solvents[190,205]. Emission spectra over time obtained from Ru-Tap-Ester introduced to the microcavity array are shown in Figure 96. Typically, the emission intensity increased until a maximum was reached. The intensity then decreases and stabilised. For example, in Figure 96, the emission observed at 5 minutes is only slightly lower than that observed at 120 min. Whereas, the intensity is much higher at 80 min, indicating the phosphorescence increased and then decreased.

The emission intensity was then briefly compared between cavity and planar gold samples to observe the enhancement factor of structured hotspots, however the confocal volume of the two would be different. As discussed in Section 2.3.3, simulations indicated that the shape of the cavities should focus the laser, resulting in enhancement at the bottom of the cavity, whereas planar gold should only give reflectance. Consistently, across all samples, cavities showed enhanced emission. Ru-Tap-Ester complex in aqueous solution at bare cavity arrays showed a 2.6-fold compared to free solution and 1.5-fold enhancement compared to planar gold. Whereas, the Ru-Tap-R8 at identical concentration and under the same experimental conditions yielded a 1.6-fold increase compared to both solution and planar gold. The difference in emission intensity between the parent and peptide complexes indicates that the presence of a peptide has an influence on the luminescence properties of the complex.

The emission peak area for each metal complex at the cavity samples was then examined to determine the dynamics of intensity evolution as cavities are filled in the absence of a bilayer (Figure 97). As expected, in the absence of the bilayer, qualitatively the behaviour was similar for each compound. The ester and peptide complexes showed an increase in emission peak area until about 20-30 minutes, which can be attributed to the dye diffusing into the cavity. The peak area then plateaus with some decrease in signal evident for the peptide which is likely due to photodecomposition, which previous studies has shown to occur with these dyes[191,193,194,202,203]. To minimise this effect, the laser was turned off between measurements.

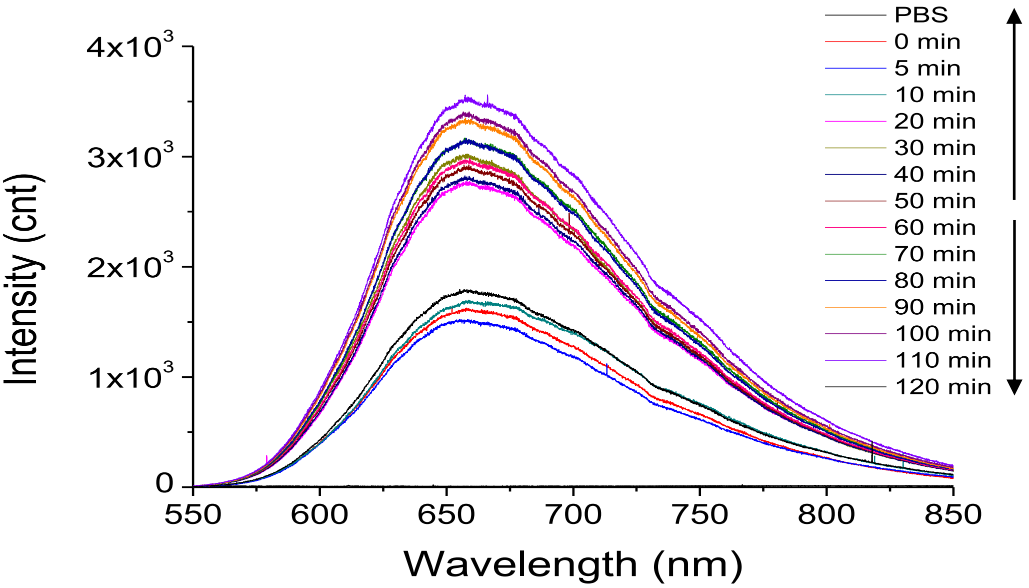

Figure 96: Time evolution of luminescence spectra obtained when 0.1 mM Ru-Tap-Ester was introduced to 1 µm bare cavities at 473 nm excitation. Where "PBS" is bilayer spectrum prior to addition of the drug, 0 min is immediately after drug introduction, and the following are spectra obtained every 5 minutes for up to two hours. Measurements was focused on a single cavity pore. Arrows are indicative of the time frames associated to the fluorescence increase and decrease.

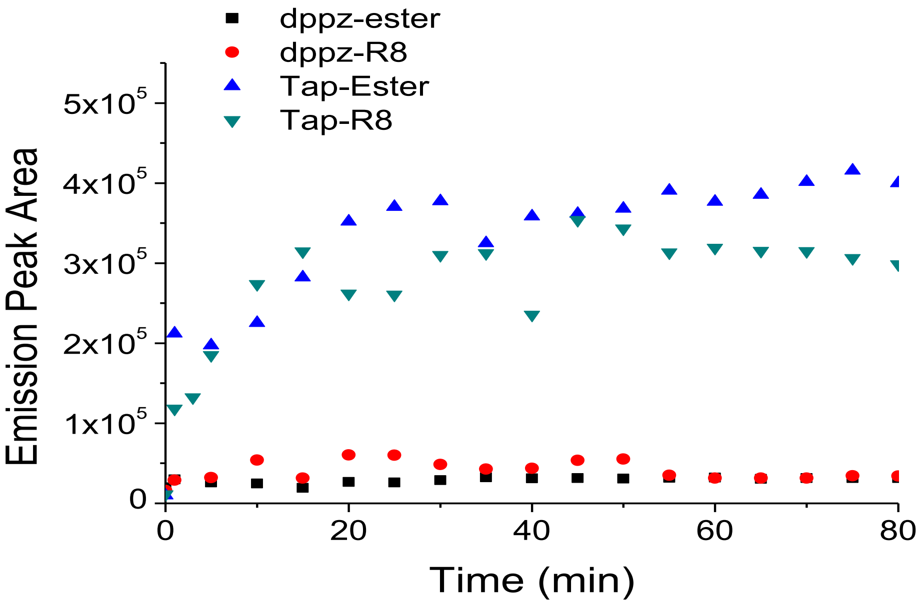

Figure 97: Emission peak area (550 – 850 nm) at 660 nm obtained from 473 nm excitation luminescence spectra of 1 µm bare gold cavities. 0.1 mM of ruthenium complexes, Ru-Tap-Ester, Ru-Tap-R8, Ru-DPPZ-Ester and Ru-DPPZ-R8 were added and monitored over two hours.

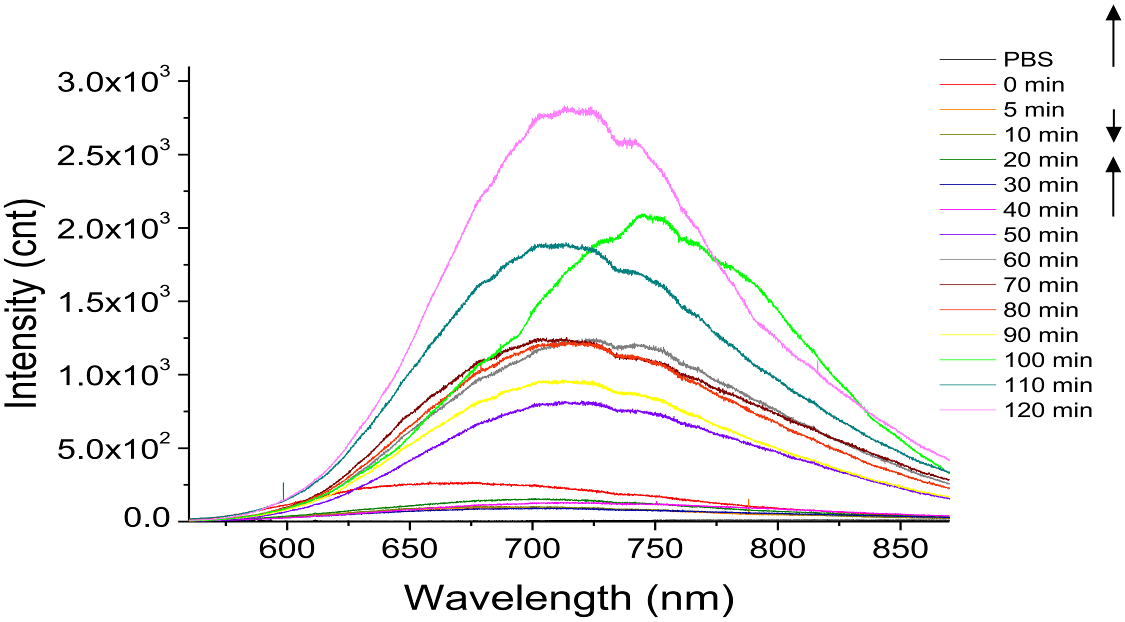

Figure 98: Time evolution of luminescence spectra obtained when 0.1 mM Ru-DPPZ-Ester was introduced to 1 µm bare cavities at 473 nm excitation. Where "PBS" is bilayer spectrum prior to addition of the drug, 0 min is immediately after drug introduction, and the following are spectra obtained every 5 minutes for up to two hours. Measurements was focused on a single cavity pore. A defined spectral shift is observable between 50-110 min.

Ru-DPPZ is a highly sensitive to aqueous media and is known to only emit in non-aqueous environments such as a lipid bilayer[327]. Hence, Ru-DPPZ complexes should emit only very weakly in an aqueous environment such as PBS. Emission from Ru-DPPZ could only be observed by using a high sensitivity CCD detector. The emission upon introduction of the Ru-DPPZ probes showed a very dramatic intensity increase in comparison to Ru-Tap complexes, where it showed a 4-fold and 16-fold intensity increase in comparison to solution alone for the parent and peptide complexes respectively. This may be due to contribution from the excited plasmon as weaker emission is known to result in higher enhancement through MEF[157]. However, it may also indicate that the complex had formed a monolayer along the gold, meaning it had surrounded itself within a SAM rather than aqueous media. This prevents hydrogen bonding from occurring with the free nitrogen's[321] which would result in "switch off".

Interestingly, Ru-DPPZ-Ester, but not the Ru-Tap complexes, showed a spectral shift over time (shown in Figure 98). Based on the experiment described in section 5.3.4.1, the λmax should be observed at 695 nm. However, at 0 min, a blue shift of the spectra was observed, which then returns to around 695 nm at 5 min. At 50 min, a spectral red shift to 710 nm was noted. The spectra returns to 695 nm at 110 min. The red shift occurred across repeats; however, the time of the shifts differed slightly. Interestingly, Ru-DPPZ in solution showed a λmax at 680 nm, whereas in contact with planar gold showed a λmax at 710 nm. This suggests that the spectral shift can be attributed to the presence of the gold. Previous studies completed on ruthenium complexes with gold have noted spectral shifts, for example, studies completed by Rogers et al.[328] and Osbourne et al.[329] have noted a blue and red shift attributed to Ru polypyridyl complexes binding to gold nanoparticles, respectively. Such phenomena are associated with metal enhanced fluorescence. In particular, one effect is attributed to the fluorophores excited state dipole moment interacting with the surrounding polar solvent molecules[101].

The fluorophores spectral shift is also dependent on the viscosity of the media. In "modest" viscosities, blue-shifts can be attributed to the reduced lifetime of polarity-sensitive fluorophores due to close proximity to the metal surface. At high viscous or glassy media, the blue shift may be attributed to the fluorophore relaxing at a faster rate than solvent reorientation[101]. However, we note a red rather than a blue shift here, also notably, the shift was not observed in the presence of the peptide complex. This strongly suggests that the shift was due to adsorption of the complex at the gold interface, which would be likely hindered due to steric effects of the peptide. Red-shifts in emission maxima on adsorption have been noted previously and can be attributed to changes in the microenvironment of the probe when it is in a SAM[242]. As explained above, this will also make the complex less water accessible and may along with MEF, explain the emission enhancement observed.

As expected, in Figure 97 showing the dynamics of the emission peak area, the Ru-DPPZ complexes showed a much lower peak area than observed for Ru-Tap complexes, but the profile of intensity area increase were roughly the same. A window of 120 minutes is shown here, but measurements were also completed over 5 hours and no additional changes were evident. Therefore, for control experiments, a two-hour window was maintained.

Due to the high emission intensities observed on planar gold samples, the large increase in emission intensity and shifting emission maxima at the cavities, it was suspected that the Ru complexes may be adsorbing onto the gold surface and forming a monolayer. This was considered likely as the Ru-DPPZ ligand contains free nitrogen, which may bind to the gold. Although, to our knowledge, Ru-DPPZ adsorption on gold has not been explored before. To test for adsorption, planar and bare cavity samples were incubated in 0.1 mM Ru-Tap-Ester and Ru-DPPZ-Ester overnight. These were then measured using 785 nm excitation for SERS and 473 nm excitation for MEF. The samples were rinsed with deionised water and remeasured to determine if adsorption had occurred.

Both Ru-Tap and Ru-DPPZ ester showed both SERS and MEF spectra on cavity and planar gold after overnight incubation. After rinsing, Ru-Tap-Ester only showed gold background signal for SERS on both planar and cavity samples. At 473nm excitation, emission intensity was notably weak on bare cavities and negligible emission was seen on planar samples. Interestingly, Ru-DPPZ-Ester showed weak SERS from both substrates. However, vibrational bands could not be observed consistently across the sample, indicating a homogenous continuous layer had not formed. Weak luminescence was observed, similar to what was observed for free solution, suggesting that the dyes were adsorbing onto the gold. The monolayer formation appeared to occur more readily for the Ru-DPPZ complex than the Ru-Tap complex. Monolayer formation may explain why such a large luminescence intensity was observed for planar samples, as 4-fold enhancement on monolayer formation of similar Ru(II) polypyridyl complexes on similar sized cavities have been previously reported[104].

Numerous studies have been completed to modify gold nanoparticles and other nanostructures with ruthenium complexes for DNA targeting etc[328–331]. For example, in one study, a ruthenium complex containing a phenanthroline with an aromatic-diimine ligand was used to modify nanoparticles for a nano-probe sensor of DNA. They found that the adsorption band at 518 nm decreased and a new broad band appeared at 670 nm. The presence of the gold nanoparticles appeared to quench the ruthenium complex emission; however, upon addition of DNA, the emission intensity was found to increase 3.6 fold, meaning the gold created a signal enhancement when there was a distance between the gold and the metal complex[332]. This is consistent with other studies that have shown that ruthenium complexes attached to coated gold structures resulting in emission quenching[330,333]. Huang & Murry reported quenching of Ru-trisbipyridyl complexes by thiol coated gold nanorods. The complex was quenched in aqueous solution due to collisional and static quenching owing to the binding of the Ru and the thiol[333]. In another study, by Jebb et al., Ru-trisbipyridyl complexes showed a 60% decrease in emission intensity due to binding with gold nanorods. This was due to the rods deactivating the excited Ru complex by an energy transfer pathway[330].

Such observations suggest that emission enhancement will compete with quenching when monolayer formation has transpired directly onto the gold substrate. However, according to the simulations completed in chapter 2, the plasmonic field extends for 3-5 nm for MEF and 8-10 nm for SERS. Meaning the molecule does not require direct adsorption onto the gold to be enhanced. Interestingly, the maximum emission intensity at bare cavities for the Ru-peptide complexes was typically higher than its ester counterparts, which may suggest that the peptide had created a “spacer”, preventing the ruthenium complex from being quenched to the same degree as the esters.

5.3.4.2.2 Permeation Studies of Ruthenium Complexes of a DOPC Bilayer.

Having established the diffusion time taken for the complexes to fill the cavity array and the expected order of magnitude of emission enhancement, the ruthenium complexes were then introduced to DOPC bilayer spanned cavities to investigate their membrane interaction and permeation. The studies were completed as described for bare cavities, where PBS prefilled platforms were measured focusing on a single pore, and then dye of interest was introduced and monitored every 5 minutes for 2 hours. The experiments were completed at three concentrations 0.2 mM, 0.1 mM and 0.05 mM. These values were selected as they are typically used for imaging applications within cells[193,194,202]. The effect of concentration is of great interest for imaging purposes, as it can influence the uptake mechanism and targeting. It can also impact cyctotoxicity[334]. As previously mentioned, Ru-Tap complexes luminescence should "switch off" when bound to guanine in DNA and have been shown to decrease in luminescence intensity in organic media[190,206,312]. Whereas Ru-DPPZ complexes should "switch on" in the presence of the organic media, i.e. in principle, this means that we should observe a significant increase in emission if Ru-DPPZ associates with the bilayer.

Emission profiles obtained from 0.1 mM Ru-Tap-ester's and Ru-Tap-R8 introduction to a DOPC bilayer are shown in Figure 99 and Figure 100, respectively. The spectra clearly show no emission from blank PBS solution. Upon dye addition, a rise in emission intensity occurred, which remained consistent over the course of two hours. The emission profile for the Ru complexes (Ru-DPPZ-Ester excluded) showed superficial differences between the bare cavities and DOPC spanned cavities. On bare cavities, it was suspected that the initial intensity increase was due to the dye diffusing into the cavity. A decrease in emission was then observed. This decrease may be attributed to quenching of the complex or to photodecomposition due to ligand exchange in water. Photocomposition of these complexes has been previously reported[193,194,202], and in this case may have been prompted by heat within the plasmonic microcavities. However, on DOPC samples, no gradual increase in emission is observable, implying that the dye is not diffusing into the cavity. This indicates that these dyes are impermeable to a DOPC membrane.

The emission peak area was plotted against time, to identify the rate of intensity increase occurring upon addition of the complexes to a DOPC spanned bilayer. This was completed for all dyes at all three concentrations. Figure 101 shows the emission peak area for Ru-Tap-Ester, after dye administration, no further change is evident, indicating that the complex did not cross the membrane. The final peak area was found to be approximately an order of magnitude lower than what was observed for the same concentration in the absence of the bilayer. Repeatedly, all three explored concentrations showed broadly the same response. There was a modest decrease in emission peak area over longer time scales for the lower concentration, that was attributed to some photodecomposition. As previously mentioned, the axial resolution should encompass the containing solution above the membrane as well as the bilayer and cavities. The initial emission enhancement can be attributed to the introduction of the dye in the containing solution. However, as clearly shown in Figure 101 where no permeation of the dye is evident, no further contribution to emission change from the contacting solution is observed. This further proves that once the dye has diffused throughout the solution, it does not give any contribution to changes in emission, and this can be solely attributed to the dye interaction with the bilayer and/or cavity.

The normalised peak area for the Ru-Tap-R8 conjugate at a DOPC bilayer is shown in Figure 102. 0.1 mM showed the maximum peak area reaching 1.8 x 10^5 cnt, whereas the ester complex only reached 4 x 10^4 cnt at this concentration. At all three concentrations, Ru-Tap-R8 showed similar dynamics. Overall, this data suggests that the Ru-Tap complexes cannot permeate a DOPC membrane. Ru-Tap is known to be strongly luminescent in aqueous media, where it is "switched off" by reduction of guanine when it binds to DNA[196] and luminescence decreases in the presence of organic media. Therefore, it was expected to observe a decrease in luminescence as it interacts with the bilayer. However, this was not observed, indicating that the Ru-Tap complexes cannot enter a cell by simple diffusion and require some form of protein or another active transport mechanism.

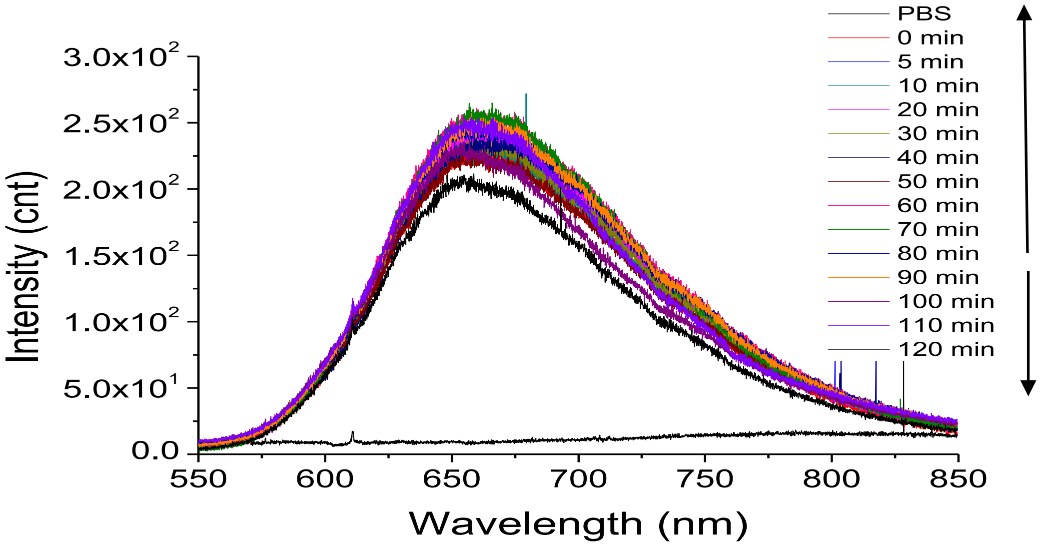

Figure 99: Time evolution of luminescence spectra obtained when 0.1 mM Ru-Tap-Ester was introduced to DOPC spanned 1 µm cavities at 473 nm excitation (single pore was monitored). Where "PBS" is bilayer spectrum prior to addition of the drug, 0 min is immediately after drug introduction, and the following are spectra obtained every 5 minutes for up to two hours. Arrows are indicative of the time frames associated to the fluorescence increase and decrease. (n ≥ 3, at RT)

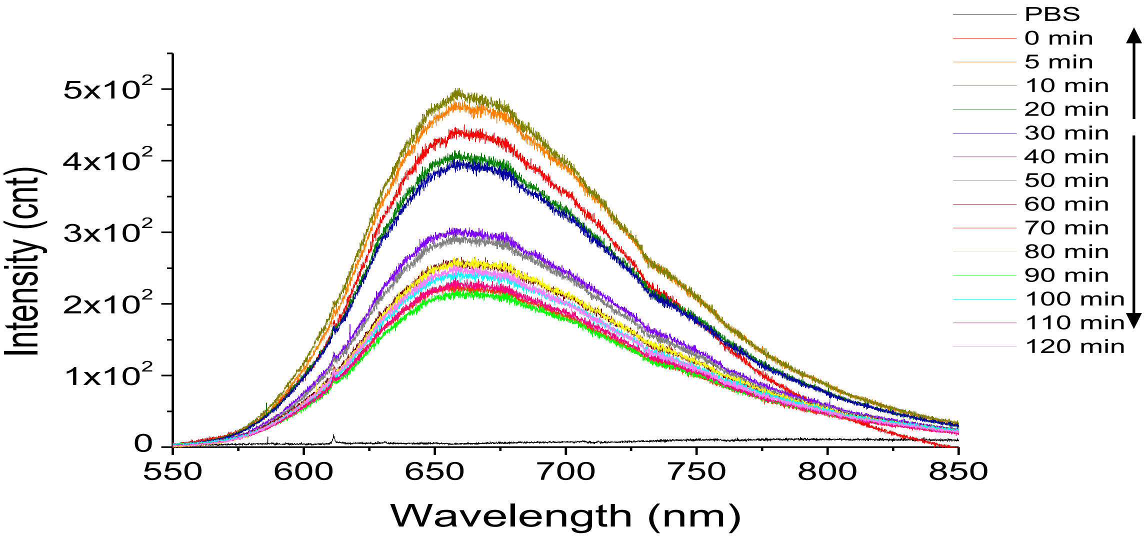

Figure 100: Time evolution of luminescence spectra obtained when 0.1 mM Ru-Tap-R8 was introduced to DOPC spanned 1 µm cavities at 473 nm excitation (single pore was monitored). Where "PBS" is bilayer spectrum prior to addition of the drug, 0 min is immediately after drug introduction, and the following are spectra obtained every 5 minutes for up to two hours. Arrows are indicative of the time frames associated to the fluorescence increase and decrease. (n ≥ 3, at RT)

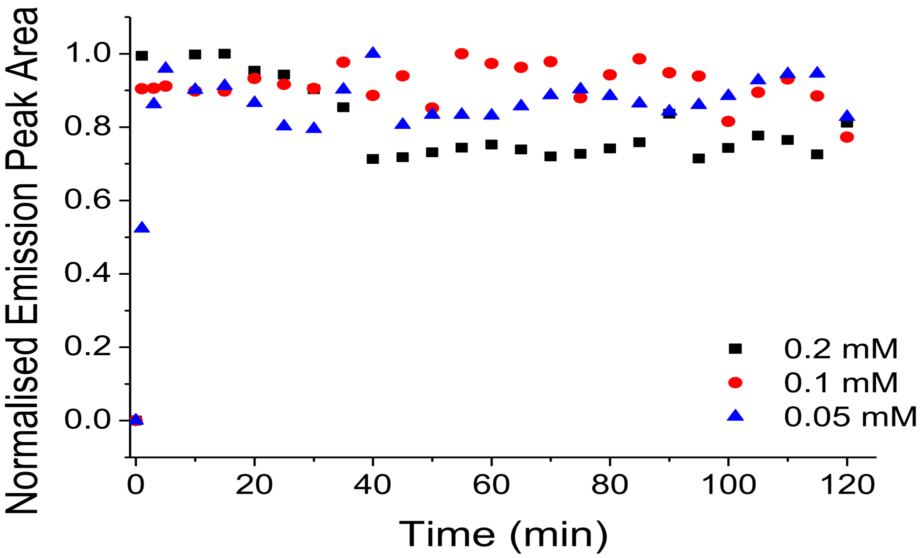

Figure 101: Dynamic changes to emission peak Area at 660 nm obtained from 473 nm excitation luminescence spectra from DOPC lipid bilayer spanned over 1 µm gold cavity array in 0.2 mM, 0.1 mM & 0.05 mM Ru-Tap-Ester. Data was normalised for comparison purposes.

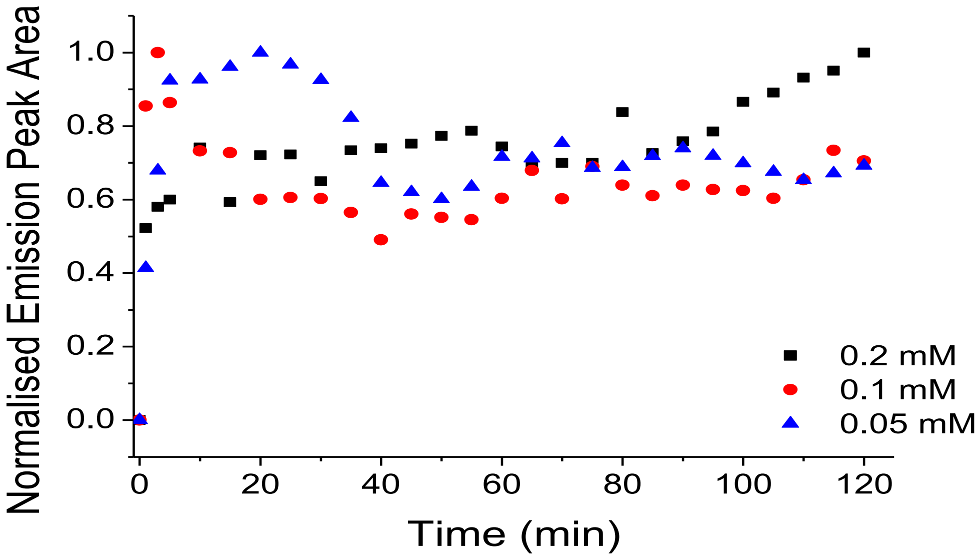

Figure 102: Dynamic changes to emission peak Area at 660 nm obtained from 473 nm excitation luminescence spectra from DOPC lipid bilayer spanned over 1 µm gold cavity array in 0.2 mM, 0.1 mM & 0.05 mM Ru-Tap-R8. Data was normalised for comparison purposes.

As Figure 103 shows, Ru-DPPZ-Ester introduced to a DOPC spanned cavity array showed notable spectral shifts, which strongly contrasts to the behaviour seen in Ru-Tap complexes. However, though the shifts were also observed in the bilayer's absence, there are some differences in its behaviour. At the earliest time points, the spectra were the same, both with and without the bilayer, where weak emission centred around 670 nm. The emission intensity then rose rapidly and shifted to the red at approximately 730 nm, which is far more red-shifted than any other spectrum for the same compound without bilayer. The far red-shift and the enhanced emission intensity may be assumed to be due to the complex associating with the bilayer, or aggregating at the bilayer, changing its microenvironment[101,242]. Although, Ru complex aggregation is unlikely to occur due to their 2^+ charge. This spectral shift is noticeably absent in the Ru-DPPZ-R8 introduction to a DOPC bilayer (spectra shown in Figure 104). Interestingly, the peptide conjugate showed an initial intensity increase followed by a small decrease and no further change. The intensity differences between the Ru-DPPZ-Ester and Ru-DPPZ-R8 suggests that the dye may be somewhat binding to the bilayer in the former and has minimal to no association with the bilayer in the latter. This could be due to the charge and hydrophobicity of the peptide molecule.

We and others have shown that Ru-DPPZ complexes intercalate and emit from liposomes. Although in previous reports, the Ru-DPPZ complex was regarded as non-emissive in water, and therefore comparisons could not be made with the shift in emission. However, Norden et al. reported a related, simpler Ru-DPPZ containing complex with 2 phenanthrole ligands emitting at 674 nm, which was a dramatic red shift from emission of 609 nm in propanediol. The emission from 670 nm in water to 730 nm in lipids would be consistent with intercalation into the bilayer here. However, with time, the intense emission was reduced and then blue shifted to 700 by 40 min, and then reduced further in intensity and centred at 670 nm by 100 min. This reduction in intensity cannot be simply ascribed to photodecomposition, as this would result in lower emission not a shift.

The spectral shift was observed across all three dye concentrations, although it is more pronounced at the higher 0.2 mM concentration. The spectral shift may be due to the superimposition of the peak maxima in different environments. This would be attributed to a ligand effect, and to its free and bound states to the bilayer and gold. As previous studies have noted spectral shifts due to binding with gold[328,329] or lipids[321], this seems likely to be occurring here. Finn et al. completed a study where lipid tails were attached to Ru(II) complexes to cause them to self-aggregate. This resulted in an emission enhancement and a red emission shift[335]. This shows that self-quenching does not occur, however the red shift may be due to the lipophilicity of the environment or due to aggregation of the complex. Interestingly, the peak maxima of the previously discussed monolayer adsorption studies of the Ru-DPPZ-Ester, was around 650 nm. However, when gold cavities were in solution after overnight incubation, the peak maxima was around 700 nm. Suggesting that when the dye is in solution, it creates a bilayer effect, resulting in a spectral shift.

A study completed by Ardhammar et al. showed through linear dichroism and lifetime results, that various Ru-DPPZ ligands can orientate themselves parallel along the surface of the bilayer, dip down into the bilayer or embedded itself into the bilayer[336]. The former two orientations are mediated by surface interactions and environmental polarity. Meaning, Ru-DPPZ complex should be localised in the bilayer or along the surface, which results in the phenazine nitrogen's being shielded, causing luminescence to be observed. However, as the luminescence intensity is only showing minor increase, where it reaches lower intensities than those observed for bare or planar gold, it suggests that the complex is not penetrating deep enough into the bilayer to receive gold plasmonic enhancement.

The intensity peak area was integrated to determine the rate of permeation. Ru-DPPZ-Ester (Figure 105) showed a similar rate and peak area for 0.05, 0.1 and 0.2 mM. Where an initial sharp increase in intensity was observed due to dye addition. The peak area then remains stable, indicating no bilayer interaction and no permeation is occurring.

Ru-DPPZ-R8 (Figure 106) showed different rates to Ru-DPPZ-Ester. 0.1 mM and 0.05 mM had a similar peak area; however, this was slightly lower than what is seen for the ester complex. 0.2 mM has a higher peak area than what was seen for the ester complex. 0.1 mM behaves similarly to what was observed in Ru-DPPZ-Ester, where there was an initial increase followed by a plateau. Whereas both 0.2 mM and 0.05 mM show an initial increase followed by a decrease in peak area. The kinetics suggest that the dye is not permeating the bilayer, regardless of concentration. The decrease in peak area for the peptide complex was suspected to be due to the peptide complex precipitating out of solution. One possibility may be due to the phosphate ions interacting with the peptide, as it has a large positive charge[337], resulting in precipitation. Ru-DPPZ is more hydrophobic than the Ru-Tap complex, which could clarify why it was more evident with Ru-DPPZ than the Ru-Tap.

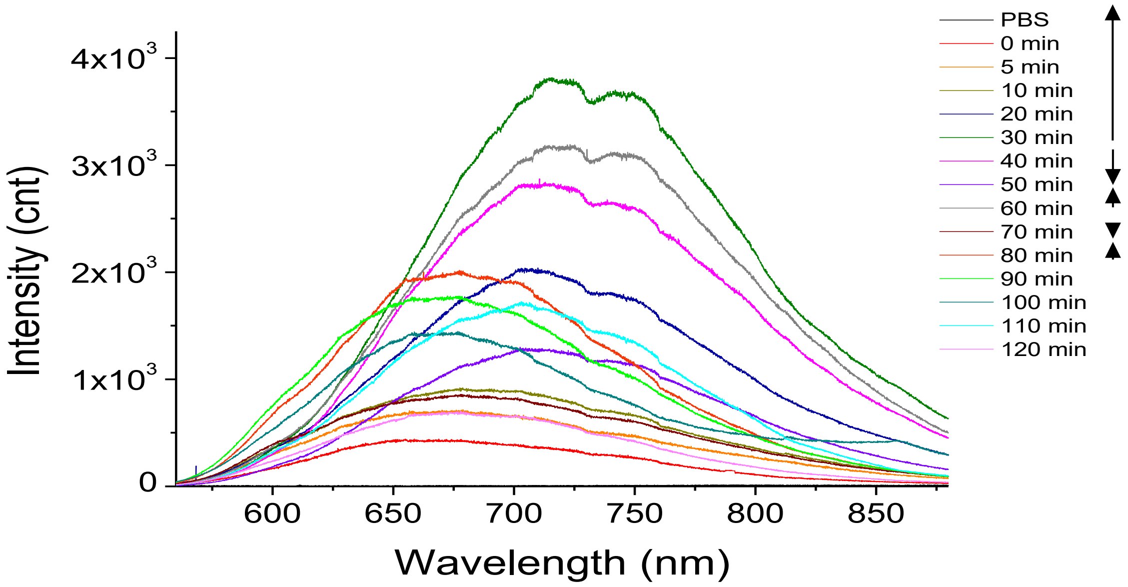

Figure 103: Time evolution of luminescence spectra obtained when 0.2 mM Ru-DPPZ-Ester was introduced to DOPC spanned 1 µm cavities at 473 nm excitation. Where "PBS" is bilayer spectrum prior to addition of the drug, 0 min is immediately after drug introduction, and the following are spectra obtained every 5 minutes for up to two hours. A clear spectral shift was observable over time. Measurements was focused on a single cavity pore. (n ≥ 3, at RT)

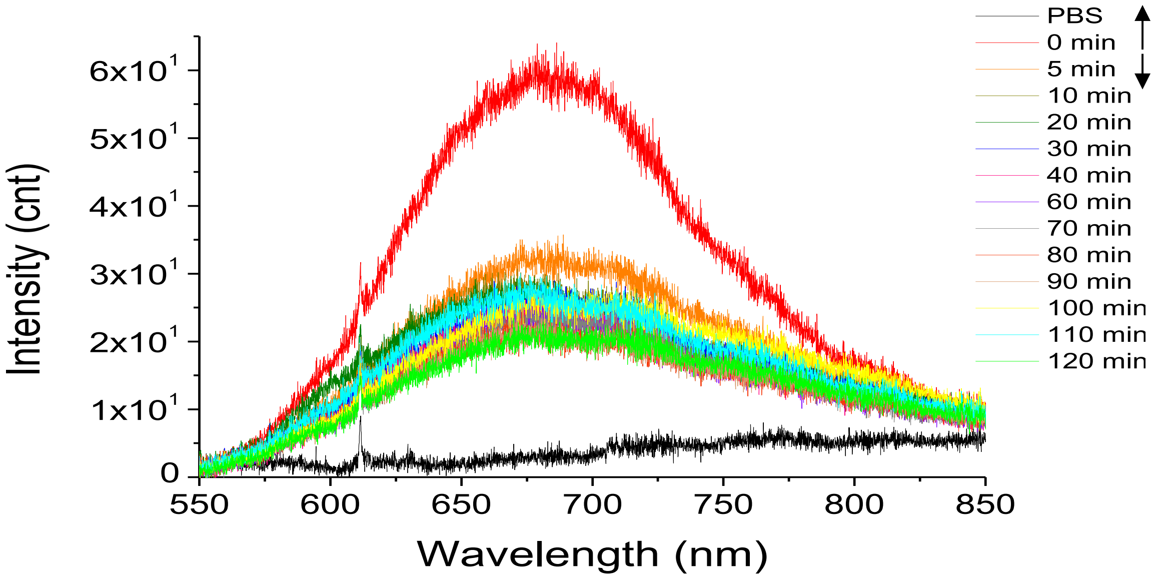

Figure 104: Time evolution of luminescence spectra obtained when 0.1 mM Ru-DPPZ-R8 was introduced to DOPC spanned 1 µm cavities at 473 nm excitation. Where "PBS" was prior to the addition of dye, 0 min was immediately after dye introduction, and the following were spectra obtained every 5 minutes for up to two hours. Measurements was focused on a single cavity pore. (n ≥ 3, at RT)

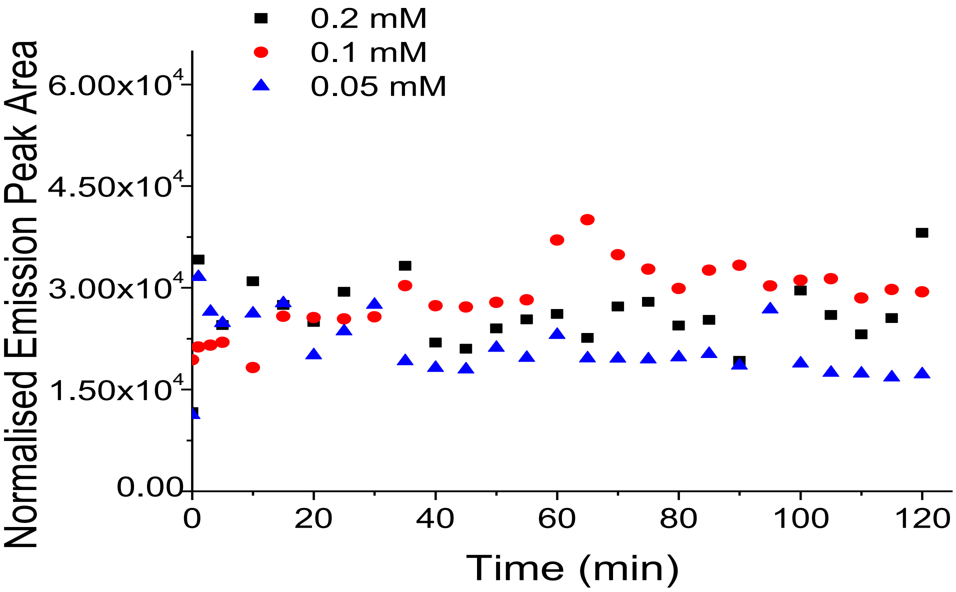

Figure 105: Dynamic changes to emission peak Area at 680-720 nm obtained from 473 nm excitation luminescence spectra from DOPC lipid bilayer spanned over 1 µm gold cavity array in 0.2 mM, 0.1 mM & 0.05 mM Ru-DPPZ-Ester.

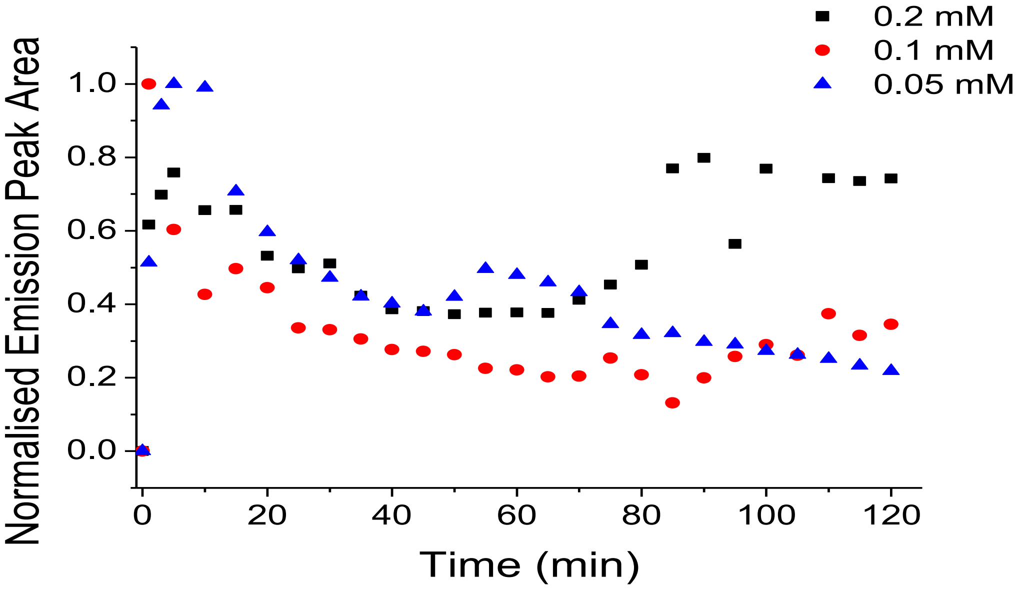

Figure 106: Dynamic changes to emission peak Area at 680 nm obtained from 473 nm excitation luminescence spectra from DOPC lipid bilayer spanned over 1 µm gold cavity array in 0.2 mM, 0.1 mM & 0.05 mM Ru-DPPZ-R8. Data was normalised for comparison purposes.

5.3.4.2.3 Ruthenium Complexes Interaction with Nature's Own Bilayer

Given the positive charge on the complex, and that this is likely to have an impact on the membrane, a more natural lipid composition was then examined for permeation. As described, Nature's own composition is composed of five readily occurring components of the bilayer, where DOPC is the most abundantly occurring[31]. As we saw previously with anthracyclines, the change in the bilayer structure can have a profound effect on the permeation of the drug/dye. As DOPS is anionic under physiological conditions, this may have an impact on its interactions with cationic probes and peptides. The experiments were conducted as described above. An example of the emission spectra is shown in Figure 107.

The emission peak area was integrated to follow the dynamic changes in emission intensity over time. An example of which can be seen in Figure 108, where Ru-DPPZ-R8 dynamics upon introduction to nature's own bilayer spanned cavities is shown. Interestingly, across all four dyes, repeatedly, similar dynamics were observed, where an initial increase until 5 minutes was observed due to dye introduction, followed by a steady plateau. This indicates that in spite of the charge, the complexes and peptide conjugates are impermeable to the bilayer. Rarely, an outlier occurs where a decrease in peak area was seen, which suggested photodecomposition had occurred, and these samples were removed. As the initial increase may be attributed to the dye's introduction, there does not appear to be any luminescence that may be attributed to plasmonic enhancement due to the bilayer or gold. When compared to results obtained for DOPC samples, similar dynamics indicating impermeability were observed.

Nature's own composition dynamics did not show the same decrease over time in emission peak area as observed in DOPC samples. The rate of permeation suggest that the peptide was not photo-decomposing when exposed to nature's own bilayers, unlike what was seen with DOPC and bare cavities. As the peptide contains numerous positive charges, it is likely that it had bonded/interacted with the negatively charged DOPS lipid. This interaction is therefore likely to be causing greater stability for the complex meaning bilayer composition has an effect on the complex. However, permeation was still not observed in the peptide's presence. The results suggest that the ruthenium complexes enter a cell through protein-mediated transport or other active transport methods as they cannot passively diffuse across the bilayer. Previous studies have shown variations of Ru-DPPZ complexes binding to negatively charged membranes (DOPC/DOPG, 4:1), where permeation into the liposome was determined by the ligands lipophilicity[327,338]. This suggests that Ru-DPPZ should interact with nature's own bilayer, however permeation was not observed.

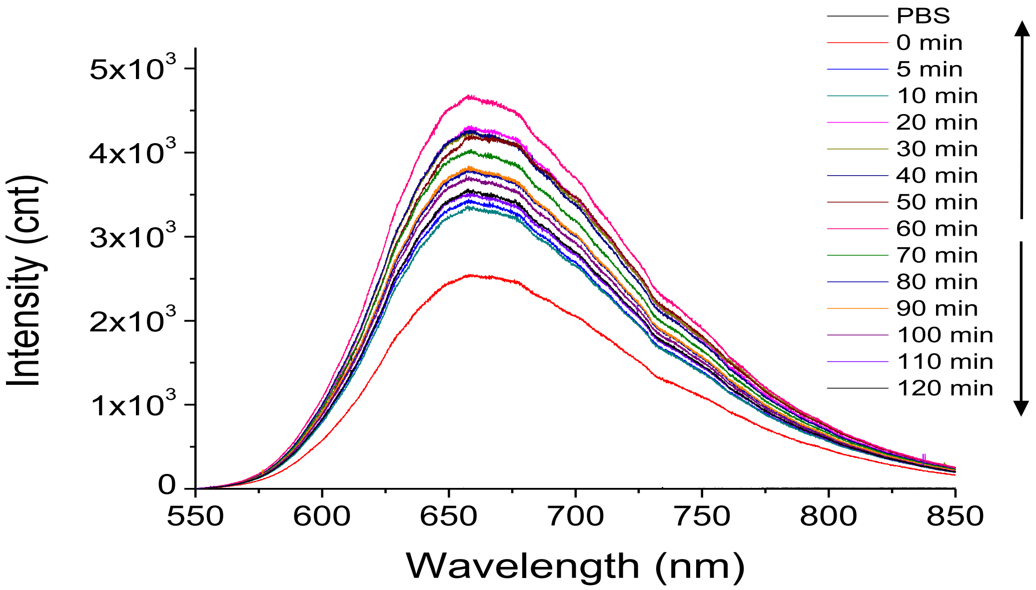

Figure 107: Time evolution of emission spectra obtained when 0.1 mM Ru-Tap-Ester was introduced to Nature's own spanned 1 µm cavities at 473 nm excitation. Where "PBS" is bilayer spectrum prior to addition of the drug, 0 min is immediately after drug introduction, and the following are spectra obtained every 5 minutes for up to two hours. Arrows are indicative of the time frames associated to the fluorescence increase and decrease. (N ≥3, RT)

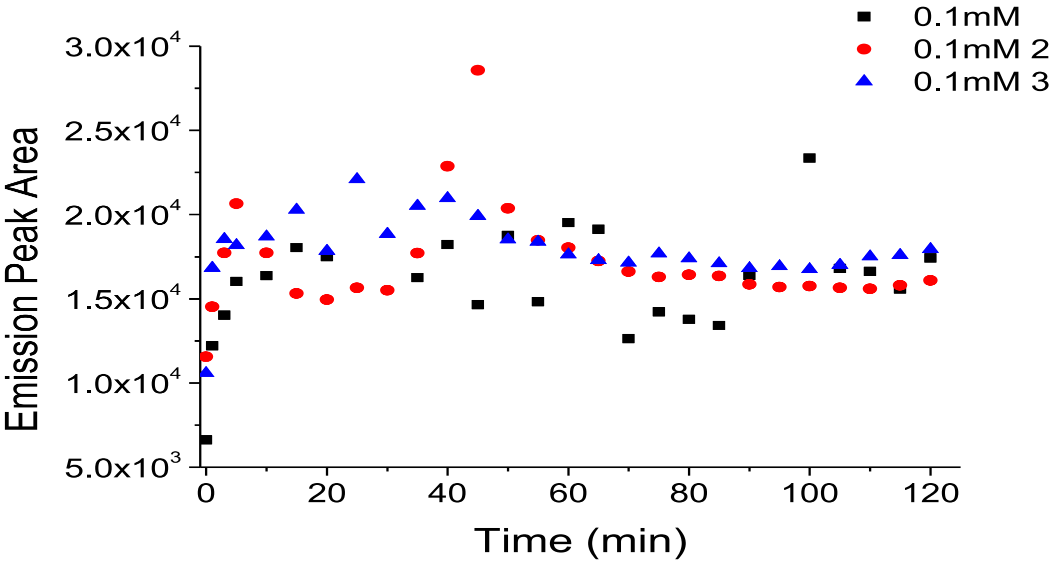

Figure 108: Dynamic changes to emission peak Area at 680 nm obtained from 473 nm excitation luminescence spectra from Nature's own lipid bilayer spanned over 1 µm gold cavity array in 0.1 mM Ru-DPPZ-R8. (N ≥3, RT)

5.4 Conclusions

In this chapter, a bilayer spanned cavity array of complex composition; DOPC/DOPE/CH/SM/DOPS (32/25/20/15/8%), intended to mimic more closely the eukaryotic plasma membrane[31], was prepared and characterised as the gold microarrays, that were assembled into an enclosed microfluidic system. This microfluidic system was designed for the purpose to reduce the diffusive mixing equilibrating time upon sample introduction to the bilayer spanned cavity array and also to reduce reagent volume and systematic errors due to temperature change, evaporation from the open system used in previous chapters.

The integrity and stability of "Nature's own" bilayers were established using EIS. Capacitance values for the bilayer were found to be 5.27 ±4.69 x10^{-2} μF, over a range of 10 hours, which is similar to 5.01 ±0.39 x10^{-2} μF shown by ternary bilayers. Resistance values were found to remain within the established parameters previously reported within the group[21,102], indicating the bilayers were stable for 10 hours. Integrity was confirmed using membrane impermeable probe, DRAQ7. However, the fluorescence signal evolution was more intense than expected, attributed to the negative charge conferred to the membrane by DOPS, which lead to electrostatic binding of the probe to the membrane. This was confirmed by preparing analogous membranes without PS, which were found to show no such association and were similarly impermeable to DRAQ7.

The permeability of the anthracycline drugs, doxorubicin and daunorubicin, explored in earlier chapters, were then examined at nature's own composition and interestingly, the evolution profile of fluorescence signal was reproducibly different for each drug which had not been observed at previous membranes. Daunorubicin appears to associate with the membrane but did not permeate through into the cavity. Whereas, doxorubicin showed evolution of metal enhanced fluorescence signal, indicating membrane penetration and diffusion. This behaviour could be rationalised on the basis of different charges of the two drugs with the membrane containing anionic lipids. That the two behaviours could be distinguished demonstrated that, notwithstanding the challenges associated with the method discussed in the previous chapter, it is a sensitive means of qualitatively distinguishing membrane interaction of closely related drugs.

Finally, we demonstrate that the platform can provide insights into uptake mechanisms for species permeable to cells. A cell impermeable ruthenium (II) polypyridyl complex and its associated permeable peptide conjugates were examined at "natures own" spanned cavity array. The complexes showed characteristic emission when excited at 473nm in PBS[203]. Typically Ru-DPPZ luminescence only very weakly from aqueous solutions[314,322], and weak emission could be observed from the parent Ru-DPPZ-ester complex in water due to the sensitivity of the CCD detector. The emissions of the parent complexes in contact with the bilayer spanned array grew over time and also exhibited a complex sequence of spectral shifts. Spectral shifts occurred both in the presence and absence of the bilayer. From previous reports[328,329,339], Ru polypyridyl complex emission shows red-shifts due to plasmon interaction at the cavity but also on association with membrane, suggesting both effects are at play.

Across both complex and its peptide conjugates, comparing intensity profiles in the absence and the presence of bilayer, it was evident that in the presence of bilayer, none of the complexes accessed the cavity/exhibited MEF. This result indicates that they are not passively permeable to the plasma membrane. This result correlates well with observations in cells, where for the peptide conjugates permeation switches off at 4 ^{0}C[193], indicating that the complexes are permeable through an activated protein mediated mechanism in cells. To continue on work from here, incorporation of proteins into the membrane could be completed and investigation of their effect on the Ru complexes permeation dynamics.

Overall, notwithstanding the limitations in terms of reproducibility MEF signal, discussed in the previous chapter, the platform can provide useful qualitative insights into permeation and interaction of different species at the cell membrane.

Chapter 6: Conclusions and Future Work

This thesis set out to evaluate if, using microcavity supported lipid bilayers, it would be possible to exploit the localised plasmonic hot spot present toward the bottom of gold microcavity wells to identify if and when a molecular species permeates the membrane and so provide a qualitative assay of molecular permeability.

In Chapter 2, optimisation of fabrication protocol for microcavity array platform was accomplished. Through a combination of capillary force and evaporation techniques[123,124], a consistently hexagonally close packed array was faithfully reproduced through a method that was significantly superior to our previous method[18,27]. The protocol for lipid bilayer assembly across the array was established, and consistent with the literature, lipid bilayers were found to be stable when spanned over our cavity arrays[27]. Through electrochemical studies it was observed that the stability was maintained for a minimal of 7 hours for the most basic DOPC composition used and stability increased with complexity of the bilayer. Nature's own composition, described in Chapter 5, showed long-term stability beyond 10 hours. This was attributed to the presence of other lipid components such as cholesterol, which is known to increase stability[31].

Chapter 3 explored whether Raman signature could be used to assess the permeation of a drug molecule through an artificial bilayer spanned over a microcavity array using Raman spectroscopy. Here, using our platform to focus on a single cavity as a single cell membrane mimic. Due to the plasmonic enhancement arising from both the top-surface and the cavity well, high quality SERS spectra were readily obtainable for the first time for a truly fluidic lipid bilayer, where different membrane compositions and drug contributions could readily be distinguished by Raman (Table 1 & Table 2).

SERS permitted interactions between the drug and bilayer to be followed over time. However, at 1 nM concentration, deciphering between lipid and drug vibrational bands was challenging and this was taken as the lowest possible concentration for analysis. However defined Raman spectra was still clearly distinguished from the background. The data also indicated both drugs showed poor permeability through a ternary bilayer composition. Comparable studies completed on planar substrates demonstrated the extent of signal enhancement obtained from the cavity arrays was significantly larger. The microcavity array also allowed for qualitative identification of differences between two drugs of very similar structures. However, limitations were identified that would limit potential quantitative study such as focal spot drift with the microscope and discrepancies in enhancement from sample to sample. Through SERS we could monitor the occurring molecular drug-membrane interactions, allowing to detect if the drug had permeated the membrane.

Following this, analogous metal enhanced fluorescence studies were completed in chapter 4. Here, fluorescence emission profiles were obtained as doxorubicin and daunorubicin were introduced to DOPC and DOPC/SM/CH bilayers spanned on microcavity arrays. As seen in Raman measurements, planar substrates proved to give inferior enhancement in comparison to cavity substrates for MEF. The fluorescence peak area was then examined to identify the occurring dynamics and from this we could distinguish between when the drug was diffusing through the contacting solution, residing within the bilayer and diffused into the cavity. Not only did this method allow for the diffusion process to be detected, lipid composition and drug concentration dependant dynamics could be identified, where ternary bilayer composition proved impermeable.

Chapter 5 developed a one-use microfluidic platform, to reduce the diffusive mixing time, volumes of reagent required, and errors associated with drug introduction to the sample. A biomimetic composition reported in liposomes to be a good mimic of mammalian plasma membrane coined "natures own" was implemented in the microfluidic platform[31]. This incorporates 5 common lipids, DOPC(32 %), DOPE (25 %), SM (15 %), CH (20 %), DOPE (8 %), and this composition was found by EIS to be stable for a minimum of 10 hours, which was further confirmed using MEF.

Anthracyclines were then introduced to nature's own bilayers, unlike other bilayers, significant differences were observed between the two drug's fluorescence intensity profiles. Where Daunorubicin showed no emission change after the diffusive mixing stage, indicating impermeablity. Whereas, a large degree of enhancement was seen for doxorubicin, indicating interaction and permeability. The difference could be ascribed to the different charges on the drugs in PBS, at the membrane which contains anionic lipid DOPS.

To evaluate if the platform could provide new insights into species of unknown permeability mechanism, we then examined cell membrane impermeable Ruthenium complexes and its peptide conjugates which are known to be permeable to live cells but through an unknown mechanism. Interestingly Ru-DPPZ showed a spectral shift over time, which did not occur in the other complexes. This was tentatively attributed to the drug binding to the gold surface[328,329] and the lipid bilayer[321]. The ruthenium complexes were all impermeable to both the DOPC and Nature's own bilayer composition, indicating they do not enter cells through passive diffusion. The ruthenium peptide conjugates showed a decrease in their emission peak area over time, indicating that precipitation or aggregation had occurred.

From this work, information on the dynamics of permeation was investigated. Through the use of a microfluidic device, immediate information on drug-membrane permeability was obtained, where even subtle difference between similar compounds were identified. This was completed through both Raman and fluorescence spectroscopy. Both methods proved to provide information on drug membrane permeability, however, different information can be elicited depending on the method. Raman spectroscopy proved to provide information on the drug-membrane interactions. This was seen in the changes of the Raman modes over time; from the original lipid bilayer, to the Raman of the drug and bilayer, until finally only the SERS from the drug in the cavity was observable. Due to the bilayers weak Raman modes, they became overshadowed by the strong SERS signal from the drug, clearly identifying when the drug has permeated the membrane. Whereas, MEF showed the dynamic response over time. The initial drug diffusion step was clearly identifiable through MEF which wasn't possible through Raman. Through the dynamic change in signal, we could identify when the drug was interacting with the membrane, and if it was permeable, in a concentration dependent manor. MEF proved to be less ambiguous than Raman for determining is a drug/dye was membrane permeable. Both methods proved to have merits, however they are not without limitations and more research is required to improve them.

Overall, we have demonstrated through bilayer spanned cavity arrays using Raman but in particular fluorescence can provide qualitative insight, into passive membrane permeation. Limitations in this method included reproducibility in signal enhancement and enhancement of signal at low drug concentrations. To minimise the variation in SERS and MEF signal intensity, greater uniformity in the cavity array is required, as well as greater control in focus drift, power variations etc.. The current method allows for variation, which is unideal if this method was to be taken for quantitative purposes. To rectify this, work is currently being completed using 2-photon 3D printing, which will ensure identical cavities. This method also allows greater control of the spacing between cavities, meaning isolation of a cavity pore is possible. This would allow for ensuring the measurement is locating within a single pore and obtaining the full enhancement, which is ideal for qualitative measurements. The enhancement properties of the cavity could be further improved by developing more hotpots within the cavities through nanostructures. This would then be followed by quenching experiments to determine the degree of enhancement from the cavities. Permeable drugs whose fluorescence is not enhanced in the bilayer would be required for this.

With further development of the microfluidic device, it can be developed into a dual detection method, where it will allow for EIS measurements while completing Raman or fluorescence measurements. This will allow for insight on the resistance and capacitance changes to the membrane as it interacts with the drug/dye. Following this, experiments to examine how pH may affects the drugs permeability through charged membranes, in particular for daunorubicin would be completed. However, this will require control experiments to ensure the pH change does not damage or alter the bilayer. Proteins shall also be incorporated into the bilayer. This is a difficulty in current methods as the protein typically becomes denatured, but due to our submerged method and space located below the bilayer, this may be less of an issue. Experiments will be done on both symmetric and asymmetric bilayers to increase the biomimicry of the permeability assay. This would be in particular interest for study with the ruthenium complexes, to demonstrate if they permeate with protein assistance, which would allow for insight into the uptake of the dyes into the cell.

The work in this thesis demonstrated that cavity substrates can be used with various biomimetic bilayer compositions to detect drug permeability. The platform allowed for reproducible identification of the presence of membrane-molecular interactions, presence of permeation and the dynamics of these processes in a novel way. Ideally all this will be used to develop a membrane permeability model that may be used in the future to accurately test an early stage, a drugs permeability and therefore reduce the number of unsuitable drugs proceeding to expensive late stage testing. Overall, with further improvement, the platform looks highly promising as a method for understanding membrane permeability across diverse membrane compositions.

References:

1. Giuliano, K. A. *et al.* High-Content Screening: A New Approach to Easing Key Bottlenecks in the Drug Discovery Process. *J. Biomol. Screen.* **2**, 249–259 (1997).
2. Paul, S. M. *et al.* How to improve R&D productivity: the pharmaceutical industry's grand challenge. *Nat. Rev. Drug Discov.* **9**, 203–214 (2010).
3. Pardridge, W. M. The Blood-Brain Barrier: Bottleneck in Brain Drug Development. *NeuroRx* **2**, 3–14 (2005).
4. Lipinski, C. A., Lombardo, F., Dominy, B. W. & Feeney, P. J. Experimental and computational approaches to estimate solubility and permeability in drug discovery and development. *Adv. Drug Deliv. Rev.* **46**, 3–26 (2001).
5. Benet, L. Z., Hosey, C. M., Ursu, O. & Oprea, T. I. BDDCS, the Rule of 5 and Drugability. *Adv. Drug Deliv. Rev.* **101**, 89–98 (2016).
6. Kirsch, S. A. & Böckmann, R. A. Membrane pore formation in atomistic and coarse-grained simulations. *Biochim. Biophys. Acta BBA - Biomembr.* **1858**, 2266–2277 (2016).
7. Bassolino, D., Alper, H. & Stouch, T. R. Drug-membrane interactions studied by molecular dynamics simulation: size dependence of diffusion. *Drug Des. Discov.* **13**, 135–141 (1996).
8. Seydel, J. K. & Wiese, M. *Drug-Membrane Interactions: Analysis, Drug Distribution, Modeling.* (John Wiley & Sons, 2009).
9. Shinoda, W. Permeability across lipid membranes. *Biochim. Biophys. Acta BBA - Biomembr.* **1858**, 2254–2265 (2016).
10. Kokate, A., Li, X. & Jasti, B. Effect of Drug Lipophilicity and Ionization on Permeability Across the Buccal Mucosa: A Technical Note. *AAPS PharmSciTech* **9**, 501–504 (2008).
11. Fossati, L. *et al.* Use of simulated intestinal fluid for Caco-2 permeability assay of lipophilic drugs. *Int. J. Pharm.* **360**, 148–155 (2008).
12. Kerns, E. H. *et al.* Combined application of parallel artificial membrane permeability assay and Caco-2 permeability assays in drug discovery. *J. Pharm. Sci.* **93**, 1440–1453 (2004).
13. M. Reis, J., Sinko, B. & H.R. Serra, C. Parallel Artificial Membrane Permeability Assay (PAMPA) - Is it Better than Caco-2 for Human Passive Permeability Prediction? *Mini Rev. Med. Chem.* **10**, 1071–1076 (2010).
14. Khan, M., Dosoky, N. & Williams, J. Engineering Lipid Bilayer Membranes for Protein Studies. *Int. J. Mol. Sci.* **14**, 21561–21597 (2013).
15. Castellana, E. T. & Cremer, P. S. Solid supported lipid bilayers: From biophysical studies to sensor design. *Surf. Sci. Rep.* **61**, 429–444 (2006).
16. Richter, R. P., Bérat, R. & Brisson, A. R. Formation of Solid-Supported Lipid Bilayers: An Integrated View. *Langmuir* **22**, 3497–3505 (2006).

17. Ramadurai, S. *et al.* Microcavity-Supported Lipid Bilayers; Evaluation of Drug–Lipid Membrane Interactions by Electrochemical Impedance and Fluorescence Correlation Spectroscopy. *Langmuir* **35**, 8095–8109 (2019).
18. Maher, S., Basit, H., Forster, R. J. & Keyes, T. E. Micron dimensioned cavity array supported lipid bilayers for the electrochemical investigation of ionophore activity. *Bioelectrochemistry* **112**, 16–23 (2016).
19. Kahya, N., Scherfeld, D., Bacia, K., Poolman, B. & Schwille, P. Probing Lipid Mobility of Raft-exhibiting Model Membranes by Fluorescence Correlation Spectroscopy. *J. Biol. Chem.* **278**, 28109–28115 (2003).
20. Kilin, V. *et al.* Fluorescence Lifetime Imaging of Membrane Lipid Order with a Ratiometric Fluorescent Probe. *Biophys. J.* **108**, 2521–2531 (2015).
21. Basit, H., Gaul, V., Maher, S., Forster, R. J. & Keyes, T. E. Aqueous-filled polymer microcavity arrays: versatile & stable lipid bilayer platforms offering high lateral mobility to incorporated membrane proteins. *Analyst* **140**, 3012–3018 (2015).
22. Steinem, C., Janshoff, A., Ulrich, W.-P., Sieber, M. & Galla, H.-J. Impedance analysis of supported lipid bilayer membranes: a scrutiny of different preparation techniques. *Biochim. Biophys. Acta BBA - Biomembr.* **1279**, 169–180 (1996).
23. Schlücker, S. Surface-Enhanced Raman Spectroscopy: Concepts and Chemical Applications. *Angew. Chem. Int. Ed.* **53**, 4756–4795 (2014).
24. Moerner, W. E. & Fromm, D. P. Methods of single-molecule fluorescence spectroscopy and microscopy. *Rev. Sci. Instrum.* **74**, 3597–3619 (2003).
25. Fromm, D. P. *et al.* Exploring the chemical enhancement for surface-enhanced Raman scattering with Au bowtie nanoantennas. *J. Chem. Phys.* **124**, 61101 (2006).
26. Baumberg, J. J. *et al.* Angle-Resolved Surface-Enhanced Raman Scattering on Metallic Nanostructured Plasmonic Crystals. *Nano Lett.* **5**, 2262–2267 (2005).
27. Jose, B., Mallon, C. T., Forster, R. J., Blackledge, C. & Keyes, T. E. Lipid bilayer assembly at a gold nanocavity array. *Chem. Commun.* **47**, 12530–12532 (2011).
28. Clark, M. A., Choi, J. & Douglas, M. Components and Structure. in *Biology 2e* (OpenStax Biology 2nd Edition, 2018).
29. Siontorou, C. G., Nikoleli, G.-P., Nikolelis, D. P. & Karapetis, S. K. Artificial Lipid Membranes: Past, Present, and Future. *Membranes* **7**, 38 (2017).
30. Li, J. *et al.* A review on phospholipids and their main applications in drug delivery systems. *Asian J. Pharm. Sci.* **10**, 81–98 (2015).
31. Haque, Md. E., McIntosh, T. J. & Lentz, B. R. Influence of Lipid Composition on Physical Properties and PEG-Mediated Fusion of Curved and Uncurved Model Membrane Vesicles: "Nature's Own" Fusogenic Lipid Bilayer. *Biochemistry* **40**, 4340–4348 (2001).

32. Heberle, F. A. & Feigenson, G. W. Phase Separation in Lipid Membranes. *Cold Spring Harb. Perspect. Biol.* **3**, (2011).
33. Lodish, H. *et al. Membrane Proteins*. (2000).
34. Bull, S. C. & Doig, A. J. Properties of Protein Drug Target Classes. *PLoS ONE* **10**, (2015).
35. Jesorka, A. & Orwar, O. Liposomes: Technologies and Analytical Applications. *Annu. Rev. Anal. Chem.* **1**, 801–832 (2008).
36. Bangham, A. D. & Horne, R. W. Negative staining of phospholipids and their structural modification by surface-active agents as observed in the electron microscope. *J. Mol. Biol.* **8**, 660-IN10 (1964).
37. Gaul, V. Integrin αIIbβ3: from platelet membrane to biomimetic models. (Dublin City University, 2016).
38. Hope, M. J., Bally, M. B., Webb, G. & Cullis, P. R. Production of large unilamellar vesicles by a rapid extrusion procedure. Characterization of size distribution, trapped volume and ability to maintain a membrane potential. *Biochim. Biophys. Acta BBA - Biomembr.* **812**, 55–65 (1985).
39. Shen, J. *et al.* A Liposome Encapsulated Ruthenium Polypyridine Complex as a Theranostic Platform for Triple-Negative Breast Cancer. *Nano Lett.* **17**, 2913–2920 (2017).
40. Zhu, D. *et al.* Ag@4ATP-coated liposomes: SERS traceable delivery vehicles for living cells. *Nanoscale* **6**, 8155–8161 (2014).
41. Gallois, L., Fiallo, M. & Garnier-Suillerot, A. Comparison of the interaction of doxorubicin, daunorubicin, idarubicin and idarubicinol with large unilamellar vesicles: Circular dichroism study. *Biochim. Biophys. Acta BBA - Biomembr.* **1370**, 31–40 (1998).
42. Matos, C., Moutinho, C. & Lobão, P. Liposomes as a Model for the Biological Membrane: Studies on Daunorubicin Bilayer Interaction. *J. Membr. Biol.* **245**, 69–75 (2012).
43. Sadeghi, N. *et al.* Influence of cholesterol inclusion on the doxorubicin release characteristics of lysolipid-based thermosensitive liposomes. *Int. J. Pharm.* **548**, 778–782 (2018).
44. Sackmann, E., Duwe, H.-P. & Engelhardt, H. Membrane bending elasticity and its role for shape fluctuations and shape transformations of cells and vesicles. *Faraday Discuss. Chem. Soc.* **81**, 281–290 (1986).
45. Wesołowska, O., Michalak, K., Maniewska, J. & Hendrich, A. Giant unilamellar vesicles - a perfect tool to visualize phase separation and lipid rafts in model systems. *Acta Biochim. Pol.* **56**, 33–39 (2009).
46. Scherfeld, D., Kahya, N. & Schwille, P. Lipid Dynamics and Domain Formation in Model Membranes Composed of Ternary Mixtures of Unsaturated and Saturated Phosphatidylcholines and Cholesterol. *Biophys. J.* **85**, 3758–3768 (2003).
47. Shimokawa, N., Hishida, M., Seto, H. & Yoshikawa, K. Phase separation of a mixture of charged and neutral lipids on a giant vesicle induced by small cations. *Chem. Phys. Lett.* **496**, 59–63 (2010).
48. Gaul, V. *et al.* The lateral diffusion and fibrinogen induced clustering of platelet integrin αIIbβ3 reconstituted into physiologically mimetic GUVs. *Integr. Biol.* **7**, 402–411 (2015).
49. Langmuir–Blodgett method. http://eng.thesaurus.rusnano.com/wiki/article1797.(Image source)

50. Hardy, G. J., Nayak, R. & Zauscher, S. Model cell membranes: Techniques to form complex biomimetic supported lipid bilayers via vesicle fusion. *Curr. Opin. Colloid Interface Sci.* **18**, 448–458 (2013).
51. Contreras, F.-X., Sánchez-Magraner, L., Alonso, A. & Goñi, F. M. Transbilayer (flip-flop) lipid motion and lipid scrambling in membranes. *FEBS Lett.* **584**, 1779–1786 (2010).
52. Kung, L. A., Kam, L., Hovis, J. S. & Boxer, S. G. Patterning Hybrid Surfaces of Proteins and Supported Lipid Bilayers. *Langmuir* **16**, 6773–6776 (2000).
53. Reviakine, I. & Brisson, A. Streptavidin 2D Crystals on Supported Phospholipid Bilayers: Toward Constructing Anchored Phospholipid Bilayers. *Langmuir* **17**, 8293–8299 (2001).
54. Reviakine, I., Bergsma-Schutter, W. & Brisson, A. Growth of Protein 2-D Crystals on Supported Planar Lipid Bilayers Imagedin Situby AFM. *J. Struct. Biol.* **121**, 356–362 (1998).
55. Leverette, C. L. & Dluhy, R. A. Vibrational characterization of a planar-supported model bilayer system utilizing surface-enhanced Raman scattering (SERS) and infrared reflection–absorption spectroscopy (IRRAS). *Colloids Surf. Physicochem. Eng. Asp.* **243**, 157–167 (2004).
56. Yuan, J., Hao, C., Chen, M., Berini, P. & Zou, S. Lipid Reassembly in Asymmetric Langmuir–Blodgett/Langmuir–Schaeffer Bilayers. *Langmuir* **29**, 221–227 (2013).
57. Lenz, P., Ajo-Franklin, C. M. & Boxer, S. G. Patterned Supported Lipid Bilayers and Monolayers on Poly(dimethylsiloxane). *Langmuir* **20**, 11092–11099 (2004).
58. Kam, L. & Boxer, S. G. Spatially Selective Manipulation of Supported Lipid Bilayers by Laminar Flow: Steps Toward Biomembrane Microfluidics. *Langmuir* **19**, 1624–1631 (2003).
59. Jackman, J. A., Knoll, W. & Cho, N.-J. Biotechnology Applications of Tethered Lipid Bilayer Membranes. *Materials* **5**, 2637–2657 (2012).
60. Bain, C. D. *et al.* Formation of monolayer films by the spontaneous assembly of organic thiols from solution onto gold. *J. Am. Chem. Soc.* **111**, 321–335 (1989).
61. Ivanova, E. P. *et al.* Natural bactericidal surfaces: mechanical rupture of Pseudomonas aeruginosa cells by cicada wings. *Small Weinh. Bergstr. Ger.* **8**, 2489–2494 (2012).
62. Chadli, M. *et al.* New Tethered Phospholipid Bilayers Integrating Functional G-Protein-Coupled Receptor Membrane Proteins. *Langmuir* **33**, 10385–10401 (2017).
63. Im, H., J. Wittenberg, N., Lesuffleur, A., C. Lindquist, N. & Oh, S.-H. Membrane protein biosensing with plasmonic nanopore arrays and pore -spanning lipid membranes. *Chem. Sci.* **1**, 688–696 (2010).
64. Bayley, H. *et al.* Droplet interface bilayers. *Mol. Biosyst.* **4**, 1191–1208 (2008).
65. Leptihn, S., Thompson, J. R., Ellory, J. C., Tucker, S. J. & Wallace, M. I. In Vitro Reconstitution of Eukaryotic Ion Channels Using Droplet Interface Bilayers. *J. Am. Chem. Soc.* **133**, 9370–9375 (2011).
66. Castell, O. K., Berridge, J. & Wallace, M. I. Quantification of Membrane Protein Inhibition by Optical Ion Flux in a Droplet Interface Bilayer Array. *Angew. Chem. Int. Ed.* **51**, 3134–3138 (2012).
67. Hwang, W. L., Chen, M., Cronin, B., Holden, M. A. & Bayley, H. Asymmetric Droplet Interface Bilayers. *J. Am. Chem. Soc.* **130**, 5878–5879 (2008).

68. Maglia, G. *et al.* Droplet networks with incorporated protein diodes show collective properties. *Nat. Nanotechnol.* **4**, 437–440 (2009).
69. Harayama, T. & Riezman, H. Understanding the diversity of membrane lipid composition. *Nat. Rev. Mol. Cell Biol.* **19**, 281–296 (2018).
70. Maxfield, F. R. Plasma membrane microdomains. *Curr. Opin. Cell Biol.* **14**, 483–487 (2002).
71. Schmid, F. Physical mechanisms of micro- and nanodomain formation in multicomponent lipid membranes. *Biochim. Biophys. Acta BBA - Biomembr.* **1859**, 509–528 (2017).
72. Simons, K. & Ikonen, E. Functional rafts in cell membranes. *Nature* **387**, 569–572 (1997).
73. Sevcsik, E. *et al.* GPI-anchored proteins do not reside in ordered domains in the live cell plasma membrane. *Nat. Commun.* **6**, 6969 (2015).
74. R. Dent, M. *et al.* Imaging phase separation in model lipid membranes through the use of BODIPY based molecular rotors. *Phys. Chem. Chem. Phys.* **17**, 18393–18402 (2015).
75. Tian, M. *et al.* A single fluorescent probe enables clearly discriminating and simultaneously imaging liquid-ordered and liquid-disordered microdomains in plasma membrane of living cells. *Biomaterials* **120**, 46–56 (2017).
76. Lorent, J. H. & Levental, I. Structural determinants of protein partitioning into ordered membrane domains and lipid rafts. *Chem. Phys. Lipids* **192**, 23–32 (2015).
77. Sharpe, H. J., Stevens, T. J. & Munro, S. A comprehensive comparison of transmembrane domains reveals organelle-specific properties. *Cell* **142**, 158–169 (2010).
78. Diaz-Rohrer, B. B., Levental, K. R., Simons, K. & Levental, I. Membrane raft association is a determinant of plasma membrane localization. *Proc. Natl. Acad. Sci.* **111**, 8500–8505 (2014).
79. Bayburt, T. H. & Sligar, S. G. Self-assembly of single integral membrane proteins into soluble nanoscale phospholipid bilayers. *Protein Sci.* **12**, 2476–2481 (2003).
80. Scotto, A. W. & Zakim, D. Reconstitution of membrane proteins. Spontaneous incorporation of integral membrane proteins into preformed bilayers of pure phospholipid. *J. Biol. Chem.* **263**, 18500–18506 (1988).
81. Nguyen, P. A., Field, C. M., Groen, A. C., Mitchison, T. J. & Loose, M. Chapter 12 - Using supported bilayers to study the spatiotemporal organization of membrane-bound proteins. in *Methods in Cell Biology* (eds. Ross, J. & Marshall, W. F.) vol. 128 223–241 (Academic Press, 2015).
82. Tethered Polymer-Supported Planar Lipid Bilayers for Reconstitution of Integral Membrane Proteins: Silane-Polyethyleneglycol-Lipid as a Cushion and Covalent Linker. *Biophys. J.* **79**, 1400–1414 (2000).
83. Patel, A. G. & Kaufmann, S. H. How does doxorubicin work? *eLife* **1**, (2012).
84. Heywang, C., Saint-Pierre Chazalet, M., Masson, M. & Bolard, J. Orientation of Anthracyclines in Lipid Monolayers and Planar Asymmetrical Bilayers: A Surface-Enhanced Resonance Raman Scattering Study. *Biophys. J.* **75**, 2368–2381 (1998).

85. Iversen, T.-G., Skotland, T. & Sandvig, K. Endocytosis and intracellular transport of nanoparticles: Present knowledge and need for future studies. *Nano Today* **6**, 176–185 (2011).

86. Vale, R. D. The Molecular Motor Toolbox for Intracellular Transport. *Cell* **112**, 467–480 (2003).

87. Bareford, L. M. & Swaan, P. W. Endocytic mechanisms for targeted drug delivery. *Adv. Drug Deliv. Rev.* **59**, 748–758 (2007).

88. Salama, N. N., Eddington, N. D. & Fasano, A. Tight junction modulation and its relationship to drug delivery. *Adv. Drug Deliv. Rev.* **58**, 15–28 (2006).

89. Li, S., Hu, P. & Malmstadt, N. Confocal Imaging to Quantify Passive Transport across Biomimetic Lipid Membranes. *Anal. Chem.* **82**, 7766–7771 (2010).

90. Bennion, B. J. *et al.* Predicting a Drug's Membrane Permeability: A Computational Model Validated With in Vitro Permeability Assay Data. *J. Phys. Chem. B* **121**, 5228–5237 (2017).

91. Liu, X., Testa, B. & Fahr, A. Lipophilicity and its relationship with passive drug permeation. *Pharm. Res.* **28**, 962–977 (2011).

92. Manallack, D. T. The pKa Distribution of Drugs: Application to Drug Discovery. *Perspect. Med. Chem.* **1**, 25–38 (2007).

93. Drumetix | In Vitro DMPK-Protein binding. http://www.drumetix.com/php/dmpk-permeability.php. (Image source)

94. Yee, S. In Vitro Permeability Across Caco-2 Cells (Colonic) Can Predict In Vivo (Small Intestinal) Absorption in Man—Fact or Myth. *Pharm. Res.* **14**, 763–766 (1997).

95. Irvine, J. D. *et al.* MDCK (Madin–Darby canine kidney) cells: A tool for membrane permeability screening. *J. Pharm. Sci.* **88**, 28–33 (1999).

96. Zhu, C., Jiang, L., Chen, T.-M. & Hwang, K.-K. A comparative study of artificial membrane permeability assay for high throughput profiling of drug absorption potential. *Eur. J. Med. Chem.* **37**, 399–407 (2002).

97. Potter, T., Ermondi, G., Newbury, G. & Caron, G. Relating Caco-2 permeability to molecular properties using block relevance analysis. *MedChemComm* **6**, 626–629 (2015).

98. di Cagno, M., Bibi, H. A. & Bauer-Brandl, A. New biomimetic barrier Permeapad™ for efficient investigation of passive permeability of drugs. *Eur. J. Pharm. Sci.* **73**, 29–34 (2015).

99. Berben, P. *et al.* Drug permeability profiling using cell-free permeation tools: Overview and applications. *Eur. J. Pharm. Sci.* **119**, 219–233 (2018).

100. Smith, E. & Dent, G. *Modern Raman spectroscopy: a practical approach.* (J. Wiley, 2005).

101. Geddes, C. D. *Metal-enhanced fluorescence.*

102. Maher, S. Microcavity PDMS and gold substrates for supported lipid bilayers. (Dublin City University. School of Chemical Sciences, 2016).

103. Burmeister, F. *et al.* From Mesoscopic to Nanoscopic Surface Structures: Lithography with Colloid Monolayers. *Adv. Mater.* **10**, 495–497 (1999).

104. Jose, B. *et al.* Emission enhancement within gold spherical nanocavity arrays. *Phys. Chem. Chem. Phys.* **11**, 10923–10933 (2009).

105. Bartlett, P. N., Baumberg, J. J., Coyle, S. & Abdelsalam, M. E. Optical properties of nanostructured metal films. *Faraday Discuss.* **125**, 117–132; discussion 195-219 (2004).

106. Jose, B., Mallon, C. T., Forster, R. J. & Keyes, T. E. Regio-selective decoration of nanocavity metal arrays: contributions from localized and delocalized plasmons to surface enhanced Raman spectroscopy. *Phys. Chem. Chem. Phys.* **13**, 14705–14714 (2011).

107. Colson, P., Henrist, C. & Cloots, R. Nanosphere Lithography: A Powerful Method for the Controlled Manufacturing of Nanomaterials. *J. Nanomater.* (2013) doi:10.1155/2013/948510.

108. Hulteen, J. C. & Van Duyne, R. P. Nanosphere lithography: A materials general fabrication process for periodic particle array surfaces. *J. Vac. Sci. Technol. A* **13**, 1553–1558 (1995).

109. Cai, Y. & Ocko, B. M. Large-Scale Fabrication of Protein Nanoarrays Based on Nanosphere Lithography. *Langmuir* **21**, 9274–9279 (2005).

110. Adachi, E., Dimitrov, A. S. & Nagayama, K. Stripe Patterns Formed on a Glass Surface during Droplet Evaporation. *Langmuir* **11**, 1057–1060 (1995).

111. Dimitrov, A. S. & Nagayama, K. Continuous Convective Assembling of Fine Particles into Two-Dimensional Arrays on Solid Surfaces. *Langmuir* **12**, 1303–1311 (1996).

112. Dugay, J. *et al.* Tuning Deposition of Magnetic Metallic Nanoparticles from Periodic Pattern to Thin Film Entrainment by Dip Coating Method. *Langmuir* **30**, 9028–9035 (2014).

113. Aleksandrovic, V. *et al.* Preparation and Electrical Properties of Cobalt−Platinum Nanoparticle Monolayers Deposited by the Langmuir−Blodgett Technique. *ACS Nano* **2**, 1123–1130 (2008).

114. Guo, Q., Teng, X., Rahman, S. & Yang, H. Patterned Langmuir−Blodgett Films of Monodisperse Nanoparticles of Iron Oxide Using Soft Lithography. *J. Am. Chem. Soc.* **125**, 630–631 (2003).

115. Lee, D. K., Kim, Y. H., Kim, C. W., Cha, H. G. & Kang, Y. S. Vast Magnetic Monolayer Film with Surfactant-Stabilized Fe3O4 Nanoparticles Using Langmuir−Blodgett Technique. *J. Phys. Chem. B* **111**, 9288–9293 (2007).

116. Meldrum, F. C., Kotov, N. A. & Fendler, J. H. Utilization of Surfactant-Stabilized Colloidal Silver Nanocrystallites in the Construction of Mono- and Multiparticulate Langmuir-Blodgett Films. *Langmuir* **10**, 2035–2040 (1994).

117. Tanaka, H., Mitsuishi, M. & Miyashita, T. Tailored-Control of Gold Nanoparticle Adsorption onto Polymer Nanosheets. *Langmuir* **19**, 3103–3105 (2003).

118. Ruan, W. *et al.* Facile Fabrication of Large Area Polystyrene Colloidal Crystal Monolayer via Surfactant-free Langmuir-Blodgett Technique. *Chem. Res. Chin. Univ.* **23**, 712–714 (2007).

119. Adamson, K. *et al.* Peptide-Mediated Platelet Capture at Gold Micropore Arrays. *ACS Appl. Mater. Interfaces* **8**, 32189–32201 (2016).

120. Lone, S., Zhang, J. M., Vakarelski, I. U., Li, E. Q. & Thoroddsen, S. T. Evaporative Lithography in Open Microfluidic Channel Networks. *Langmuir* **33**, 2861–2871 (2017).

121. Deegan, R. D. *et al.* Capillary flow as the cause of ring stains from dried liquid drops. *Nature* **389**, 827–829 (1997).

122. Monteux, C. & Lequeux, F. Packing and Sorting Colloids at the Contact Line of a Drying Drop. *Langmuir* **27**, 2917–2922 (2011).

123. Jung, J.-Y., Kim, Y. W. & Yoo, J. Y. Behavior of Particles in an Evaporating Didisperse Colloid Droplet on a Hydrophilic Surface. *Anal. Chem.* **81**, 8256–8259 (2009).

124. Morales, V. L. *et al.* Surfactant-Mediated Control of Colloid Pattern Assembly and Attachment Strength in Evaporating Droplets. *Langmuir* **29**, 1831–1840 (2013).

125. Cheung, C. L., Nikolić, R. J., Reinhardt, C. E. & Wang, T. F. Fabrication of nanopillars by nanosphere lithography. *Nanotechnology* **17**, 1339–1343 (2006).

126. Mallon, C. T., Jose, B., Forster, R. J. & Keyes, T. E. Protein nanopatterning and release from gold nano-cavity arrays. *Chem. Commun.* **46**, 106–108 (2010).

127. Abdelsalam, M. E. *et al.* Electrochemical SERS at a structured gold surface. *Electrochem. Commun.* **7**, 740–744 (2005).

128. Zhang, Z., Matin, M. A., Ha, M. Y. & Jang, J. Molecular Dynamics Study of the Hydrophilic-to-Hydrophobic Switching in the Wettability of a Gold Surface Corrugated with Spherical Cavities. *Langmuir* **32**, 9658–9663 (2016).

129. Diederichs, T., Nguyen, Q. H., Urban, M., Tampé, R. & Tornow, M. Transparent Nanopore Cavity Arrays Enable Highly Parallelized Optical Studies of Single Membrane Proteins on Chip. *Nano Lett.* **18**, 3901–3910 (2018).

130. Peng, P.-Y., Chiang, P.-C. & Chao, L. Mobile Lipid Bilayers on Gold Surfaces through Structure-Induced Lipid Vesicle Rupture. *Langmuir* **31**, 3904–3911 (2015).

131. Bumbrah, G. S. & Sharma, R. M. Raman spectroscopy – Basic principle, instrumentation and selected applications for the characterization of drugs of abuse. *Egypt. J. Forensic Sci.* **6**, 209–215 (2016).

132. Vandenabeele, P. *Practical Raman spectroscopy: an introduction.* (John Wiley & Sons, 2013).

133. Kudelski, A. Analytical applications of Raman spectroscopy. *Talanta* **76**, 1–8 (2008).

134. Li, M., Kang, J. W., Sukumar, S., Dasari, R. R. & Barman, I. Multiplexed detection of serological cancer markers with plasmon-enhanced Raman spectro-immunoassay. *Chem. Sci.* **6**, 3906–3914 (2015).

135. Xu, L. *et al.* SERS Encoded Silver Pyramids for Attomolar Detection of Multiplexed Disease Biomarkers. *Adv. Mater.* **27**, 1706–1711 (2015).

136. Shan, B., Pu, Y., Chen, Y., Liao, M. & Li, M. Novel SERS labels: Rational design, functional integration and biomedical applications. *Coord. Chem. Rev.* **371**, 11–37 (2018).

137. Virkler, K. & Lednev, I. Raman spectroscopic signature of blood and its potential application to forensic body fluid identification. *Anal. Bioanal. Chem.* **396**, 525–534.

138. Kneipp, K. *et al.* Single Molecule Detection Using Surface-Enhanced Raman Scattering (SERS). *Phys. Rev. Lett.* **78**, 1667–1670 (1997).
139. Kneipp, K., Kneipp, H., Itzkan, I., Dasari, R. R. & Feld, M. S. Ultrasensitive Chemical Analysis by Raman Spectroscopy. *Chem. Rev.* **10**, 2957–2976 (1999).
140. Levin, C. S. *et al.* Interactions of Ibuprofen with Hybrid Lipid Bilayers Probed by Complementary Surface-Enhanced Vibrational Spectroscopies. *J. Phys. Chem. B* **112**, 14168–14175 (2008).
141. Bruzas, I., Lum, W., Gorunmez, Z. & Sagle, L. Advances in surface-enhanced Raman spectroscopy (SERS) substrates for lipid and protein characterization: sensing and beyond. *Analyst* **143**, 3990–4008 (2018).
142. Li, Y., Driver, M., Decker, E. & He, L. Lipid and lipid oxidation analysis using surface enhanced Raman spectroscopy (SERS) coupled with silver dendrites. *Food Res. Int.* **58**, 1–6 (2014).
143. Millo, D. *et al.* Characterization of hybrid bilayer membranes on silver electrodes as biocompatible SERS substrates to study membrane–protein interactions. *Colloids Surf. B Biointerfaces* **81**, 212–216 (2010).
144. E. Smith, W. Practical understanding and use of surface enhanced Raman scattering/surface enhanced resonance Raman scattering in chemical and biological analysis. *Chem. Soc. Rev.* **37**, 955–964 (2008).
145. Hutter, E. & Fendler, J. H. Exploitation of Localized Surface Plasmon Resonance. *Adv. Mater.* **16**, 1685–1706 (2004).
146. Chu, Y. & Crozier, K. B. Experimental study of the interaction between localized and propagating surface plasmons. *Opt. Lett.* **34**, 244–246 (2009).
147. Yonzon, C. & Duyne, R. Localized and Propagating Surface Plasmon Resonance Sensors: A Study Using Carbohydrate Binding Protein. in *Nanoporous and Nanostructured Materials for Catalysis, Sensor, and Gas Separation Applications* vol. 876 107–112 (2005).
148. Li, W. Physics Models of Plasmonics: Single Nanoparticle, Complex Single Nanoparticle, Nanodimer, and Single Nanoparticle over Metallic Thin Film. *Plasmonics* **13**, 997–1014 (2018).
149. Kelf, T. A., Sugawara, Y., Baumberg, J. J., Abdelsalam, M. & Bartlett, P. N. Plasmonic Band Gaps and Trapped Plasmons on Nanostructured Metal Surfaces. *Phys. Rev. Lett.* **95**, 116802 (2005).
150. Moerner, W. E. & Orrit, M. Illuminating Single Molecules in Condensed Matter. *Science* **283**, 1670–1676 (1999).
151. Chen, C. *et al.* Direct Evidence of High Spatial Localization of Hot Spots in Surface-Enhanced Raman Scattering. *Angew. Chem. Int. Ed.* **48**, 9932–9935 (2009).
152. Marqués-González, S., Matsushita, R. & Kiguchi, M. Surface enhanced Raman scattering of molecules in metallic nanogaps. *J. Opt.* **17**, 114001 (2015).
153. Li, P. *et al.* Fundamentals and applications of surface-enhanced Raman spectroscopy–based biosensors. *Curr. Opin. Biomed. Eng.* **13**, 51–59 (2020).

154. Keyes, T., Gimenez, A. V. & Kho, K. W. Nano-substructured Plasmonic Pore Arrays: A robust, low cost route to reproducible hierarchical structures extended across macroscopic dimensions. *Nanoscale Adv.* (2020) doi:10.1039/D0NA00527D.
155. Chang, R. *Physical Chemistry for the Biosciences*. (University Science Books, 2015).
156. What is the Jablonski diagram? | Organic Chemistry - Quora. https://www.quora.com/What-is-the-Jablonski-diagram. (Image source)
157. Lakowicz, J. R. *Principles of fluorescence spectroscopy*.
158. Harris, D. C. *Quantitative chemical analysis*. (W.H. Freeman and Company, 2016).
159. Sharma, A. & Schulman, S. G. (Stephen G. *Introduction to fluorescence spectroscopy*. (Wiley, 1999).
160. Prodi, A. *et al.* Photophysics of Pyridylporphyrin Ru(II) Adducts: Heavy-Atom Effects and Intramolecular Decay Pathways. *Inorg. Chem.* **40**, 3498–3504 (2001).
161. Campagna, S., Puntoriero, F., Nastasi, F., Bergamini, G. & Balzani, V. Photochemistry and Photophysics of Coordination Compounds: Ruthenium. in *Photochemistry and Photophysics of Coordination Compounds I* (eds. Balzani, V. & Campagna, S.) 117–214 (Springer, 2007). doi:10.1007/128_2007_133.
162. Albani, J. R. *Principles and Applications of Fluorescence Spectroscopy*. (John Wiley & Sons, Incorporated, 2007).
163. Valeur, B., Berberan-Santos, M. N. & Berberan-Santos, M. N. *Molecular Fluorescence: Principles and Applications*. (John Wiley & Sons, Incorporated, 2013).
164. Fort, E. & Grésillon, S. Surface enhanced fluorescence. *J. Phys. Appl. Phys.* **41**, 013001 (2008).
165. Jeong, Y., Kook, Y.-M., Lee, K. & Koh, W.-G. Metal enhanced fluorescence (MEF) for biosensors: General approaches and a review of recent developments. *Biosens. Bioelectron.* **111**, 102–116 (2018).
166. Gryczynski, Z. *et al.* Metal-Enhanced Fluorescence: A Novel Approach to Ultra-Sensitive Fluorescence Sensing Assay Platforms. *Proc. SPIE-- Int. Soc. Opt. Eng.* **5321**, 275–282 (2004).
167. Aslan, K. *et al.* Metal-enhanced fluorescence: an emerging tool in biotechnology. *Curr. Opin. Biotechnol.* **16**, 55–62 (2005).
168. Kim, J. K. & Jang, D.-J. Metal-enhanced fluorescence of gold nanoclusters adsorbed onto Ag@SiO2 core–shell nanoparticles. *J. Mater. Chem. C* **5**, 6037–6046 (2017).
169. Lakowicz, J. R. Radiative Decay Engineering: Biophysical and Biomedical Applications. *Anal. Biochem.* **298**, 1–24 (2001).
170. Sokolov, K., Chumanov, G. & Cotton, T. M. Enhancement of Molecular Fluorescence near the Surface of Colloidal Metal Films. *Anal. Chem.* **70**, 3898–3905 (1998).
171. Attridge, J. W., Daniels, P. B., Deacon, J. K., Robinson, G. A. & Davidson, G. P. Sensitivity enhancement of optical immunosensors by the use of a surface plasmon resonance fluoroimmunoassay. *Biosens. Bioelectron.* **6**, 201–214 (1991).
172. Zhang, Y., Aslan, K., Previte, M. J. R. & Geddes, C. D. Low Temperature Metal-Enhanced Fluorescence. *J. Fluoresc.* **17**, 627–631 (2007).

173. Aslan, K., Wu, M., Lakowicz, J. R. & Geddes, C. D. Metal Enhanced Fluorescence Solution-based Sensing Platform 2: Fluorescent Core-Shell Ag@SiO2 Nanoballs. *J. Fluoresc.* **17**, 127–131 (2007).

174. Punj, D., Torres, J. de, Rigneault, H. & Wenger, J. Gold nanoparticles for enhanced single molecule fluorescence analysis at micromolar concentration. *Opt. Express* **21**, 27338–27343 (2013).

175. Pradhan, B. *et al.* Gold-Nanorod-Enhanced Fluorescence Correlation Spectroscopy of Fluorophores with High Quantum Yield in Lipid Bilayers. *J. Phys. Chem. C* **120**, 25996–26003 (2016).

176. Winkler, P. M. *et al.* Transient Nanoscopic Phase Separation in Biological Lipid Membranes Resolved by Planar Plasmonic Antennas. *ACS Nano* **11**, 7241–7250 (2017).

177. Lohmüller, T. *et al.* Single Molecule Tracking on Supported Membranes with Arrays of Optical Nanoantennas. *Nano Lett.* **12**, 1717–1721 (2012).

178. Lohmüller, T. *et al.* Supported Membranes Embedded with Fixed Arrays of Gold Nanoparticles. *Nano Lett.* **11**, 4912–4918 (2011).

179. Regmi, R. *et al.* Planar Optical Nanoantennas Resolve Cholesterol-Dependent Nanoscale Heterogeneities in the Plasma Membrane of Living Cells. *Nano Lett.* **17**, 6295–6302 (2017).

180. Winkler, P. M. *et al.* Optical Antenna-Based Fluorescence Correlation Spectroscopy to Probe the Nanoscale Dynamics of Biological Membranes. *J. Phys. Chem. Lett.* **9**, 110–119 (2018).

181. Bagatolli, L. A. & Gratton, E. Two Photon Fluorescence Microscopy of Coexisting Lipid Domains in Giant Unilamellar Vesicles of Binary Phospholipid Mixtures. *Biophys. J.* **78**, 290–305 (2000).

182. Lordan, F., Rice, J. H., Jose, B., Forster, R. J. & Keyes, T. E. Surface enhanced resonance Raman and luminescence on plasmon active nanostructured cavities. *Appl. Phys. Lett.* **97**, 153110 (2010).

183. Carvalho, C. *et al.* Doxorubicin: the good, the bad and the ugly effect. *Curr. Med. Chem.* **16**, 3267–3285 (2009).

184. Thorn, C. F. *et al.* Doxorubicin pathways: pharmacodynamics and adverse effects. *Pharmacogenet. Genomics* **21**, 440–446 (2011).

185. Motlagh, N. S. H., Parvin, P., Ghasemi, F. & Atyabi, F. Fluorescence properties of several chemotherapy drugs: doxorubicin, paclitaxel and bleomycin. *Biomed. Opt. Express* **7**, 2400–2406 (2016).

186. Alves, A. C. *et al.* Influence of doxorubicin on model cell membrane properties: insights from in vitro and in silico studies. *Sci. Rep.* **7**, 1–11 (2017).

187. loren, A. *et al.* Feasibility of quantitative determination of doxorubicin with surface enhanced Raman spectroscopy. *J. Raman Spectrosc.* **32**, 971–974 (2001).

188. Litti, L., Amendola, V., Toffoli, G. & Meneghetti, M. Detection of low-quantity anticancer drugs by surface-enhanced Raman scattering. *Anal. Bioanal. Chem.* **408**, 2123–2131 (2016).

189. Brennaman, M. *et al.* Turning the [Ru(bpy)2dppz]2+ Light-Switch On and Off with Temperature | Journal of the American Chemical Society. *J. Am. Chem. Soc.* **124**, 15094–15098 (2002).

190. Del Guerzo, A., Kirsch-De Mesmaeker, A., Demeunynck, M. & Lhomme, J. Photophysics of Bifunctional Ru(II) Complexes Bearing an Aminoquinoline Organic Unit. Potential New Photoprobes and Photoreagents of DNA. *J. Phys. Chem. B* **101**, 7012–7021 (1997).
191. Byrne, A. The application of Ru(II) polypyridyl complexes to cellular imaging and sensing. (Dublin City University, 2016).
192. Mital, M. & Ziora, Z. Biological applications of Ru(II) polypyridyl complexes. *Coord. Chem. Rev.* **375**, 434–458 (2018).
193. Burke, C. S., Byrne, A. & Keyes, T. E. Highly Selective Mitochondrial Targeting by a Ruthenium(II) Peptide Conjugate: Imaging and Photoinduced Damage of Mitochondrial DNA. *Angew. Chem. Int. Ed.* **57**, 12420–12424 (2018).
194. Byrne, A., Burke, C. S. & Keyes, T. E. Precision targeted ruthenium(II) luminophores; highly effective probes for cell imaging by stimulated emission depletion (STED) microscopy. *Chem. Sci.* **7**, 6551–6562 (2016).
195. Lin, K., Zhao, Z.-Z., Bo, H.-B., Hao, X.-J. & Wang, J.-Q. Applications of Ruthenium Complex in Tumor Diagnosis and Therapy. *Front. Pharmacol.* **9**, (2018).
196. Ortmans, I., Elias, B., M. Kelly, J., Moucheron, C. & Kirsch-DeMesmaeker, A. [Ru(TAP) 2 (dppz)] 2+ : a DNA intercalating complex, which luminesces strongly in water and undergoes photo-induced proton-coupled electron transfer with guanosine-5'-monophosphate. *Dalton Trans.* **0**, 668–676 (2004).
197. Marcélis Lionel, Moucheron Cécile & Kirsch-De Mesmaeker Andrée. Ru–TAP complexes and DNA: from photo-induced electron transfer to gene photo-silencing in living cells. *Philos. Trans. R. Soc. Math. Phys. Eng. Sci.* **371**, 20120131 (2013).
198. Friedman, A. E., Chambron, J. C., Sauvage, J. P., Turro, N. J. & Barton, J. K. A molecular light switch for DNA: Ru(bpy)2(dppz)2+. *J. Am. Chem. Soc.* **112**, 4960–4962 (1990).
199. Puckett, C. A. & Barton, J. K. Methods to Explore Cellular Uptake of Ruthenium Complexes. *J. Am. Chem. Soc.* **129**, 46–47 (2007).
200. Cosgrave, L., Devocelle, M., Forster, R. J. & Keyes, T. E. Multimodal cell imaging by ruthenium polypyridyl labelled cell penetrating peptides. *Chem. Commun.* **46**, 103–105 (2010).
201. Neugebauer, U. *et al.* Ruthenium polypyridyl peptide conjugates: membrane permeable probes for cellular imaging. *Chem. Commun.* **0**, 5307–5309 (2008).
202. Burke, C. S., Byrne, A. & Keyes, Tia. E. Targeting Photoinduced DNA Destruction by Ru(II) Tetraazaphenanthrene in Live Cells by Signal Peptide. *J. Am. Chem. Soc.* **140**, 6945–6955 (2018).
203. Burke, C. S. Peptide-directed metal complex luminophores: candidates for photodynamic therapeutics. (Dublin City University. School of Chemical Sciences, 2018).
204. Poynton, F. E. *et al.* Direct observation by time-resolved infrared spectroscopy of the bright and the dark excited states of the [Ru(phen)2(dppz)]2+ light-switch compound in solution and when bound to DNA. *Chem. Sci.* **7**, 3075–3084 (2016).

205. Kirsch-De Mesmaeker, A., Jacquet, L. & Nasielski, J. Ruthenium(II) complexes of 1,4,5,8-tetraazaphenanthrene (TAP) and 2,2'-bipyridine (bpy). Ground- and excited-state basicities of Ru2+(bpy)n(TAP)3-n (n = 0,1,2): their luminescence quenching by organic buffers. *Inorg. Chem.* **27**, 4451–4458 (1988).
206. Lecomte, J.-P., Kirsch-De Mesmaeker, A., Feeney, M. M. & Kelly, J. M. Ruthenium(II) Complexes with 1,4,5,8,9,12-Hexaazatriphenylene and 1,4,5,8-Tetraazaphenanthrene Ligands: Key Role Played by the Photoelectron Transfer in DNA Cleavage and Adduct Formation. *Inorg. Chem.* **34**, 6481–6491 (1995).
207. Elias, B. & Kirsch-De Mesmaeker, A. Photo-reduction of polyazaaromatic Ru(II) complexes by biomolecules and possible applications. *Coord. Chem. Rev.* **250**, 1627–1641 (2006).
208. Berselli, G. B., Sarangi, N. K., Ramadurai, S., Murphy, P. V. & Keyes, T. E. Microcavity-Supported Lipid Membranes: Versatile Platforms for Building Asymmetric Lipid Bilayers and for Protein Recognition. *ACS Appl. Bio Mater.* **2**, 3404–3417 (2019).
209. Basit, H. *et al.* Tethered Bilayer Lipid Membranes on Mixed Self-Assembled Monolayers of a Novel Anchoring Thiol: Impact of the Anchoring Thiol Density on Bilayer Formation. *Langmuir* **27**, 14317–14328 (2011).
210. Nagpal, P., Lindquist, N. C., Oh, S.-H. & Norris, D. J. Ultrasmooth Patterned Metals for Plasmonics and Metamaterials. *Science* **325**, 594–597 (2009).
211. Rehg, T. J. & Higgins, G. Spin coating of colloidal suspensions. *AIChE J.* **38**, 489–501 (1992).
212. Chen, J. *et al.* Controllable fabrication of 2D colloidal-crystal films with polystyrene nanospheres of various diameters by spin-coating. *Appl. Surf. Sci.* **270**, 6–15 (2013).
213. Watanabe, S., Mino, Y., Ichikawa, Y. & Miyahara, M. T. Spontaneous Formation of Cluster Array of Gold Particles by Convective Self-Assembly. *Langmuir* **28**, 12982–12988 (2012).
214. Li, X. *et al.* Periodic Parallel Array of Nanopillars and Nanoholes Resulting from Colloidal Stripes Patterned by Geometrically Confined Evaporative Self-Assembly for Unique Anisotropic Wetting. *ACS Appl. Mater. Interfaces* **6**, 20300–20308 (2014).
215. Born, P., Blum, S., Munoz, A. & Kraus, T. Role of the Meniscus Shape in Large-Area Convective Particle Assembly. *Langmuir* **27**, 8621–8633 (2011).
216. Coe-Sullivan, S., Steckel, J. S., Woo, W.-K., Bawendi, M. G. & Bulović, V. Large-Area Ordered Quantum-Dot Monolayers via Phase Separation During Spin-Casting. *Adv. Funct. Mater.* **15**, 1117–1124 (2005).
217. Hong, Y.-K. *et al.* Controlled two-dimensional distribution of nanoparticles by spin-coating method. *Appl. Phys. Lett.* **80**, 844–846 (2002).
218. Kim, S.-G., Hagura, N., Iskandar, F., Yabuki, A. & Okuyama, K. Multilayer film deposition of Ag and SiO2 nanoparticles using a spin coating process. *Thin Solid Films* **516**, 8721–8725 (2008).

219. Liu, F.-K., Chang, Y.-C., Ko, F.-H., Chu, T.-C. & Dai, B.-T. Rapid fabrication of high quality self-assembled nanometer gold particles by spin coating method. *Microelectron. Eng.* **67–68**, 702–709 (2003).
220. Johnston-Peck, A. C., Wang, J. & Tracy, J. B. Formation and Grain Analysis of Spin-Cast Magnetic Nanoparticle Monolayers. *Langmuir* **27**, 5040–5046 (2011).
221. Wang, H. *et al.* Deposition and characterization of large-scale FePt nanoparticle monolayers on SiO2/Si surface. *Surf. Coat. Technol.* **204**, 1509–1513 (2010).
222. Zhang, C., Cvetanovic, S. & Pearce, J. M. Fabricating ordered 2-D nano-structured arrays using nanosphere lithography. *MethodsX* **4**, 229–242 (2017).
223. Brûlet, A., Boué, F., Menelle, A. & Cotton, J. P. Conformation of Polystyrene Chain in Ultrathin Films Obtained by Spin Coating. *Macromolecules* **33**, 997–1001 (2000).
224. Jose, B. Biomimetic Photonic Nanocavity Arrays. (Dublin City University, 2011).
225. van Meer, G., Voelker, D. R. & Feigenson, G. W. Membrane lipids: where they are and how they behave. *Nat. Rev. Mol. Cell Biol.* **9**, 112–124 (2008).
226. Koynova, R. & Caffrey, M. An index of lipid phase diagrams. *Chem. Phys. Lipids* **115**, 107–219 (2002).
227. Konyakhina, T. M. & Feigenson, G. W. Phase diagram of a polyunsaturated lipid mixture: Brain sphingomyelin/1-stearoyl-2-docosahexaenoyl-sn-glycero-3-phosphocholine/cholesterol. *Biochim. Biophys. Acta BBA - Biomembr.* **1858**, 153–161 (2016).
228. Zhang, X. & Wang, S. Voltametric Behavior of Noradrenaline at 2-Mercaptoethanol Self-Assembled Monolayer Modified Gold Electrode and its Analytical Application. *Sensors* **3**, 61–68 (2003).
229. Semwogerere, D. & Weeks, E. R. Confocal Microscopy. in *Encyclopedia of Biomaterials and Biomedical Engineering* (2005).
230. St. Croix, C. M., Shand, S. H. & Watkins, S. C. Confocal microscopy: comparisons, applications, and problems. *BioTechniques* **39**, S2–S5 (2005).
231. neurobiology - Voltage sensitive dyes technique: 2-photons microscopy vs confocal microscopy - Cognitive Sciences Stack Exchange. https://cogsci.stackexchange.com/questions/13829/voltage-sensitive-dyes-technique-2-photons-microscopy-vs-confocal-microscopy.
232. Ferraro, J. R. & Nakamoto, K. *Introductory Raman spectroscopy*. (Academic Press, 1994).
233. Raman Spectroscopy | Science Facts. https://www.sciencefacts.net/raman-spectroscopy.html.
234. Cha, N.-G., Echegoyen, Y., Kim, T.-H., Park, J.-G. & Busnaina, A. A. Convective Assembly and Dry Transfer of Nanoparticles Using Hydrophobic/Hydrophilic Monolayer Templates. **25**, 11375–11382 (2009).
235. Ultra-high ordered, centimeter scale preparation of microsphere Langmuir films. *J. Colloid Interface Sci.* **446**, 237–243 (2015).
236. Khoury, C. G. & Vo-Dinh, T. Plasmonic Nanowave Substrates for SERS: Fabrication and Numerical Analysis. *J. Phys. Chem. C* **116**, 7534–7545 (2012).

237. Katz, E. Yu. & Solov'ev, A. A. Chemical modification of platinum and gold electrodes by naphthoquinones using amines containing sulphhydryl or disulphide groups. *J. Electroanal. Chem. Interfacial Electrochem.* **291**, 171–186 (1990).

238. Wirde, M., Gelius, U. & Nyholm, L. Self-Assembled Monolayers of Cystamine and Cysteamine on Gold Studied by XPS and Voltammetry. *Langmuir* **15**, 6370–6378 (1999).

239. Colson, P., Cloots, R. & Henrist, C. Experimental Design Applied to Spin Coating of 2D Colloidal Crystal Masks: A Relevant Method? *Langmuir* **27**, 12800–12806 (2011).

240. Deegan, R. D. *et al.* Contact line deposits in an evaporating drop. *Phys. Rev. E* **62**, 756–765 (2000).

241. Lordan, F., Rice, J. H., Jose, B., Forster, R. J. & Keyes, Tia. E. Site selective surface enhanced Raman on nanostructured cavities. *Appl. Phys. Lett.* **99**, 033104 (2011).

242. Lordan, F., Rice, J. H., Jose, B., Forster, R. J. & Keyes, T. E. Effect of Cavity Architecture on the Surface-Enhanced Emission from Site-Selective Nanostructured Cavity Arrays. *J. Phys. Chem. C* **116**, 1784–1788 (2012).

243. Brooks, L. J. *et al.* Polarisation-selective hotspots in metallic ring stack arrays. *Opt. Express* **24**, 3663–3671 (2016).

244. Johnson, P. B. & Christy, R. W. Optical Constants of the Noble Metals. *Phys. Rev. B* **6**, 4370–4379 (1972).

245. FDTD Solutions Reference Guide Release 7.5. (2003).

246. Dulkeith, E., Morteani, A., Niedreeichholz, T. & Gittins, D. Fluorescence Quenching of Dye Molecules near Gold Nanoparticles: Radiative and Nonradiative Effects. *Phys. Rev. Lett.* **89**, 203002 (2002).

247. Than Htun, M. Photophysical study on daunorubicin by fluorescence spectroscopy. *J. Lumin.* **129**, 344–348 (2009).

248. Basics of EIS: Electrochemical Research-Impedance. https://www.gamry.com/application-notes/EIS/basics-of-electrochemical-impedance-spectroscopy/.

249. Porter, M. D., Bright, T. B., Allara, D. L. & Chidsey, C. E. D. Spontaneously organized molecular assemblies. 4. Structural characterization of n-alkyl thiol monolayers on gold by optical ellipsometry, infrared spectroscopy, and electrochemistry. *J. Am. Chem. Soc.* **109**, 3559–3568 (1987).

250. de Meyer, F. & Smit, B. Effect of cholesterol on the structure of a phospholipid bilayer. *Proc. Natl. Acad. Sci. U. S. A.* **106**, 3654–3658 (2009).

251. Łotowski, Z, K., P. Spectroscopic and Electrochemical Studies of Bilayer Lipid Membranes Tethered to the Surface of Gold. *J. Electrochem. Soc.* **149**, 189–194 (2002).

252. Richter, R. P., Lai Kee Him, J., Tessier, B., Tessier, C. & Brisson, A. R. On the Kinetics of Adsorption and Two-Dimensional Self-Assembly of Annexin A5 on Supported Lipid Bilayers. *Biophys. J.* **89**, 3372–3385 (2005).

253. Ho, C.-C., Zhao, K. & Lee, T.-Y. Quasi-3D gold nanoring cavity arrays with high-density hot-spots for SERS applications via nanosphere lithography. *Nanoscale* **6**, 8606–8611 (2014).

254. Abdelhalim, M., Mady, M. & Ghannam, M. Physical Properties of Different Gold Nanoparticles: Ultraviolet-Visible and Fluorescence Measurements. *J. Nanomedicin Nanotechnol.* **3**, 1000133 (2112).

255. Opilik, L., Bauer, T., Schmid, T., Stadler, J. & Zenobi, R. Nanoscale chemical imaging of segregated lipid domains using tip-enhanced Raman spectroscopy. *Phys. Chem. Chem. Phys.* **13**, 9978–9981 (2011).

256. Czamara, K. *et al.* Raman spectroscopy of lipids: a review. *J. Raman Spectrosc.* **46**, 4–20 (2015).

257. Akagi, J. *et al.* Real-time cell viability assays using a new anthracycline derivative DRAQ7®. *Cytom. Part J. Int. Soc. Anal. Cytol.* **83**, 227–234 (2013).

258. Duong, H. T. T. *et al.* Functionalizing Biodegradable Dextran Scaffolds Using Living Radical Polymerization: New Versatile Nanoparticles for the Delivery of Therapeutic Molecules. *Mol. Pharm.* **9**, 3046–3061 (2012).

259. Gallois, L., Fiallo, M., Laigle, A., Priebe, W. & Garnier-Suillerot, A. The overall partitioning of anthracyclines into phosphatidyl-containing model membranes depends neither on the drug charge nor the presence of anionic phospholipids. *Eur. J. Biochem.* **241**, 879–887 (1996).

260. Le Ru, E. C. & Etchegoin, P. G. (Pablo G. *Principles of surface-enhanced raman spectroscopy: and related plasmonic effects*. (Elsevier Science, 2009).

261. Ameling, R. & Giessen, H. Cavity Plasmonics: Large Normal Mode Splitting of Electric and Magnetic Particle Plasmons Induced by a Photonic Microcavity. *Nano Lett.* **10**, 4394–4398 (2010).

262. Jain, P. & El-Sayed, M. Plasmonic Coupling in Noble Metal Nanostructures. *Chem. Phys. Lett.* **487**, 153–164 (2009).

263. C. Bantz, K. *et al.* Recent progress in SERS biosensing. *Phys. Chem. Chem. Phys.* **13**, 11551–11567 (2011).

264. Dhara, S. Origin of Shifts in the Surface Plasmon Resonance Frequencies for Au and Ag Nanoparticles. in *arXiv:1504.01503 [cond-mat]* (2015).

265. Adamson, K. *et al.* Peptide-Mediated Platelet Capture at Gold Micropore Arrays. *ACS Appl. Mater. Interfaces* **8**, 32189–32201 (2016).

266. Sweetenham, C. S., Larraona-Puy, M. & Notingher, I. Simultaneous Surface-Enhanced Raman Spectroscopy (SERS) and Atomic Force Microscopy (AFM) for Label-Free Physicochemical Analysis of Lipid Bilayers. *Appl. Spectrosc.* **65**, 1387–1392 (2011).

267. Taylor, R. W. *et al.* Watching individual molecules flex within lipid membranes using SERS. *Sci. Rep.* **4**, 5940 (2014).

268. Kundu, J., S. Levin, C. & J. Halas, N. Real-time monitoring of lipid transfer between vesicles and hybrid bilayers on Au nanoshells using surface enhanced Raman scattering (SERS). *Nanoscale* **1**, 114–117 (2009).

269. Szafraniec, E. *et al.* Spectroscopic studies of anthracyclines: Structural characterization and in vitro tracking. *Spectrochim. Acta. A. Mol. Biomol. Spectrosc.* **169**, 152–160 (2016).

270. Langevin, P. B. & Atlee, J. L. Chapter 30 - Chemotherapeutic Agents. in *Complications in Anesthesia (Second Edition)* (ed. Atlee, J. L.) 110–118 (W.B. Saunders, 2007). doi:10.1016/B978-1-4160-2215-2.50035-1.

271. Morjani, H., Sharonov, S., Manfait, M., Sokolov, K. & Nabiev, I. SERS and micro-SERS analysis of doxorubicin interaction in vitro and in living human cancer cells. in *1992 14th Annual International Conference of the IEEE Engineering in Medicine and Biology Society* vol. 1 330–331 (1992).

272. Speelmans, G., Staffhorst, R. W., de Kruijff, B. & de Wolf, F. A. Transport studies of doxorubicin in model membranes indicate a difference in passive diffusion across and binding at the outer and inner leaflets of the plasma membrane. *Biochemistry* **33**, 13761–13768 (1994).

273. Alves Ana Catarina *et al.* A biophysical approach to daunorubicin interaction with model membranes: relevance for the drug's biological activity. *J. R. Soc. Interface* **14**, 20170408 (2017).

274. Nabiev, I. R., Morjani, H. & Manfait, M. Selective analysis of antitumor drug interaction with living cancer cells as probed by surface-enhanced Raman spectroscopy. *Eur. Biophys. J.* **19**, 311–316 (1991).

275. David S. dos Santos, J. & Aroca, R. F. Selective surface-enhanced fluorescence and dye aggregation with layer-by-layer film substrates. *Analyst* **132**, 450–454 (2007).

276. Le Ru, E. C., Blackie, E., Meyer, M. & Etchegoin, P. G. Surface Enhanced Raman Scattering Enhancement Factors: A Comprehensive Study. *J. Phys. Chem. C* **111**, 13794–13803 (2007).

277. Devid, E. J. *et al.* The influence of molecular mobility on the properties of networks of gold nanoparticles and organic ligands. *Beilstein J. Nanotechnol.* **5**, 1664–1674 (2014).

278. Li, B., Calvet, A., Casamayou-Boucau, Y., Morris, C. & Ryder, A. G. Low-Content Quantification in Powders Using Raman Spectroscopy: A Facile Chemometric Approach to Sub 0.1% Limits of Detection. *Anal. Chem.* **87**, 3419–3428 (2015).

279. Noh, J., Kato, H. S., Kawai, M. & Hara, M. Surface Structure and Interface Dynamics of Alkanethiol Self-Assembled Monolayers on Au. *J. Phys. Chem. B* **110**, 2793–2797 (2006).

280. Bantz, K. C., Nelson, H. D. & Haynes, C. L. Plasmon-Enabled Study of Self-Assembled Alkanethiol Ordering on Roughened Ag Substrates. *J. Phys. Chem. C* **116**, 3585–3593 (2012).

281. Clark, B. K., Gregory, B. W., Avila, A., Cotton, T. M. & Standard, J. M. Surface-Enhanced Electronic Raman Scattering from Self-Assembled Alkanethiol Monolayers on Gold Surfaces. *J. Phys. Chem. B* **103**, 8201–8204 (1999).

282. Hong, P. P., Boerio, F. J., Clarson, S. J. & Smith, S. D. An investigation of the interdiffusion of polystyrene and deuterated polystyrene using surface-enhanced Raman scattering. *Macromolecules* **24**, 4770–4776 (1991).

283. Cherney, D., Conboy, J. & Harris, J. M. Optical-Trapping Raman Microscopy Detection of Single Unilamellar Lipid Vesicles. **75**, 6621–6628 (2003).

284. Ando, J. *et al.* Sphingomyelin distribution in lipid rafts of artificial monolayer membranes visualized by Raman microscopy. *Proc. Natl. Acad. Sci. U. S. A.* **112**, 4558–4563 (2015).

285. Abe, M. & Kobayashi, T. Chapter 2 - Dynamics of sphingomyelin- and cholesterol-enriched lipid domains during cytokinesis. in *Methods in Cell Biology* (ed. Echard, A.) vol. 137 15–24 (Academic Press, 2017).

286. de Almeida, R. F. M., Fedorov, A. & Prieto, M. Sphingomyelin/Phosphatidylcholine/Cholesterol Phase Diagram: Boundaries and Composition of Lipid Rafts. *Biophys. J.* **85**, 2406–2416 (2003).

287. Wei, H., McCarthy, A., Song, J., Zhou, W. & Vikesland, P. J. Quantitative SERS by Hot Spot Normalization – Surface Enhanced Rayleigh Band Intensity as an Alternative Evaluation Parameter for SERS Substrate Performance. *Faraday Discuss.* **205**, 491–504 (2017).

288. Multivariate evaluation of doxorubicin surface-enhanced Raman spectra. *Spectrochim. Acta. A. Mol. Biomol. Spectrosc.* **57**, 1907–1915.

289. Fülöp, Z., Gref, R. & Loftsson, T. A permeation method for detection of self-aggregation of doxorubicin in aqueous environment. *Int. J. Pharm.* **454**, 559–561 (2013).

290. Pyne, A., Kundu, S., Banerjee, P. & Sarkar, N. Unveiling the Aggregation Behavior of Doxorubicin Hydrochloride in Aqueous Solution of 1-Octyl-3-methylimidazolium Chloride and the Effect of Bile Salt on These Aggregates: A Microscopic Study. *Langmuir* **34**, 3296–3306 (2018).

291. Taha, M. Buffers for the Physiological pH Range: Acidic Dissociation Constants of Zwitterionic Compounds in Various Hydroorganic Media. *Ann. Chim.* **95**, 105–109 (2005).

292. Jedrzejczak, M., Koceva-Chyla, A., Gwozdzinski, K. & Józwiak, Z. Changes in plasma membrane fludity of immortal rodent cells induced by anticancer drugs Doxorubicin, Aclarubin and Mitoxantrone. *Cell Biol. Int.* **23**, 497–506 (1999).

293. Šimáková, P., Kočišová, E. & Procházka, M. Sensitive Raman spectroscopy of lipids based on drop deposition using DCDR and SERS. *J. Raman Spectrosc.* **44**, 1479–1482 (2013).

294. Tsinman, O., Tsinman, K., Sun, N. & Avdeef, A. Physicochemical Selectivity of the BBB Microenvironment Governing Passive Diffusion—Matching with a Porcine Brain Lipid Extract Artificial Membrane Permeability Model. *Pharm. Res.* **28**, 337–363 (2011).

295. Jin, F., Li, H. & Xu, D. Enzyme-free fluorescence microarray for determination of hepatitis B virus DNA based on silver nanoparticle aggregates-assisted signal amplification. *Anal. Chim. Acta* **1077**, 297–304 (2019).

296. Della Ventura, B. *et al.* Biosensor for Point-of-Care Analysis of Immunoglobulins in Urine by Metal Enhanced Fluorescence from Gold Nanoparticles. *ACS Appl. Mater. Interfaces* **11**, 3753–3762 (2019).

297. Swierczewska, M., Lee, S. & Chen, X. The design and application of fluorophore–gold nanoparticle activatable probes. *Phys. Chem. Chem. Phys. PCCP* **13**, 9929–9941 (2011).

298. Wlodkowic, D. *et al.* Kinetic viability assays using DRAQ7 probe. *Curr. Protoc. Cytom.* **09**, (2013).

299. Nielsen, M. M. B. & Simonsen, A. C. Imaging Ellipsometry of Spin-Coated Membranes: Mapping of Multilamellar Films, Hydrated Membranes, and Fluid Domains. *Langmuir* **29**, 1525–1532 (2013).

300. Bleecker, J. V. *et al.* Thickness Mismatch of Coexisting Liquid Phases in Noncanonical Lipid Bilayers. *J. Phys. Chem. B* **120**, 2761–2770 (2016).

301. Kiang, K., Berselli, G. B. & Keyes, T. E. A Nano-Plasmonic Assay of Oligonucleotide-Cargo Delivery from Cationic Lipoplexes, submitted.

302. Farhane, Z., Bonnier, F., Casey, A. & J. Byrne, H. Raman micro spectroscopy for in vitro drug screening: subcellular localisation and interactions of doxorubicin. *Analyst* **140**, 4212–4223 (2015).

303. Ebrahimi, M., Mashreghi, M., Teymouri, M. & Farzaneh, N. H. A study on the role of cholesterol and phosphatidylcholine in various features of liposomal doxorubicin: From liposomal preparation to therapy - ScienceDirect. *Int. J. Pharm.* **551**, 300–308 (2018).

304. Raffy, S. & Teissié, J. Control of Lipid Membrane Stability by Cholesterol Content. *Biophys. J.* **76**, 2072–2080 (1999).

305. Langner, M. & Sek Wen Hui. Iodide penetration into lipid bilayers as a probe of membrane lipid organization. *Chem. Phys. Lipids* **60**, 127–132 (1991).

306. Chen, R. F. & Knutson, J. R. Mechanism of fluorescence concentration quenching of carboxyfluorescein in liposomes: Energy transfer to nonfluorescent dimers. *Anal. Biochem.* **172**, 61–77 (1988).

307. Pike, L. J. Lipid rafts bringing order to chaos. *J. Lipid Res.* **44**, 655–667 (2003).

308. McIntosh, T. J., Simon, S. A., Needham, D. & Huang, C. H. Structure and cohesive properties of sphingomyelin/cholesterol bilayers. *Biochemistry* **31**, 2012–2020 (1992).

309. Simon, S. A., McIntosh, T. J. & Latorre, R. Influence of cholesterol on water penetration into bilayers. *Science* **216**, 65–67 (1982).

310. Murugova, T. N. & Balgavý, P. Molecular volumes of DOPC and DOPS in mixed bilayers of multilamellar vesicles. *Phys. Chem. Chem. Phys.* **16**, 18211–18216 (2014).

311. Coverdale, J. P. C., Laroiya-McCarron, T. & Romero-Canelón, I. Designing Ruthenium Anticancer Drugs: What Have We Learnt from the Key Drug Candidates? *Inorganics* **7**, 31 (2019).

312. Feeney, M. M., Kelly, J. M., Tossi, A. B., Mesmaeker, A. K. & Lecomte, J.-P. Photoaddition of ruthenium(II)-tris-1,4,5,8-tetraazaphenanthrene to DNA and mononucleotides. *J. Photochem. Photobiol. B* **23**, 69–78 (1994).

313. Coates, C. G. *et al.* Resonance-Raman probing of the interaction between dipyridophenazine complexes of ruthenium(II) and DNA. *Chem. Commun.* 35–36 (1996) doi:10.1039/CC9960000035.

314. Nair, R. B., Cullum, B. M. & Murphy, C. J. Optical Properties of [Ru(phen)2dppz]2+ as a Function of Nonaqueous Environment. *Inorg. Chem.* **36**, 962–965 (1997).

315. Xu, W. *et al.* Quenching of Luminescent Ruthenium(II) Complexes by Water and Polymer-Based Relative Humidity Sensors. *Appl. Spectrosc.* **61**, 1238–1245 (2007).

316. Chambron, J.-C. & Sauvage, J.-P. Ru (bipy)2dppz2+ : a highly sensitive luminescent probe for micellar sodium dodecyl sulfate solutions. *Chem. Phys. Lett.* **182**, 603–607 (1991).

317. Zhu, B.-Z., Chao, X.-J., Huang, C.-H. & Li, Y. Delivering the cell-impermeable DNA 'light-switching' Ru(II) complexes preferentially into live-cell nucleus via an unprecedented ion-pairing method. *Chem. Sci.* **7**, 4016–4023 (2016).

318. Puckett, C. A. & Barton, J. K. Fluorescein Redirects a Ruthenium−Octaarginine Conjugate to the Nucleus. *J. Am. Chem. Soc.* **131**, 8738–8739 (2009).

319. Groessl, M., Zava, O. & Dyson, P. J. Cellular uptake and subcellular distribution of ruthenium-based metallodrugs under clinical investigation versus cisplatin. *Metallomics* **3**, 591–599 (2011).

320. Deng, Z. *et al.* Ruthenium complexes with phenylterpyridine derivatives target cell membrane and trigger death receptors-mediated apoptosis in cancer cells. *Biomaterials* **129**, 111–126 (2017).

321. Guo, X.-Q., Castellano, F. N., Li, L. & Lakowicz, J. R. A long-lifetime Ru(II) metal–ligand complex as a membrane probe. *Biophys. Chem.* **71**, 51–62 (1998).

322. Ling, L.-S., Song, G.-W., He, Z.-K., Liu, H.-Z. & Zeng, Y. A Novel Method to Determine DNA by Use of Molecular "Light Switch" of Ru(phen)2(dppz)2+. *Microchem. J.* **63**, 356–364 (1999).

323. Martin, A., Byrne, A., Burke, C. S., Forster, R. J. & Keyes, T. E. Peptide-Bridged Dinuclear Ru(II) Complex for Mitochondrial Targeted Monitoring of Dynamic Changes to Oxygen Concentration and ROS Generation in Live Mammalian Cells. *J. Am. Chem. Soc.* **136**, 15300–15309 (2014).

324. Hill, S. J., Katz, E., Eksteen, P., Schoenmaker, P. & Miller, N. *Handbook of HPLC*. vol. 14 (2000).

325. Eustis, S. & El-Sayed, M. A. Why gold nanoparticles are more precious than pretty gold: Noble metal surface plasmon resonance and its enhancement of the radiative and nonradiative properties of nanocrystals of different shapes. *Chem. Soc. Rev.* **35**, 209–217 (2006).

326. Malicka, J., Gryczynski, I., Kusba, J. & Lakowicz, J. R. Effects of metallic silver island films on resonance energy transfer between N,N'-(dipropyl)-tetramethyl- indocarbocyanine (Cy3)- and N,N'-(dipropyl)-tetramethyl- indodicarbocyanine (Cy5)-labeled DNA. *Biopolymers* **70**, 595–603 (2003).

327. Svensson, F. R., Matson, M., Li, M. & Lincoln, P. Lipophilic ruthenium complexes with tuned cell membrane affinity and photoactivated uptake. *Biophys. Chem.* **149**, 102–106 (2010).

328. Rogers, N. J. *et al.* High coating of Ru(II) complexes on gold nanoparticles for single particle luminescence imaging in cells. *Chem. Commun.* **50**, 617–619 (2013).

329. Osborne, S. A. M. & Pikramenou, Z. Highly luminescent gold nanoparticles: effect of ruthenium distance for nanoprobes with enhanced lifetimes. *Faraday Discuss.* **185**, 219–231 (2015).

330. Jebb, M., Sudeep, P. K., Pramod, P., Thomas, K. G. & Kamat, P. V. Ruthenium(II) Trisbipyridine Functionalized Gold Nanorods. Morphological Changes and Excited-State Interactions. *J. Phys. Chem. B* **111**, 6839–6844 (2007).

331. Elmes, R. B. P., Orange, K. N., Cloonan, S. M., Williams, D. C. & Gunnlaugsson, T. Luminescent Ruthenium(II) Polypyridyl Functionalized Gold Nanoparticles; Their DNA Binding Abilities and Application As Cellular Imaging Agents. *J. Am. Chem. Soc.* **133**, 15862–15865 (2011).

332. Li, M.-J., Nie, M.-J., Wu, Z.-Z., Liu, X. & Chen, G.-N. Colorimetric and luminescent bifunctional Ru(II) complex-modified gold nano probe for sensing of DNA. *Biosens. Bioelectron.* **29**, 109–114 (2011).

333. Huang, T. & Murray, R. W. Quenching of [Ru(bpy)3]2+ Fluorescence by Binding to Au Nanoparticles. *Langmuir* **18**, 7077–7081 (2002).

334. Gkika, K. S., Byrne, A. & Keyes, T. E. Mitochondrial targeted osmium polypyridyl probe shows concentration dependent uptake, localisation and mechanism of cell death. *Dalton Trans.* (2019) doi:10.1039/C9DT02967B.

335. Finn, S., Byrne, A., Gkika, K. S. & Keyes, T. E. Photophysics and Cell Uptake of Self-Assembled Ru(II)Polypyridyl Vesicles. *Front. Chem.* **8**, (2020).

336. Ardhammar, M., Lincoln, P. & Nordén, B. Ligand Substituents of Ruthenium Dipyridophenazine Complexes Sensitively Determine Orientation in Liposome Membrane. *J. Phys. Chem. B* **105**, 11363–11368 (2001).

337. Puckett, C. A. & Barton, J. K. Targeting a ruthenium complex to the nucleus with short peptides. *Biorgan. Med. Chem.* **18**, 3464–3569 (2010).

338. Matson, M., Svensson, F. R., Nordén, B. & Lincoln, P. Correlation Between Cellular Localization and Binding Preference to RNA, DNA, and Phospholipid Membrane for Luminescent Ruthenium(II) Complexes. *J. Phys. Chem. B* **115**, 1706–1711 (2011).

339. Sharmin, A. *et al.* Photophysical Studies of Bioconjugated Ruthenium Metal–Ligand Complexes Incorporated in Phospholipid Membrane Bilayers. *Inorg. Chem.* **52**, 10835–10845 (2013).

Appendix

Chapter 2: Fabrication and Characterisation of Plasmonic Microcavity Array

2.3.1.2 Spin Coating Method

Initially, rpm speed was tested to obtain the optimal speed for sphere packing and monolayer formation, results can be seen in the appendix. 100 µl of 5 % (w/v) unfunctionalised Spheres in ethanol/ethylene glycol (85:15) were added at different speeds. Figure 109 shows the obtained results. As can be seen, speeds of 1000 rpm and below (A & B) resulted in multilayers. Whereas higher speeds of 2000+ rpm (D & E) resulted in disperse spreading over the gold. The packing indicated other parameters required optimisation prior to speed optimisation. Ethylene glycol was then removed from the composition, leading to faster drying of the spheres and ideally less dispersity as this affected the viscosity. It has been noted by Khoury & Vo-Dinh that similar packing can be seen in ethylene glycols absence with speed and volume adjustments[236].

Sulphate functionalised spheres were attempted on cysteamine pre-treated gold. The charge interaction between the spheres and the gold should encourage close packing, while the high speed encourages mono-dispersal. However, functionalised spheres proved to feature no better than unfunctionalised. This indicates the cysteamine-sulphate interaction is effective.

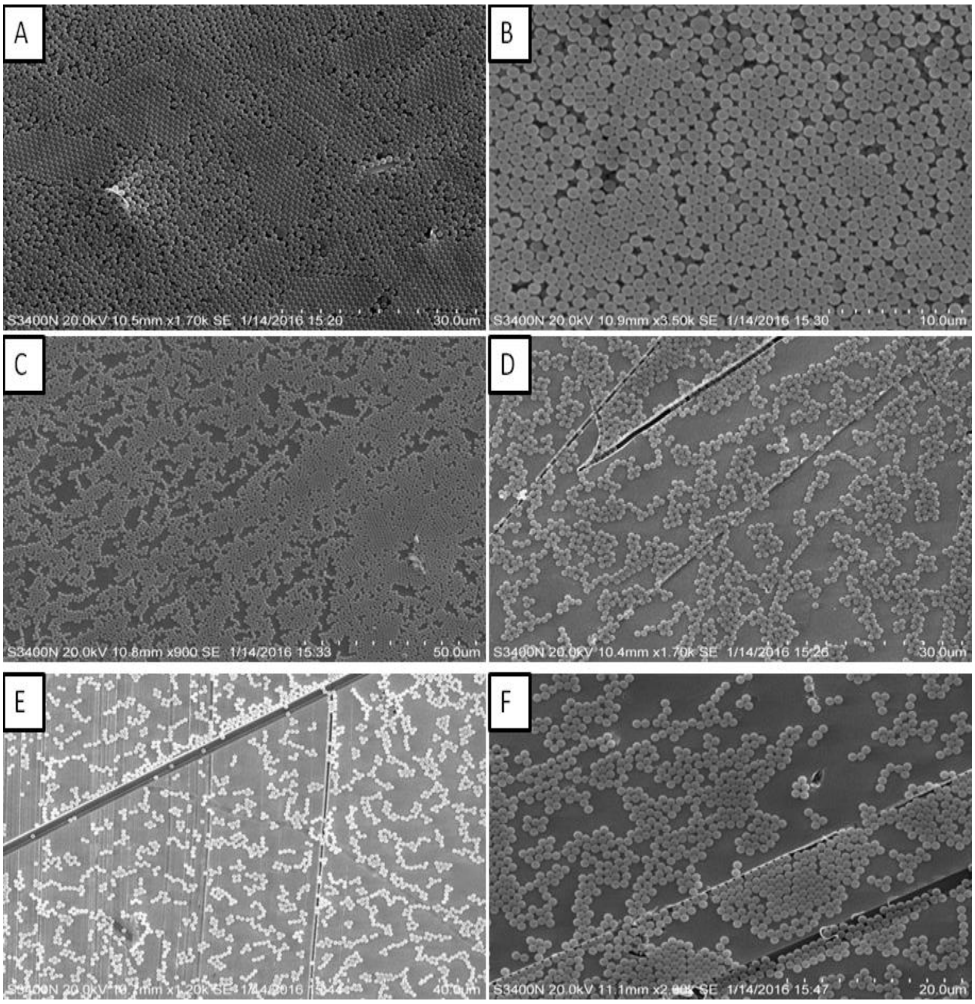

Figure 109: Representative SEM images of gold sputter coated unfunctionalised Ps spheres deposited (100 µl) through spin coating at speed range of 500 rpm – 3000 rpm at room temperature. Where at low rotation speeds multilayers of spheres occurred and at higher speeds, sphere devoid regions occurred in the monolayer. A) 500 rpm, B) 1000 rpm, C) 1500 rpm, D) 2000 rpm, E) 2500 rpm, F)3000 rpm

2.3.1.4 Air/Water Interface Method

As shown in Figure 110 A) samples dried at angles < 30°, resulted in packing in a non-hexagonal fashion, whereas at angles (B), ≥ 60°, ideal packing was obtained. The method was modified slightly and attempted with sulphate functionalised spheres. The results observed in C) & D) were obtained, showing desired packing. Unfortunately, as can be seen in image D, a large region of hexagonal packing is observed surrounded by non-hexagonal regions. Indicating this method also has difficulties in reproducibility. Although the air/water interface method gave better packing than previously observed, the method proved inconsistent, as depending on humidity and temperature, different packing was observed.

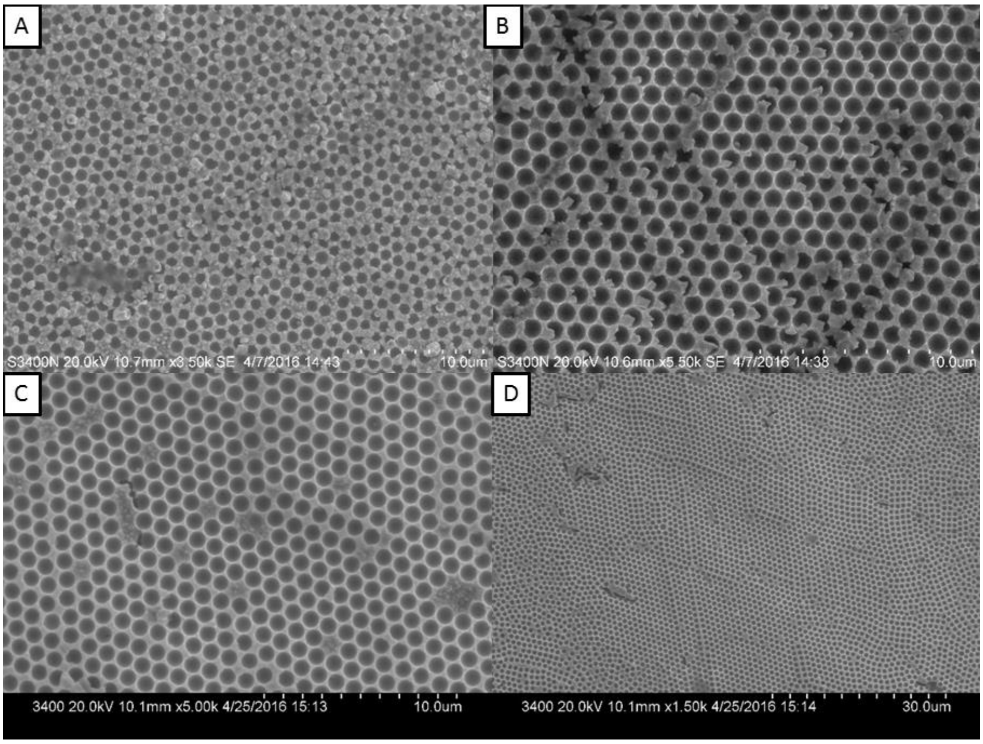

Figure 110: Representative SEM images of A) dried in petri dish B) dried in small beaker C & D) 0.1 % sulfate spheres, cysteamine pre-treated, grown at -0.7 V 0.25 C

2.3.6 Spectroscopic Characterisation of Drug Models

Drug/Dye	**Absorption (nm)**	**Emission (nm)**	**Lifetime (ns)**	**Quantum Yield**
DRAQ7	599, 645	697 nm	-	-
Doxorubicin	480	590	1.5 [247]	9 %[185]
Daunorubicin	48	590	1.5 [247]	9 %[185]
Ru-Tap-Ester	216, 280, 414, 450, 467	640	230 [247]	0.28 ϕ_{1um}[d 203]
Ru-Tap-R8	216, 280, 414, 450, 467	640	205 [247]	-
Ru-DPPZ-Ester	216, 280, 360, 456.2	695	230 [247]	0.29 ϕ_{1um}[d 203]
Ru-DPPS-R8	216, 280, 360, 456.2	640	205 [247]	-

Table A: Table depicting spectroscopic properties for the drugs & dyes used in this study.

5.3.1 Development of Enclosed Raman Platform.

A mask was created by laser cutting 1.5 mm PMMA into a 68.4 x 35. 8 mm rectangular shape and a 50 x 12 mm inner channel and was glued together. PDMS was cured onto the mask, leaving a channel for the chip (Figure 85, PDMS 1). A glass coverslip was then glued onto the surface, leaving the end portion of the channel free for the addition of liquids (Figure 111, Sample 1). When tested, the added solution evaporated within an hour, making it unsuitable.

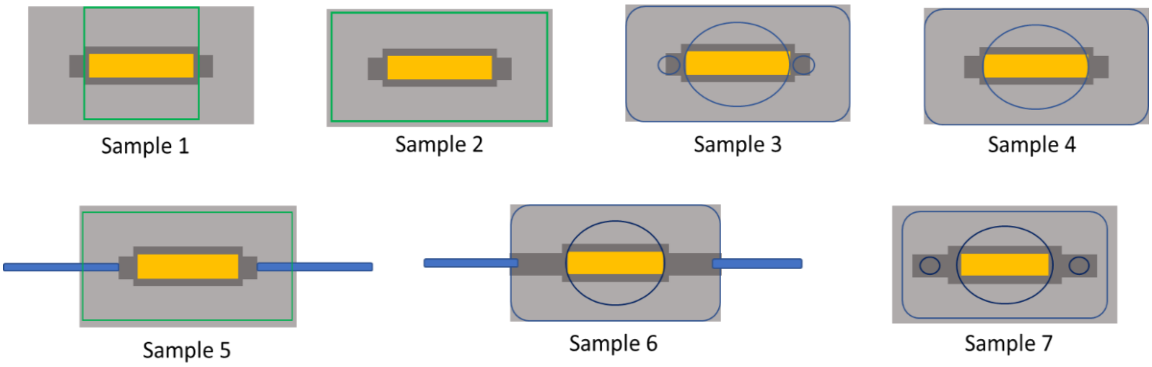

Figure 111: Schematic diagrams of attempted platforms. Grey colour signifies PDMS; Green lines indicate the position of the glass coverslip, Light blue indicates tubing, Dark blue is PMMA and yellow indicates the position of the gold cavity array.

The next approach used a similar set up, except the coverslip fully enclosed the top surface of the PDMS, and the solutions were injected directly through the PDMS and into the cavity (Sample 2). Unfortunately, with this approach, the pressure created when piercing the PDMS, repeatedly resulted in either the cover-glass shattering or its separation from the PDMS. Following this, the next method used PDMS 1. A 300 nm rectangle of PMMA was cut with three circles, one large (161 mm diameter) in the middle and two smaller (2.1 mm diameter) outside it (PMMA 1). A circular cover-glass was glued to the larger circle. The smaller holes were used as injection ports (Sample 3). When tested, it was found that the seal was insufficient and the solution would either evaporate or leak over the course of three hours, resulting in air bubbles across the sample. Air bubbles would result in disruption of the bilayer, making imaging and spectroscopic monitoring unreliable. Tubing was then added to the holes to enclose the system and prevent evaporation; however, leakage remained a problem. A method was also attempted in a set up where PMMA 1 consisted of only the optical window, without the tubing holes (PMMA 2) (Sample 4). Solutions were then injected through the PDMS, but the internal pressure created without the holes resulted in the cover-glass shattering.

The next set up attempted used PDMS 1, where in this approach, the tubing was inserted prior to curing, resulting in the PDMS polymerising around the tubing (Sample 5). This was attempted to minimise leakage at the tubing connection. A glass coverslip fully enclosed the top surface, as an optical window, and the tubing would come out through the sides. Unfortunately, regardless of method, tubing would clog during the curing process. An alternative to this method, involved PDMS 1 being altered to fully extend the channels to the end of the platform (PDMS 2). PMMA 2 was added to fully cover the top surface. Tubing was then inserted through the sides of the platform through holes left from the extended channels (Sample 6). When tested, tubing connections resulted in leakage.

Following this, PDMS 1 and PMMA 1 was re-approached. However, PMMA 1 was modified to be smaller in size (53.3 x 21.8 mm), and therefore, did not fully cover the top surface of the PDMS (PMMA 3); this allowed for a better seal. Tubing was added through the holes (Sample 7). When tested, this appeared more successful than previous methods as leakage only occurred at tubing connections and not at the edge of the PMMA cover. With the success of this method (Sample 7), it was further optimised to minimise leakage. Final version is described in Section 5.3.1.